

Hydrological and erosional response of a small catchment in Sicily

Feliciano Licciardello^{1*}, Salvatore Barbagallo¹, Francesc Gallart²

¹ University of Catania, Department of Agriculture, Food and Environment, Catania, Italy.

² Institute of Environmental Assessment and Water Research (IDAEA-CSIC), Barcelona, Spain.

* Corresponding author. E-mail: flicciar@unict.it

Abstract: Increasing our understanding of the main processes acting in small Mediterranean catchments is essential to planning effective soil and water conservation practices in semi-arid areas. A monitoring program of a Sicilian catchment started in 1996 and ended in 2006. The factors driving the hydrological response for 170 events with runoff generation and 46 with sediment production were specified. The catchment response varied greatly over the year. Rainfall intensity was a poor driver of runoff generation, whereas both the simulations made with the Thornthwaite-Mather water balance model and hydrograph recession analyses, pointed to the chief importance of wet antecedent conditions and soil saturation processes in runoff generation. The influence of rainfall spatial variability was also examined. *SSC-Q* relationships, classified by following their shapes for all sediment production events, suggested that the principal role of small poorly vegetated hillslope patches was as sediment sources and confirmed the complexity of the hydrological response in this small Mediterranean catchment.

Keywords: Hydrological response; Mediterranean hydrology; Runoff generation processes; Flood events.

INTRODUCTION

In many semi-arid regions, upland areas are of crucial importance as a source of water that is necessary for the human life and activities that are mainly concentrated in the drier downstream areas. The seasonality of the Mediterranean climate means that Mediterranean regions are characterized by unevenly distributed water resources, which mainly depend on runoff generated in mountain areas (Latron et al., 2009; Viviroli and Weingartner, 2004), which are, in addition, highly sensitive to changes in their environment. On the one hand, land cover change may seriously affect the hydrological behaviour of Mediterranean catchments (Licciardello et al., 2017). Vegetation removal following fire increases annual runoff, sediment yields and flood frequency and magnitude, whereas the development and densification of forest cover, often occurring after land abandonment, generally leads to a reduction in annual flows (Nunes et al., 2011). On the other hand, climate change in Mediterranean areas will have a hydrological impact that needs to be assessed and for which water management will have to be adapted (Merheb et al., 2016). Thus, improved understanding of the hydrology of Mediterranean mountain areas may help to anticipate the hydrological consequences of both climate and land cover changes.

In Mediterranean mountain areas, hydrological processes are widely variable in time and space owing to the great variability of rainfall and evapotranspirative demand dynamics. The seasonal dynamics of rainfall and evapotranspiration cause high seasonal variations in soil water content and water table depth, leading to the marked non-linearity of the rainfall–runoff relationship. Examples of this non-linearity of hydrological response have been described in several studies of Mediterranean mountain catchments (Latron et al., 2009). Latron et al. (2008) found that evapotranspirative demand was a factor that introduced most of the non-linearity observed into the monthly rainfall–runoff relationship of the small Cal Rodó catchment. High seasonality was also apparent at the event scale, with a storm-flow coefficient characterized by alternation between wet and dry periods during the year. This seasonal behaviour was also seen in the Ciciriello catchment (Cuomo and Guida, 2016).

Here the authors demonstrated experimentally that this behaviour was due to the existence of a typical hydro-geomorphic threshold system at the event scale, in particular to a steady addition of water from distinct components, each with originally different mechanisms of runoff production and response time.

The complexity of Mediterranean hydrological systems also causes marked variation throughout the year in the dominating runoff generation processes, which change from season to season (Latron and Gallart, 2008; Merheb et al., 2016). This leads to some disagreement among hydrologists on the primary runoff generation mechanism in Mediterranean areas. Some studies (Calvo-Cases et al., 2003; Cantón et al., 2011; Gallart et al., 2008; Martínez-Mena et al., 1998) have argued the traditional perception that the primary runoff generation mechanism is Hortonian overland flow and showed that saturation mechanisms are also relevant, being dominant in subhumid climates.

Small mountainous catchments comprise both hillslopes, where the main sediment sources are located, and river channels, where deposition, riverbed erosion and sediment transfer occur. The interplay between these two compartments is complex and remains largely unknown. In particular, small mountainous Mediterranean catchments are characterized by intermittent river flow coupled with high suspended sediment concentrations transiently reached during events. This leads to great unpredictability and non-linearity of discharge and sediment concentration relations (Soler et al., 2008; García-Rama et al., 2016). In this context, the analysis of this relationship allows not only improved calculation of sediment yield, but may also help in understanding the runoff and sediment production processes active in these catchments.

Better knowledge of these processes is essential for planning effective soil and water conservation practices in semi-arid environments, where accurate runoff and sediment yield predictions are difficult, particularly in the absence of adequate data.

The main objective of this article is to analyse the hydrological factors and processes that control runoff and sediment yield in a small mountainous Mediterranean catchment. To achieve this aim, a monitoring program of a Sicilian catchment started in 1996. More precisely, the present paper aims: 1) to analyse the hydrological response of the small catchment at different

temporal scales; 2) to explore to what extent runoff is generated by rainfall excess or saturation mechanisms; 3) to examine how the various hydrological factors affect the hydrological response of the catchment; 4) to explore discharge and suspended sediment concentrations at the event scale, with a view to establishing the relationships between these two variables.

MATERIAL AND METHODS

Study site

The small Cannata catchment is drained by a mountain stream, ephemeral in flow, tributary of the Flascio River and located in eastern Sicily (37° 53' 5" N, 14° 52' 48" E). Climate is Mediterranean sub-humid with a mean annual precipitation (1996–2005) of 715 ± 163 mm, mainly falling between October and January. Mean monthly temperature is between 6°C (January) and 24°C (August). Mean monthly values of Potential Evapotranspiration are between 22.6 mm (December) and 160.7 mm (July), whereas the annual total is 1001 ± 48 mm. The catchment covers about 1.3 km² between 903 m and 1,270 m a.s.l. with an average slope of 21%. The longest pathway is about 2.4 km, with an average slope of approximately 12%. Alluvium in the main drainage net is rather coarse and fraction finer than 2 mm is scarce (<10% for 11 samples).

The Cannata catchment bedrock belongs entirely to the Monte Soro Flysch unit (lower Cretaceous), which consists of a thrust system lying between the Numidian Flysch at the base and the Argille Scagliose Speriore unit. The latter is represented by a tectonic mélange, within which there are exotic blocks, formed by clayey quartz-arenite alternations very similar to those attributed to the Monte Soro unit, from which they can be distinguished only by geometrical position (ISPRAMBIENTE, 2018).

To characterize the topsoil, eleven field soil samples were taken on the hydrological network and fifty-seven on the hillslopes inside the catchment, in the latter starting from the same point and following three main directions (northeast-southwest, north-south and northwest-southeast) in a squared scheme with a side length of 200 m based on the observed variation in the texture samples (Figure 1). The survey identified the dominant (63%) soil texture in the catchment as clay-loam (USDA classification for fine fraction). The rest of the catchment is characterized as loam (21%), loam-sand (10.5%), clay (3.5%) and loam-sand-clay (2.0%). The skeleton is between 2.3 and 36.8%. The soil's saturated hydraulic conductivity (at 10–15 cm of depth), measured with a Guelph permeameter (model 2800, Eijkelkamp, Giesbeek, The Netherlands), was determined at 0.2 to 17.6 mm h⁻¹. Soil profile is characterized by two main layers, the first of which has a dominant loam-sand texture (73% of samples) and the second has a prevalent sandy-loam texture. In about 30% of the catchment, located in the upper part of the hydrological network, the soil depth is from a few centimetres to 0.3 meters. In the rest of the catchment, the soil depth is up to 0.7 m with the exception of about 5% of the catchment where the soil depth reaches 1 m. Some shrinking cracks are visible in bare soil areas during dry spells.

Land use and ground cover modifications were monitored every six months at 24 sites within the catchment, using a 1 m² grid with 0.4 m² sub-grids. Land use monitoring highlighted the prevalence of pasture areas (ranging between 87% and 92% of the catchment area during the observation period) with different vegetation (up to 15 species) and ground cover. The four dominant soil covers included: (1) high-density herbaceous vegetation (eventually subjected to tillage operations) characterized by *Ranunculus bulbosus*, *Trifolium stellatum*, *Trifolium repens*

and *Festuca circummediterranea*, with a ground cover value in the observation period between 17% and 86% (mean of 47%); (2) medium-density herbaceous vegetation characterized by *Dactylis glomerata*, *Trifolium repens*, *Cynosoras cristatus* and *Hedysarum coronarium*, with a ground cover value between 14% and 67% (mean of 36%); (3) sparse shrubs characterized in the higher layer of vegetation by *Crataegus monogyna*, *Genista aetnensis*, *Calicotome infesta*, *Rabus ulmifolium* and *Pyras communis* and in the lower layer by the same species as the high-density herbaceous vegetation, with a ground cover value in the observation period between 30% and 70% (mean of 50%); and (4) cultivated winter wheat planted at the end of October and harvested at the end of July with a wheat-fallow rotation.

The occurrence of overland flow is revealed by a few shallow gullies scattered in mid- and low-slope positions. Most of these gullies are discontinuous ephemeral forms up to 40 cm deep, but two larger ones are up to 2 m deep. None of these gullies is longer than 5 m. Small mass movement features in the form of shallow slumps are scattered in the basin, particularly in the margins of incised stream channels.

In the same area and quite close to the hydrological network, there are some ponds for animal watering (Figure 1).

Additional catchment characteristics and sampling information are reported by Licciardello et al. (2006).

Hydrological measurements

Air temperature, wind, solar radiation and pan evaporation data were recorded by a weather station located close to the catchment (A in Figure 1) with a time resolution of 1 h. Rainfall data were collected at three locations close to and within the Cannata catchment (A, B and C) at 15 s intervals. Flow levels were recorded right before the confluence with the Flascio river (D), using a floating hydrometrograph (MECHEL mod. ID 5755) hydraulically connected to a slow strait created by a weir. Potential evapotranspiration (PET) was evaluated by using the equation based on the Penman-Monteith (P-M) method reported by the Food and Agricultural Organization (Allen et al., 1998). The P-M method is the recommended PET method for the region that includes the Cannata catchment. Actual evapotranspiration was evaluated by starting from potential evapotranspiration and taking into account evaporation of rainfall intercepted by the plant canopy as well as amounts of transpiration and sublimation/soil evaporation. This was based on an approach similar to that of Ritchie (1972), described in detail in Neitsch et al. (2002).

Suspended sediment concentration was measured by drying filtered stream samples in the oven at 105°C for at least 48 hours. Stream water was obtained by an automated water sampler (MODUS mod. 201) with bottles of 200 cc which samples stream water when discharge is above 0.1 m³ s⁻¹, with increasing intervals (between 2 and 30 minutes) in the first 90 minutes and with constant intervals (30 minutes) until the sixth hour. Coarse sediment particles (diameter > 2mm) occasionally taken by the sampler from the channel bottom were excluded from the calculation. The bedload transport was measured by topographic measurements upstream from the weir for about 10 m (measured for groups of events up to June 2004). The database covers a period from October 1996 to March 2006 with some gaps (Figure 1). Due to the gaps, for some purposes SSY had to be estimated for erosive events occurring from October 1996 to March 1997 (observed sediment data started on November 1997, Figure 1) and during December 2002 (2 events occurred in December 2002).

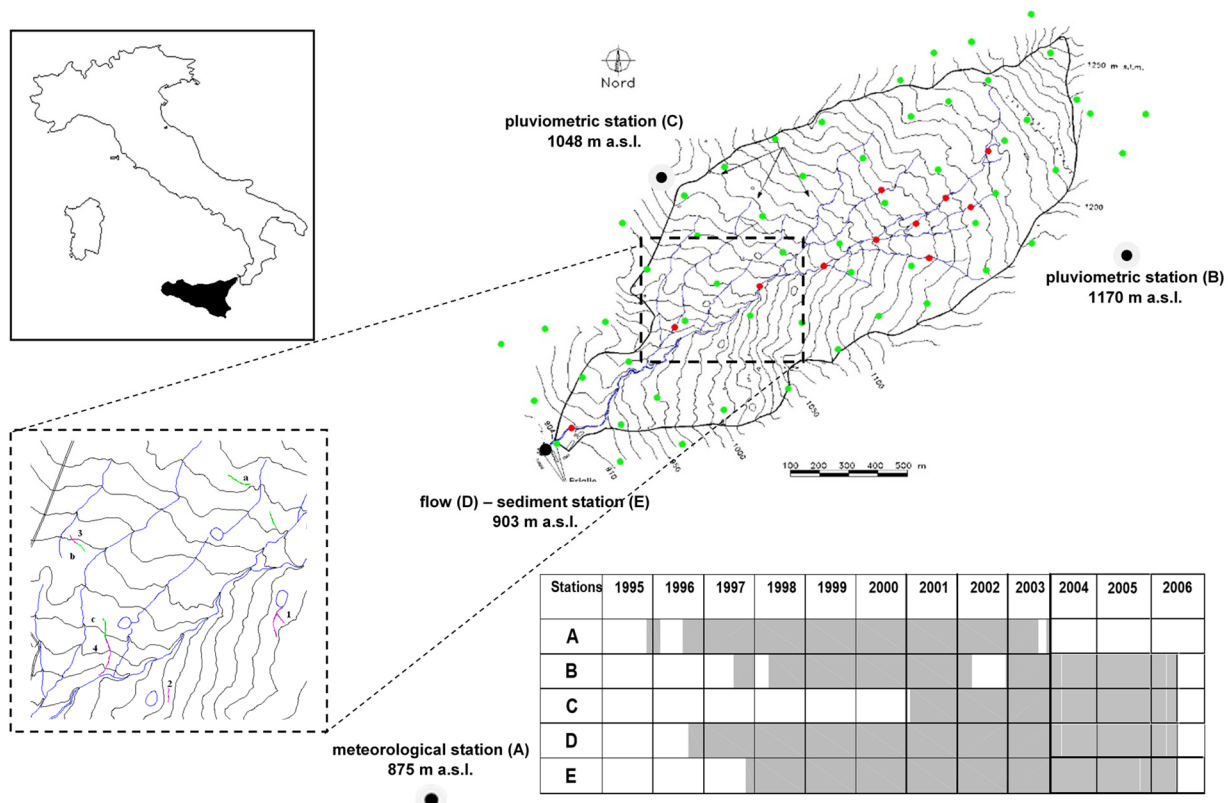


Fig. 1. Layout of sub-watersheds and hydrological network in the Cannata watershed, Sicily. Small dots indicate the location of soil samples. The figure enlargement on the left shows gully formations and small ponds for animal watering. The table shows the recording periods for the diverse stations.

The following abbreviations will be used for the listed variables in the present paper:

- BT* Bedload transport (Mg)
- I5* Event maximal rainfall intensity in 5 minutes (mm h^{-1})
- I30* Event maximal rainfall intensity in 30 minutes (mm h^{-1})
- NP* Number of rainy days with depth > 1 mm (–)
- AET* Actual evapotranspiration (mm)
- PET* Potential evapotranspiration (mm)
- PF* Event peak flow ($\text{m}^3 \text{s}^{-1}$)
- Q* Discharge ($\text{m}^3 \text{s}^{-1}$)
- P* Rainfall depth > 1 mm (mm)
- RC* Storm runoff coefficient (%)
- Ru* Runoff (mm)
- SSC* Suspended sediment concentration (g l^{-1})
- SSY* Suspended sediment yield (Mg)
- TS* Total sediment yield (Mg)

Analysis of hydrological and sediment data

First, basic statistics, water balance and simple correlation (by using the coefficient of correlation r) of the variables describing the main characteristics of P and Ru depths, $I30$, RC , PF , SSY , SSC and BT were analysed at aggregated temporal scales (annual, monthly and mean monthly scale) and the event scale. In particular, monthly and annual maximum values of $I30$ and PF were the highest values by month and year, respectively. The rest of the monthly and annual data was calculated by adding event data by month and year. Mean monthly data for all considered variables (cumulative or maximum values) were obtained by calculating the averages of monthly data, taking the same month of each year. To analyse the changing behaviour of the catchment throughout the year, basic statistics and simple correlation of the variables were analysed all together and by

grouping them in two periods, defining a “wet period” from December to May and a “dry period” from June to November at aggregated and event temporal scales. All the relationships between the main hydrological factors tested were analysed by using the correlation coefficient after the verification of significance. Rainfall variables used in the paper (when it is not specified) are areal averages calculated by the Thiessen polygons method, taking the available measurements for each event.

The patterns and variability of the main rainfall characteristics, depth and intensity, were analysed. In particular, the return period of the P depth and of the $I30$ was evaluated for all the events by comparing them with the probability curve of the Randazzo meteorological station (located 6.7 km from the Cannata outlet). The curve was implemented by using the Gumbel distribution (Generalized Extreme Value distribution Type-I). Frequency distributions of P and Ru depths, $I30$ and SSY at event scale were also analysed. Moreover, the spatial variability of P depth, $I30$ and $I5$ among the observations at the three available pluviographic stations was evaluated by calculating the percentage difference between the values recorded for most significant events. Events recorded in the three pluviographic stations were categorized in classes of 5 mm of depth and 5 mm h^{-1} of intensities and frequencies per each rainfall class were then calculated. In particular, the comparison was carried out for events with P depth greater than 15 mm, then for events with $I30$ greater than 10 mm h^{-1} , and finally for events with $I5$ greater than 25 mm h^{-1} .

Afterwards, when rainfall intensity appeared as a poor driver of runoff response in the catchment, the likely effect of soil saturation on runoff generation was investigated by comparing observed monthly Ru depths with saturation excess water calculated with the Thornthwaite-Mather (T-M) water balance model (Steenhuis and Van der Molen, 1986; Thornthwaite and

Mather, 1955). This conceptual model was selected because it is based in very few assumptions. Precipitation is stored in the soil reservoir until the soil water reaches its maximal value (soil water retention capacity) then the excess water is moved to runoff. The quotient between actual and potential evapotranspiration grows linearly from 0 to 1 following soil water content from 0 to soil water retention capacity, which is the only parameter of the model. The optimisation of this parameter was made using the Nash-Sutcliffe (NS) efficiency criterion (Nash and Sutcliffe, 1970) to test the quality of the simulations. Tutorials of this model can be found on the Internet (https://wwwbrr.cr.usgs.gov/projects/SW_MoWS/Thorntwaite.html). A period consisting of one year with average monthly precipitation and potential evapotranspiration followed by six months of real data was used to warm-up the model, thus obtaining adequate simulated initial soil water content.

A further test to investigate the runoff generation processes was made with the recession limbs of a subset of events without precipitation after the flow peak, for obtaining the recession constants K following the method recommended by Dunne (1978):

$$Q_t = Q_0 \cdot K^t \tag{1}$$

where Q_t is discharge at time t , Q_0 is peak discharge, K is a recession constant and t is the time since the discharge peak (hr). Then the recession constants obtained were analysed for relationships with other hydrological variables and compared with the constants reported by Dunne (1978) for catchments with rainfall excess overland flow, saturation overland flow and subsurface stormflow hydrographs.

Finally, 46 significant events, i.e. those having continuous data and absence of anomalies in the time series, were selected for analysing sediment response varying in time. The data, recorded at different time scales, were used to analyse the relationships between SSC and Q during flood events. The loop-shaped curves observed between SSC and Q were used to infer the sediment availability that derives from the sediment source areas and/or from possible intermediate sediment deposits (Williams, 1989). In the clockwise loop, a rapid increase in suspended sediment at the beginning of the flood event is attributed to the presence of available sediment at the water course. If the SSC decreases before the falling limb of the hydrograph, the sediment source areas can be considered limited. In the anti-clockwise loop, however, the sediment source areas are mainly located on hillslopes or at headwaters, and/or the sediment moves slower than the peak discharge (Gentile et al., 2010).

RESULTS

General patterns and water balance

Over the observation period (October 1996–March 2006), the mean P pattern showed a contrast between summer with a low total amount ($P = 91$ mm) and the other seasons with a total P amount of 153 mm (spring), 195 mm (winter) and 264 mm (autumn). Sediment yield followed the same trend, being null in summer, 8 Mg in spring, 58 Mg in winter and 97 Mg in autumn. During the same period, mean Ru totals had a somewhat different pattern, with winter the most responsive period ($Ru = 72$ mm) followed by autumn (54 mm), spring (25 mm) and summer ($Ru = 0$ mm).

Mean monthly data of P and NP measured at the Cannata catchment and long-term monthly mean values of P measured at the Randazzo station were compared (Figure 2). Monthly mean P depths during this 10-year period were quite representative of the trend observed in the long term (48 years) in the

area, although P amounts observed in February, July, August and October were underestimated in the 10-year period, and April and December totals were overestimated.

November and December were the months with the highest mean value of P , while the highest values of Ru depths and SSY values were in December and January. In particular, during the observation period the seasonal Ru in autumn ranged from the minimum (0 mm) to the maximum (195 mm) recorded values.

On the annual scale, wide variability in the main hydrological response variables (Ru , RC , PF , SSC , SSY and BT) can be observed (coefficient of variation, CV, between 61% for PF and 131.5% for BT), corresponding to minor variability of P , NP and $I30$ (CV up to 37%) (Table 1). The annual RC , in particular, varied from 5.72 to 40%, while annual SSY ranged from a minimum of 17.6 to 405.9 Mg ha⁻¹. The annual BT in the observation period was of the same order of magnitude as the SSY ; the statistical parameters calculated at the annual scale between the two variables were also very similar (Table 1).

The best results of the T-M water balance model (Figure 3) were obtained by calibration when a soil water-holding capacity of 224 mm was used. Runoff was simulated as soil saturation excess when this capacity was reached, resulting in good discrimination of the periods with and without runoff (70%), although the best NS efficiency was only 0.14. The analysis of the results showed that this poor efficiency was due to the temporal shifts of two of the months with relevant runoff, November 1996 and December 2002, attributable to the limitations of the monthly temporal scale. Indeed, on shifting backwards one month the Ru simulated for these two months, NS efficiency rose to 0.57 and runoff period discrimination to 99%. Despite some limitations, the monthly temporal scale was adequate for describing the variation in water balance over the year in the Cannata catchment. In particular, the seasonal dynamics of both P and PET promote different periods during the year (Figure 2). A dry period occurs during late spring and summer, when low precipitation and high evapotranspiration losses deplete soil water to the point that the AET to PET ratio may be lower than 20%. Under these conditions most of the rainfall re-evaporates and only long or repeated events are able to generate runoff. A transition period occurs in autumn, as rainfall needs to fill catchment water reserves before runoff is generated. After the filling of water reserves, the wet period usually occurs up to early spring.

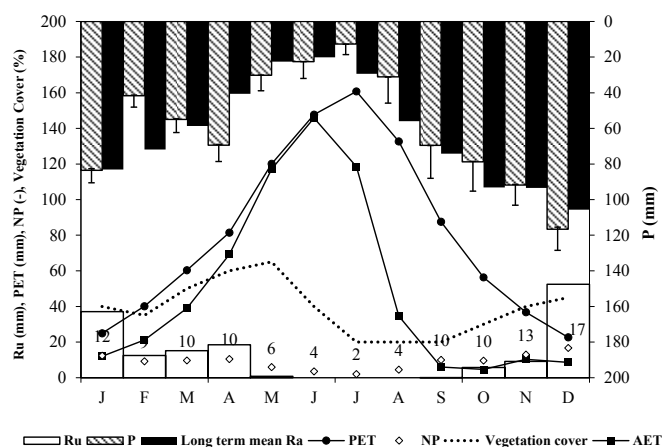
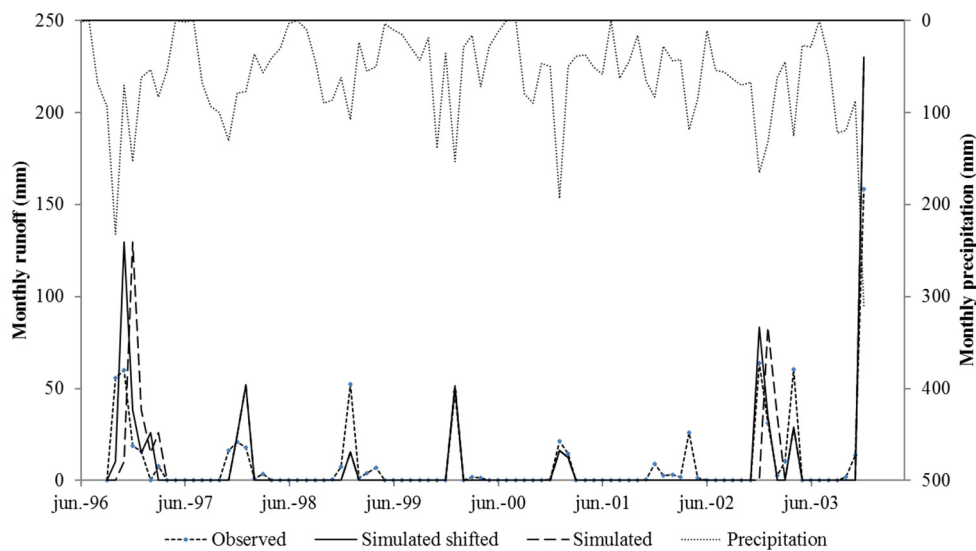


Fig. 2. Monthly mean values of precipitation depths (P and its standard deviation), number of rainy days (NRA), potential evapotranspiration (PET), actual evapotranspiration (AET), runoff depths (Ru) and Vegetation Cover observed at the Cannata watershed (1996–2006) and long term monthly mean P measured at the Randazzo pluviometric station.

Table 1. Summary of annual hydrological records at the Cannata watershed. CV: coefficient of variation, Stdev: standard deviation. *1996 is an incomplete year.

Year/ Statistics	Precipitation Depth (<i>P</i>) mm	Rainy days (<i>NP</i>)	Max rain intensity (<i>I30</i>) mm h ⁻¹	Runoff depth (<i>Ru</i>) mm	Runoff coefficient (<i>RC</i>) %	Peak flow (<i>PF</i>) m ³ s ⁻¹	Susp. sed. conc. (<i>SSC</i>) g l ⁻¹	Susp. sed. yield (<i>SSY</i>) Mg	Bedload transport (<i>BT</i>) Mg
1996*	646.6	74.0	51.8	134.6	20.8	2.4	2.1	286.2	136.7
1997	730.4	135.0	28.8	62.3	8.5	1.0	0.9	56.8	29.0
1998	537.0	118.0	21.4	30.7	5.7	0.4	0.6	17.6	68.4
1999	523.0	113.0	29.1	104.4	20.0	1.4	0.5	50.5	12.5
2000	590.2	119.0	33.0	65.5	11.1	1.2	1.1	73.2	70.2
2001	621.4	115.0	26.8	45.8	7.4	0.9	0.4	18.7	9.0
2002	757.0	109.0	38.8	73.6	9.7	1.1	0.7	48.5	85.4
2003	894.8	89.0	37.6	358.1	40.0	3.4	1.1	405.9	550.8
2004	724.2	96.0	61.2	276.9	38.2	2.2	0.9	242.4	197.3
2005	685.2	70.0	20.6	213.1	31.1	3.3	1.5	313.3	
Median	665.9	111.0	31.0	89.0	15.5	1.3	0.9	65.0	70.2
Average	671.0	103.8	34.9	136.5	19.3	1.7	1.0	151.3	128.8
Stdev	112.3	21.0	13.0	110.4	13.0	1.0	0.5	144.8	169.4
CV%	16.7	20.2	37.3	80.9	67.7	60.6	53.5	95.7	131.5
Min	523.0	70.0	20.6	30.7	5.72	0.37	0.4	17.6	9.0
Max	894.8	135.0	61.2	358.1	40.0	3.4	2.1	405.9	550.8

**Fig. 3.** Monthly precipitation *P* and runoff *Ru* observed and simulated with the T-M model.

Analysis of the response at the annual and monthly scales

As well as the soil water balance and T-M model results analysed above, the effects of the main factors driving the response at the Cannata catchment were investigated at different temporal scales by correlations between hydrological variables (Table 2).

The correlation between *NP* and all the selected hydrological response variables was negative and significant at the annual scale, while being positive and always significant at the mean monthly scale. The fact that the correlation was not always significant at the monthly scale was attributed to that the years with few rainfall events generally had a more significant response than those with many events. A clear concentration of major events into a few months was also seen; about 35% of the total *P* and 78% of the total *Ru* was recorded in just 14% of the 120 months in the study.

Precipitation was a better driver of the Cannata hydrological response in terms of *Ru*, *RC*, *PF*, *SSC* and *SSY* than *I30*. In particular, the correlations *P-Ru*, *P-PF* and *P-SSY* always had significant correlation coefficients equal to or higher than 0.57 at annual, monthly and mean monthly time scales. The fact that *I30* was not a good driver of the hydrological response was clearly seen at annual, monthly and mean monthly scales by

coefficients of correlation always smaller than 0.51 and frequently non-significant when all the months of the year were taken together (Table 2). Annual *I30* explained 70% of variability on the *SSC* scale if just the events with runoff higher than 1 mm were included (data not shown). *Ru* explained somewhat better than *P* the variability of the sediment response (Table 2) at each analysed temporal scale; in this case, months with zero value of runoff were excluded from the correlation.

The correlation of *TS* (*SSY+BT*) with *P* and with *Ru* slightly increased with respect to the correlation with the *SSY* ($r = 0.75$ and 0.91 respectively) at the annual and mean monthly scales. At the monthly scale the correlation decreased because *TS* data were collected on a seasonal scale (Table 2).

Given the strong differences in water balance during the year, the correlations were also tested after dividing the year into two periods: the wet period from December to May and the dry period from June to November. After this division, the correlations driven by *P*, *Ru* and *I30* generally improved at the monthly and mean monthly scales.

In particular, the wet period was the one with the strongest *P-Ru* relationship (followed by *P-SSC* and *P-SSY*), attributable to the soil being already wet and the evapotranspirative demand low during this period (Table 2).

Table 2. Coefficient of correlation between the main hydrological factors at annual, monthly and mean monthly scales in the Cannata watershed.

	Coefficient of correlation, r^*						
	Annual (n = 10)	Monthly (n = 112)	Monthly wet (n = 58)	Monthly dry (n = 54)	Mean monthly all (n = 12)	Mean monthly wet (n = 6)	Mean monthly dry (n = 6)
<i>P-Ru</i>	0.70	0.69	0.82	0.58	0.74	0.98	0.81
<i>P-RC</i>	0.55	0.36	0.33	0.49	0.62	0.83	0.81
<i>P-PF</i>	0.57	0.73	0.84	0.60	0.79	0.96	0.81
<i>P-SSC</i>	0.23	0.66	0.72	0.58	0.64	0.95	0.63
<i>P-SSY</i>	0.63	0.69	0.78	0.60	0.77	0.93	0.72
<i>P-TS</i>	0.75	0.58	0.66	0.51	0.76	0.91	0.55
<i>NP-P</i>	-0.29	0.60	0.33	0.82			
<i>NP-Ru</i>	-0.65	0.24	0.11	0.28	0.80	0.98	0.78
<i>NP-RC</i>	-0.70	0.25	0.04	0.29	0.75	0.89	0.78
<i>NP-PF</i>	-0.86	0.32	0.17	0.34	0.79	0.97	0.76
<i>NP-SSC</i>	-0.72	0.40	0.32	0.41	0.51	0.97	0.53
<i>NP-SSY</i>	-0.84	0.23	0.11	0.35	0.75	0.93	0.63
		(n = 54 ^{**})	(n = 46 ^{**})	(n = 8 ^{**})			
<i>Ru-RC</i>	0.97	0.44	0.41	0.85	0.69	0.44	–
<i>Ru-PF</i>	0.88	0.87	0.90	0.75	0.99	0.99	–
<i>Ru-SSC</i>	0.35	0.51	0.62	0.60	0.86	0.96	–
<i>Ru-SSY</i>	0.90	0.86	0.89	0.77	0.91	0.95	–
<i>Ru-TS</i>	0.91	0.81	0.83	0.72	0.91	0.95	–
<i>I30-Ru</i>	0.45	0.28	0.46	0.45	-0.27	0.51	–
<i>I30-RC</i>	0.48	-0.20	-0.12	0.06	-0.67	-0.47	–
<i>I30-PF</i>	0.28	0.48	0.49	0.75	-0.26	0.42	–
<i>I30-SSC</i>	0.36	0.51	0.25	0.70	-0.01	0.52	–
<i>I30-SSY</i>	0.40	0.50	0.50	0.85	0.03	0.65	–

All the correlations are significant at $p < 0.05$, except those shown in *italics*.

* Months with no observed runoff were not included when *Ru* and *I30* were used as independent variables

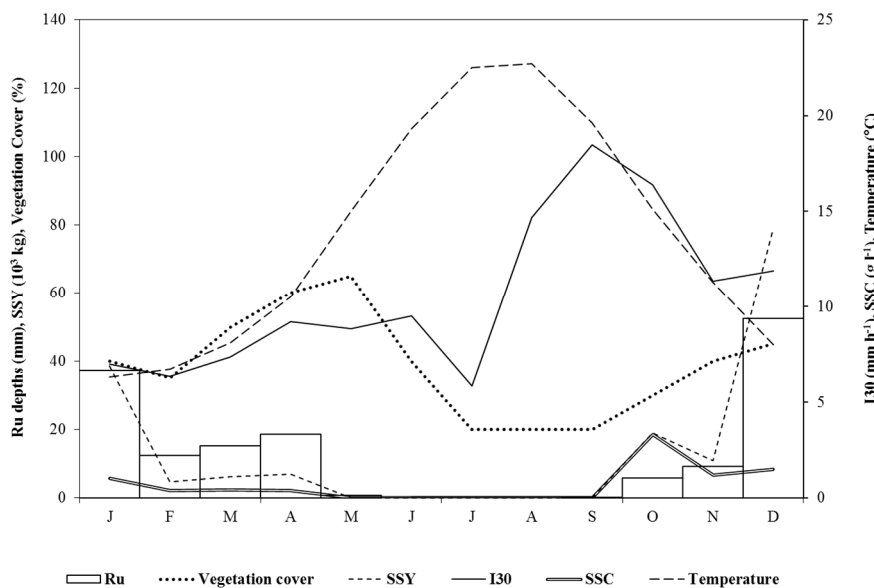


Fig. 4. Mean monthly variation of runoff (*Ru*), vegetation cover, maximal rainfall intensity in 30 min (*I30*), suspended sediment yield (*SSY*) and suspended sediment concentration (*SSC*).

After the division of the data into two periods, *I30* was a better driver of *PF*, *SSC* and *SSY* in the dry period than in the wet period. This behaviour was attributed mainly to the relationship between *I30* and *Ru* throughout the year (Figure 4). In particular, the highest *I30* values were observed from May to October (8.8–16.5 mm h⁻¹), when mean monthly *Ru* values were very close to zero, with the exception of October, when mean monthly *SSY* actually rose (reaching 18.9 Mg) and *SSC* values reached the highest mean monthly value in the year (3.3 g l⁻¹). The values of both *SSY* and *SSC* decreased in November, linked to decreased *I30* and mean monthly *Ru* depths still being not very high compared with other months.

Then, in December and January we had the highest values of mean monthly *SSY* (79.2 and 38.6 Mg) and high values of *SSC* (1.0 and 1.5 g l⁻¹, respectively) linked to the highest values of mean monthly *Ru* depths observed during these months. February was the month with the lowest values of *Ru* depth and *I30* of the wet months, when both *SSY* and *SSC* reached a minimum. Starting from this month, vegetation cover might also affect the *SSY* and *SSC* values. In particular, even though *I30* increased in March and April, *SSY* and *SSC* did not increase a lot (6.3 and 6.9 Mg for *SSY* and 0.40 g l⁻¹ for *SSC*): vegetation cover growth might well reduce the role of more water and energy.

The greater rise of the correlation coefficients at the mean monthly scale than of those at the monthly scale was significant just for the correlations driven by *NP*; mean monthly scale correlations for the dry period were not evaluated because of few data different from zero (Table 2).

Analysis of the response at the event scale

As explained above, aggregated temporal scales (annual, monthly and mean monthly) are not sufficient to explain the hydrological behaviour of the Cannata catchment. Therefore, the data were also analysed at the event scale.

There were 170 rainfall events with observed *Ru* higher than 0.03 mm recorded at the Cannata catchment during the monitoring period; just 23 of these events occurred in the dry period (in October and November) and the rest in the wet period (Table 3). Most events had a *P* depth below the expected 2-year return period for this location; few events showed a *P* depth higher than the expected value for the 5-year return period (03/10/1996; 09/10/1996; 30/11/1996; 05/04/2003); and two events observed on 12/12/2003 and 13/12/2005 had a *P* depth higher than the expected value for a 200-year return period. Most events had an *I30* below the expected value for a 2-year return period equal to 35.66 mm h⁻¹; few events showed a *I30* very close to (19/10/2003; 12/12/2003; 13/12/2005) or higher (08/10/1996 and 11/10/1996 with a value equal to 51.8 and 37.1 mm h⁻¹) than the expected value for a 2-year return period

(expected values for 3 and 5-year return period were 44.34 and 54.0 mm h⁻¹). The combination of high *P* and *I30* resulted in the highest *SSY* observed during the observation period (289 Mg for 13/12/2005; 281 Mg for 12/12/2003; 157 Mg for 08-09/10/1996).

P, *Ru* and *SSY* variables showed skewed distributions, with many more observation of low magnitude especially for *Ru* depth and *SSY* and especially in the wet period (Table 3). For these two variables, only a few events had high or very high values.

While the five largest rainfall events represented 18% of the *P* accumulated during these ten years, their records represented around 33% of accumulated *Ru* and 45% of accumulated *SSY*.

High spatial variability of the main rainfall characteristics was found (Table 4). *P* depth, *I30* and *I5* values were recorded for most significant events at the pluviographic stations in the Cannata catchment. *P* depth differences, evaluated for events greater than 15 mm, were up to 46%. *I30* and *I5* differences, evaluated for events greater than 10 and 25 mm h⁻¹, respectively, were up to 60%. The events with the highest spatial variability in rainfall depth and intensity occurred during the dry period (in the months from September to November).

At the event scale, correlation coefficients confirmed and even clarified some behaviour already noted at aggregated temporal scales (Table 5). *P* was a better driver of the overall hydrological response than *I30*, which had non-significant relationships with *RC* for all the periods, making clear the low importance of rainfall excess processes in the generation of

Table 3. Summary of the statistics of the variables at the event scale observed at the Cannata watershed (1996–2006) in wet and dry periods as well as all events together. *RD*: rainfall duration, *RUD*: runoff duration, *N*: sample size, *Stdev*: standard deviation, *CV*: coefficient of variation. The other abbreviations are as in Table 1.

Wet period	<i>P</i>	<i>RD</i>	<i>I30</i>	<i>RUD</i>	<i>PF</i>	<i>Ru</i>	<i>RC</i>	<i>SSC</i>	<i>SSY</i>
	mm	h	mm h ⁻¹	H	m ³ /s	mm	%	g/l	Mg
<i>N</i> events in wet period	146	146	146	146	146	146	146	50	50
Median	11.5	12.0	4.8	19.5	0.2	2.6	0.3	0.8	8.7
Average	18.0	14.2	5.4	26.6	0.4	7.8	0.4	1.1	27.2
Stdev	23.2	10.1	4.2	21.8	0.5	17.1	0.3	0.9	56.5
CV%	128.6	70.7	77.8	81.9	136.9	220.8	72.1	85.8	207.4
Min	1.2	0.6	0.4	4.5	0.0	0.0	0.0	0.1	0.6
Max	200.6	48.7	15.3	169.5	3.4	145.3	1.0	4.9	289.2
Skewness	4.9	0.9	2.4	3.5	3.4	5.7	0.7	1.9	4.0
Dry period	<i>P</i>	<i>RD</i>	<i>I30</i>	<i>RUD</i>	<i>PF</i>	<i>Ru</i>	<i>RC</i>	<i>SSC</i>	<i>SSY</i>
	mm	h	mm h ⁻¹	H	m ³ /s	mm	%	g/l	Mg
<i>N</i> events in dry period	23	23	23	23	23	23	23	8	9
Median	14.8	7.8	7.7	13.0	0.2	2.4	0.2	1.4	32.4
Average	22.5	10.3	13.0	20.4	0.5	6.4	0.2	2.7	33.1
Stdev	20.0	11.3	12.1	17.8	0.6	12.6	0.2	3.1	32.1
CV%	89.0	109.7	93.0	87.3	117.7	195.9	94.8	112.5	97.0
Min	2.8	0.4	2.0	5.5	0.0	0.0	0.0	0.0	0.1
Max	82.4	53.8	51.8	81.0	2.4	54.0	0.7	9.7	96.6
Skewness	1.9	2.8	2.0	2.3	1.4	3.2	1.2	1.6	0.9
All events	<i>P</i>	<i>RD</i>	<i>I30</i>	<i>RUD</i>	<i>PF</i>	<i>Ru</i>	<i>RC</i>	<i>SSC</i>	<i>SSY</i>
	mm	h	mm h ⁻¹	H	m ³ /s	mm	%	g/l	Mg
<i>N</i> all events	170	170	170	170	170	170	170	58	59
Median	12.3	11.6	4.8	19.3	0.2	2.4	29.1	0.9	8.8
Average	18.3	13.7	6.5	26.4	0.4	7.5	33.2	1.3	27.7
Stdev	22.7	10.3	6.5	22.9	0.5	16.5	25.0	1.5	53.0
CV%	124.2	75.0	100.7	86.7	133.8	219.0	75.4	120.6	191.0
Min	1.2	0.4	0.4	4.5	0.0	0.0	0.2	0.0	0.1
Max	200.6	53.8	51.8	169.5	3.4	145.3	99.3	9.7	289.2
Skewness	4.6	1.2	3.5	3.3	3.0	5.6	0.7	3.5	4.1

Table 4. Percentage differences between rainfall depths (*P*), along with 30 and 5-minute intensities (*I30* and *I5*) observed for most significant events at the pluviographic stations in the Cannata watershed (indications of event number and data of the event with the maximum difference in brackets).

Stations	Relative differences		
	<i>P</i> [for values>15mm]	<i>I30</i> [for values>10mm h ⁻¹]	<i>I5</i> [for values>25mm h ⁻¹]
A-B	46% (42, 28/11/1999)	60% (18, 19/11/1999)	62% (25, 20/08/1997)
A-C	35% (22, 18/11/2002)	47% (14, 21/08/2001)	47% (12, 15/10/2003)
B-C	46% (37, 26/11/2003)	53% (17, 29/09/2003)	57% (19, 01/09/2001)

Table 5. Correlation coefficients between the main hydrological factors at the Cannata watershed (1996–2006) at the event scale. Abbreviations as in Table 1. All the correlations except those in *italics* are significant at least at $p < 0.05$.

	Correlation coefficient values at the event scale		
	Whole period	Wet period	Dry period
<i>P-Ru</i>	0.86	0.88	0.80
<i>P-RC</i>	0.26	0.26	0.43
<i>P-PF</i>	0.76	0.82	0.45
<i>P-SSC</i>	0.14	0.31	-0.07
<i>P-SSY</i>	0.90	0.92	0.60
<i>RD-P</i>	0.23	0.17	0.74
<i>RD-Ru</i>	0.23	0.14	0.86
<i>Ru-RC</i>	0.54	0.53	0.75
<i>Ru-PF</i>	0.84	0.90	0.60
<i>Ru-SSC</i>	0.04	0.24	-0.23
<i>Ru-SSY</i>	0.89	0.92	0.52
<i>PF-SSY</i>	0.91	0.93	0.89
<i>PF-RC</i>	0.57	0.59	0.75
<i>PF-SSC</i>	0.40	0.46	0.41
<i>I30-Ru</i>	0.42	0.48	0.33
<i>I30-RC</i>	0.05	0.07	0.30
<i>I30-PF</i>	0.51	0.49	0.58
<i>I30-SSC</i>	0.48	0.35	0.93
<i>I30-SSY</i>	0.67	0.74	0.79

runoff. However, *I30* was the best driver of *SSC* and, after the subdivision into two periods, also became the best driver of *PF* and *SSY* in the dry period. The improvement of the correlations driven by *I30* during the dry period can be explained by the events' wider range in this period, with *I30* varying from 2.0 to 51.8 mm h⁻¹. Therefore, once runoff is generated in this period, even if it is low, the transported sediment rises. For example, two events observed in October and November 1996 gave *SSY* equal to 0.15 and 4.1 Mg with *Ru* equal to only 2.0 and 3.0 mm.

Rainfall duration did not drive the hydrological response; the high values of *r* in the dry period are due to a very long event for this climate (53 hours) observed in November 1996. Apart from this correlation, *r* was generally higher in the wet than in the dry period with the exception of correlations involving *RC* and *I30*.

The values of the recession constants *K* obtained for 54 events with the Dunne (1978) method had a range between 0.33 and 0.83 with a median of 0.6. These values of *K* showed a marginally significant negative correlation with *PF* ($r = -0.29$, $p = 0.087$), but significant negative relationships with *SSC* ($r = -0.70$) and *I30* ($r = -0.44$). The negative signs were to be expected because the lower the constant *K* is, the sharper the recession hydrograph. The four events with the lowest *K* values occurred in October and November.

SSC-Q dynamics during events

The relationships between *SSC* and *Q* were analysed for all 46 events with *SSY* in the Cannata catchment. Four classes of the five identified in the literature (Williams, 1989) were identified. The number of events in each class was different. In particular, most of the events, 25, revealed a clockwise relationship: the sediment peak arrives at the gauging section before the

water-discharge peak and the concentration values on the rising limb of the graph are greater for the same discharge than those on the falling limb. These events were characterized by high values of *I30*. Eight out of ten events with the highest observed values of *I30* ($> 8 \text{ mm h}^{-1}$) revealed a clockwise relationship. The other two events characterized by high values of *I30* revealed a figure-eight loop. The shape of these two intense events may be explained by their occurrence just after events with sediment production, so limiting sediment availability. Of the remaining events, seven revealed an anti-clockwise loop with the water-discharge peak arriving at the gauging section before the sediment peak; nine events were characterized by a figure-eight loop (first an anti-clockwise loop and then clockwise) and two were characterized by a single-line-plus loop (Figure 5). It was not possible to identify a prevalent type of event depending on the wet or dry periods because only 3 events with sediment production occurred in the dry period.

DISCUSSION

Although the analysis of the results for hydrological factors and processes driving runoff and sediment yield in the Cannata catchment showed some similarities with other small mountainous Mediterranean catchments, it also highlighted some behaviour that in the literature was not usually attributed to this area.

With the sub-division of the Mediterranean region into three areas (Merheb et al., 2016), even if Italy is included in the north-western area, the Cannata catchment shared climate characteristics similar to the eastern and southern areas in terms of annual precipitation, runoff, aridity index and coefficient of runoff. Eastern areas were characterized by the highest variability of hydrological response, while southern areas were characterized by the highest aridity index.

The characteristics of precipitation of this Mediterranean climate and the non-linearity of the rainfall-runoff relationships determined very large inter-annual variability in hydrological response in the Cannata catchment, with CV equal to 83%, 125% and 128% for *RC*, *Ru* and *TS*, respectively. Similar CV values were found in La Conchuela, a small olive catchment on a vertic soil, by Gómez et al. (2014), corresponding with *P* characterized by CV values higher (CV about 40% for *P* and mean *I30*) than those observed in the Cannata catchment.

Seasonality

The large temporal variability of monthly rainfall found in the Cannata catchment is also typical of the Mediterranean area. It was also found in the Chicamo catchment in Spain by Martínez-Mena et al. (1998), where about 50% of precipitation fell in 14% of the 36 months of the study. More generally, the *P* pattern identified here is characteristic of the western Mediterranean, being minimal in summer and maximal in autumn–winter. Monthly *Ru* and *SSY* followed the pattern of precipitation during the winter-spring season, being delayed in autumn due to the deep water deficit in summer. The succession of three different periods during the year, determined by *AET*, that

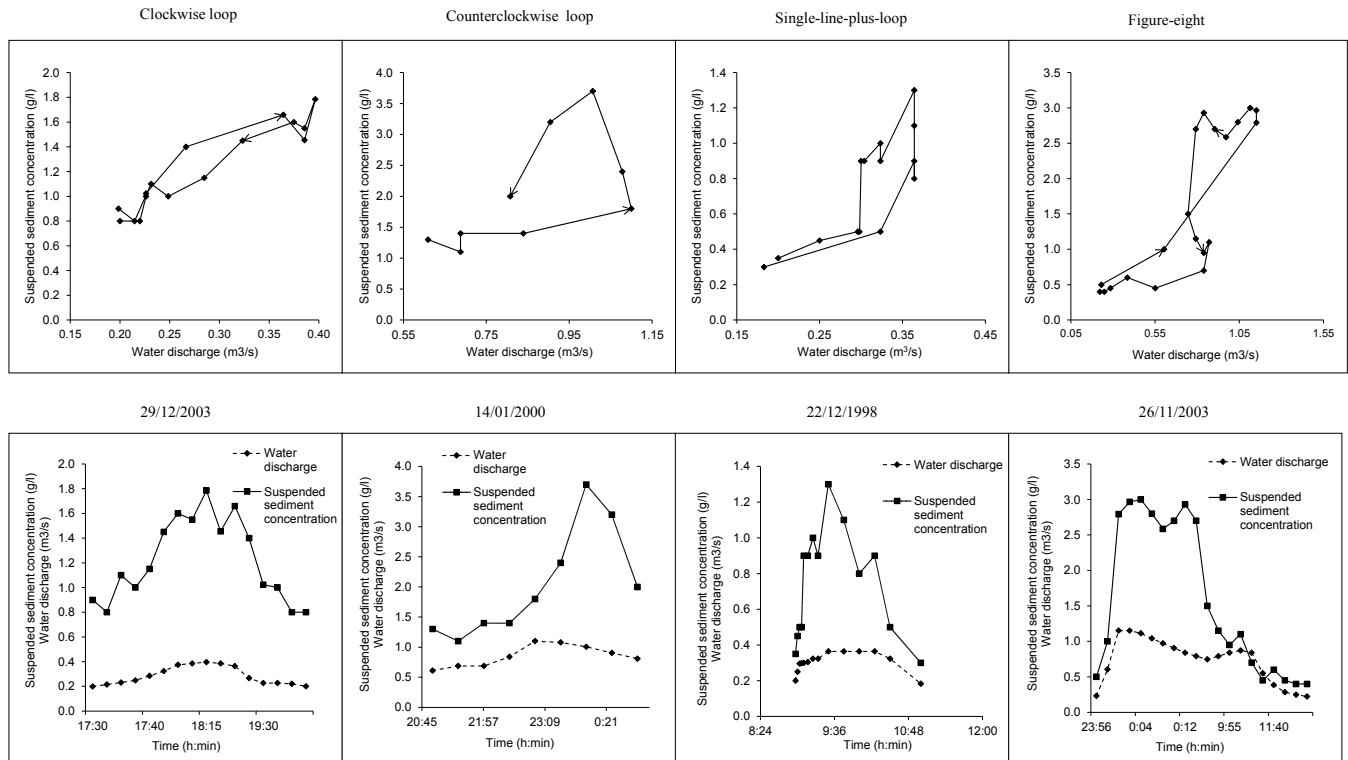


Fig. 5. Examples of suspended sediment concentration - water discharges relationships observed in the Cannata watershed.

were described for the Cannata catchment had already been pointed out by Gallart et al. (2002), Latron et al. (2008) and Estrany et al. (2010) in small mountainous catchments in the western Mediterranean. Predictions of runoff generation in similar catchments should take into account this high variability in soil hydraulics properties (Gómez et al., 2014), which are very difficult to simulate in modelling exercises, especially during the transition period (Licciardello et al., 2007; Taguas et al., 2015).

Runoff coefficient was also very variable between the two semesters of the years; i.e. if we consider two periods with a similar mean P value, i.e. September–November with 73 mm and February–April with 57 mm, we find an RC of 7% in the first case and 28% in the second. Similar differences between RC values in dry and wet periods were found by Latron et al. (2008) and Tuset et al. (2016). These authors suggested the same explanation given for the Cannata catchment: the content of water in the soil before flood events in the wet period is generally higher than in the dry period, conditions that determine the higher RC observed in the former. The month of September with a monthly P in the range 42.4–114 mm (mean monthly P depth = 69.6 mm) always showed Ru and SSY equal to zero. This different behaviour between the two periods is the reason why for all the correlations, especially those driven by P and Ru , r coefficients reached higher values after the division of the data into two periods.

After the division into two periods, $I30$ was a good driver of the hydrological response in the Cannata catchment only during the dry period and not during the wet period, as generally seen in Mediterranean areas (Martínez-Mena et al., 1998). In the Cannata catchment this behaviour can be explained by the interaction of the vegetation during the wet period and by the fact that runoff and sediment transport were limited despite high P and $I30$ during the dry period (really during October and November, the only two months without null Ru). Vegetation

cover and lithology are the main reasons explaining the lower specific sediment yield found in the Cannata catchment ($1.16 \text{ Mg km}^{-2} \text{ y}^{-1}$) than in other Mediterranean catchments, along with SSC event values (up to 9.3 g/l during October–November before the increase in vegetation). In fact, according to Vanmaercke et al. (2012) the sediment yield of Mediterranean catchments with area $< 10 \text{ km}^2$ varies between 0.5 and $50,000 \text{ Mg km}^{-2} \text{ y}^{-1}$. Tuset et al. (2016) found an SSC max value of 3 g l^{-1} , while a total of 5 floods out of 73 reached concentrations exceeding 2 g l^{-1} for a catchment mostly covered by forest. Similarly, in the Cannata catchment this concentration was exceeded by a total of 9 floods out of 46.

Runoff generation processes

It is more difficult to explain the hydrological response in the Cannata catchment in terms of either P or $I30$ for the first events with runoff of each hydrological year. These events were characterized by a mean value of cumulative P from the preceding event with runoff (generally in April or May) of 290 mm. Moreover, the events were characterized by an empirical relative frequency of about 20% when taking into account the mean values of P depth and $I30$. This frequency rose to 50–80% with the mean values of PF , Ru and RC , and to 70–80% with the mean values of SSC and SSY . The exceptional event that occurred on 13/12/2005 was excluded from this analysis. These results corroborated those of Gómez et al. (2014) for an olive orchard on a Vertic soil, among others (e. g. Allen et al., 2006).

Even though, at the event scale, $I30$ improved its driving role of SSC and SSY (only in the dry period), it remained a weak driver of PF and poor of RC . Estrany et al. (2010)'s findings were the same. They explained that the negative correlation between $I30$ and PF was due to the most intense rainfall occurring in the summer, when the soil water content was low

and there was no flow into the channel. This meant that maximum PF was lower although rainfall intensities were higher. As stated above, this was also true for the Cannata catchment. Thus, the results in the Cannata catchment contradicted the common opinion that rainfall excess runoff generation process prevails in semi-arid areas. In our case, saturation overland flow seemed to prevail, as confirmed by the lack of significance of correlation coefficients between $I30$ and RC but also by the success of the T-M water balance model for simulating the main runoff periods observed in the catchment. Gallart et al. (2008) found similar results in a set of Mediterranean headwater catchments characterized by the temporariness of flow. Ries et al. (2017) also found the prevalence of rainfall excess runoff generation process only in arid areas, while in semi-arid area catchments, characterized also by different rainfall intensities, soil water storage and bedrock capacity, excess saturation overland flow prevailed. Bracken et al. (2008) found that floods also seem to be more highly related to the total rainfall occurring in a spell of rain (starting after 12 hours without rain) than to the intensity of a storm, although intense bursts of rain control the nature and timing of the flood hydrograph. Conclusive considerations concerning the importance of rainfall intensity for flood generation are made even more difficult due to the complexity of significant storm rainfall. Reaney et al. (2007) highlighted the importance of the temporal fragmentation of high-intensity rainfall to determine the amount of runoff temporal fragmentation of high-intensity rainfall. Storms may have the same amount of high-intensity rainfall, but produce very different amounts of discharge if they are characterized by different degree of high-intensity fragmentation. Consequently, the use of constant intensity during the whole event could lead to incorrect estimations of hydrological response in modelling exercises applied in semi-arid conditions.

The recession constants K obtained for the analysed events also support the prevalence of saturation mechanisms over rainfall excess ones. Indeed, the K values obtained in this study (0.33–0.83) are well within the range of those reported by Dunne (1978) for the 0.59 km² Sleepers River watershed W-2 characterized by saturation (variable source area) mechanisms (0.42–0.81), while they are clearly larger (smoother) than those reported by the same author for the 0.83 km² Stillwater Watershed –4 characterized by rainfall excess overland flow (0.032–0.27).

Moreover, in catchments with prevalent fine texture, the delay of the hydrological response observed during the transition period, which is due to the filling of soil water reserves, may be more marked in the event of crack formations (Gómez et al., 2014). This is a working hypothesis for the case of the Cannata catchment where shrinking cracks were observed during the transition period, in summer and at the beginning of autumn. Afterwards, once the rainy season begins, the soil surface becomes moist, the soils swell and the fine cracks close, reducing infiltration and allowing the generation of overland flow because of rainfall-excess generation mechanisms. Arnold and Fohrer (2005) found that, in Texas, crack volume and PET have similar distributions, but there is about a 3-month lag between peak AET and peak crack volume. Based on the similarities of PET and AET characteristics found by Arnold and Fohrer (2005) and simulated in the Cannata catchment by SWAT (Licciardello et al., 2011), crack volume started to increase in May, reached its maximum in September and decreased between October and November. These months were still part of the dry period that started in May.

It may therefore be argued that the T-M model successfully mimics the periods of high soil wetness, but runoff in these periods may be caused by precipitation over either saturated or

crack-sealed ground. In other words, the model success shows the importance of the wet antecedent conditions on runoff generation but not necessarily the operating mechanisms. In the lack of field surveys on the occurrence of saturated areas in the Cannata catchment, the relatively high values of the recession constant K suggest that runoff is not only due to overland flow, but that there is also some contribution of return flow usually associated with high water-table levels, at least in the riparian area (Dunne, 1978). Periods of high soil-water content in the Cannata catchment are denoted by the occurrence of shallow soil slumps.

The prevalence of saturation overland flow may also be due to the limited soil thickness of the Cannata catchment. Landscape factors such as soil depth (i.e., available water storage capacity), upland watershed area, and local topography are the important factors determining whether or not a particular area in a watershed will generate runoff (Steenhuis et al., 2005). But following the variable source area (VSA) hydrology concept as rainfall continues, the extent of saturated areas in a watershed expands varying temporally. Thus, both hydrologic and soil water (i.e., porous media) concepts are combined to evaluate potential runoff areas in the landscape. In this view, the developing of simple methods to identify the locations more prone to generate runoff could help in the interpretation of the hydrological of small catchments.

Sediment – discharge relationships

That most events are characterized by a clockwise relationship between SSC and Q is attributable their following a period in which, even if some rainfall occurs, there is no runoff, for example at the beginning of the runoff season or during the early part of a storm. These events are quite intense, so SSC rapidly increases in the rising limb of the hydrograph. This is particular evident for intermittent river, due to the presence of available sediment in the water course (Gentile et al., 2010). In fact, the approaching wave can bring quite a lot of stream bed sediment, that was settled and immobile during no- or low-flow conditions. Then, after reaching the peak, the SSC decreases even if the water discharge is still high, which is attributable to several reasons, such as sediment depletion, the conclusion or decrease in rainfall intensity and the growing contribution of return flow. The prevalence of this kind of relationship may also be because the Cannata stream is quite small (Heidel, 1956). A particular kind of clock-wise loop observed at the Cannata catchment was the single-line-plus-loop. While clockwise, anti-clockwise and mixed loop are well known and very common, not a lot of single-line-plus-loop published (Gentile et al., 2010). These events are characterized by a linear relationship between SSC and Q at the beginning and end of the hydrograph, when the SSC varies directly with discharge. The loop at higher discharge indicates that during the middle of the hydrograph SSC is not in synchronization with Q , instead peaking either before or after the discharge. In most cases, the anti-clockwise events in the Cannata catchment occurred when the flood started on the falling limb of the previous intense event; with the water discharge peak occurring before the sediment concentration peak because there was still base flow from the previous event. These events occurred only between January and April, never at the start of the runoff season. Mixed loop occurred when there were graded floods, which are characterized by a clockwise relationship at the beginning of the event and an anti-clockwise one afterwards or *vice versa*.

On the whole event scale, the close correlation coefficients between PF and SSY found in Cannata are common in small

catchments elsewhere and attributable to the role of peak flow as a measurement of overall event power (Duvert et al., 2012). PF proved to be the best descriptor of SSY as found by Duvert et al. (2012) with similar α and β describing the single power law between the two variables ($SSY = \alpha Q^\beta$) for events recorded during the wet period. In particular, α was in the lower part of the identified range 25–5039 ($\alpha = 22.9$) and β in the upper part (0.9–1.9) ($\beta = 1.9$). Even lower values for α and higher for β were found analysing events recorded during the dry period, supporting the very peculiar response of the Cannata watershed during this conditions.

SSC was also positively related to $I30$, which is a measurement of event rainfall power, negatively related with the recession constant K , which measures recession softness, and quite independent of Ru , which suggests that neither concentration nor dilution was associated with runoff. Although it has been suggested above that the main runoff generation mechanism is not rainfall excess, the very high correlation coefficient between $I30$ and SSC during the dry season suggests that sediments are mainly produced in small hillslope source areas of low vegetation cover and poor soil characteristics, such as discontinuous gullies, during intense rainfall events. Even if these events were not sufficient to generate runoff at the catchment outlet, they could carry the sediments to the elementary drainage net, which would permit the occurrence of positive loops in the SSC - Q relationship primarily in the first events of the wet season.

CONCLUSION

The research reported in this paper provided an analysis of water balance and the main hydrological factors and processes controlling runoff and sediment in a small mountainous Mediterranean catchment. Some similarities and differences with other catchments were highlighted. Seasonal climate forcing in Cannata showed a characteristic Mediterranean pattern with high temporal and spatial variability of precipitation and high concentration of relevant runoff events into a few months. The inter-annual and seasonal variability of the hydrological response of the catchment was even higher than the variability of rainfall, due to the interaction of other factors, among them potential evapotranspiration (PET), vegetation cover and the role of the soil as a water buffer. Evapotranspiration was the main factor driving the succession of wet, dry and transition periods in the Cannata catchment. The differences in runoff coefficient (RC) values between the different periods were higher than those cited in the literature. Vegetation was also suggested as a factor affecting the response of reduced sediment production in the catchment (as against other catchments in similar environmental conditions). The refining of the analysis divided the data into two periods and, by taking the event scale into account, clarified some behaviour discussed above. For example, rainfall intensity ($I30$) became a driver for peak flow (PF) and suspended sediment concentration (SSC) during the dry period (really October and November, the only two months of the dry period with runoff) when $I30$ values were higher than the rest of the year and the vegetation cover was still low. The fact that $I30$ was generally not a driver of the hydrological response was coherent with the results of the Thornthwaite-Mather soil saturation model simulations. These showed, in contrast with much literature on semi-arid catchments, that runoff generation was dominated by saturation processes in the Cannata watershed. The analysis of the hydrograph recessions suggested rainfall over saturated areas and return flow as the dominant runoff generation processes. The

role of soil crack formation and closure in the temporal patterns of runoff was also hypothesized on the basis of their field occurrence, but there is no other evidence to support this. All SSC - Q relationships were positive, with different hysteresis types, but with a prevalence of the clockwise shape, especially at the beginning of the runoff season. This and the clear role of $I30$ on SSC during the dry season suggest that sediments are mainly produced during intense storms in small hillslope patches with low vegetation cover and poor soil characteristics.

Analysis of results confirmed the complexity and variability of hydrological processes in small Mediterranean catchments. These findings have to be taken into account in land and water management and planning. In particular, they need to be included in modelling exercises at the beginning of the runoff generation season.

Acknowledgements. The research was performed with the Project MASCC (Mediterranean Agricultural Soils Conservation under global Change) funded by Ministero delle politiche agricole, alimentari e forestali, as well as TransHyMed (CGL2016-75957-R AEI/FEDER, UE) and MASCC-DYNAMITE (PCIN-2017-061/AEI) funded by the Spanish Government and the European Union. The authors thank Michael Eade for English style improvements and two anonymous reviewers for their constructive questions and comments.

REFERENCES

- Allen, R.G., Pereira, L.S., Raes, D., Smith, M., 1998. Crop evapotranspiration: Guidelines for computing crop water requirements. FAO Irrigation and Drainage Paper 56. United Nations FAO, Rome, Italy.
- Allen, H.D., Randall, R.E., Amable, G.S., Devereux, B.J., 2006. The impact of changing olive cultivation practices on the ground flora of olive groves in the Messara and Psiloritis regions, Crete, Greece. *Land Degradation & Development*, 17, 249–273.
- Arnold, J.G., Fohrer, N., 2005. SWAT2000: Current capabilities and research opportunities in applied watershed modelling. *Hydrol. Process.*, 19, 3, 563–572.
- Bracken (née Bull), L.J., Cox, N.J., Shannon, J., 2008. The relationship between rainfall inputs and flood generation in south-east Spain. *Hydrological Processes*, 22, 683–696.
- Calvo-Cases, A., Boix-Fayos, C., Imeson, A.C., 2003. Runoff generation, sediment movement and soil water behaviour on calcareous (limestone) slopes of some Mediterranean environments in southeast Spain. *Geomorphology*, 50, 1–3, 269–291.
- Cantón, Y., Solé-Benet, A., De Vente, J., Boix-Fayos, C., Calvo-Cases, A., Asensio, C., Puigdefàbregas, J., 2011. A review of runoff generation and soil erosion across scales in semiarid south-eastern Spain. *Journal of Arid Environments*, 75, 12, 1254–1261.
- Cuomo, A., Guida, D., 2016. Using hydro-chemograph analyses to reveal runoff generation processes in a Mediterranean catchment. *Hydrol. Process.*, 30, 4462–4476.
- Dunne, T., 1978. Field studies of hillslope flow processes. *Hillslope Hydrology*, 227–293.
- Duvert, C., Nord, G., Gratiot, N., Navratil, O., Nadal-Romero, E., Mathys, N., Némery, J., Regüés, D., Garcia-Ruiz, J.M., Gallart, F., Esteves, M., 2012. Towards prediction of suspended sediment yield from peak discharge in small erodible mountainous catchments (0.45–22 km²) of France, Mexico and Spain. *Journal of Hydrology*, 454–455, 42–55.
- Estrany, J., Garcia, C., Batalla R.J., 2010. Hydrological response of a small Mediterranean agricultural catchment. *Journal of Hydrology*, 380, 180–190.

- Gallart, F., Llorens, P., Latron, J., Regüés, D., 2002. Hydrological processes and their seasonal controls in a small Mediterranean mountain catchment in the Pyrenees. *Hydrology and Earth System Sciences Discussions, European Geosciences Union*, 6, 3, 527–537.
- Gallart, F., Amaxidis, Y., Botti, P., Canè, G., Castillo, V., Chapman, P., Froebrich, J., García-Pintado, J., Latron, J., Llorens, P., Lo Porto, A Morais, M., Neves, R., Ninov, P., Perrin, J.-L., Ribarova, I., Skoulikidis, N., Tournoud, M.-G., 2008. Investigating hydrological regimes and processes in a set of catchments with temporary waters in Mediterranean Europe. *Hydrological Sciences Journal*, 53, 3, 618–628.
- García-Rama, A., Pagano, S.G., Gentile, F., Lenzi, M.A., 2016. Suspended sediment transport analysis in two Italian instrumented catchments. *Journal of Mountain Science*, 13, 6, 957–970.
- Gentile, F., Bisantino, T., Corbino, R., Milillo, F., Romano, G., Trisorio Liuzzi, G., 2010. Monitoring and analysis of suspended sediment transport dynamics in the Carapelle torrent (Southern Italy). *Catena*, 80, 1–8.
- Gómez, J., Vanwallegem, T., De Hoces, A., Taguas, E.V., 2014. Hydrological and erosive response of a small catchment under olive cultivation in a vertic soil during a five-year period: Implications for sustainability. *Agriculture Ecosystems & Environment*, 188, 229–244.
- Heidel, S.G., 1956. The progressive lag of sediment concentration with flood waves. *Eos Trans. AGU*, 37, 1, 56–66.
- ISPRAMBIENTE, 2018. <http://www.isprambiente.gov.it> accessed on Oct 24th 2018.
- Latron, J., Gallart, F., 2008. Runoff generation processes in a small Mediterranean research catchment (Vallcebre, Eastern Pyrenees). *Journal of Hydrology*, 358, 3–4, 206–220.
- Latron, J., Soler, M., Llorens, P., Gallart, F., 2008. Spatial and temporal variability of the hydrological response in a small Mediterranean research catchment (Vallcebre, Eastern Pyrenees). *Hydrol. Processes*, 22, 775–787.
- Latron, J., Llorens, P., Gallart, F., 2009. The Hydrology of Mediterranean Mountain Areas. *Geography Compass*, 3/6, 2045–2064.
- Licciardello, F., Amore, E., Nearing, M.A., Zimbone, S.M., 2006. Runoff and Erosion Modelling by WEPP in an Experimental Mediterranean Watershed. In: Owens, P.N., Collins, A.J. (Eds.): *Soil Erosion and Sediment Redistribution in River Catchments: Measurement, Modelling and Management*. Place. CABI Publisher, Wallingford, Oxfordshire OX10 8DE, UK, pp. 186–208.
- Licciardello, F., Zema, D.A., Zimbone, S.M., Bingner, R.L., 2007. Runoff and soil erosion evaluation by the AnnAGNPS model in a small Mediterranean watershed. *Transactions of the American Society of Agricultural and Biological Engineers (ASABE)*, 50, 5, 1585–1593.
- Licciardello, F., Rossi, C.G., Srinivasan, R., Zimbone, S.M., Barbagallo, S., 2011. Hydrologic evaluation of a Mediterranean watershed using the SWAT Model with Multiple PET Estimation Methods. *Transactions of the ASABE*, 54, 5, 1615–1625.
- Licciardello, F., Toscano, A., Cirelli, G.L., Consoli, S., Barbagallo, S., 2017. Evaluation of sediment deposition in a Mediterranean reservoir: comparison of long term bathymetric measurements and SWAT estimations. *Land Degradation & Development*, 28, 566–578.
- Martínez-Mena, M., Albaladejo, J., Castillo, V., 1998. Factors influencing surface runoff generation in a Mediterranean semi-arid environment: Chicamo watershed, SE Spain. *Hydrol. Processes*, 12, 741–754.
- Merheb, M., Moussa, R., Abdallah, C., Colin, F., Perrin, C., Baghdadi, N., 2016. Hydrological response characteristics of Mediterranean catchments at different time scales: a meta-analysis. *Hydrological Sciences Journal*, 61, 14, 2520–2539.
- Nash, J.E., Sutcliffe, J.V., 1970. River flow forecasting through conceptual models: 1. A discussion of principles. *J. Hydrol.*, 10, 3, 282–290.
- Neitsch, J.G., Arnold, J.G., Kiniry, J.R., Williams, J.R., King, K.W., 2002. *Soil and Water Assessment Tool: Theoretical Documentation*. Version 2000. TWRI Report TR-191. Texas Water Resources Institute, College Station, TX, USA.
- Nunes, A.N., de Almeida, A.C., Coelho, C.O.A., 2011. Impacts of land use and cover type on runoff and soil erosion in a marginal area of Portugal. *Applied Geography*, 31, 2, 687–699.
- Reaney, S.M., Bracken, S.M., Kirkby, M.J., 2007. Use of the Connectivity of Runoff Model (CRUM) to investigate the influence of storm characteristics on runoff generation and connectivity in semi-arid areas. *Hydrological Processes*, 21, 894–906.
- Ries, F., Schmidt, S., Sauter, M., Lange, J., 2017. Controls on runoff generation along a steep climatic gradient in the Eastern Mediterranean. *Journal of Hydrology: Regional Studies*, 9, 18–33.
- Ritchie, J.T., 1972. Model for predicting evaporation from a row crop with incomplete cover. *Water Resour. Res.*, 8, 1204–1213.
- Soler, M., Latron, J., Gallart, F., 2008. Relationships between suspended sediment concentrations and discharge in two small research basins in a mountainous Mediterranean area (Vallcebre, Eastern Pyrenees). *Geomorphology*, 98, 1, 143–152.
- Steenhuis, T.S., Van der Molen, W.H., 1986. The Thornthwaite-Mather procedure as a simple engineering method to predict recharge. *J. Hydrol.*, 84, 221–229.
- Steenhuis, T.S., Agnew, L., Gérard-Marchant, P., Walter, M.T., 2005. Overland flow. Reference Module in Earth Systems and Environmental Sciences - *Encyclopedia of Soils in the Environment*, 130–133.
- Taguas, E.V., Yuan, Y., Licciardello, F., Gómez, J.A., 2015. Curve Numbers for olive orchard catchments: a case study in Southern Spain. *Journal of Irrigation and Drainage Engineering*, 141, 11, 05015003/1-05015003/11.
- Thornthwaite, C.W., Mather, J.R., 1955. *The water balance*. Laboratory of Climatology. Report no. 8. Drexel Institute of Technology, New Jersey, USA.
- Tuset, J., Vericat, D., Batalla, R.J., 2016. Rainfall, runoff and sediment transport in a Mediterranean mountainous catchment. *Science of the Total Environment*, 540, 114–132.
- Vanmaercke, M., Maetens, W., Poesen, J., Jankauskas, B., Jankauskiene, G., Verstraeten, G., De Vente, J., 2012. A comparison of measured catchment sediment yields with measured and predicted hillslope erosion rates in Europe. *J. Soils Sediments*, 12, 586–602.
- Viviroli, D., Weingartner, R., 2004. The hydrological significance of mountains: from regional to global scale. *Hydrology and Earth System Sciences*, 8, 1016–1029.
- Williams, G.P., 1989. Sediment concentration versus water discharge during single hydrologic events in rivers. *Journal of Hydrology*, 111, 89–106.

Received 19 July 2018
 Accepted 19 December 2018

Finding behavioral parameterization for a 1-D water balance model by multi-criteria evaluation

Markus C. Casper¹, Hadis Mohajerani^{1*}, Sibylle Hassler^{2,3}, Tobias Herdel¹, Theresa Blume²

¹ University of Trier, Faculty VI, Dep. of Physical Geography, Universitätsring 12, 54286 Trier, Germany.

² GFZ German Research Centre for Geosciences, Section 5.4 Hydrology, Telegrafenberg, 14473 Potsdam, Germany.

³ Karlsruhe Institute of Technology (KIT), Institute for Water and River Basin Management, Chair of Hydrology, Kaiserstr. 12, 76131 Karlsruhe, Germany.

* Corresponding author. Tel.: +49 651 2014557. FAX: +49 651 2013976. E-mail: s6hsmoha@uni-trier.de

Abstract: Evapotranspiration is often estimated by numerical simulation. However, to produce accurate simulations, these models usually require on-site measurements for parameterization or calibration. We have to make sure that the model realistically reproduces both, the temporal patterns of soil moisture and evapotranspiration. In this study, we combine three sources of information: (i) measurements of sap velocities; (ii) soil moisture; and (iii) expert knowledge on local runoff generation and water balance to define constraints for a “behavioral” forest stand water balance model. Aiming for a behavioral model, we adjusted soil moisture at saturation, bulk resistance parameters and the parameters of the water retention curve (WRC). We found that the shape of the WRC influences substantially the behavior of the simulation model. Here, only one model realization could be referred to as “behavioral”. All other realizations failed for a least one of our evaluation criteria: Not only transpiration and soil moisture are simulated consistently with our observations, but also total water balance and runoff generation processes. The introduction of a multi-criteria evaluation scheme for the detection of unrealistic outputs made it possible to identify a well performing parameter set. Our findings indicate that measurement of different fluxes and state variables instead of just one and expert knowledge concerning runoff generation facilitate the parameterization of a hydrological model.

Keywords: Forest evapotranspiration; Water balance simulation; Soil parameterization; Behavioral model.

INTRODUCTION

Extraction of water from the soil by the root system and return of water to the atmosphere as plant transpiration are important processes in the global circulation of water (Kramer and Boyer, 1995). Quantitative means of describing transpiration are essential for an improved understanding of water and energy exchange processes between the land surface and the atmosphere. Transpiration is controlled by a combination of biotic factors (e.g. stomatal functions; leaf area; root depth and distribution, and hydraulic characteristics) and abiotic factors (e.g. soil water availability; climate, and depth to groundwater) (Durigon et al., 2016).

There is a variety of techniques to measure transpiration at different scales such as direct measurements of sap flow on individual trees (Lu et al., 2004), eddy flux gradient analyses (Saugier et al., 1997), or gauged watersheds (Wilson et al., 2001). Alternatively, simulation models are used to estimate transpiration. However, to produce accurate simulations, these usually require on-site parameterization or calibration (Durigon et al., 2016; Vose et al., 2003). Recently, a simple approach was developed by Ayyoub et al (2017) relating the normalized daily sap velocities and the daily reference evapotranspiration (ET₀). This method used both, FAO-Penman-Monteith (FAO-PM) method and Hargreaves-Samani (HARG) method to estimate ET₀. The FAO-PM method produced the highest correlations to daily sap velocities (Ayyoub et al., 2017).

System state (“soil moisture”) and actual evapotranspiration are known to be highly correlated. Therefore, all water balance models directly couple these two components. Wrong estimates of temporal or spatial patterns of soil moisture result in erroneous temporal or spatial patterns of transpiration (Casper and Vohland, 2008; Koch et al., 2017). Therefore, soil parameteri-

zation, and especially the representation of the Water Retention Curve - as one of the most important soil-physical characteristics - strongly influence the simulation of evapotranspiration. A similar effect can be observed when canopy resistances are wrongly estimated (Bie et al., 2015). In order to find an appropriate model parametrization, we have to verify that the model realistically reproduces both, the temporal patterns of soil moisture and evapotranspiration. This has been done in a study carried out by Holst et al. (2010) where the water balance of two beech stands in Southwest Germany was investigated using two different forest hydrological models (DNDC and BROOK90). They demonstrated that both models were able to reproduce the observed dynamics of the soil water content in the uppermost 30 cm and the transpiration estimates from sap flow measurements (Holst et al., 2010).

To analyze different assumptions on catchment behavior and hydrological processes, it is necessary to evaluate the model performance with respect to multiple indicators that evaluate the contribution of different sources of data (Gupta et al., 1998). The value of these additional data sources has been demonstrated by Fenicia et al. (2008a). They evaluated the accuracy of a hydrological simulation with respect to the observed discharge, groundwater level dynamics, and isotope signatures. If appropriate data is lacking, incorporation of expert knowledge (as an alternative source of information) into hydrological modeling and water management issues becomes more important (Bromley et al., 2005; Cash et al., 2003; Mohajerani et al., 2017). As recent studies suggest, use of expert knowledge in choosing parameter sets and introducing constraints by forcing the model to reproduce the processes observed in the real system, can also improve the model performance even without traditional calibration (Bahremand, 2016; Gharari et al., 2014; Hrachowitz et al., 2014). For instance,

having expert knowledge on local runoff generation processes, as a potential source of information in every hydrologic unit, can considerably improve hydrological simulations (Antonetti and Zappa, 2018; Casper et al., 2015; Franks et al., 1998; Seibert and McDonnell, 2002). Modelers need to consider a proper balance between parameter identifiability and the model's ability to precisely represent the observed system response. This has prompted the development of alternative approaches to hydrological modeling including the dominant process concept (Fenicia et al., 2008b; Grayson and Blöschl, 2001; Wagener et al., 2001). The concept of dominant runoff generation process (DRGP) assumes that at a particular location one particular runoff generation mechanism is dominant (Blöschl, 2001). In most of the studies, however, modelers have evaluated the model performance with respect to discharge data alone. This may cloud model realism and hamper understanding of catchment behavior. In fact, to accurately evaluate hydrological models, one has to carefully look at the hydrological responses that a model is challenged to represent rather than just being satisfied with a simple calibration. This interestingly takes us back to what Fenicia et al. (2008a) call the “Art of Modeling” and what Gupta et al. (2005) call the “Behavioral Model”. The former says: “...modeling is both an Art and a Science. The science lies in the use of fundamental scientific principles and the formality of analysis; the art accounts for professional experience, insight, creativity and intuition. The latter is particularly important in developing a perceptual and conceptual model that captures the main processes at play, while maintaining minimum levels of complexity...”. A “behavioral” model has the following characteristics: (i) the input-state-output behavior of the model is consistent with the measurements, (ii) the model predictions are accurate (i.e. they have negligible bias) and (iii) model structure and behavior are consistent with our hydrologic understanding of reality (Fenicia et al., 2008a; Gupta et al., 2005).

The present study combines three sources of information: measurements of sap velocities; soil moisture data; and expert knowledge of local runoff generation and water balance to define constraints for a “behavioral” forest stand water balance model. We evaluated the model by defining multi-criteria performance measures according to the constraints that data are supposed to impose on model behavior. In particular, we investigated the following research questions: (i) How can we combine different sources of information to modify the parameterization scheme in order to achieve a “behavioral model”? (ii) How does the implementation of expert knowledge of site-specific dominant runoff generation processes affect the simulation results? (iii) What are the impacts of model setup, i.e. the parameterization approach and the parameter allocation strategy on the simulated soil moisture and evapotranspiration dynamics (e.g. the effect of different parameterizations of the water retention curve of the soil)?

To address the research questions listed above, we used a one-dimensional (1-D) hydrological model (WaSiM-ETH) to simulate the soil water content as well as the actual transpiration at stand level. The basic motivation of 1-D models is often to simulate soil water content, and water balance components such as evapotranspiration, deep drainage and runoff. In the 1-D models, no groundwater flow is simulated and the upper and lower limits are soil water content at field capacity and permanent wilting point, and upper and lower loss of soil water is caused by evapotranspiration and deep percolation, respectively (Walker and Zhang, 2002). WaSiM-ETH was selected due to its highly differentiated 1-D model structure. The model represents all relevant hydrological processes at the point scale in a

physically meaningful way (Schulla, 2017). As all measured data including soil moisture and sap velocity are point measurements, setting up a “1-D model” is sufficient for our purpose. A site in the sandstone region of western Luxembourg was used as a test case. On sandstone, we expect neither stream channels nor surface runoff due to the high hydraulic conductivities of the sandy soils. The headwaters start at springs on top of the less permeable marls underlying the sandstone. While this work is not going to provide new insights of the behavior of the study catchment, it arguably is going to contribute to understanding of the value of different sources of data and information for hydrological modeling. The test case is used as a “proof-of-concept” location to investigate how different parameterization with different content of information can affect the model behavior. Our investigation is subdivided into four scenarios, i.e. different soil parameterizations. For each scenario the simulation results are evaluated by the model performance criteria defined in the section 2.4. In scenario A, the soil parameterization is taken from Tepee et al. 2003. In the two scenarios B1 and B2, we parameterize the water retention curve with three different variations of the van Genuchten parameters according to (Sauer, 2007). In a last step (scenario C), we evaluate the model performance using the soil parameter set provided by Sprenger et al. (2016). All scenarios are summarized in Table 6.

METHODS

Site description

The study area is the Huewelerbach, a sub-catchment (2.7 km² in area, ranging from 280 to 400 m in elevation) of the Attert River basin located in the west of Luxembourg (for detailed information see Martínez-Carreras et al. (2010)). The whole area is part of the “Catchments As Organized Systems” (CAOS) observatory investigating landscape-scale structures, patterns and interactions in hydrological processes for model development (Zehe et al., 2014). The catchment is mainly forested, but the alluvial section of the area is dominated by grassland. The mean annual precipitation of the area is approximately 850 mm (Pfister et al., 2000). In terms of lithology, the Huewelerbach catchment consists of jurassic Luxembourg sandstone which is underlain by marls (Martínez-Carreras et al., 2012, 2010). According to previous studies, the sandstone bedrock and the underlying marls produce a very stable base flow regime (Juilleret et al., 2012). Rainfall–runoff reaction is delayed on the deep sandy soils on hillslopes (deep percolation and subsurface flow). Siltation and compaction in the valley bottom may cause sporadic surface runoff (Sprenger et al., 2016). Measurements at sites Sa_G and Sa_K include meteorological variables such as air temperature, humidity and solar radiation and soil moisture at three depths in three different profiles. At the forested site Sa_G there are also measurements of sap velocity at 4 trees, two of them European Beech (*Fagus sylvatica* L.) and two hornbeams (*Carpinus betulus* L.). Figure 1 shows the study area and the location of the selected sites. Dominant vegetation at site Sa_G is a relatively young beech forest with a basal area of 16 m²/ha. Within the measurement plot we find 34 stems with a mean diameter of 19 cm (median: 14 cm).

Hydrological model

To simulate the actual evapotranspiration (ET_a), we applied a hydrological model – WaSiM-ETH (Schulla, 1997). This model is a distributed, deterministic, mainly physical and grid-based hydrological model running with variable time steps

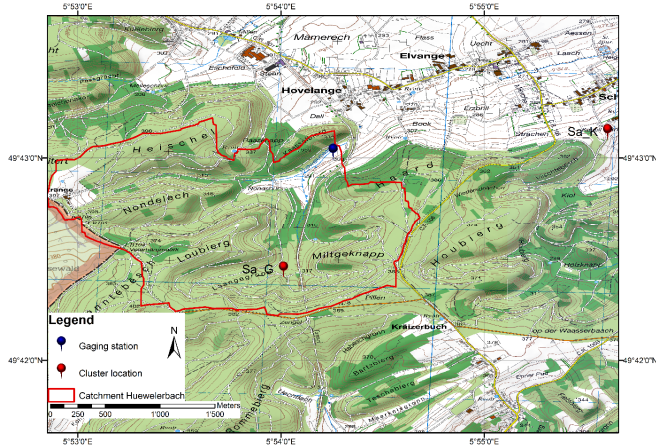


Fig. 1. Location of the study area Huewelerbach catchment with the test sites Sa_G (forest) and Sa_K (grassland).

(Schulla, 2017). The WaSiM-ETH model has performed well in sub-alpine and alpine catchments (Cullmann et al., 2006; Gurtz et al., 2003; Jasper, 2001; Jasper et al., 2002; Klok et al., 2001; Verbunt et al., 2003), also in middle-mountain (Bie et al., 2015; Grigoryan et al., 2010; Middelkoop et al., 2001), and lowland catchments (Elfert and Bormann, 2010). The model is documented in both English and German and can be used free of cost (<http://www.wasim.ch>). The model comprises different components (e.g. evapotranspiration model, soil model, snow model, glacier model, silting up, surface routing, groundwater model, discharge routing model, lake model etc.). In our case only the modules related to the soil model and evapotranspiration were used and all other components were disregarded.

Calculation of evapotranspiration

There are three main steps to estimate the ETa (plant transpiration as well as evaporation from the soil separately) in WaSiM-ETH. First, estimation of potential evapotranspiration (ETp) on the basis of the ground-measured meteorological data; second, simulation of soil water content in vertical direction via Richards equation (Richards, 1931). In the third step, the amount of ETa is simulated at every time step by reducing ETp according to the actual soil water content.

There are four different methods available in WaSiM-ETH model to calculate the ETp rates: Penman-Monteith approach (Monteith, 1981; Monteith et al., 1965); Wendling (Wendling, 1975); Haude (Haude, 1955) and Hamon (Federer and Lash, 1978). In this study, we choose Penman-Monteith equation (Monteith et al., 1965) (see equation 1). It is the most widely used and recommended method for ETp estimation, first developed for agricultural contexts and later also applied to other land covers such as forests (Allen et al., 1998; Droogers and Allen, 2002). This method is based on simulated potential transpiration and the available water content. In our case, actual plant transpiration is simulated in hourly time steps. However, the Penman-Monteith approach has some limitations in practical terms, as a large number of environmental variables are required to determine ETa. This is particularly challenging especially when there is a lack of appropriate atmospheric data (Allen et al., 1998).

$$\lambda E = \frac{3.6 \frac{\Delta}{\gamma_p} (Rn - G) + \frac{\rho c_p}{\gamma_p} (e_s - e) t_i}{\frac{\Delta}{\gamma_p} + 1 + \frac{r_s}{r_a}} \quad (1)$$

where λ is the latent vaporization heat, $\lambda = (2500.8 - 2.372 \cdot T)$ kJ kg⁻¹, with T is the temperature in °C; E is the latent heat flux in mm m⁻² \equiv kg m⁻²; Δ is the tangent to the saturated vapor pressure curve in hPa K⁻¹; Rn is the net radiation in Wh m⁻² and $G = 0.1 \cdot Rn$ is the soil heat flux in Wh m⁻², the factor 3.6 is used to convert both fluxes from Wh m⁻² to kJ m⁻²; ρ is the density of dry air, $\rho = p/(RL \cdot T)$, at 0 °C and 1013.25 hPa, $\rho = 1.29$ kg m⁻³; c_p is the specific heat capacity of the dry air at constant pressure, $c_p = 1.005$ kJ kg⁻¹ K⁻¹; e_s is the saturation vapor pressure at temperature T , in hPa; e is the observed actual vapor pressure in hPa; t_i is the number of seconds within a time step; γ_p is the psychrometric constant in hPa K⁻¹; r_a and r_s are the bulk-aerodynamic resistance and the bulk-surface resistance in s m⁻¹, respectively.

Resistances for evapotranspiration

The two resistance parameters in the Penman-Monteith equation: the bulk aerodynamic resistance r_a and the bulk surface resistance r_s play an important role. However, r_s (with diurnal and seasonal variations) is more important than r_a in a forested area for ETa estimation (Beven, 1979). The bulk surface resistance r_s can be divided into two terms, the soil surface resistance r_{se} for evaporation from bare soil; and the canopy surface resistance r_{sc} describing the plant resistances in the transpiration process. There are default values of bulk surface resistance parameters in WaSiM-ETH. The maximum amount of canopy surface resistance r_{sc} is in November to February, whereas in May to September, it reduces to its annual lowest level (Bie et al., 2015; Schulla, 2017). The soil surface resistance r_{se} remains constant for the entire year. Table 1 shows the standard values applied for surface resistances parameters in the WaSiM-ETH model (Schulla, 2017).

Table 1. Canopy surface resistance r_{sc} (s m⁻¹) and soil surface resistance r_{se} (s m⁻¹).

	Jan	Feb	Mar	Apr	May	Jun	Jul	Aug	Sep	Oct	Nov	Dec
r_{sc}	100	100	95	75	65	65	65	65	65	85	100	100
r_{se}	230	230	230	230	230	230	230	230	230	230	230	230

Simulation of soil water content

For estimation of actual transpiration, WaSiM-ETH simulates soil moisture in the root zone. The soil module in WaSiM-ETH uses the van Genuchten method (Van Genuchten, 1980) for parameterization of the water retention curve to solve the Richard Equation. Water fluxes are simulated vertically in one dimension. Soil moisture in the root soil layer can potentially limit transpiration (Paço et al., 2014). In WaSiM-ETH, soil moisture simulation and ETa are linked, reduction of ETa would result in more water availability in the soil whereas increase of ETa will decrease the soil moisture. The Penman-Monteith equation implicitly includes the influence of soil moisture on plant transpiration through parameter r_{sc} (canopy surface resistance). Water content in soil profiles changes with time and values of the r_{sc} also show diurnal and seasonal variations. In dry periods, r_{sc} is very sensitive to soil moisture. When soil moisture content falls below a given point, the plants start decreasing transpiration to prevent internal water losses. Below that point, soil water availability becomes a key factor in obtaining ETa. ETa is gradually reduced until soil moisture reaches the wilting point at which water is no longer available for transpiration (Allen et al., 1998; Anderson et al., 2007).

Soil parameterization

Certain predefined parameters of the WaSiM-ETH model are specific for the area where the model was developed. Thus, these parameters should be modified for each new study area. In the investigated area, the predominant soil type was described as “Podzolic Cambisol”. The soil texture is loamy sand. It developed on a sandstone bedrock. The maximum rooting depth for the soil was observed at approx. 100 cm. The stone content is relatively low and the unaltered parent sandstone is usually not reached within the first 200 cm below soil surface (Sprenger et al., 2016). These quite sandy soils show a high permeability resulting in deep percolation as the dominant hydrological process.

In the model, the van Genuchten parameters α (m^{-1}) and n (–) are empirical constants that determine the shape of the WRC, and therefore influence substantially the behavior of the simulation model. We chose three different methods to determine the parameters of the WRC.

(i) Baseline parameterization after Teepe et al. 2003

We derived the corresponding van Genuchten parameters in the different soil horizons based on soil texture and bulk density classification obtained by Teepe et al. (2003). This formed our baseline parameterization of the soil in our study area (Table 2).

Table 2. Baseline soil parameterization of the WaSiM-ETH soil model (based on Teepe et al. (2003)).

PMacroThresh	20					
MacroCapacity	4					
CapacityRedu	0.5					
MacroDepth	1					
Horizon	1	2	3	4	5	6
Name	Ahe	Ae	Bvs	Bsv	IIBvs	IIBvs
Ksat	1.01E-4	7.95E-05	1.65E-04	1.29E-04	4.84E-05	4.84E-05
K_recession	1	1	1	1	1	1
Theta_sat	0.41	0.41	0.41	0.41	0.41	0.41
Theta_res	0.11	0.05	0.06	0.06	0.13	0.13
Alpha	0.3	0.3	0.26	0.41	0.2	0.2
Par_n	1.17	1.17	1.203	1.191	1.191	1.191
Par_tau	0.5	0.5	0.5	0.5	0.5	0.5
Thickness	0.1	0.1	0.1	0.1	0.1	1
Layers	1	1	1	3	4	7

PMacroThresh (mm/h) is given by the precipitation threshold value and if is reached or exceeded, water can infiltrate into the macropore; MacroDepth (m) is depth of the macropores; MacroCapacity (mm/h) is capacity of the macropores; CapacityRedu (m^{-1}) defines the reduction of the macropore capacity per meter soil depth; Ksat ($m s^{-1}$) is saturated hydraulic conductivity that can be given for each soil layer; K_recession (–) is specified for each soil type describing the recession of the saturated conductivity with depth; theta_sat (m^3/m^3) is saturated water content; theta_res (–) is the residual water content which cannot be extracted by transpiration; alpha (m^{-1}) and Par_n (–) are empirical van-Genuchten parameters; Par_tau is Mualem parameter; thickness (m) is the thickness of every single numerical layer in the given horizon, and layers defines the number of layers in the given horizon.

(ii) Parameterization after Sauer (2007)

Sauer (2007) proposes three different methods to derive the van-Genuchten parameters α and n :

Variation 1: Fitting of WRC based on grain size fractions, bulk density and water content at pF 2.5 and 4.2 using the software “Rosetta Lite” (Schaap et al., 2001).

Variation 2: Fitting of WRC based on water content at pF 1.8, 2.5, 4.2 and Theta_sat (= 41%) using the software “RETc” (Van Genuchten et al., 1991).

Variation 3: Fitting of WRC based on water content at pF 1.8, 2.5, 4.2 using the software “RETc” (Van Genuchten et al., 1991). See Table 3 for the three variations of parameters α and n .

Table 3. Variations of van Genuchten parameters α (m^{-1}) and n (dimensionless) in different soil horizons as re-parameterization of the baseline (Table 2).

Horizon		Ahe	Ae	Bvs	Bsv	IIBvs	IIBvs
Variation 1	alpha	0.83	0.83	0.58	0.58	0.88	1.83
	n	1.5653	1.5653	1.6416	1.6416	1.4974	1.4553
Variation 2	alpha	2.86	2.86	3.97	3.97	4.96	1.83
	n	1.3656	1.3656	1.3965	1.3965	1.4598	1.4553
Variation 3	alpha	25.73	25.73	35.87	35.87	29.34	1.83
	n	1.2138	1.2138	1.2506	1.2506	1.3009	1.4553

(iii) Parameterization after Sprenger et al. (2016)

Sprenger et al. (2016) list soil parameters for the same site (Sa_G). These parameters were obtained by fitting the simulation results to observed soil moisture and pore water stable isotope data. In this case the soil profile was divided into three different horizons (Table 4).

Table 4. Parameterization of WRC for the site Sa_G (Sprenger et al., 2016).

Horizon	Ah	B	II_B
width	11 cm	110 cm	> 80 cm
theta_sat	0.546	0.319	0.470
alpha	0.033	0.005	0.005
n	1.228	1.194	1.194
k _{sat}	6.11E-04	1.53E-04	6.16E-04

Data description

To simulate transpiration and soil water content at the forest site Sa_G, climate data from the grassland site Sa_K were used as input for the model (Figure 1). These data better represent the atmospheric conditions above the trees which mainly drive the transpiration of the trees. In contrast, climate data from site Sa_G represents the conditions inside the forest and therefore this data cannot be used in our simulation study. To run the model, climate data between 2013 and 2016 is available. All subsequent model evaluation is done for the year 2015. The years 2013 and 2014 are used as spin-up period until stabilization of the model. Climate data includes air temperature, relative humidity, wind speed, global radiation as five-minute measurements, and precipitation as hourly data. All data were checked for errors and the data gaps were filled. Soil moisture was measured in three profiles per site at 10 cm, 30 cm and 50 cm depth. For our analyses we took the average across all depths and profiles estimating the average soil moisture in the top 60 cm for each site (Hassler et al., 2018). Precipitation data (station Useldange) are available as hourly values with annual mean value of 791 mm for the year 2015 (Agrarmeteorologie Luxemburg: /http://www.agrimeteo.lu). Therefore, all other climate variables and the soil moisture measurements are averaged to hourly values.

Based on the soil moisture and grain size distribution characteristics of the study area, deep percolation is usually observed as dominant runoff generation process. Saturation excess flow or Hortonian overland flow can be excluded.

For the year 2015, transpiration of the adult beech overstorey was analyzed by determining sap velocities using the heat ratio method with a central heater needle and two thermistor needles located upstream and downstream of the heater (Köstner et al., 1996). The sap velocity sensors, manufactured by East30Sensors in Washington, were installed at breast height on the north-facing side of the stem and protected with a reflective cover (Hassler et al., 2018). Sap velocities at each of those locations were calculated.

ed from the temperatures measured at the corresponding thermistor pairs according to Equation (2) (Campbell et al., 1991):

$$V_{sap} = \frac{2k}{C_w(r_u + r_d)} \ln\left(\frac{\Delta T_u}{\Delta T_d}\right) \quad (2)$$

where V_{sap} is the sap velocity (m s^{-1}), k is the thermal conductivity of the sapwood, set to $0.5 \text{ W m}^{-1} \text{ K}^{-1}$, C_w is the specific heat of water ($\text{J m}^{-3} \text{ K}^{-1}$), r is the distance (m) from the heater needle to the sensor (in our case 6 mm) and ΔT is the temperature difference (K) before heating and 60 seconds after the heat pulse. Subscripts u and d stand for location upstream and downstream of the heater.

These values were corrected to account for wounding of the xylem tissue because of the drilling according to the numerical model solutions for the heat pulse velocity method as suggested by Burgess et al. (2001):

$$V_c = bV_{sap} + cV_{sap}^2 + dV_{sap}^3 \quad (3)$$

where V_c is the corrected sap velocity (m s^{-1}) and b , c and d are correction coefficients; for the 2-mm-wounds we have set $b = 1.8558$, $c = -0.0018 \text{ s m}^{-1}$, $d = 0.0003 \text{ s}^2 \text{ m}^{-2}$ (Burgess et al., 2001).

We selected a dataset of continuous sap velocity measurements from four trees. Daily mean values of the sap velocities were used for the photosynthetically active period from May to October 2015 in which there was a complete time series of sap flow measurements available. Simulated daily sums of actual transpiration from the model were then compared with the average sap velocity of the four trees at the site for the same period (growing season).

For better comparison sap velocities and simulated transpiration were normalized.

Evaluation of model behavior

In our definition, a model is “behavioral”, when it is able to simulate runoff generation, water balance and the temporal pattern of soil moisture and evapotranspiration consistently with the reality. Therefore, we propose a scheme including four qualitative performance evaluation criteria to check the simulated output. This scheme allows excluding simulations that are not realistic in terms of the four sources of information mentioned above (see Table 5). Sap velocity (SV) and soil moisture (SM) criteria define the necessity of temporal consistency between observed and simulated time series of transpiration and soil water content (by comparing stand transpiration simulations with sap velocity measurements, and by comparing simulated and observed temporal pattern of soil moisture, re-

spectively). Therefore, all simulated time series that would be less consistent with the temporal variability of observations will be rejected. Since actual evapotranspiration is usually less than precipitation in the water budget (Hasenmueller and Criss, 2013), the RETa (“Realistic amount of actual evapotranspiration”) criterion eliminates simulations in which the total amount of evapotranspiration exceeds 750 mm/year. According to our knowledge of local terrain properties and field surveys, RRGP (“Realistic Runoff Generation Process”) criterion was set to deep percolation as the most plausible hydrological process at our site.

In addition to the criteria mentioned above, three widely used statistical goodness-of-fit measures complement the qualitative evaluation of model performance: Mean absolute error (MAE), correlation (R^2) and Nash-Sutcliffe efficiency index (NSE) provide additional information on the goodness-of-fit between normalized simulated transpiration and normalized sap velocity (SV) and simulated and observed soil moisture (SM). MAE (Eq. 4) is a basic index (McKeen et al., 2005; Savage et al., 2013) derived from the mean error (difference) between simulated variable and observed variable with the same length and dimensions. This measure is recommended for model performance evaluation (Fox, 1981). It is calculated as follows:

$$MAE = N^{-1} \sum_{i=1}^N |P_i - O_i| \quad (4)$$

where N is the number of the cases, $i = 1, 2, 3, \dots, N$; P is the simulation time series, and O is the observation time series.

While MAE estimates the size of difference, the correlation index R^2 quantitatively estimates the agreement between observations and simulations. R^2 can be expressed as the squared ratio between the covariance and the multiplied standard deviations of the predicted and observed values. Higher R^2 value indicates higher correlation (Legates and McCabe, 1999; Willmott, 1982).

The Nash-Sutcliffe efficiency index (NSE), is dimensionless describing the relative error between simulations and measured data (Nash and Sutcliffe, 1970). It is calculated as:

$$NSE = 1 - \frac{\sum_{i=1}^n (O_i - P_i)^2}{\sum_{i=1}^n (O_i - \bar{O})^2} = 1 - N \frac{RMSE^2}{\sum_{i=1}^n (O_i - \bar{O})^2} \quad (5)$$

where the NSE index demonstrates the normalized ratio of residual variance (noise) to the observation variance ranging between $-\infty$ and 1. An NSE value is considered to be acceptable when it ranges between 0 and 1. Fewer errors between simulations and observations always lead to a bigger NSE value and a better model performance. It is important to mention that a negative NSE value ($NSE < 0$) indicates a bad model performance that is even worse than the mean of the observed variable.

Table 5. Model performance evaluation criteria.

<i>Evaluation element</i>	<i>Description</i>	<i>Evaluation criterion</i>
Sap velocity measurements (SV)	Temporal pattern of sap velocities in terms of normalized values	SV criterion : There should be similar variability and no high deviations between the sap velocities and simulated transpiration amounts
Soil moisture measurements (SM)	Temporal pattern of soil moisture measurements in terms of mean values (%) for uppermost 50 cm of soil layer	SM criterion : There should be similar variability and no high deviations between the soil moisture measurements and simulated soil moisture amounts
Realistic amount of actual evapotranspiration (RETa)	Total amount of evapotranspiration as a component of the water budget in terms of mm/year	RETa criterion : Total evapotranspiration simulated should be between 450 to 750 mm/year
Realistic runoff generation process (RRGP)	Derived from runoff component of the water balance	RRGP criterion : The simulated runoff generation process should be deep percolation and no direct runoff as saturation or Hortonian overland flow

Based on the four evaluation criteria from Table 5 and three performance measures, unrealistic simulations will be eliminated from consideration to attain the best parameterization which provides an overall agreement among the combined performance criteria. Therefore, only under this condition, the simulation will be categorized as “behavioral”.

Applying three groups of scenarios (Table 6), we investigated the soil parameterization that reaches to the behavioral model. The simulation results of each scenario were evaluated by the model performance criteria and statistical goodness-of-fit measures. The soil parameterization in scenario A was taken from Tepee et al. (2003). In the two scenarios B1 and B2, the water retention curve was parameterized with three different variations of the van-Genuchten parameters according to (Sauer, 2007). In scenario C, the model performance was evaluated using the soil parameter set provided by Sprenger et al. (2016).

RESULTS

SCENARIO A: Model parameterization according to Tepee et al. (2003)

Since logged air or stone fraction may reduce maximum soil moisture at saturation by up to 30% (Mualem, 1974), theta_sat (saturated water content) is reduced in scenario A1 in three steps from 41% (baseline parameterization according to Tepee et al. (2003), see Table 2) to 35% and finally to 30%. Soil moisture simulated with the baseline parameterization of the soil Table (theta_sat = 41%) shows much higher values than the measurements (Figure 2). As the parameter theta_sat decreases, the simulated soil moisture values also decrease. Simulated soil water content with theta_sat = 30% shows the highest similarity with the measurements. However, the simulated dynamics of the soil moisture simulations do not match the measured dynamics.

Sap velocity rose in the transition from spring to summer and it started to decrease again with the end of the summer (Figure 3). A rapid drop in the sap velocity was observed in June and August 2015 while there was a steep rise in July 2015 for all measuring points. The simulated transpiration with different theta_sat values and the sap velocity measurements have a similar temporal pattern. Changing the theta_sat value has only a negligible effect on transpiration (Figure 3).

Evaluation of the water balance (see Table A in the appendix) unveiled that total simulated evapotranspiration (775, 773 and 762 mm/year for theta_sat = 41, 35 and 30 respectively) is too high. It is close to the annual precipitation amount (791 mm) which is not realistic. The dominant runoff

generation process was saturation excess flow or Hortonian overland flow which is not realistic according to landscape characteristics. Table 7 illustrates the model performance in scenario A1 evaluated by the three statistical efficiency measures as well as by four criteria. Meeting or not meeting a criterion is expressed in terms of “Yes” or “No” respectively. All simulations are highly correlated with the corresponding measurements ($R^2 \geq 0.73$ for all simulations). Model performances for transpiration show the same values for all theta_sat. While for the soil moisture, the simulation with theta_sat = 30 Vol% shows the lowest bias (MAE = 0.02) and a positive NSE (0.55). This confirms the results obtained from visual inspection.

To investigate the effect of scaling the bulk surface resistance parameters (r_{sc} and r_{se}), in scenario A2, the parameters r_{sc} and r_{se} are adjusted in the evapotranspiration module of the WaSiM-ETH model. The applied percentage changes were 25, 50, 75, 150, 200 and 400% according to the standard values in the model for deciduous forest (Table 1). Parameter theta_sat was set to 30 Vol% due to the relatively satisfactory simulation results obtained from scenario A1.

Changing the bulk surface resistance parameters affects the simulated soil water content. The dynamics of the soil moisture simulations are now more consistent with measured values (Figure 2). The best fit could be obtained by decreasing the r_{sc} and r_{se} values to 75% and 50% of their standard values, respectively. By lowering the bulk surface resistance parameters, the (potential) evapotranspiration increases. This extracts more water through plant transpiration and soil evaporation. Hence, under these conditions, simulated soil moisture was reduced and became closer to the measured values. The dynamics of the simulated transpiration also corresponds well to the sap velocity measurements (Figure 3).

However, the amount of evapotranspiration losses (850 mm and 867 mm with $r_{sc} = 75\%$ and $r_{se} = 50\%$, respectively) exceeded precipitation input. The simulated runoff generation process was saturation excess flow or Hortonian overland flow which was unrealistic with regard to real soil characteristics at site Sa_G (Table A in appendix). Evaluation of the results obtained from the scenario A2 is shown in Table 8. Here, all measures indicate an almost perfect fit after scaling the bulk surface resistance (NSE = 0.74 for transpiration, and NSE = 0.85 or 0.91 for soil moisture). This confirms a substantial improvement of simulation accuracy. Nevertheless, runoff generation process and water balance are not correctly reproduced.

Table 6. Overview of different scenario combinations.

SCENARIO A (using soil parameterization after Tepee et al. (2003))	A1 (Scaling theta_sat)	-41% -35% -30%
	A2 Scaling bulk surface resistances theta_sat = 30%	A2-1 (Scaling soil surface resistance r_{se}) 25%-50%-75%-100%- 150%-200%-400%
		A2-2 (Scaling canopy surface resistance r_{sc}) 25%-50%-75%-100%- 150%-200%-400%
SCENARIO B (using soil parameterization after Sauer (2007))	B1 Re-parameterization of Water Retention Curve with theta_sat = 30%	-Variation 1 -Variation 2 -Variation 3
	B2 Re-parameterization of Water Retention Curve with theta_sat = 41%	-Variation 1 -Variation 2 -Variation 3
	SCENARIO C Soil parameterization after Sprenger et al. (2016)	Comparison to best performing parameter set (theta_sat = 41%, Var1)

Table 7. Criteria evaluation and efficiency measures in scenario A1.

Scenario A1: scaling theta_sat						
Criterion	30 Vol%		35 Vol%		41 Vol%	
SV	Yes		Yes		Yes	
SM	No		No		No	
RETA	No		No		No	
RRGP	No		No		No	
Efficiency measure	Transpiration	Soil moisture	Transpiration	Soil moisture	Transpiration	Soil moisture
	R ²	0.73	0.95	0.73	0.95	0.73
MAE	0.42	0.02	0.42	0.08	0.42	0.13
NSE	0.71	0.55	0.71	-2.66	0.71	-8.92

Table 8. Criteria evaluation and efficiency measures in scenario A2.

Criterion	30 Vol% (baseline)		A2-1 (r _{sc} = 50%)		A2-2 (r _{sc} = 75%)	
SV	Yes		Yes		Yes	
SM	No		Yes		Yes	
RETA	No		No		No	
RRGP	No		No		No	
Efficiency measure	Transpiration	Soil moisture	Transpiration	Soil moisture	Transpiration	Soil moisture
	R ²	0.73	0.95	0.73	0.94	0.76
MAE	0.42	0.02	0.39	0.01	0.39	0.01
NSE	0.71	0.55	0.74	0.91	0.74	0.85

Table 9. Criteria evaluation and efficiency measures for model performances in scenarios B1 and B2.

Criterion	Re-parameterization of the water retention curve – scenario B															
	scenario B1 (theta_sat = 30 %)								scenario B2 (theta_sat = 41%)							
	Baseline		Var1		Var2		Var3		Baseline		Var1		Var2		Var3	
SV	Yes	No	No	No	No	No	No	No	Yes	Yes	No	No	No	No	No	No
SM	No	No	No	No	No	No	No	No	No	Yes	No	No	No	No	No	No
RETA	No	Yes	Yes	Yes	Yes	Yes	Yes	Yes	No	Yes	Yes	Yes	Yes	Yes	Yes	Yes
RRGP	No	Yes	Yes	Yes	Yes	Yes	Yes	Yes	No	Yes	Yes	Yes	Yes	Yes	Yes	Yes
Efficiency measure	SM	Tr	SM	Tr	SM	Tr	SM	Tr	SM	Tr	SM	Tr	SM	Tr	SM	Tr
	R ²	0.95	0.73	0.75	0.64	0.60	0.37	0.62	0.11	0.93	0.61	0.74	0.73	0.67	0.5	0.62
MAE	0.02	0.42	0.05	0.53	0.07	0.75	0.06	0.97	0.13	0.42	0.02	0.43	0.04	0.66	0.06	0.97
NSE	0.55	0.71	-0.44	0.6	-1.98	0.21	-1.64	-0.34	-8.92	0.71	0.65	0.71	-0.01	0.41	-1.64	-0.34

SCENARIO B: Re-parameterization of Water Retention Curve

In scenario B1, van Genuchten parameters of the baseline parametrization of the soil were re-parameterized according to Sauer (2007), where three variations of the parameters “alpha” and “n” were proposed for the same soil type “loamy sand”. Figure 2 depicts soil moisture of the three variations of van Genuchten parameters for a soil with theta_sat = 30%. All variants underestimate the measured values. Variation of van Genuchten parameters also affects simulated actual transpiration rates: In Figure 3, we clearly see that simulated transpiration does not match the temporal pattern of sap velocity measurements.

In all three variations, the soil was significantly dryer than the measured value. In variation 2 and 3 the soil water content came close to the residual water content. For the simulated transpiration, its temporal consistency with sap velocity decreased from variation 1 to 3. As all three variations performed worse than the best A1 scenario all three variants are rejected.

In scenario B2 we changed theta_sat from 30 to 41 Vol% and then repeated the three variations of alpha and n after Sauer (2007) and then checked both soil moisture (Figure 2) and

transpiration dynamics (Figure 3). Simulation results with theta_sat = 41% for the transpiration dynamics are relatively consistent with the observed sap velocities over the entire vegetation period for variation 1. In scenario B2, variation 1 provided sufficient soil water during the vegetation period for plant transpiration. This corresponds well to temporal patterns of sap velocities. Nevertheless, in variation 2 and 3, simulated transpiration did not reproduce the temporal patterns of the sap velocity data. There is a strong deviation in July and August 2015 and at some points the simulated transpiration drops to zero. This is the result of the low soil water content in summer (close to residual water content) for these two variations.

Table 9 provides all evaluation results related to the scenario B. Runoff generation process for all three variations with theta_sat = 30% and 41% is now deep percolation (Table A in appendix). Furthermore, the total amount of evapotranspiration was less than 750 mm for all variations. Variation 1 with theta_sat = 41% fulfills all four evaluation criteria. This is confirmed by the three statistical efficiency measures. Here, variation 1 with theta_sat = 41% clearly performs the best. In accordance with our definition we can label this model parameterization as “behavioral”.

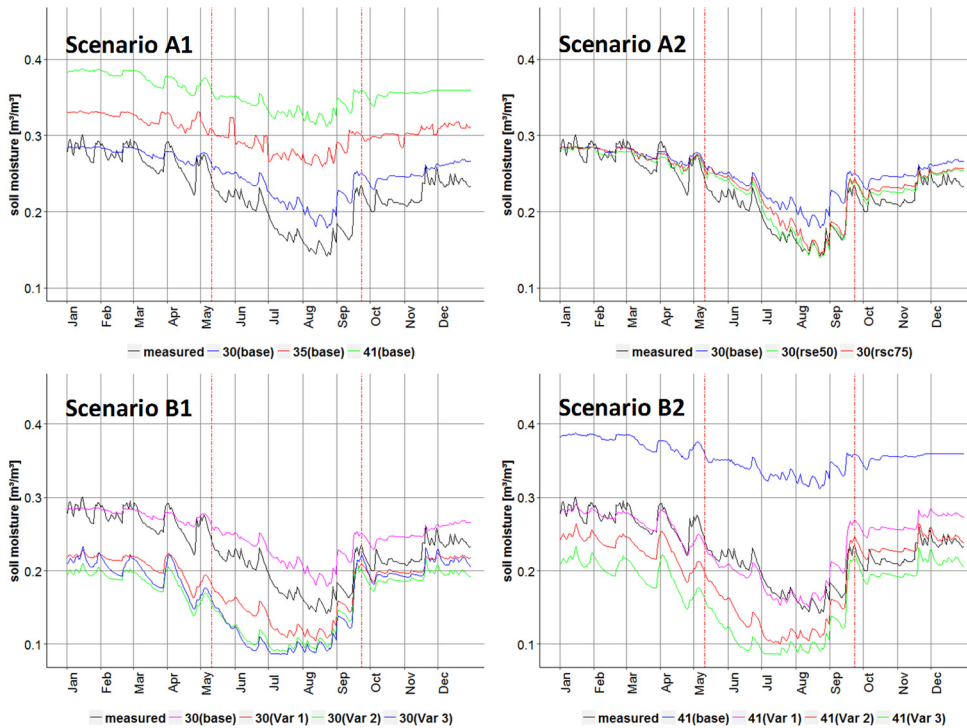


Fig. 2. Simulated and measured soil moisture in the root zone (Vol%) in 2015 for Scenarios A1, A2, B1 and B2. Red vertical lines indicate the growing season.

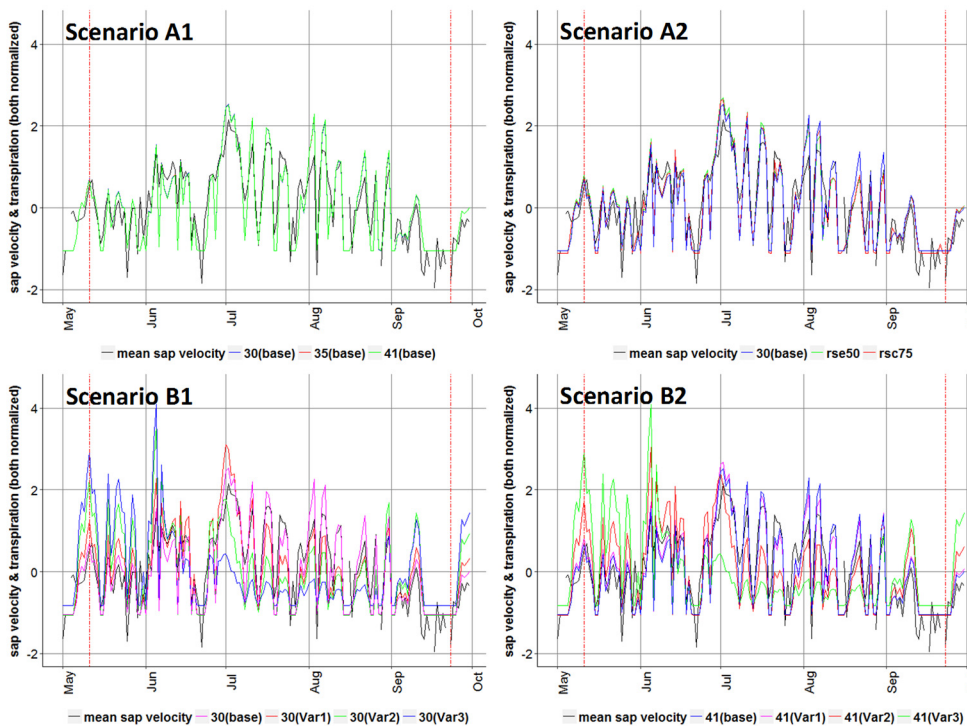


Fig. 3. Simulated transpiration (normalized) and normalized mean values of sap velocity (measured) for growing season 2015 (Scenarios A1, A2, B1, B2). In Scenario A1 all simulations show the same transpiration (identical lines).

SCENARIO C: Soil parameterization after Sprenger et al. (2016)

Sprenger et al. (2016) provided a soil parameter set for the Site Sa_G. In the scenario C, this parameter set was determined by automatic fitting to soil moisture measurements and stable isotope data. We compared this parameterization with our best performing model from the previous section (variation 1 from scenario B2 with $\theta_{sat} = 41\%$).

The simulated runoff generation process was deep percolation which is plausible (Table A in appendix). Total

evapotranspiration (602 mm) was estimated to be lower than precipitation (791 mm) which is also correct. But it can be seen in Figure 4 that soil moisture simulation does not show the correct dynamics compared to the measured time series. Here again, the parameterization of WRC is the reason that the soil is drying out in summer. This causes a significant reduction in transpiration during August which does not correspond to our sap velocity measurements. Additionally, the statistical efficiency measures (Table 10) reveal that the model performs very weak in simulating soil moisture (negative value for NSE). Simulated transpiration is therefore not consistent with the

corresponding sap velocity time series (Figure 5). It shows an overestimation in spring and a slight underestimation in summer, which is also indicated by lower model performance measures compared to the simulation with the optimal parameter set (B2, variation 1 with $\theta_{\text{sat}} = 41\%$) from the previous section.

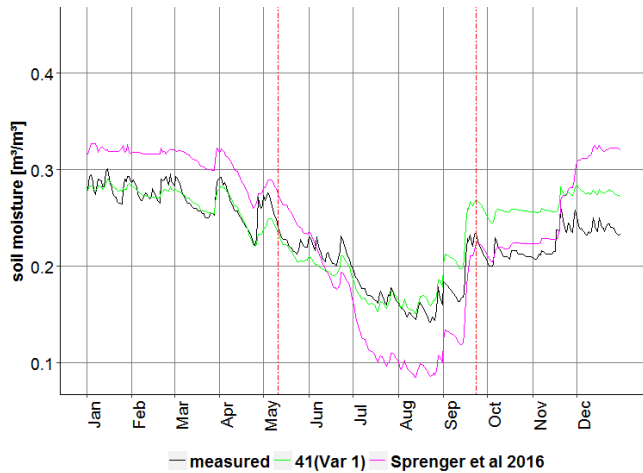


Fig. 4. Simulated soil water content for soil parameters according to Sprenger et al. 2016 compared to corresponding measured values and simulated soil moisture from variation 1 ($\theta_{\text{sat}} = 41\%$) in 2015. Red vertical lines indicate the growing season.

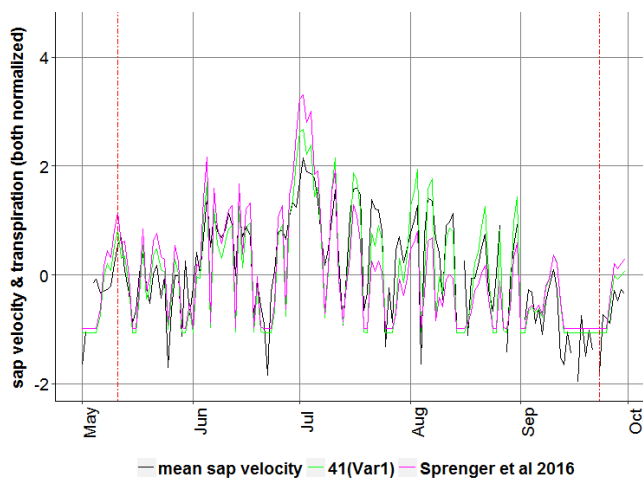


Fig. 5. Normalized simulated transpiration for soil parameters according to Sprenger et al. 2016 compared to normalized mean sap velocity (measured) and normalized simulated transpiration for variation 1 ($\theta_{\text{sat}} = 41\%$) in growing season 2015.

Table 10. Criteria evaluation and efficiency measures for soil parameterization according to Sprenger et al. (2016).

Criterion	Optimal parameter set ($\theta_{\text{sat}} = 41\%$, Variation 1)		Sprenger et al. 2016	
	Transpiration	Soil moisture	Transpiration	Soil moisture
SV	Yes		No	
SM	Yes		No	
REtr	Yes		Yes	
RRGP	Yes		Yes	
Efficiency measure				
	R ²	0.73	0.74	0.61
	MAE	0.43	0.02	0.55
	NSE	0.71	0.65	0.57
				0.89
				0.04
				-0.11

DISCUSSION

The main objective of this study was to build up a behavioral forest stand water balance model to characterize the temporal changes in hydrological components of water balance by making use of both observed soil moisture and sap velocities as well as expert knowledge of local runoff generation processes. A behavioral model was defined as a model in which simulation results have to be consistent with measurements of soil moisture and sap velocity and with our hydrologic understanding of runoff generation processes in the area of investigation. To accomplish the objectives, a multi-criteria evaluation scheme was developed. While 24 model realizations were tested, only one model realization could be categorized as “behavioral”.

Results of this study demonstrated that without the use of additional information (e.g. using sap velocity measurements for transpiration dynamics; different soil parameterizations, and expert knowledge), it is not possible to identify a model which captures these processes and dynamics adequately. This sheds light on the value of the contribution of different forms of data in representing the catchment behavior. In a case study in a Swiss Pre-Alpine catchment, it was also found that the application of expert knowledge and the concept of dominant processes can increase the realism of the hydrological models (Antonetti and Zappa, 2018). Taking into consideration that model evaluation would always be partly subjective, we looked at the model behavior from different perspectives through application of multi criteria evaluation that integrated this additional information. Therefore, we were able to select a behavioral parameter set from a number of equally likely soil parameterizations. The development of a multi-criteria approach for model evaluation is based on the consideration that a single measure of performance does not properly extract the information contained in the data (Gupta et al., 1998). This approach includes multiple performance measures and allows to evaluate if the hydrological model is able to represent the behavior of internal catchment processes (Fenicia et al., 2008b). Moreover, our results are also in line with Livneh (2012). He improved model performance significantly by the application of a multi-criteria scheme to evaluate multiple model outputs and by adding supplementary information in the parameterization process (Livneh, 2012). Another study showed that the introduction of constraints was efficient in reducing simulation uncertainty, in conditioning parameters, and in identifying critical parameters (Senapati et al., 2016).

All functions describing soil water retention imply a specific soil hydraulic behavior. Soil parameterization schemes according to Teepe et al. (2003) and Sauer (2007) use different amounts of soil information to derive pedo-transfer functions to translate soil information into van Genuchten parameters. Our results revealed that different parameterizations of the corresponding soil led to diverse simulation results. This issue is of great significance in all models applying the Richard’s equation (e.g. WaSiM-ETH). Therefore, finding a behavioral model for evapotranspiration is highly dependent on the identification of an appropriate WRC. This is consistent with the results of Garrigues et al. (2018). They compared the performance of two water transfer models in simulating evapotranspiration using different soil parameterizations. They found an unexpectedly high model sensitivity to soil moisture at field capacity, root extinction coefficient, and the proportion of homogeneous root distribution (Garrigues et al., 2018). In our proof-of-concept study based on a 1-D model, we took the measurements of sapflow and soil moisture as representative for the “sandstone area” where the dominant hydrologic process is deep percola-

tion. This made it possible to identify a behavioral model. It is known that models might work for the wrong reasons (i.e. reproducing discharge with incorrect process representations) (Beven, 2006; Walker and Zhang, 2002). This makes it advisable to implement expert knowledge to develop a proper parameterization to reflect our perceptions of the processes observed.

CONCLUSION

A considerable amount of effort is still being devoted to the development of hydrological models, and there is a continuing need to advance the techniques for their parameter estimation. It is also important to develop a good working knowledge of their sensitivity, and strengths and weaknesses.

This study underlines the importance of correctly setting up the 1-D water balance simulation model WaSiM-ETH in order to reproduce the dynamics of soil water fluxes and the physiological control of water loss through transpiration at a specific site (beech forest in Western Luxembourg). Adjustment of the parametrization of the WRC showed a high impact on simulation results. Our main finding was that: even though all parameter sets refer to the same soil (“loamy sand”), a slightly different parameterization of soil moisture at saturation (θ_{sat}), bulk surface resistance parameters and WRC may result in implausible model behavior. Even if transpiration and soil moisture are simulated consistently with our observations, runoff generation or total water balance may be wrongly estimated. Therefore, only the introduction of a multi-criteria evaluation scheme for exclusion of unrealistic outputs allowed finding a well performing parameter set for our test site. These findings suggest that using different sources of information such as expert knowledge on the dominant hydrological processes and the understanding of local controls facilitate parameterization and evaluation of a hydrological model. We should question the generally accepted procedure to parametrize soils using “default” parameter sets based on soil texture description or similar. Only if porosity and WRC for all soil horizons are correctly adjusted, a “physically based” model may simulate runoff processes and transpiration consistently with observations. Only in this case, we may refer to a model as “behavioral” (Gupta et al., 2005). We recommend finding “prototype soils” which are in accordance with soil description (e.g. texture) and expert knowledge on runoff processes in the area under investigation. This in turn implies that model parameterization, evaluation or calibration has to incorporate this “soft” knowledge.

Setups identified as optimal for 1-D simulations will go a long way of improving the application of WaSiM-ETH water balance model on catchment scale to answer questions about watershed characteristics and water resources management. Since point measurements are not valid on catchment scale, we may try to address the spatiotemporal distribution of evapotranspiration, soil moisture and runoff generation processes at catchment scale as well as the estimation of overall water balance at the corresponding gaging station(s) (Koch et al., 2016, 2015). The current study showed that soil parameterization affects not only the temporal distribution of soil moisture and transpiration, but also the runoff generation process. This also highlights the need to consider the incorporation of several data products to increase knowledge about the hydrological processes on catchment scale (Casper et al., 2015). Remotely sensed data will open up the possibility to analyze spatial patterns of actual evapotranspiration (ETa) or soil moisture (Koch et al., 2017). Together with additional knowledge of the spatial distribution of dominant runoff processes on catchment scale this

will facilitate the parameterization of the hydrological model WaSiM-ETH and its subsequent optimization by extending the traditional model evaluation procedure at gaging stations with the search for a best fit of spatial patterns of ETa and runoff processes on catchment scale. A number of automatic mapping approaches for delineation of dominant runoff process exist, which can be used to constrain the uncertainty of hydrological simulations (Antonetti et al., 2016; Behrens et al., 2010). The model RoGeR (Runoff Generation Research) demonstrated its ability to quantify runoff process in high spatial and temporal resolution without the need of parameter calibration (Steinbrich et al., 2016). This approach combines knowledge of runoff process gained through long term research with spatially distributed data sets and can thus be used to extend the here presented approach to the catchment scale.

Acknowledgements. The data was collected within the DFG Research Unit FOR 1598 “Catchments As Organized Systems (CAOS)” in a project led by Markus Weiler and Theresa Blume. All datasets can be obtained from Theresa Blume (blume@gfz-potsdam.de) upon request. We thank the technicians Britta Kattenstroth and Tobias Vetter for the maintenance of the sensor network.

REFERENCES

- Allen, R.G., Pereira, L.S., Raes, D., Smith, M., others, 1998. Crop evapotranspiration-guidelines for computing crop water requirements. FAO Irrigation and Drainage Paper 56. FAO Rome 300, D05109.
- Anderson, M.C., Norman, J.M., Mecikalski, J.R., Otkin, J.A., Kustas, W.P., 2007. A climatological study of evapotranspiration and moisture stress across the continental United States based on thermal remote sensing: 1. Model formulation. *J. Geophys. Res.-Atmospheres*, 112, Article Number: D10117.
- Antonetti, M., Buss, R., Scherrer, S., Margreth, M., Zappa, M., 2016. Mapping dominant runoff processes: an evaluation of different approaches using similarity measures and synthetic runoff simulations. *Hydrol. Earth Syst. Sci.*, 20, 2929–2945. <https://doi.org/10.5194/hess-20-2929-2016>
- Antonetti, M., Zappa, M., 2018. How can expert knowledge increase the realism of conceptual hydrological models? A case study based on the concept of dominant runoff process in the Swiss Pre-Alps. *Hydrol. Earth Syst. Sci.*, 22, 4425–4447.
- Ayyoub, A., Er-Raki, S., Khabba, S., Merlin, O., Ezzahar, J., Rodriguez, J., Bahlaoui, A., Chehbouni, A., 2017. A simple and alternative approach based on reference evapotranspiration and leaf area index for estimating tree transpiration in semi-arid regions. *Agric. Water Manag.*, 188, 61–68.
- Bahremand, A., 2016. HESS Opinions: Advocating process modeling and de-emphasizing parameter estimation. *Hydrol. Earth Syst. Sci.*, 20, 1433–1445.
- Behrens, T., Zhu, A.-X., Schmidt, K., Scholten, T., 2010. Multi-scale digital terrain analysis and feature selection for digital soil mapping. *Geoderma*, 155, 175–185. <http://dx.doi.org/10.1016/j.geoderma.2009.07.010>
- Beven, K., 2006. A manifesto for the equifinality thesis. *J. Hydrol.*, 320, 18–36.
- Beven, K., 1979. A sensitivity analysis of the Penman-Monteith actual evapotranspiration estimates. *J. Hydrol.*, 44, 169–190.
- Bie, W., Casper, M.C., Reiter, P., Vohland, M., 2015. Surface resistance calibration for a hydrological model using evapotranspiration retrieved from remote sensing data in Nahe catchment forest area. *Proc. Int. Assoc. Hydrol. Sci.*, 368, 81–86. <https://doi.org/10.5194/piahs-368-81-2015>
- Blöschl, G., 2001. Scaling in hydrology. *Hydrol. Process.*, 15, 709–711.
- Bromley, J., Jackson, N.A., Clymer, O., Giacomello, A.M., Jensen, F.V., 2005. The use of Hugin® to develop Bayesian networks as an aid to integrated water resource planning. *Environ. Model. Softw.*, 20, 231–242.

- Burgess, S.S., Adams, M.A., Turner, N.C., Beverly, C.R., Ong, C.K., Khan, A.A., Bleby, T.M., 2001. An improved heat pulse method to measure low and reverse rates of sap flow in woody plants. *Tree Physiol.*, 21, 589–598.
- Campbell, G., Calissendorff, C., Williams, J., 1991. Probe for measuring soil specific heat using a heat-pulse method. *Soil Sci. Soc. Am. J.*, 55, 291–293.
- Cash, D.W., Clark, W.C., Alcock, F., Dickson, N.M., Eckley, N., Guston, D.H., Jäger, J., Mitchell, R.B., 2003. Knowledge systems for sustainable development. *Proc. Natl. Acad. Sci.*, 100, 8086–8091.
- Casper, M.C., Gronz, O., Gemmar, P., 2015. Process-oriented parameterisation and calibration of a water balance model. *Hydrol. Wasserbewirtsch.*, 59, 136–144.
- Casper, M.C., Vohland, M., 2008. Validation of a large scale hydrological model with data fields retrieved from reflective and thermal optical remote sensing data – A case study for the Upper Rhine Valley. *Phys. Chem. Earth Parts ABC*, 33, 1061–1067. <http://dx.doi.org/10.1016/j.pce.2008.06.001>
- Cullmann, J., Mishra, V., Peters, R., 2006. Flow analysis with WaSiM-ETH? model parameter sensitivity at different scales. *Adv. Geosci.*, 9, 73–77.
- Droogers, P., Allen, R.G., 2002. Estimating reference evapotranspiration under inaccurate data conditions. *Irrig. Drain. Syst.*, 16, 33–45.
- Durigon, A., Van Lier, Q.D.J., Metselaar, K., 2016. Forcing variables in simulation of transpiration of water stressed plants determined by principal component analysis. *Int. Agrophysics*, 30, 431–445.
- Elfert, S., Bormann, H., 2010. Simulated impact of past and possible future land use changes on the hydrological response of the Northern German lowland ‘Hunte’ catchment. *J. Hydrol.*, 383, 245–255.
- Federer, C.A., Lash, D., 1978. Simulated streamflow response to possible differences in transpiration among species of hardwood trees. *Water Resour. Res.*, 14, 1089–1097.
- Fenicia, F., McDonnell, J.J., Savenije, H.H., 2008a. Learning from model improvement: On the contribution of complementary data to process understanding. *Water Resour. Res.*, 44, 6, Article Number: W06419.
- Fenicia, F., Savenije, H.H., Matgen, P., Pfister, L., 2008b. Understanding catchment behavior through stepwise model concept improvement. *Water Resour. Res.*, 44, 1, Article Number: W01402.
- Fox, D.G., 1981. Judging air quality model performance. *Bull. Am. Meteorol. Soc.*, 62, 599–609.
- Franks, S.W., Gineste, P., Beven, K.J., Merot, P., 1998. On constraining the predictions of a distributed model: the incorporation of fuzzy estimates of saturated areas into the calibration process. *Water Resour. Res.*, 34, 787–797.
- Garrigues, S., Boone, A., Decharme, B., Olioso, A., Albergel, C., Calvet, J.-C., Moulin, S., Buis, S., Martin, E., 2018. Impacts of the soil water transfer parameterization on the simulation of evapotranspiration over a 14-year Mediterranean crop succession. *J. Hydrometeorol.*, 19, 3–25.
- Gharari, S., Hrachowitz, M., Fenicia, F., Gao, H., Savenije, H., 2014. Using expert knowledge to increase realism in environmental system models can dramatically reduce the need for calibration. *Hydrol. Earth Syst. Sci.*, 18, 4839.
- Grayson, R., Blöschl, G., 2001. Summary of pattern comparison and concluding remarks. In: Grayson, R., Blöschl, G. (Eds): *Spatial Patterns in Catchment Hydrology – Observations and Modelling*. Cambridge University Press, Cambridge, UK, pp. 355–367.
- Grigoryan, G.V., Casper, M.C., Gauer, J., Vasconcelos, A.C., Reiter, P.P., 2010. Impact of climate change on water balance of forest sites in Rhineland-Palatinate, Germany. *Adv. Geosci.*, 27, 37–43. <https://doi.org/10.5194/adgeo-27-37-2010>
- Gupta, H.V., Beven, K.J., Wagener, T., 2005. Model calibration and uncertainty estimation. In: Anderson, M. (Ed.): *Encyclopedia of Hydrological Sciences*, Vol. 3, Chapter 131, pp. 2015–2032.
- Gupta, H.V., Sorooshian, S., Yapo, P.O., 1998. Toward improved calibration of hydrologic models: Multiple and noncommensurable measures of information. *Water Resour. Res.*, 34, 751–763.
- Gurtz, J., Zappa, M., Jasper, K., Lang, H., Verbunt, M., Badoux, A., Vitvar, T., 2003. A comparative study in modelling runoff and its components in two mountainous catchments. *Hydrol. Process.*, 17, 297–311.
- Hasenmueller, E.A., Criss, R.E., 2013. Water balance estimates of evapotranspiration rates in areas with varying land use. In: Alexandris, S. (Ed.): *Evapotranspiration-An Overview*. IntechOpen, DOI: 10.5772/52811.
- Hassler, S.K., Weiler, M., Blume, T., 2018. Tree-, stand- and site-specific controls on landscape-scale patterns of transpiration. *Hydrol. Earth Syst. Sci.*, 22, 13–30.
- Haude, W., 1955. Zur Bestimmung der Verdunstung auf möglichst einfache Weise. *Dt. Wetterdienst*, Bad Kissingen.
- Holst, J., Grote, R., Offermann, C., Ferrio, J.P., Gessler, A., Mayer, H., Rennenberg, H., 2010. Water fluxes within beech stands in complex terrain. *Int. J. Biometeorol.*, 54, 23–36.
- Hrachowitz, M., Fovet, O., Ruiz, L., Euser, T., Gharari, S., Nijzink, R., Freer, J., Savenije, H., Gascuel-Oudou, C., 2014. Process consistency in models: The importance of system signatures, expert knowledge, and process complexity. *Water Resour. Res.*, 50, 7445–7469.
- Jasper, K., 2001. Hydrological modelling of Alpine river catchments using output variables from atmospheric models (PhD Thesis). ETH Zurich.
- Jasper, K., Gurtz, J., Lang, H., 2002. Advanced flood forecasting in Alpine watersheds by coupling meteorological observations and forecasts with a distributed hydrological model. *J. Hydrol.*, 267, 40–52.
- Juilleret, J., Iffly, J.-F., Hoffmann, L., Hissler, C., 2012. The potential of soil survey as a tool for surface geological mapping: a case study in a hydrological experimental catchment (Huewelerbach, Grand-Duchy of Luxembourg). *Geologica Belgica*, 15, 1–2, 36–41.
- Klok, E., Jasper, K., Roelofsma, K., Gurtz, J., Badoux, A., 2001. Distributed hydrological modelling of a heavily glaciated Alpine river basin. *Hydrol. Sci. J.*, 46, 553–570.
- Koch, J., Jensen, K.H., Stisen, S., 2015. Toward a true spatial model evaluation in distributed hydrological modeling: Kappa statistics, Fuzzy theory, and EOF-analysis benchmarked by the human perception and evaluated against a modeling case study. *Water Resour. Res.*, 51, 1225–1246. <https://doi.org/10.1002/2014WR016607>
- Koch, J., Mendiguren, G., Mariethoz, G., Stisen, S., 2017. Spatial sensitivity analysis of simulated land surface patterns in a catchment model using a set of innovative spatial performance metrics. *J. Hydrometeorol.*, 18, 1121–1142. <https://doi.org/10.1175/JHM-D-16-0148.1>
- Koch, J., Siemann, A., Stisen, S., Sheffield, J., 2016. Spatial validation of large-scale land surface models against monthly land surface temperature patterns using innovative performance metrics. *J. Geophys. Res. Atmospheres*, 121, 5430–5452.
- Köstner, B., Biron, P., Siegwolf, R., Granier, A., 1996. Estimates of water vapor flux and canopy conductance of Scots pine at the tree level utilizing different xylem sap flow methods. *Theor. Appl. Climatol.*, 53, 105–113.
- Kramer, P.J., Boyer, J.S., 1995. *Water Relations of Plants and Soils*. Academic Press.
- Legates, D.R., McCabe, G.J., 1999. Evaluating the use of “goodness-of-fit” measures in hydrologic and hydroclimatic model validation. *Water Resour. Res.*, 35, 233–241.
- Livneh, B., 2012. Development of a unified land model with multi-criteria observational data for the simulation of regional hydrology and land-atmosphere interaction. PhD Thesis. University of Washington, Seattle, USA.
- Lu, P., Urban, L., Zhao, P., 2004. Granier’s thermal dissipation probe (TDP) method for measuring sap flow in trees: theory and practice. *ACTA Bot. Sin. (Engl. Ed.)*, 46, 631–646.
- Martínez-Carreras, N., Krein, A., Gallart, F., Iffly, J.-F., Hissler, C., Pfister, L., Hoffmann, L., Owens, P.N., 2012. The influence of sediment sources and hydrologic events on the nutrient and metal content of fine-grained sediments (Attert River basin, Luxembourg). *Water. Air. Soil Pollut.*, 223, 5685–5705.
- Martínez-Carreras, N., Udelhoven, T., Krein, A., Gallart, F., Iffly, J.F., Ziebel, J., Hoffmann, L., Pfister, L., Walling, D.E., 2010. The use of sediment colour measured by diffuse reflectance spectrometry to determine sediment sources: application to the Attert River catchment (Luxembourg). *J. Hydrol.*, 382, 49–63.
- McKeen, S., Wilczak, J., Grell, G., Djalalova, I., Peckham, S., Hsie, E.-Y., Gong, W., Bouchet, V., Menard, S., Moffet, R., others, 2005. Assessment of an ensemble of seven real-time ozone forecasts over eastern North America during the summer of 2004. *J. Geophys. Res.-Atmospheres*, 110, Article Number: D21307.
- Middelkoop, H., Daamen, K., Gellens, D., Grabs, W., Kwadijk, J.C.,

Lang, H., Parmet, B.W.A.H., Schädler, B., Schulla, J., Wilke, K., 2001. Impact of climate change on hydrological regimes and water resources management in the Rhine basin. *Clim. Change*, 49, 105–128.

Mohajerani, H., Kholghi, M., Mosaedi, A., Farmani, R., Sadoddin, A., Casper, M., 2017. Application of Bayesian decision networks for groundwater resources management under the conditions of high uncertainty and data scarcity. *Water Resour. Manag.*, 31, 1859–1879.

Monteith, J., 1981. Evaporation and surface temperature. *Q. J. R. Meteorol. Soc.*, 107, 1–27.

Monteith, J., Szeicz, G., Waggoner, P., 1965. The measurement and control of stomatal resistance in the field. *J. Appl. Ecol.*, 345–355.

Mualem, Y., 1974. A conceptual model of hysteresis. *Water Resources Research*, 10, 514–520.

Nash, J.E., Sutcliffe, J.V., 1970. River flow forecasting through conceptual models part I—A discussion of principles. *J. Hydrol.*, 10, 282–290.

Paço, T.A., Pôças, I., Cunha, M., Silvestre, J.C., Santos, F.L., Paredes, P., Pereira, L.S., 2014. Evapotranspiration and crop coefficients for a super intensive olive orchard. An application of SIMDualKc and METRIC models using ground and satellite observations. *J. Hydrol.*, 519, 2067–2080.

Pfister, L., Humbert, J., Hoffmann, L., 2000. Recent trends in rainfall-runoff characteristics in the Alzette river basin, Luxembourg. *Clim. Change*, 45, 323–337.

Richards, L.A., 1931. Capillary conduction of liquids through porous mediums. *Physics*, 1, 318–333.

Sauer, T., 2007. Modellierung von Bodenwasserhaushalt und Abflussprozessen auf der Plotskale in Abhängigkeit von Substrat und Landnutzung (Dissertation). University of Trier, Trier, Germany.

Saugier, B., Granier, A., Pontailler, J., Dufrene, E., Baldocchi, D., 1997. Transpiration of a boreal pine forest measured by branch bag, sap flow and micrometeorological methods. *Tree Physiol.*, 17, 511–519.

Savage, N., Agnew, P., Davis, L., Ordóñez, C., Thorpe, R., Johnson, C., O’Connor, F., Dalvi, M., 2013. Air quality modelling using the Met Office Unified Model (AQUAM OS24-26): model description and initial evaluation. *Geosci. Model Dev.*, 6, 353.

Schaap, M.G., Leij, F.J., Van Genuchten, M.T., 2001. Rosetta: A computer program for estimating soil hydraulic parameters with hierarchical pedotransfer functions. *J. Hydrol.*, 251, 163–176.

Schulla, J., 2017. Model Description WaSiM (Water balance Simulation Model), completely revised version 2017. Zür. Switz. Hydrol. Softw. Consult., 347.

Schulla, J., 1997. Hydrologische Modellierung von Flussgebieten zur Abschätzung der Folgen von Klimaänderungen. PhD Thesis. ETH Zurich.

Seibert, J., McDonnell, J.J., 2002. On the dialog between experimentalist and modeler in catchment hydrology: Use of soft data for multicriteria model calibration. *Water Resour. Res.*, 38, 11, Article Number: 1241.

Senapati, N., Jansson, P.-E., Smith, P., Chabbi, A., 2016. Modelling heat, water and carbon fluxes in mown grassland under multi-objective and multi-criteria constraints. *Environ. Model. Softw.*, 80, 201–224.

Sprenger, M., Seeger, S., Blume, T., Weiler, M., 2016. Travel times in the vadose zone: Variability in space and time. *Water Resour. Res.*, 52, 5727–5754.

Steinbrich, A., Leister, H., Weiler, M., 2016. Model-based quantification of runoff generation processes at high spatial and temporal resolution. *Environ. Earth Sci.*, 75, 1423.

Teepe, R., Dilling, H., Beese, F., 2003. Estimating water retention curves of forest soils from soil texture and bulk density. *J. Plant Nutr. Soil Sci.*, 166, 111–119.

Van Genuchten, M.T., 1980. A closed-form equation for predicting the hydraulic conductivity of unsaturated soils 1. *Soil Sci. Soc. Am. J.*, 44, 892–898.

Van Genuchten, M.T., Leij, F.J., Yates, S.R., Williams, J.R., 1991. The RETC code for quantifying the hydraulic functions of unsaturated soils. U.S. Salinity Laboratory, USDA, Riverside, California.

Verbunt, M., Gurtz, J., Jasper, K., Lang, H., Warmerdam, P., Zappa, M., 2003. The hydrological role of snow and glaciers in alpine river basins and their distributed modeling. *J. Hydrol.*, 282, 36–55.

Vose, J.M., Harvey, G.J., Elliott, K.J., Clinton, B.D., 2003. Measuring and modeling tree and stand level transpiration. In: Lehr, J.H., Keeley, J. (Eds.): *Water Encyclopedia*, Volume 3, Surface and Agricultural Water. Wiley, pp. 732–740.

Wagner, T., Boyle, D.P., Lees, M.J., Wheeler, H.S., Gupta, H.V., Sorooshian, S., 2001. A framework for development and application of hydrological models. *Hydrol. Earth Syst. Sci.*, 5, 13–26.

Walker, G.R., Zhang, L., 2002. Plot Scale Models and their Application to Recharge Studies. Part 10 of Basics of Recharge and Discharge Series. CSIRO Publishing.

Wendling, U., 1975. Zur Messung und Schätzung der potentiellen Verdunstung. *Z. Für Meteorol.*, 25, 103–111.

Willmott, C.J., 1982. Some comments on the evaluation of model performance. *Bull. Am. Meteorol. Soc.*, 63, 1309–1313.

Wilson, K.B., Hanson, P.J., Mulholland, P.J., Baldocchi, D.D., Wullschleger, S.D., 2001. A comparison of methods for determining forest evapotranspiration and its components: sap-flow, soil water budget, eddy covariance and catchment water balance. *Agric. For. Meteorol.*, 106, 153–168.

Zehe, E., Ehret, U., Pfister, L., Blume, T., Schröder, B., Westhoff, M., Jackisch, C., Schymanski, S. J., Weiler, M., Schulz, K., Allroggen, N., Tronicke, J., van Schaik, L., Dietrich, P., Scherer, U., Eccard, J., Wulfmeyer, V., Kleidon, A., 2014. HESS Opinions: From response units to functional units: a thermodynamic reinterpretation of the HRU concept to link spatial organization and functioning of intermediate scale catchments. *Hydrol. Earth Syst. Sci.*, 18, 4635–4655.

Received 30 April 2018
Accepted 14 November 2018

APPENDIX

Table A. Water balance for all simulation runs, DP = Deep Percolation, SOF = Saturation Overland Flow, HOF = Hortonian Overland Flow.

Scenario	A1			A2		B1:			B2			C
	base-line 41	baseline 35%	baseline 30%	r _{sc} 75%	r _{se} 50%	Var. 1 30%	Var. 2 30%	Var. 3 30%	Var. 1 41%	Var. 2 41%	Var. 3 41%	
Pot. Evaporation	270	270	270	281	471	270	270	270	270	270	270	270
Real Evaporation	261	259	250	254	372	174	167	179	183	168	179	160
Interception Evaporation	146	146	146	157	146	146	146	146	146	146	146	146
ETp	851	851	851	978	1051	851	851	851	851	851	851	851
ETr	776	774	762	850	867	613	536	497	676	569	497	602
ETr_Layer1 = Transpiration	368	368	365	438	348	293	222	172	347	255	172	296
Baseflow	145	166	107	117	73	212	278	316	251	267	316	196
Direct Runoff	161	11	82	63	73	0	0	0	0	0	0	0
Interflow	0	0	0	0	0	0	0	0	0	0	0	0
Total Runoff	306	177	190	180	146	212	278	316	251	267	316	196
GW recharge	68	114	94	103	64	190	268	307	130	248	307	156
Delta Storage	-290	-160	-161	-239	-222	-33	-22	-22	-136	-45	-22	-7
Precipitation	791	791	791	791	791	791	791	791	791	791	791	791
Total Balance Error	0	0	0	0	0	0	0	0	0	0	0	0
Runoff Process	SOF/HOF	SOF/HOF/DP	SOF/HOF	SOF/HOF	SOF/HOF	DP	DP	DP	DP	DP	DP	DP

Variability of throughfall quantity in a mixed evergreen-deciduous broadleaved forest in central China

Lei Su^{1,2}, Zongqiang Xie^{1*}, Wenting Xu¹, Changming Zhao¹

¹ State Key Laboratory of Vegetation and Environmental Change, Institute of Botany, Chinese Academy of Sciences, Beijing 100093, China.

² International Joint Research Laboratory for Global Change Ecology, School of Life Sciences, Henan University, Kaifeng, Henan 475004, China.

* Corresponding author. E-mail: xie@ibcas.ac.cn

Abstract: Mixed evergreen-deciduous broadleaved forest is the transitional type of evergreen broadleaved forest and deciduous broadleaved forest, and plays a unique eco-hydrologic role in terrestrial ecosystem. We investigated the spatio-temporal patterns of throughfall volume of the forest type in Shennongjia, central China. The results indicated that throughfall represented 84.8% of gross rainfall in the forest. The mean CV (coefficient of variation) of throughfall was 27.27%. Inter-event variability in stand-scale throughfall generation can be substantially altered due to changes in rainfall characteristics, throughfall CV decreased with increasing rainfall amount and intensity, and reached a quasi-constant level when rainfall amount reached 25 mm or rainfall intensity reached 2 mm h⁻¹. During the leafed period, the spatial pattern of throughfall was highly temporal stable, which may result in spatial heterogeneity of soil moisture.

Keywords: Throughfall; Spatial variability; Temporal stability; Mixed evergreen-deciduous broadleaved forest; Shennongjia.

INTRODUCTION

Understory rainfall is composed of throughfall and stemflow, throughfall is the proportion of rainwater penetrating through canopy gaps (free throughfall) or dripping to the ground from the canopy (canopy drip), stemflow is the proportion that reaches the ground by funneling down the stems or trunks. In contrast to the former, stemflow is generally a smaller proportion, typically ranges between 0% and 10% of gross rainfall; it is a concentrated point source of water that reaches tree base (Van Stan and Gordon, 2018). Relatively speaking, the quantification of throughfall is substantial and therefore is an indispensable component in the watershed water budget (Dohnal et al., 2014; Nanko et al., 2016). At the stand scale, throughfall represents the largest volumetric component of gross precipitation, and usually constitutes more than 70% of incident rainfall (Loustau et al., 1992; Shi et al., 2010). Throughfall is directly related to the leaching and flushing processes of adsorbate of branches and leaves, and so it is considered as a critical transfer mechanism in biogeochemical cycles of forest ecosystems. Soil nutrient availability is influenced by the magnitude and chemical composition of throughfall (Rosier et al., 2015), areas where have more throughfall tend to have higher root density (Ford and Deans, 1978). As a consequence, throughfall is key input parameter in a diverse range of applications such as moisture recharging and nutrient exchange (Guswa and Spence, 2012). Because of the intermediate functions in hydrologic processes, throughfall has the potential to determine vegetation productivity through influencing available water and nutrients availability (Carlyle-Moses et al., 2014; Carnol and Bazgir, 2013). Improved knowledge of the spatial-temporal patterns of throughfall is, therefore, of crucial importance for eco-hydrological problems.

Interception loss constitutes a large proportion of regional evapotranspiration, direct *in situ* measurement of this rainfall fraction is challenging, therefore it is typically indirectly estimated by the difference between gross rainfall and the sum of

throughfall and stemflow (Carlyle-Moses and Gash, 2011; Friesen et al., 2015). The estimation accuracy of interception loss in forest ecosystems, in most instances, is largely dependent on the measurement accuracy of gross rainfall and throughfall. Because of the unnegligible quantitative significance in the estimation of interception loss, any imprecision in observing throughfall would magnify the estimation error of interception loss, and thus in-depth knowledge on distribution patterns of throughfall becomes a precondition for studies on interception loss.

Canopy characteristics (phenoseason, canopy cover, stand density, leaf area index, crown length) (Park and Cameron, 2008; Siles et al., 2010; Zabret and Šraj, 2018), meteorological conditions (temperature, wind and vapour pressure deficit) (David et al., 2006; Dunkerley, 2000) and precipitation characteristics (rainfall amount, intensity and duration) (Levia and Frost, 2006; Zabret et al., 2018) usually exhibit considerable heterogeneity, which may increase the difficulty of understanding the throughfall distribution patterns in forest ecosystems. Of all the biotic and abiotic factors, canopy structure and architecture are deemed as the most important controls on throughfall heterogeneity. Certain leaf morphology and higher canopy epiphytic load, which can intercept and absorb substantial rainwater, results in higher throughfall variability (Park and Cameron, 2008; Van Stan and Pypker, 2015).

The arrangement of throughfall collectors is a strong influencing factor of throughfall heterogeneity. Loescher et al., (2002) didn't find any significant correlations between throughfall volumes and the distance to the nearest branch and leaf above the collector within a tropical rainforest in Costa Rica, but observed a weak relation between throughfall volumes and canopy cover. Herwatz (1987) and Sato et al. (2011) observed that collectors close to trunks were inclined to receive more throughfall in Australian tropical rainforest and Brazilian eucalyptus plantation, whereas Robson et al. (1994) reported an opposite tendency within a beech forest in southern England.

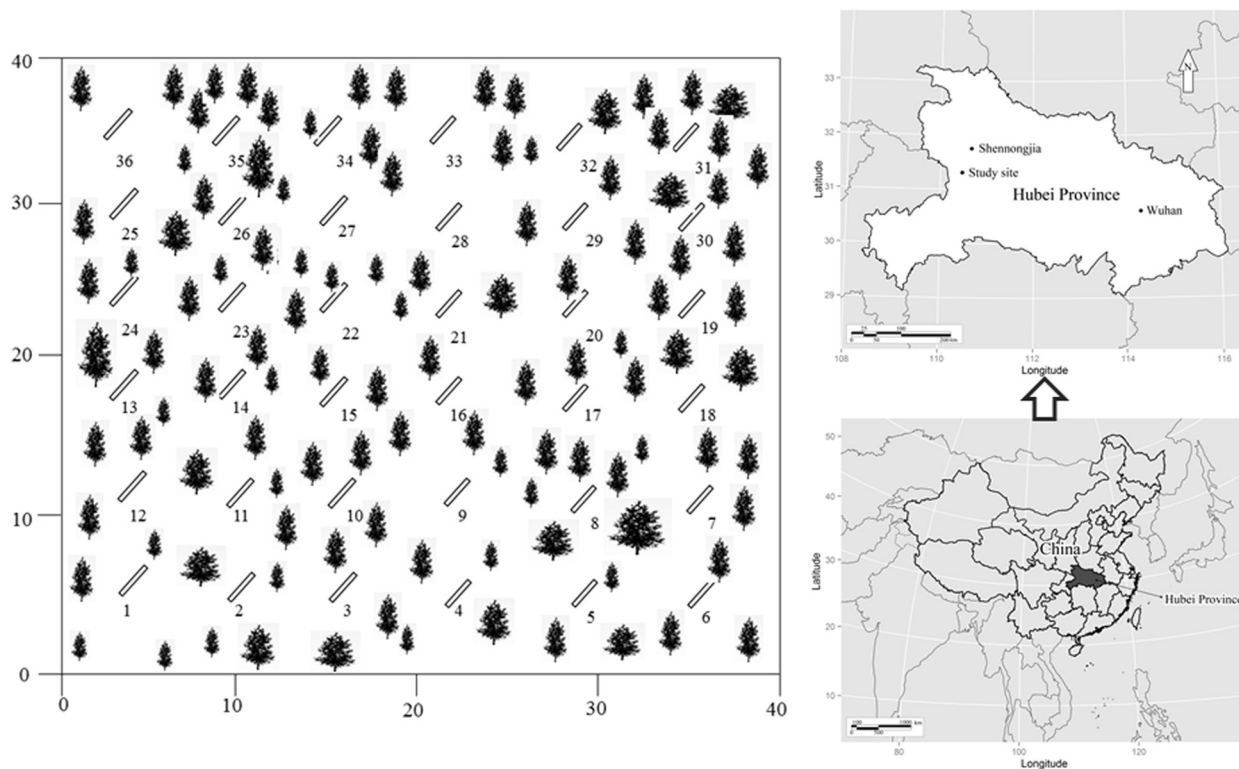


Fig. 1. Maps showing the location of the study area and throughfall collectors.

The mixed evergreen-deciduous broadleaved forest, a widely distributed forest type in the subtropical zone of China, is a complexity of evergreen broadleaved trees and deciduous broadleaved trees (Su et al., 2016a; 2016b). The stand structure is complex, the canopy composition is distinctive. Given its high biodiversity and small geographical range of the forest, the forest is among the most vulnerable ecosystems to climate change (Ge and Xie, 2017). Therefore, a better understanding of its rainfall distribution pattern is urgently required to predict the hydrological processes of the forest under climate change scenarios. Although stemflow and interception loss of the particular forest type have been described (Su et al., 2016a; 2016b), the throughfall patterns of the forest are not well known.

In the present paper, we investigate the spatio-temporal pattern of throughfall during leafed period in a mixed evergreen-deciduous broadleaved forest. The objectives of the study are (1) to identify the magnitude of throughfall in the forest; (2) to investigate the driving factors of variation of throughfall; and (3) to estimate the spatial and temporal pattern of throughfall.

MATERIALS AND METHODS

Study area

Shennongjia is located at Qinba Mountain, belonging to the “Daba Mountain evergreen forests” subcategory, which falls under the category of “Southwest China Temperate Forests” in the Global 200 categorization of world ecoregions (WWF, 2001). Based on its unique ecological system and intact preservation condition, Shennongjia can be seen as a typical representative of Daba Mountain evergreen forests, where the zonal vegetation is mixed evergreen-deciduous broadleaved forests. Shennongjia has preserved the most intact mixed evergreen-deciduous broadleaved forests in China and even in the Northern Hemisphere, and therefore offers a typical example of the biological and ecological processes of the forests (Su et al., 2016a; 2016b). These forests are the transitional zone between

warm temperate deciduous broadleaved forests and subtropical evergreen broadleaved forests (Zhao et al., 2005).

Measurements of incident gross precipitation and throughfall were carried out during the leafed period of 2014 (May 1 to October 31) at the Shennongjia Biodiversity Research Station of Chinese Academy of Sciences, which is located in northwest Hubei at 110°28'27"E, 31°18'23"N. The study site, located at the elevation of 1650 m, is classified as typical subtropical monsoon climate. Mean monthly temperature varies from 1.2°C in January to 22.0°C in July, and mean annual air temperature (MAT) is 10.6°C, and mean annual precipitation in the area between 2001 and 2010 is 1350 mm (Su et al., 2016b). According to the FAO classification, the soils at the site belong to Haplic Alisols.

The mixed evergreen-deciduous broadleaved forest, an extensively distributed forest type in Shennongjia, is the transitional type of evergreen broadleaved forest and deciduous broadleaved forest, which represents the typical forest types of the northern subtropical region of China. The study was completed in a flat 40 m × 40 m plot whose characteristics are described in detail by Su et al. (2016a). The density of trees was 2407 ha⁻¹, the total basal area was 42.56 m² ha⁻¹. The mean height and diameter at breast height were 8.0±2.2 m and 10.7±3.0 cm, respectively. The dominant evergreen species included *Cyclobalanopsis multinervis*, *Cyclobalanopsis oxyodon*, *Rhododendron hypoglaucum*, *Ilex pernyi*, *Lindera fragrans*, the dominant deciduous species included *Fagus engleriana*, *Quercus serrata* var. *brevipetiolata*, *Clethra cavaleriei*, *Sorbus folgeri*, *Betula insignis*, *Dendrobenthamia japonica* var. *chinensis*, and so on (Su et al., 2016b). Exact information of main tree species is provided in Table 1.

Experimental design

Compared with funnel-type collectors, trough-type collectors could considerably decrease the required sample sizes and

Table 1. Exact information of the main tree species in the study plot.

Species	Functional group	Density (tree/ha)	Relative abundance (%)	Relative frequency (%)	Basal area (m ² /ha)	Relative dominance (%)	Importance value (%)
<i>Quercus serrata</i> var. <i>brevipetiolata</i>	Deciduous	256	10.64	5.48	13.24	31.11	15.74
<i>Fagus engleriana</i>	Deciduous	419	17.41	9.63	5.65	13.28	13.44
<i>Betula insignis</i>	Deciduous	81	3.37	2.95	5.84	13.72	6.68
<i>Sorbus pohuashanensis</i>	Deciduous	269	11.18	1.26	2.44	5.73	6.06
<i>Dendrobenthamia japonica</i> var. <i>chinensis</i>	Deciduous	156	6.48	3.62	3.25	7.64	5.91
<i>Clethra cavaleriei</i>	Deciduous	50	2.08	1.18	1.92	4.51	2.59
<i>Euptelea pleiospermum</i>	Deciduous	56	2.33	1.16	0.54	1.27	1.59
<i>Lindera obtusiloba</i>	Deciduous	44	1.83	2.05	0.75	1.76	1.88
<i>Swida ulotricha</i>	Deciduous	25	1.04	1.62	0.10	0.23	0.96
<i>Cyclobalanopsis multinervis</i>	Evergreen	269	11.18	16.75	2.94	6.91	10.61
<i>Cyclobalanopsis oxyodon</i>	Evergreen	225	9.35	10.63	1.99	4.68	8.22
<i>Rhododendron hypoglaucom</i>	Evergreen	213	8.85	5.69	1.44	3.38	5.97
<i>Ilex pernyi</i>	Evergreen	138	5.73	2.56	0.32	0.75	3.02
<i>Lithocarpus henryi</i>	Evergreen	44	1.83	1.42	1.93	4.53	2.59
<i>Lindera fragrans</i>	Evergreen	131	5.44	1.46	0.11	0.26	1.97
<i>Quercus spinosa</i>	Evergreen	31	1.29	1.18	0.10	0.23	0.90

eliminate the sensitivity of the mean to outliers (Carlyle-Moses et al., 2014; Kostelnik et al., 1989; Zimmermann et al., 2010), so trough-type collectors were employed to measure gross precipitation and throughfall in the present study. Gross incident precipitation was collected in an open area, about 50 m away from the study site, using three trough-type collectors (the collectors were made of stainless steel with an opening area of 1 m × 0.2 m), where the collected rainwater would flow into a plastic pot through a small opening at the bottom of collectors. An automatic weather station (Model MAWS301, HydroMet™ system, Vaisala Corp., Finland) was situated approximately 500 m away from the study site, which could provide estimates of the duration and intensity of gross rainfall. The diameter of the rain gauge was 20 cm, and the sensitivity of sensor was 0.1 mm. The rainfall data were automatically collected and recorded at 30-min intervals.

Throughfall was measured with 36 collectors in accordance with the type of gross rainfall. These throughfall collectors were evenly distributed over the 40 m × 40 m study plot in fixed positions (Figure 1), and they were cleaned at a frequency of every three days. All samples were immediately quantified after the cessation of a rain event or the next morning for events that occurred or extended into nighttime hours. To qualify as an incident rainfall event, an interval of at least 8 h without rain must be separated from adjacent rainfall events (Su et al., 2016b). In this study, storms less than 1.5 mm were unable to generate measurable throughfall, and therefore storms larger than 1.5 mm were used to analyze throughfall. Although the automatic weather station (installed with a tipping bucket) was not very far from the study plot, the rainfall amount may vary between these two sites in some rainfall events because the mountainous climate may differ in very close distance apart. The automatic weather station monitored almost the same value with trough collectors in most cases, but the former was more accurate in measuring small rainfall events.

To determine leaf area index (LAI) and canopy cover, LAI-2000 was taken above each of the 36 collectors under cloudy

sky in the middle of the month from May to October in 2014.

We evaluated the temporal persistence of spatial patterns of throughfall using the methodology of Keim et al. (2005). Throughfall was quantified using standardized throughfall for each of the sample points using the formula as follows:

$$TFS_i = \frac{TF_i - TF_{mean}}{SD} \quad (1)$$

where TFS_i is normalized throughfall at sampling point i , TF_i is measured throughfall at sampling point i , TF_{mean} is the mean throughfall for the rainfall event over all sampling points, and SD is the standard deviation of throughfall for the rainfall event over all sampling points (Carlyle-Moses et al., 2014).

RESULTS

LAI and canopy cover

The variability of LAI was very small during the leafed period, LAI and canopy cover were biggest in August, and smallest in May, the mean LAI and canopy cover of August is 1.07 and 1.05 times of May, respectively. The shooting period of most of trees was April, the trees already had relative mature leaves and canopy in May and kept relatively stable during the leafed period.

Gross rainfall

During the leafed period from early May to the end of October 2014, a total of 48 events amounting to a cumulative depth of 1574.0 mm were recorded and snowfall was not detected. Mean incident rainfall event was 32.8 mm and varied from 0.1 mm to 207.7 mm, mean rainfall intensity was 2.68 mm h⁻¹ and ranged from 0.25 mm h⁻¹ to 6.94 mm h⁻¹. Of the 48 rainfall events, 8 events (with a total of 3.2 mm) were too small to produce measurable throughfall, 40 events produced a total of 1335.1 mm throughfall, accounting for 84.8% of gross rainfall.

Variability of throughfall

Throughfall rate against gross rainfall was showed in Figure 2 by means of box and whisker plots. 40 plots represented 40 rainfall events generating throughfall, and these events was ranked by rainfall amount. Throughfall rate increased with increasing gross rainfall amount, and gradually stabilize at larger rainfall events. Throughfall rate values greater than 100% were commonly monitored in larger rainfall events.

The coefficients of variation (CV) of throughfall were found to be highly variable during the leafed period, averaged 27.27%, and varied from 6.82% to 72.72% for all rainfall events (Figure 3). Throughfall CV displayed a large variability for rainfall events <25 mm, and the throughfall CV became quasi-constant after reaching a gross rainfall input of 25 mm.

There was a significant power function relationship between throughfall CV which was derived from all 36 collectors and rainfall intensity ($R^2 = 0.51, P < 0.01$) (Figure 4). With increasing rainfall intensity, throughfall CV showed a trend of rapid-decreases and was relatively stable. It appeared that for rainfall intensity $> 2 \text{ mm h}^{-1}$ in magnitude, there was little variation in throughfall CV.

Temporal stability of spatial throughfall

The normalized throughfall values were ranked by mean values in Figure 5 and the spatial distribution of throughfall was stable during the study period. Some collectors (e.g. 22, 33, 36, 27) gathered more throughfall than the mean normalized throughfall, which would result in relative wet points on the forest floor. At the same time, there were also some collectors (e.g. 31, 35, 8, 13) receiving less throughfall than the mean normalized throughfall, which would create dry points on the ground surface.

DISCUSSION

Characteristics of throughfall

The mean throughfall CV of the forest (27.27%) was close to reported values in subtropical forests. Shen et al. (2012) reported that throughfall CV of secondary succession of evergreen broadleaved forest ranged from 25% to 39%. However,

the present value was higher than the findings in broadleaved forests, which were 18% for a deciduous broadleaved forest during leafed period (Staelens et al., 2006), 17% for a broadleaved secondary forest (Deguchi et al., 2006), and 15.9%–20.1% in a deciduous forest (Siegert et al., 2016). The higher throughfall CV in our study may be attributed to the dense canopy structure, which could provide more sheltered areas and drip points. Furthermore, the type and amount of throughfall collectors, rainfall and forest characteristics, sampling time scales of the aforementioned studies differed significantly with our study, making it difficult to directly compare the spatial variation of throughfall.

As indicated in the results, relationships between storm characteristics and both throughfall amount and variability are consistent with previous work (Carlyle-Moses et al., 2004; Loustau et al., 1992; Shinohara et al., 2010). Most of the rainwater in small rainfall events is portioned as canopy storage, and almost all throughfall is in the form of free throughfall, which originates from gross rainfall that passes directly through canopy gaps to the forest floor (Zimmermann et al., 2009). Throughfall variability responds dramatically to stand variables, larger canopy interaction usually result in greater spatial throughfall variability. After rainfall saturated canopy water storage capacity, throughfall variability remains quasi-constant with increasing rainfall. A possible explanation for this phenomenon is that the canopy has established quasi-permanent canopy drip zones where throughfall is concentrated, and canopy shelter zones where intercepted rainwater is either formed as interception loss or funneled to other part of the canopy or to the trunk and stem. For gross rainfall input exceeding the threshold required for the complete establishment of drip and shelter points, the spatial distribution of throughfall will be governed by these critical points, therefore the throughfall distribution patterns reach a steady state (Carlyle-Moses et al., 2014).

Spatial distribution pattern of throughfall

Previous throughfall studies have showed that throughfall patterns displayed a high temporal stability (Fan et al., 2015; Keim et al., 2005; Sato et al., 2011; Wullaert et al., 2009), this phenomenon was verified in our study (Figure 5), the range and variability of throughfall matched previous work. As docu-

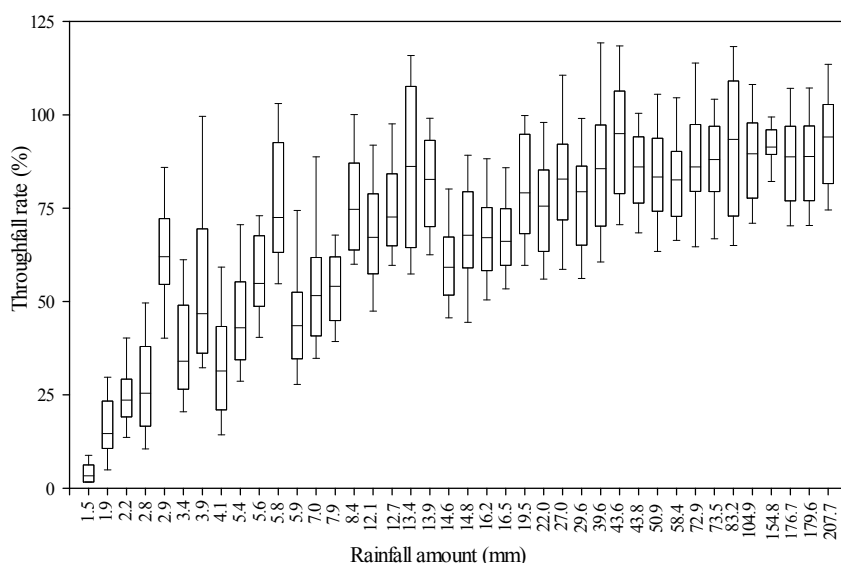


Fig. 2. Box and whisker plots of throughfall rate against rainfall amount. The center line, bottom and top of the boxes represent the median, 25th and 75th percentiles, respectively. The whiskers represent the 5th and 95th percentiles.

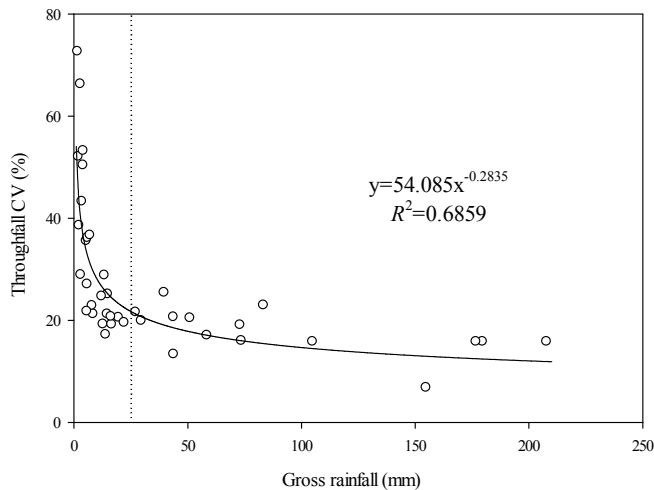


Fig. 3. Coefficient of variation of throughfall against gross rainfall.

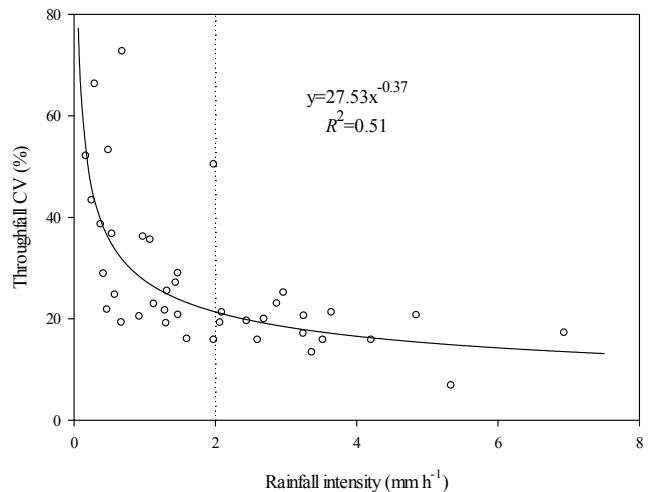


Fig. 4. The coefficient of variation of throughfall as a function of rainfall intensity.

mented in Figure 5, some collectors gathered significant more throughfall volumes than the mean, sometimes exceeded the gross rainfall. This could be explained by the fact that these collectors were located at the edge of canopy (Figure 1), the branches above the collectors were mostly down-facing, which seemed to play the role of funnelling and thus had convergence effects on throughfall volumes, consequently throughfall was concentrated at the canopy edge (Gerits et al., 2010; Fang et al., 2016; Fathizadeh et al., 2014; Staelens et al., 2006). However, inconsistent views on the relationship between the distance to the nearest trunk and throughfall volume have also been reported, Keim et al. (2005) found tree age was also a major determinant in throughfall distribution, wet gauges were close to trunks in a young conifer stand, while they were not obviously related to tree boles in an old conifer stand. The branches of young trees are straight and upward, which would transport rainwater to areas near the trunk like a funnel, whereas the relatively horizontal branches of old trees don't have this function. Besides tree age, rainfall amount may also lead to inconformity, André et al. (2011) observed that throughfall volumes would be greater at the crown periphery than adjacent to the trunks at the

early stages of rainfall events (c.a. <5 mm) and presented an opposite trend in large rainfall events. Free throughfall takes the majority of throughfall in small rainfall events, therefore areas under crown periphery could receive more water compared with those near the trunk. The funneling effect gradually increase with increasing rainfall amount, more throughfall would be gathered to trunks as canopy drips.

Spatial distribution of throughfall is greatly influenced by the spatial heterogeneity of canopy parameters. At the same time, we should not neglect the effect of meteorological parameters. Figure 3 and 4 showed that rainfall amount and intensity played crucial roles in modifying the spatial distribution of throughfall that reaches the forest floor. With the increase in rainfall amount and intensity, throughfall CV decreased by means of a negative power function, which is in agreement with the findings of Fan et al. (2015) in an exotic pine plantation of subtropical coastal Australia. Kato et al. (2013) found that throughfall increased with increasing distance to the nearest trunk in windless rainfall events, however, such a systematic throughfall pattern was not presented during windy conditions.

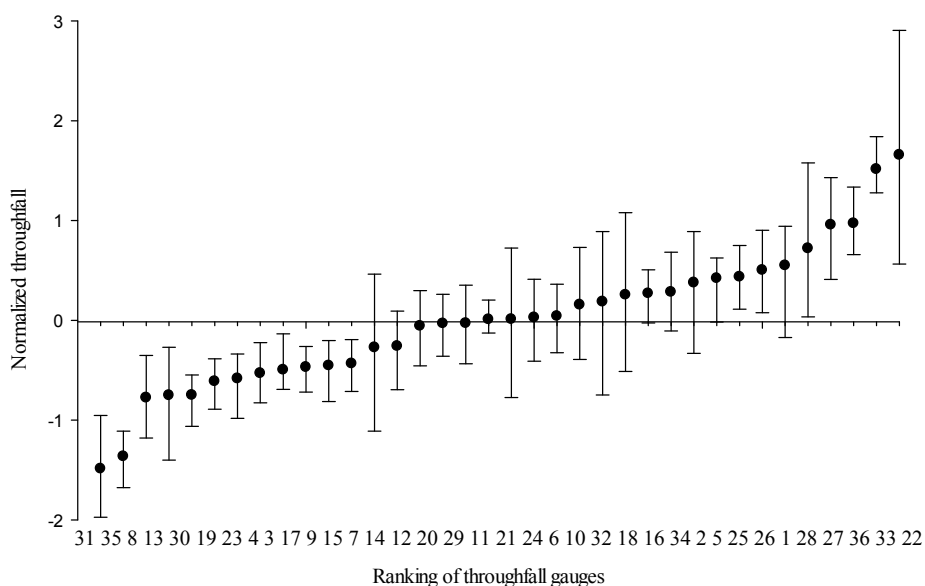


Fig. 5. Time stability plot of normalized throughfall. The upper and lower error whiskers represent the 75th and 25th percentiles, respectively.

The location of collectors is a main determinant to obtaining a representative throughfall, previous studies have indicated that random relocation of collectors after each sampling could reduce the necessary collectors and not at the expense of misestimating throughfall (Carlyle-Moses et al., 2014; Holwerda et al., 2006; Kimmins, 1973; Ritter and Regalado, 2010). He et al. (2014) suggested that the locations of collectors should be placed at the sites of mean values of plant area index (PAI, the sum of all light-blocking elements of vegetation) due to position relationship between interception loss and PAI. As a consequence, if we want to reduce the sampling points as much as possible, we must identify locations where we have mean values of these canopy parameters before we arrange the sample. Because of the canopy may form stable “canopy drip zones” and “canopy shelter zones”, the measured throughfall would be greatly influenced by extreme values if the capture area of gauges is very small (Zimmermann et al., 2010), therefore, we have to increase the capture area of gauges to reduce the impact of outliers.

CONCLUSION

In a diverse, structurally complex forest with heterogeneous throughfall patterns, the inter-event variability in stand-scale throughfall generation was greatly driven by rainfall size and intensity. The throughfall CV decreased significantly with increasing rainfall amount and intensity, and after rainfall amount reached 25 mm or rainfall intensity reached 2 mm h⁻¹, when the canopy had formed stable regions of “canopy drip zones” and “canopy shelter zones”, throughfall CV presented a stable trend. The spatial pattern of throughfall was highly temporal stable during the study period, which may lead to “wet zones” and “dry zones” in the forested land.

Acknowledgements. The study was completed with support from the Project of Chinese Academy of Sciences (No. QYZDY-SSW-SMC011), the Science and Technology Service Network Initiative of CAS (No. KFJ-SW-STS-167) and the National Natural Science Foundation of China (No. 41807158). The authors acknowledge the assistance provided by Kaiming Zhao, Hualan Qiu, Xianping Jia and Yongxiang Fu. We greatly appreciate the two anonymous reviewers for their constructive comments to improve this manuscript.

REFERENCES

- André, F., Jonard, M., Jonard, F., Ponette, Q., 2011. Spatial and temporal patterns of throughfall volume in a deciduous mixed-species stand. *Journal of Hydrology*, 400, 244–254.
- Carlyle-Moses, D.E., Laureano, J.S.F., Price, A.G., 2004. Throughfall and throughfall spatial variability in Madrean oak forest communities of northeastern Mexico. *Journal of Hydrology*, 297, 124–135.
- Carlyle-Moses, D.E., Gash, J.H.C., 2011. Rainfall Interception Loss by Forest Canopies. In: Levia, D.F., Carlyle-Moses, D., Tanaka, T. (Eds.): *Forest Hydrology and Biogeochemistry*. Springer Netherlands, Heidelberg, pp. 407–423.
- Carlyle-Moses, D.E., Lishman, C.E., McKee, A.J., 2014. A preliminary evaluation of throughfall sampling techniques in a mature coniferous forest. *Journal of Forestry Research*, 25, 407–413.
- Carnol, M., Bazgir, M., 2013. Nutrient return to the forest floor through litter and throughfall under 7 forest species after conversion from Norway spruce. *Forest Ecology and Management*, 309, 66–75.
- David, T.S., Gash, J.H.C., Valente, F., Pereira, J.S., Ferreira, M.I., David, J.S., 2006. Rainfall interception by an isolated evergreen oak tree in a Mediterranean savannah. *Hydrological Processes*, 20, 2713–2726.
- Deguchi, A., Hattori, S., Park, H.T., 2006. The influence of seasonal changes in canopy structure on interception loss: Application of the revised Gash model. *Journal of Hydrology*, 318, 80–102.
- Dohnal, M., Černý, T., Votrubová, J., Tesař, M., 2014. Rainfall interception and spatial variability of throughfall in spruce stand. *Journal of Hydrology and Hydromechanics*, 62, 277–284.
- Dunkerley, D., 2000. Measuring interception loss and canopy storage in dryland vegetation: a brief review and evaluation of available research strategies. *Hydrological Processes*, 14, 669–678.
- Fan, J., Oestergaard, K.T., Guyot, A., Jensen, D.G., Lockington, D.A., 2015. Spatial variability of throughfall and stemflow in an exotic pine plantation of subtropical coastal Australia. *Hydrological Processes*, 29, 793–804.
- Fang, S., Zhao, C., Jian, S., 2016. Spatial variability of throughfall in a *Pinus tabulaeformis* plantation forest in Loess Plateau, China. *Scandinavian Journal of Forest Research*, 31, 467–476.
- Fathizadeh, O., Attarod, P., Keim, R.F., Stein, A., Amiri, G.Z., Darvishsefat, A.A., 2014. Spatial heterogeneity and temporal stability of throughfall under individual *Quercus brantii* trees. *Hydrological Processes*, 28, 1124–1136.
- Ford, E.D., Deans, J.D., 1978. The effects of canopy structure on stemflow, throughfall and interception loss in a young *Sitka spruce* plantation. *Journal of Applied Ecology*, 15, 905–917.
- Friesen, J., Lundquist, J., Van Stan, J.T., 2015. Evolution of forest precipitation water storage measurement methods. *Hydrological Processes*, 29, 2504–2520.
- Ge, J., Xie, Z., 2017. Geographical and climatic gradients of evergreen versus deciduous broad-leaved tree species in subtropical China: Implications for the definition of the mixed forest. *Ecology and Evolution*, 7, 3636–3644.
- Gerrits, A.M.J., Pfister, L., Savenije, H.H.G., 2010. Spatial and temporal variability of canopy and forest floor interception in a beech forest. *Hydrological Processes*, 24, 3011–3025.
- Guswa, A.J., Spence, C.M., 2012. Effect of throughfall variability on recharge: application to hemlock and deciduous forests in western Massachusetts. *Ecohydrology*, 5, 563–574.
- He, Z.B., Yang, J.J., Du, J., Zhao, W.Z., Liu, H., Chang, X.X., 2014. Spatial variability of canopy interception in a spruce forest of the semiarid mountain regions of China. *Agricultural and Forest Meteorology*, 188, 58–63.
- Herwitz, S.R., 1987. Raindrop impact and water flow on the vegetative surfaces of trees and the effects on stemflow and throughfall generation. *Earth Surface Processes and Landforms*, 12, 425–432.
- Holwerda, F., Scatena, F.N., Bruijnzeel, L.A., 2006. Throughfall in a Puerto Rican lower montane rain forest: A comparison of sampling strategies. *Journal of Hydrology*, 327, 592–602.
- Kato, H., Onda, Y., Nanko, K., Gomi, T., Yamanaka, T., Kawaguchi, S., 2013. Effect of canopy interception on spatial variability and isotopic composition of throughfall in Japanese cypress plantations. *Journal of Hydrology*, 504, 1–11.
- Keim, R.F., Skaugset, A.E., Weiler, M., 2005. Temporal persistence of spatial patterns in throughfall. *Journal of Hydrology*, 314, 263–274.

- Kimmins, J.P., 1973. Some statistical aspects of sampling throughfall precipitation in nutrient cycling studies in British Columbian coastal forests. *Ecology*, 54, 1008–1019.
- Kostelnik, K.M., Lynch, J.A., Grimm, J.W., Corbett, E.S., 1989. Sample size requirements for estimation of throughfall chemistry beneath a mixed hardwood forest. *Journal of Environmental Quality*, 18, 274–280.
- Levia, D.F., Frost, E.E., 2006. Variability of throughfall volume and solute inputs in wooded ecosystems. *Progress in Physical Geography*, 30, 605–632.
- Loescher, H.W., Powers, J.S., Oberbauer, S.F., 2002. Spatial variation of throughfall volume in an old-growth tropical wet forest, Costa Rica. *Journal of Tropical Ecology*, 18, 397–407.
- Loustau, D., Berbigier, P., Granier, A., Moussa, F.E.H., 1992. Interception loss, throughfall and stemflow in a maritime pine stand. I. Variability of throughfall and stemflow beneath the pine canopy. *Journal of Hydrology*, 138, 449–467.
- Nanko, K., Hudson, S.A., Levia, D.F., 2016. Differences in throughfall drop size distributions in the presence and absence of foliage. *Hydrological Science Journal*, 61, 620–627.
- Park, A., Cameron, J.L., 2008. The influence of canopy traits on throughfall and stemflow in five tropical trees growing in a Panamanian plantation. *Forest Ecology and Management*, 255, 1915–1925.
- Ritter, A., Regalado, C.M., 2010. Investigating the random relocation of gauges below the canopy by means of numerical experiments. *Agricultural and Forest Meteorology*, 150, 1102–1114.
- Robson, A.J., Neal, C., Ryland, G.P., Harrow, M., 1994. Spatial variations in throughfall chemistry at the small plot scale. *Journal of Hydrology*, 158, 107–122.
- Rosier, C.L., Van Stan, J.T., Moore, L.D., Schrom, J.O.S., Wu, T., Reichard, J.S., Kan, J., 2015. Forest canopy structural controls over throughfall affect soil microbial community structure in an epiphyte-laden maritime oak stand. *Ecohydrology*, 8, 1459–1470.
- Sato, A.M., Avelar, A.D., Netto, A.L.C., 2011. Spatial variability and temporal stability of throughfall in a eucalyptus plantation in the hilly lowlands of southeastern Brazil. *Hydrological Processes*, 25, 1910–1923.
- Shen, H., Wang, X., Jiang, Y., You, W., 2012. Spatial variations of throughfall through secondary succession of evergreen broad-leaved forests in eastern China. *Hydrological Processes*, 26, 1739–1747.
- Shi, Z., Wang, Y., Xu, L., Xiong, W., Yu, P., Gao, J., Zhang, L., 2010. Fraction of incident rainfall within the canopy of a pure stand of *Pinus armandii* with revised Gash model in the Liupan Mountains of China. *Journal of Hydrology*, 385, 44–50.
- Shinohara, Y., Onozawa, Y., Chiwa, M., Kume, T., Komatsu, H., Otsuki, K., 2010. Spatial variations in throughfall in a Moso bamboo forest: sampling design for the estimates of stand-scale throughfall. *Hydrological Processes*, 24, 253–259.
- Siegert, C.M., Levia, D.F., Hudson, S.A., Downton, A.L., Zhang, F., Mitchell, M.J., 2016. Small-scale topographic variability influences tree species distribution and canopy throughfall partitioning in a temperate deciduous forest. *Forest Ecology and Management*, 359, 109–117.
- Siles, P., Vaast, P., Dreyer, E., Harmand, J.M., 2010. Rainfall partitioning into throughfall, stemflow and interception loss in a coffee (*Coffea arabica* L.) monoculture compared to an agroforestry system with *Inga densiflora*. *Journal of Hydrology*, 395, 39–48.
- Staelens, J., De Schrijver, A., Verheyen, K., Verhoest, N.E.C., 2006. Spatial variability and temporal stability of throughfall water under a dominant beech (*Fagus sylvatica* L.) tree in relationship to canopy cover. *Journal of Hydrology*, 330, 651–662.
- Su, L., Xu, W., Zhao, C., Xie, Z., Ju, H., 2016a. Inter- and intra-specific variation in stemflow for evergreen species and deciduous tree species in a subtropical forest. *Journal of Hydrology*, 537, 1–9.
- Su, L., Zhao, C., Xu, W., Xie, Z.Q., 2016b. Modelling interception loss using the revised Gash model: a case study in a mixed evergreen-deciduous broadleaved forest in China. *Ecohydrology*, 9, 1580–1589.
- Van Stan, J.T., Gordon, D.A., 2018. Mini-review: Stemflow as a resource limitation to near-stem soils. *Frontier in Plant Science*, 9, 248.
- Van Stan, J.T., Pypker, T.G., 2015. A review and evaluation of forest canopy epiphyte roles in the partitioning and chemical alteration of precipitation. *Science of the Total Environment*, 536, 813–824.
- World Wide Fund for Nature (WWF), 2001. The Global 200-Blueprint for a Living Planet. On the WWF website at www.panda.org/livingplanet/global200_new.cfm.
- Wullaert, H., Pohlert, T., Boy, J., Manosalvas, C.V., Wilcke, W., 2009. Spatial throughfall heterogeneity in a montane rain forest in Ecuador: Extent, temporal stability and drivers. *Journal of Hydrology*, 377, 71–79.
- Zabret, K., Šraj, M., 2018. Spatial variability of throughfall under single birch and pine tree canopies. *Acta Hydrotechnica*, 31, 1–20.
- Zabret, K., Rakovec, J., Šraj, M., 2018. Influence of meteorological variables on rainfall partitioning for deciduous and coniferous tree species in urban area. *Journal of Hydrology*, 558, 29–41.
- Zhao, C.M., Chen, W.L., Tian, Z.Q., Xie, Z.Q., 2005. Altitudinal pattern of plant species diversity in Shennongjia Mountains, Central China. *Journal of Integrative Plant Biology*, 47, 1431–1449.
- Zimmermann, A., Zimmermann, B., Elsenbeer, H., 2009. Rainfall redistribution in a tropical forest: Spatial and temporal patterns. *Water Resources Research*, 45, W11413.
- Zimmermann, B., Zimmermann, A., Lark, R.M., Elsenbeer, H., 2010. Sampling procedures for throughfall monitoring: A simulation study. *Water Resources Research*, 46, W01503.

Received 27 February 2018

Accepted 30 May 2018

Soil hydrophysical properties as affected by solid waste compost amendments: seasonal and short-term effects in an Ultisol

Dewpura A.L. Leelamanie*, Chinthani U. Manawardana

Department of Soil Science, Faculty of Agriculture, University of Ruhuna, Mapalana, Kamburupitiya, 81100, Sri Lanka.

* Corresponding author. Tel.: +94-41-2292200 ext. 220, +94-71-8614380. Fax: +94-41-2292384. E-mails: leelamanie@soil.ruh.ac.lk, leelamanie@yahoo.co.uk

Abstract: Application of compost is known to improve the hydraulic characteristics of soils. The objective of this study was to examine the seasonal and short-term effects of solid waste compost amendments on selected hydrophysical properties of soil during dry and rainy seasons and to explore any negative impacts of municipal solid waste compost (MSWC) amendments on soil hydrophysical environment concerning Agriculture in low-country wet zone, Sri Lanka. Eight (T1–T8) MSWC and two (T9, T10) agricultural-based waste compost (AWC) samples were separately applied in the field in triplicates at 10 and 20 Mg ha⁻¹ rates, with a control (T0). Field measurements (initial infiltration rate, I_i ; steady state infiltration rate, I_{ss} ; unsaturated hydraulic conductivity, k ; sorptivity, S_w) were conducted and samples were collected (0–15 cm depth) for laboratory experiments (water entry value, h_{we} ; potential water repellency: measured with water drop penetration time, WDPT) before starting (Measurement I) and in the middle of (Measurement II) the seasonal rainfall (respectively 5 and 10 weeks after the application of compost). The difference in the soil organic matter (SOM) content was not significant between the dry and rainy periods. All the soils were almost non-repellent (WDPT = <1–5 s). The h_{we} of all the samples were negative. In the Measurement I, the I_i of the T0 was about 40 cm h⁻¹, while most treatments show comparatively lower values. The I_{ss} , S_w , and k of compost amended samples were either statistically similar, or showed significantly lower values compared with T0. It was clear that all the surface hydraulic properties examined in situ (I_i , I_{ss} , S_w) were higher in the Measurement I (before rainfall) than those observed in the Measurement II (after rainfall). Water potential differences in soils might have affected the surface hydrological properties such as S_w . However, water potential differences would not be the reason for weakened I_{ss} and k in the Measurement II. Disruption of aggregates, and other subsequent processes that would take place on the soil surface as well as in the soil matrix, such as particle rearrangements, clogging of pores, might be the reason for the weakened I_{ss} and k in the Measurement II. Considering the overall results of the present study, compost amendments seemed not to improve or accelerate but tend to suppress hydraulic properties of soil. No significant difference was observed between MSWC and AWC considering their effects on soil hydraulic properties. Application of composts can be considered helpful to slower the rapid leaching by decreasing the water movements into and within the soil.

Keywords: Unsaturated hydraulic conductivity; Infiltration; Solid waste compost; Sorptivity; Water repellency.

INTRODUCTION

Recent developments in the developing countries including urbanization and industrialization have led to an accumulation of huge amounts of municipal wastes. It is reported that out of 5.2 million tons of the world daily generation of solid wastes, 3.8 million tons are generated in developing countries (Coin-treau, 2007). As the management of municipal solid waste (MSW) has become a critical problem in the recent years, numerous activities have been conducted in relation to the recycling of MSW in Sri Lanka. High requirements of energy for municipal waste incineration and the limited availability of landfills, as well as many other environmental issues, focused the attention on waste recycling and compost application to agricultural lands. The process of composting MSW reduces the waste volume, destroys malodorous compounds, kills the existing pathogens, and decreases the germination rate of weeds (Jakobsen, 1995). More than 75% of the total MSW generation in Sri Lanka are reported to be compostable wastes, confirming that the composted MSW in Sri Lanka has a high potential to be used as a good-quality soil conditioner (World Health Organization, 1999).

Municipal solid waste compost (MSWC) has been successfully used for agriculture in many countries (Ex: Grau et al., 2017; Leogrande et al., 2016). The MSWC have shown compa-

table physio-chemical characteristics to other composts derived from different agro-industrial by-products (Jodar et al., 2017). Application of MSWC is known to improve soil C storage (Peltre et al., 2017), availability of water and nutrient to the crops grown (Martínez-Blanco et al., 2013 and references therein), microbial biomass carbon, dehydrogenase activity values (Fernandez et al., 2007), and plant growth and fruit production characteristics (Leogrande, et al., 2016). However, regardless of the attempts that have already been made to popularize the application of MSWC to agricultural lands in Sri Lanka, it is still in a subordinate level compared with the application of chemical fertilizers and other agricultural-based waste composts (AWC). Lack of knowledge and limited research on the positive effects of locally available MSWC on soil physico-chemical environment are considered to be the major reasons for such behavior.

Compost amendments are usually known to improve the physical environment of soils including hydrophysical characteristics. Reports are available to show that the amendments of MSWC enhance aggregate stability, permeability coefficient (Angin et al., 2013), hydraulic conductivity (Yazdanpanah et al., 2016), total porosity, water penetration, air circulation, and water retention (Karak et al., 2016 and references therein) of soils. Pieces of evidence are also available on negative impacts of organic amendments such as noticeable increases in water

repellency (Głab et al., 2018) and decreases in hydraulic conductivity (Maule et al., 2000).

The seasonal changes in Sri Lanka is mainly characterized by the dry and rainy conditions, where very high rates of average annual rainfall (~2500 mm) is common in the wet zone. As most Sri Lankan soils show very rapid infiltration rates and high hydraulic conductivities (Panabokke, 1996), further enhancements of those processes might lead to more rapid leaching of nutrients from the root zone. Considering the current demands for information and importance in making use of MSWC, the present study aims to examine the seasonal (dry and rainy) and short-term effects of MSWC and AWC on selected hydrophysical properties of soil and to explore any negative impacts of MSWC amendments on soil hydrophysical environment concerning Agriculture in low-country wet zone, Sri Lanka.

MATERIALS AND METHODS

Compost samples and location

Basic analysis was done using 32 MSWC and 3 commonly available AWC samples collected from the compost production sites scattered throughout the country. After the basic characterization, eight MSWC samples (prepared using aerated windrow composting technique) and two AWC samples (prepared using aerated static pit composting technique) were selected for the study. Selection was done to represent composts with similar production conditions and maturity, and a wide range of pH and electrical conductivity (EC), while avoiding MSWC production sites with slaughter house- and clinical-wastes. Selected basic properties of the samples are given in Table 1. The pH of the compost samples was in a range of 6.5–9.5, the EC was in a range of 1–15 mS cm⁻¹, and the organic matter content was in a range of about 16–28 g 100 g⁻¹.

A field experiment was conducted at the Faculty of Agriculture, University of Ruhuna (6°03'29"N 80°34'13"E), located in the low country wet zone (WL2) agro-ecological region. The soil type is categorized as 'red-yellow podzolic soils' under the local classification and falls under Rhodudults (Soil Survey Staff, 2014). Before starting the field experiment, the soil was tested for basic properties. The soil is non-saline, loamy sand in texture, and showed fairly high bulk density of 1.37 g cm⁻³, nearly 50% porosity, and moderately acidic soil reaction (Table 2). A fairly uniform air temperature of about 28°C and a relative humidity of about 75% are prevailing throughout the year. The mean annual rainfall is approximately 2400–2800 mm (National Atlas of Sri Lanka, 2007).

Sample treatments in field

The field was cleared and raised beds with drainage channels were prepared. Eight MSWC samples (T1–T8) and two AWC samples (T9, T10) were added into the planting beds separately in three replicates at 10 and 20 Mg ha⁻¹ rates as an initial single dose, which is in agreement with the present practice in the region. Plots with no compost treatment were used as the control (T0). Fast growing Bush bean (*Phaseolus vulgaris* L.) with high germination rate were seeded in plots one week after the compost application in the inter-monsoonal dry period in 2016, before starting of the inter-monsoonal cyclonic rainfall or the North-east monsoon rainfall period. Irrigation (pH: 6.7; EC: 1.2 dS m⁻¹) was done when necessary considering the crop requirements (10–15 mm once in 5 d) before the beginning of the seasonal rainfall.

Collection of soil samples

Samples from the field were collected to determine the soil properties of the planting beds at 0–15 cm depth (drilled 0–15 cm samples, composited of 3 points) before starting (5 weeks after compost application; Measurement I) and in the middle of the seasonal rainfall (10 weeks after compost application; Measurement II). During the rainy season (Measurement II), the samples were collected after at least two consecutive dry days. Undisturbed samples were taken for bulk density measurements.

Laboratory experiments

The basic properties of the compost samples (for initial characterization) and the soil samples treated with composts were measured in triplicates using standard laboratory tests. The pH (1:2.5) and the EC (1:5) were measured using a pH meter (sensION 1, HACH Co., USA) and an EC meter (sensION+EC5, HACH Co., USA). The bulk density, particle density and texture were measured with soil core method, pycnometer method, and hydrometer method, respectively. Organic matter contents were measured using the loss on ignition (400°C, 6 h) method (Rowell and Coetzee, 2003).

The water entry value (h_{we}) was determined using the pressure head method following the procedure reported by Wang et al. (2000). A low negative pressure of –10 cm was initially applied to prevent the initial instantaneous wetting of the soils placed on a porous-based Buchner funnel using a tube connected to the funnel base. Then the pressure was gradually in-

Table 1. Selected basic properties (mean ± standard deviation) of municipal solid waste composts (T1–T8) and agricultural waste composts (T9–T10).

Compost sample	pH	EC (mS cm ⁻¹)	Organic matter (g 100 g ⁻¹)	K (mg kg ⁻¹)	P (mg kg ⁻¹)	NH ₄ -N (mg kg ⁻¹)	NO ₃ -N (mg kg ⁻¹)
T1	8.53±0.06	8.40±0.01	15.7±0.8	3270±44	2352±346	171.5±6.4	65.3±18.5
T2	7.6±0.0	4.41±0.03	32.6±6.7	3463±32	2204±130	76.5±10.3	63.0±5.8
T3	8.53±0.06	15.0±0.2	25.5±8.0	1110±10	2650±92	82.3±14.9	188±21
T4	9.47±0.06	13.9±1.4	23.8±9.5	626±6	3533±195	117.2±4.7	234±12
T5	8.5±0.0	15.2±0.4	22.6±11.0	990±26	2218±357	56.1±1.6	235±28
T6	8.20±0.52	7.53±0.07	20.5±5.3	2630±52	2918±115	64.8±4.5	261±8
T7	8.5±0.0	2.69±0.36	27.5±8.2	2293±21	3462±180	64.3±1.8	26.2±9.6
T8	8.13±0.06	1.05±0.01	26.5±11.4	5326±45	1833±176	55.6±16.2	6.35±2.50
T9	7.67±0.06	6.55±0.65	18.7±1.4	1696±35	2610±43	69.0±9.7	46.6±7.5
T10	6.47±0.06	5.78±0.08	29.2±6.0	3606±129	3137±25	67.2±4.9	39.6±3.3

Table 2. Selected physical and chemical properties (mean \pm standard deviation) of the field prior to the compost amendments.

Soil parameter	Value
Bulk density (g cm^{-3})	1.37 \pm 0.05
Particle density (g cm^{-3})	2.55 \pm 0.03
Porosity (%)	48.8 \pm 0.8
Sand (%)	83.3 \pm 0.5
Silt (%)	8.9 \pm 0.7
Clay (%)	7.8 \pm 0.7
Soil texture	Loamy Sand
pH	5.7 \pm 0.2
Electrical conductivity ($\mu\text{s cm}^{-1}$)	58.8 \pm 2.5
SOM ($\text{g } 100 \text{ g}^{-1}$)	2.4 \pm 0.1

creased until the water starts to enter into the soil matrix, which is the point of water entry, and the pressure head at the point was measured as the h_{we} (Liyanaage and Leelamanie, 2016).

Water repellency of samples was determined by using water drop penetration time (WDPT) test (Doerr et al., 2000, and references therein). For the WDPT test, a drop of distilled water (50 \pm 1 μl) was placed on the surface of soil samples (from a height of about 10 mm) using a burette. The time taken for the water drop to complete the penetration into the soil was recorded.

Field experiments

The infiltration rates, unsaturated hydraulic conductivity (k), and sorptivity (S_w) of the soils were determined using Mini disk infiltrometer (Decagon devices, Inc.) in the cultivated field, before starting (5 weeks after compost application; Measurement I) and in the middle of the seasonal rainfall (10 weeks after compost application; Measurement II). In the Measurement II, field was exposed to rainfall for more than 3 weeks, and care was taken to conduct the experiments in the field at least after two consecutive dry days.

The k and S_w were estimated from the cumulative infiltration data obtained in the field at a suction head of 6 cm (for a loamy sand texture). The method proposed by Zhang (1997) was used to determine the k of the soils (Lichner et al., 2007a, b). The method requires measuring cumulative infiltration versus time and fitting the results with the function:

$$I = C_1 t + C_2 \sqrt{t} \quad (1)$$

The parameters C_1 (m s^{-1}) and C_2 ($\text{m s}^{-1/2}$) are respectively related to the k and the soil S_w . The k for the soil is then computed from:

$$k = C_1/A \quad (2)$$

where C_1 is the slope of the curve of the cumulative infiltration versus the square root of time, and A is a value that relates the van Genuchten parameters for a given soil to the suction rate and the radius of the infiltrometer disk. The slope of the curve of the cumulative infiltration versus the square root of time and the hydraulic conductivity were calculated based on the infiltration data gathered with the support of Microsoft Excel spreadsheet published by Decagon (www.decagon.com/macro). The linear approximation of the cumulative infiltration versus the square root of the time relationship (Eq. 3) was used to estimate the slope, which would be the S_w .

$$I = S_w \sqrt{t} \quad (3)$$

Data analysis

Results from laboratory tests and field experiments were statistically analyzed with ANOVA and correlation at 5% level of significance ($P < 0.05$) (Microsoft Excel and SAS package).

RESULTS AND DISCUSSION

Bulk density

The bulk density of the control field (T0) was 1.30 and 1.32 g cm^{-3} in the Measurement I and II, respectively. It was slightly lower in compost amended samples showing values ranging from 1.23–1.28 g cm^{-3} at 10 Mg ha^{-1} application rate and 1.20–1.27 g cm^{-3} at 20 Mg ha^{-1} application rate in Measurement I. It ranged from 1.26–1.30 g cm^{-3} and 1.24–1.28 g cm^{-3} , respectively at 10 and 20 Mg ha^{-1} application rates, in Measurement II, without any significant difference among compost treatments. Therefore, it was clear that the type of the compost did not affect the bulk density. This might be because all the compost samples used in this study were high in maturity levels.

Soil organic matter (SOM) content

The SOM contents of the soils at two application rates for both Measurements I and II are presented in Figure 1. The SOM content of the untreated soil (T0) was about 1.7 $\text{g } 100 \text{ g}^{-1}$. Results showed that the SOM levels increased with composts

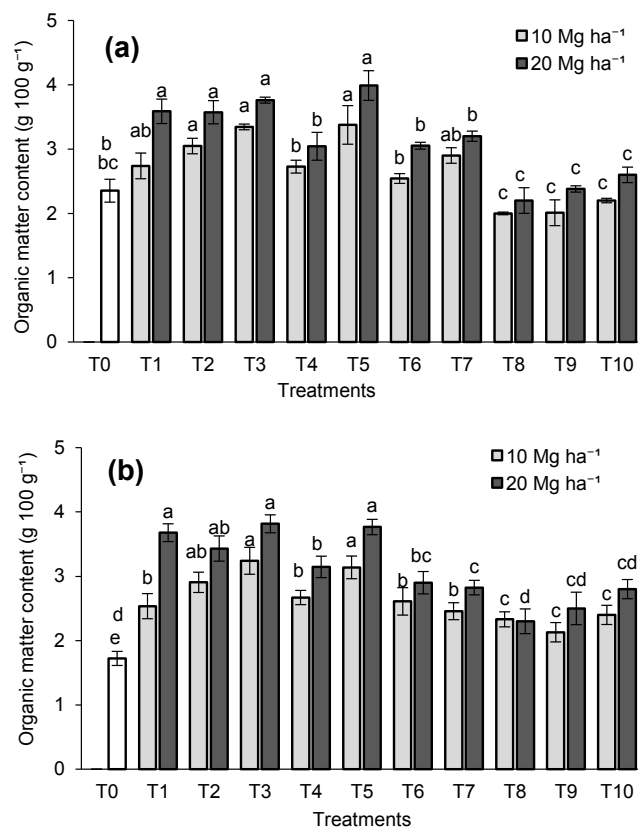


Fig. 1. Organic matter contents of the soils in (a) Measurement I and (b) Measurement II. Error bars indicate \pm standard deviation. Different lower case letters indicate significant differences between treatments, where upper and lower letters on T0 are respectively related to the 10 and 20 Mg ha^{-1} application rates ($P \leq 0.05$).

treatments showing higher SOM level at high rate of application (20 Mg ha^{-1}) than the low rate (10 Mg ha^{-1}) as expected, where the SOM content was in a range of $2\text{--}4 \text{ g } 100 \text{ g}^{-1}$. Furthermore, the difference in SOM content was not significant between the Measurements I and II. Initial rapid depletion rates of SOM after amendments due to prevailing high temperature ($\sim 28^\circ\text{C}$) and humidity ($\sim 80\%$) in the area may cause SOM to reach almost steady level at the time of Measurement I (Leelamanie, 2014). This might be the reason for showing no significant differences in SOM between Measurements I and II.

Water repellency

The potential water repellency measurements showed that soils with all the treatments were non-repellent or very slightly water repellent with WDPTs varying from $< 1 \text{ s}$ to about 5 s . Considerable differences in water repellent levels were not observed between almost all the treatments, the two application rates and the two measurements periods except for the instant penetrations of water drops observed in the control (T0) and treatments T4, T6. The reasons for the absence of water repellent condition might be the originally highly wettable nature of the soil, low levels of compost application ($10\text{--}20 \text{ Mg ha}^{-1}$), and low SOM levels.

Water-entry value (h_{we})

The h_{we} of samples with all the treatments were negative, which is reported to be a commonly found phenomenon in readily wettable soils (Wang et al., 2000). The h_{we} was varying from -1.0 to -2.0 cm at 10 Mg ha^{-1} application rate, from -0.5 to -1.0 cm at 20 Mg ha^{-1} rate, and -2.5 cm for the control (T0) at both Measurement I and II. The h_{we} of all the compost treatments at 20 Mg ha^{-1} rate were significantly higher than those at the 10 Mg ha^{-1} rate (low negative values), whereas no significant difference was observed between Measurement I and II. The h_{we} of control (T0) was significantly higher than all the other treatments (two rates, two Measurements). Treatments T1, T2, T3, and T5 showed significantly high h_{we} (low negative values) only at the 20 Mg ha^{-1} rate in Measurement I, while other compost treatments did not differ significantly. This might be due to comparatively high organic matter contents in these treatments (Figure 1).

Initial infiltration rate (I_i)

Initial infiltration rates (I_i) of the soils are presented in Figure 2. In the Measurement I (during the dry season), the I_i of untreated soil was about 40 cm h^{-1} , whereas those of compost amended soils were in a range of $30\text{--}80 \text{ cm h}^{-1}$ at 10 Mg ha^{-1} rate, and $15\text{--}90 \text{ cm h}^{-1}$ at 20 Mg ha^{-1} rate (Figure 1a). Soils amended with two MSWC samples (T4, T6) showed a significant increase ($70\text{--}80 \text{ cm h}^{-1}$) in I_i at 10 Mg ha^{-1} application rate. This might be because of the comparatively lower organic matter contents (Figure 1) and extremely wettable nature (showed by instant penetrations). Although the organic matter contents of T8, T9, and T10 were also low, they did not show highly wettable nature. All other samples did not show significant differences in I_i comparing with T0.

At the doubled application rate (20 Mg ha^{-1}), seven out of ten compost amended soils showed lower I_i compared with the T0. Compared with the 10 Mg ha^{-1} application rate, soils amended with T8, T9, and T10 showed significantly higher I_i than the other treatments at 20 Mg ha^{-1} rate (Figure 2a). These samples showed lower organic matter levels (Figure 1) in both

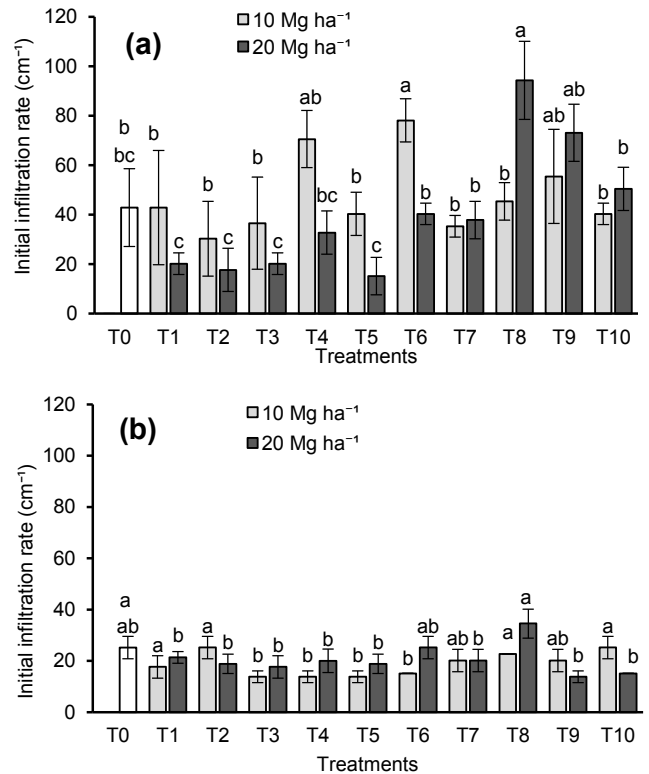


Fig. 2. Initial infiltration rates of the soils in (a) Measurement I and (b) Measurement II. Error bars indicate \pm standard deviation. Different lower case letters indicate significant differences between treatments, where upper and lower letters on T0 are respectively related to the 10 and 20 Mg ha^{-1} application rates ($P \leq 0.05$).

application rates and lower bulk densities (1.20 and 1.21 g cm^{-3}) at 20 Mg ha^{-1} rate. On the other hand, almost all the samples showed lower bulk density at the 20 Mg ha^{-1} rate than that of the 10 Mg ha^{-1} rate (which would be a result of increased organic matter levels) although the other treatments (except T8, T9, and T10) did not show higher I_i levels at 20 Mg ha^{-1} rate.

The occurrence of high I_i in T8, T9, and T10 treatments at 20 Mg ha^{-1} rate might possibly have caused by the development of minuscule cracks in soil surface, which would result in lower bulk density levels.

After exposing to the rainfall for period of 3 weeks (Measurement II), the I_i of untreated soil was about 25 cm h^{-1} , whereas those of compost amended soils were in a range of $14\text{--}25 \text{ cm h}^{-1}$ at 10 Mg ha^{-1} rate, and $15\text{--}35 \text{ cm h}^{-1}$ at 20 Mg ha^{-1} rate (Figure 1b). The highest I_i was observed in T8 ($\sim 35 \text{ cm h}^{-1}$), which was in line with the result of Measurement I, and might have resulted by similar reason because the bulk density of T8 was lower than all the other treatments in Measurement II. The I_i of soils with most treatments showed decreased values compared with the dry season values, while almost all the treatments did not show any significant differences compared with T0.

Sorptivity (S_w)

The S_w of soils at both Measurements are shown in Figure 3. In the Measurement I (Figure 3a), the S_w of soils with almost all the treatments showed no significant difference with T0 at 10 Mg ha^{-1} rate, except T4 and T7 where the S_w was significantly lower. At the 20 Mg ha^{-1} application rate, the S_w of four

treatments (T1, T2, T3, T5) were significantly lower, while all the other treatments did not show any significant difference, compared with the T0. The treatments T1, T2, T3, and T5 showed significantly higher organic matter contents than the other treatments (Figure 1a). Therefore, the low S_w at dry condition might have caused by high organic matter levels, which may restrict the sorption of water into soils due to possible minor water repellent effects.

After the rainfall period (Figure 3b), the differences in S_w among the treatments became extremely minor, showing no significant differences among almost all of the compost amendments (except T3, T4 at 10 Mg ha⁻¹ rate and T8 at 20 Mg ha⁻¹ rate). All the compost treatments showed low S_w compared with T0, where the most differences were statistically significant with few exceptions (T10 at 10 Mg ha⁻¹ rate; T1, T8 at 20 Mg ha⁻¹ rate). Although the S_w is reported to increase as a result of organic amendments (Bhattacharyya et al., 2007), results of the present study did not show increase in S_w with compost treatments. As pointed out by Wallis et al. (1991), water entry into soils may be reduced by an order of magnitude even in the soils that are visually appeared to wet in a normal manner, indicating the hydrological significance of water repellency. Accordingly, possible minor changes with compost treatments that affect water repellent nature of the soils, although could not be quantified with WDPT measurements, can be considered as the cause of lowered values of hydraulic properties with compost applications.

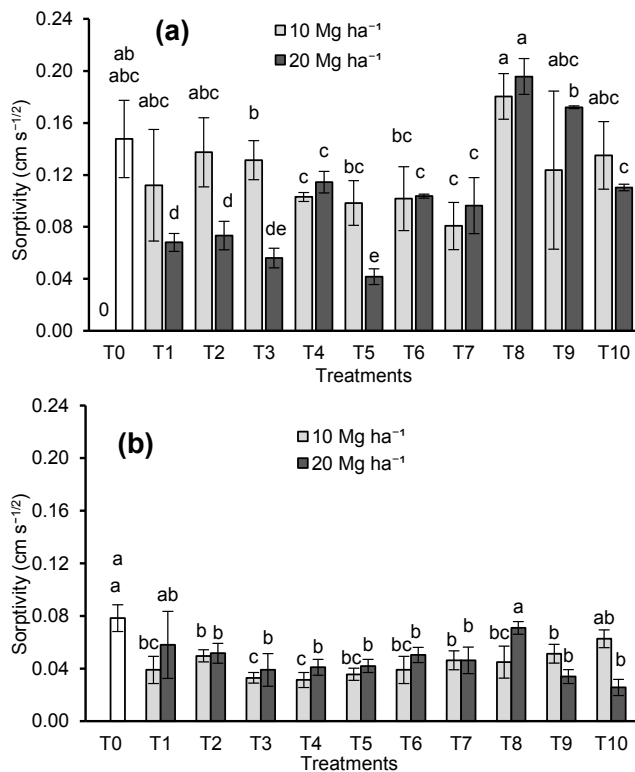


Fig. 3. Sorptivity of the soils in (a) Measurement I and (b) Measurement II. Error bars indicate \pm standard deviation. Different lower case letters indicate significant differences between treatments, where upper and lower letters on T0 are respectively related to the 10 and 20 Mg ha⁻¹ application rates ($P \leq 0.05$).

It was clear that all the surface hydraulic properties examined in situ (I_i , I_{ss} , S_w) were higher in the Measurement I than those observed in the Measurement II. As the organic matter contents in soils did not show any significant differences before

and after rainfall, it can be considered that lowered values of hydraulic processes in the Measurement II were not caused by an increase in organic matter contents and subsequent impacts related to wetting properties of soil. Another possible reason for higher rates of water movement into soils in dry state would be the water potential differences of soils in dry and comparatively moist conditions. Theoretically, the wetting of soil with water would be accelerated when the particular soil is in more dry condition. The moisture content of the field soils (top 0–1 cm) at the Measurement I was lower (about 1–2%) than that at the Measurement II (4–6%). The ability of a soil to rapidly capture water is measured through the S_w , which is considered to be the dominant parameter governing the early stages of infiltration (Shaver et al., 2003). It is possible that the difference in moisture content in soils of the present study affected the surface hydrological properties such as S_w (Figure 3) and I_i (Figure 2), showing higher values in Measurement I.

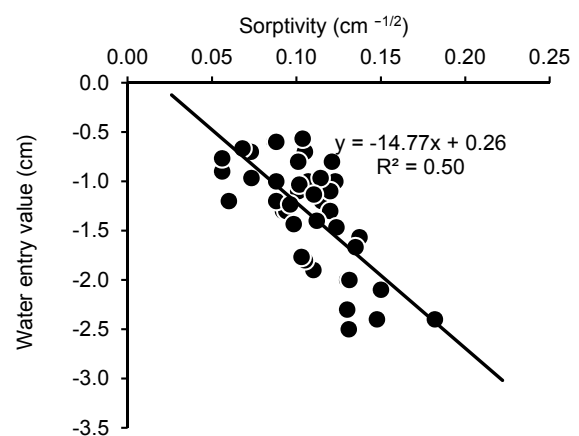


Fig. 4. Relation between sorptivity and the water entry values of the soils amended with different compost treatments.

The S_w explains the ability of a soil to rapidly capture water, or to uptake water without gravitational effects (Philip, 1969), whereas water-entry value explains a critical pressure at a point of achieving instantaneous water entry. As both h_{we} and S_w explains entering of water into the soil at different conditions, h_{we} was plotted against S_w to observe their interrelation. A moderate negative linear correlation ($R^2 = 0.50$) was observed between h_{we} and S_w (Figure 4), which was statistically significant at 0.05 probability level.

Steady-state infiltration rate (I_{ss})

As shown in Figure 5, I_{ss} did not follow the same results as I_i . In the Measurement I taken in the dry season, the I_{ss} of untreated soil was about 24 cm h⁻¹, whereas those of compost amended soils were in a range of 13–25 cm h⁻¹ at 10 Mg ha⁻¹ rate, and 8–25 cm h⁻¹ at 20 Mg ha⁻¹ rate (Figure 5a). It was clear that I_{ss} of all the compost amended samples were either statistically similar to, or significantly lower than, that of the T0 at both application rates.

At the 20 Mg ha⁻¹ application rate, eight out of ten compost amended soils showed low I_{ss} values compared with those at the 10 Mg ha⁻¹ application rate (Figure 5a). This might have caused by the differences in organic matter content of the compost amended soils as I_{ss} showed a negative linear correlation ($R^2 = 0.43$) with the SOM content. In the Measurement II, the I_{ss} did not show any significant difference among the treatments and application rates, showing low values about 8 cm h⁻¹ (Figure 5b). Possible physical changes occur with breaking

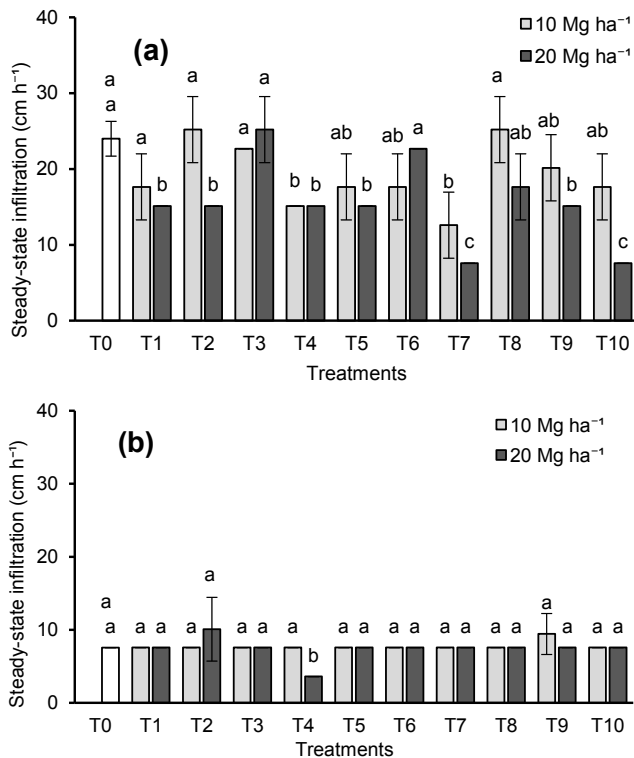


Fig. 5. Steady-state infiltration rates of the soils in (a) Measurement I and (b) Measurement II. Error bars indicate \pm standard deviation. Different lower case letters indicate significant differences between treatments, where upper and lower letters on T0 are respectively related to the 10 and 20 Mg ha⁻¹ application rates ($P \leq 0.05$).

down of aggregates, and other subsequent processes would take place on the soil surface as well as in the soil matrix might be the reason for the weakened I_{ss} in the Measurement II.

Unsaturated hydraulic conductivity (k)

The k of soils in both dry and wet periods is shown in Figure 6. During the dry period (Figure 6a), the k of the control (T0) was 18 cm h⁻¹. At 10 Mg ha⁻¹ rate, the k under compost treatments were either statistically similar, or significantly lower, compared with T0.

The k of compost treatments (except T6 and T8) decreased at the higher application rate (20 Mg ha⁻¹). All the compost treatments at the 20 Mg ha⁻¹ rate showed lower k values compared with T0, where most of the differences were statistically significant (except T3, T8). Soils treated with T8 showed high values for most tested hydraulic properties (Ex. I_i , S_w) that might have resulted from the development of minuscule cracks not only on the soil surface, but also in the matrix, which is shown by lower bulk density. As soils with T3 did not show low bulk density levels, low organic matter levels, or low values in any other tested surface hydraulic property, possible reasons for showing k values that are statistically similar to T0 is not clearly understood. However, there might be a possibility of macro-pore development in the soil matrix, which could not be confirmed in the present study.

After the rainfall (Measurement II), plots with all the treatments showed lowered k values (Figure 6b). All the compost treatments showed significantly lower k values compared with the T0 at both 10 and 20 Mg ha⁻¹ application rates, where the k was higher at 10 Mg ha⁻¹ than that of 20 Mg ha⁻¹ for all the treatments. As similar cultivation practices conducted in all the

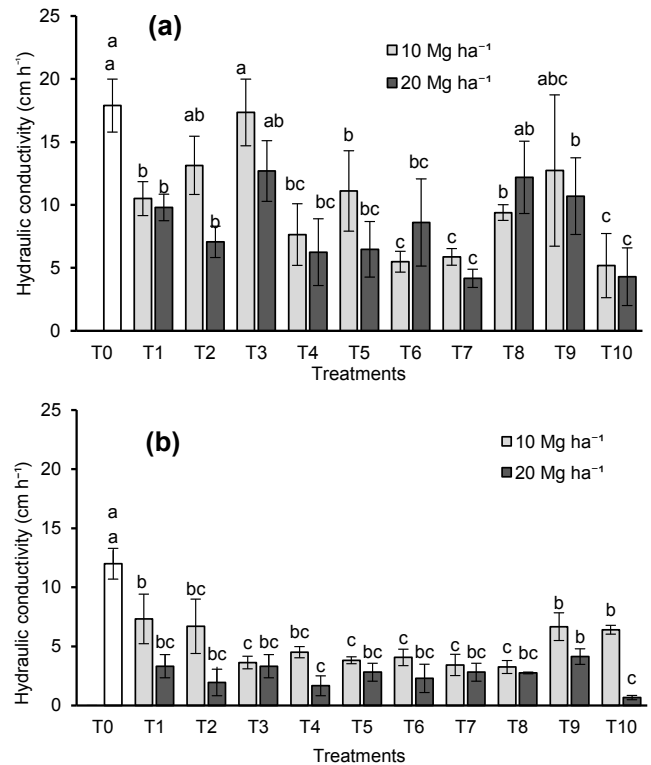


Fig. 6. Unsaturated hydraulic conductivity of the soils in (a) Measurement I and (b) Measurement II. Error bars indicate \pm standard deviation. Different lower case letters indicate significant differences between treatments, where upper and lower letters on T0 are respectively related to the 10 and 20 Mg ha⁻¹ application rates ($P \leq 0.05$).

plots including control (T0), the decreased values of k are considered to be caused by compost treatments, showing lower values at higher rates. Application of organic manure, including MSWC, is known to enhance porosity, water retention characteristics and saturated hydraulic conductivity (Głąb, 2014; Karak et al., 2016 and references therein; Yazdanpanah et al., 2016) of soils. In contrast to those reports, k in the present study showed decreasing trend with compost treatments.

To examine the relation of SOM levels to the unsaturated water movement in the soil matrix, the k was plotted against SOM content. The k showed moderate negative linear correlation with the log SOM content for the Measurements I ($R^2 = 0.50$) and II ($R^2 = 0.51$) periods (Figure 7). Comparing the Measurements I and II, k showed higher sensitivity to the increasing SOM contents at the Measurement I conducted in the dry period, indicating higher slope in the linear regression line compared with the Measurement II conducted during the rainy period (standard errors of the slopes are 6.11 and 2.02 for dry and rainy periods, respectively).

Compost treatments made to the top soil (1–10 cm) seem to affect most of the investigated hydraulic properties (h_{we} , I_i , I_{ss} , S_w) on the soil surface as well as in the soil matrix (k). In case of k , this effect was more explicit in both Measurements showing lower values in all the compost amended soils compared with T0, and higher rate of application compared with the lower rate. This effect can be confirmed considering the negative linear relationship between log organic matter content and the k (Figure 7).

Altogether, the in situ investigated hydraulic properties (such as I_i , I_{ss} , S_w , k) showed greater values before the start of the rainy season than afterwards. As the differences in SOM

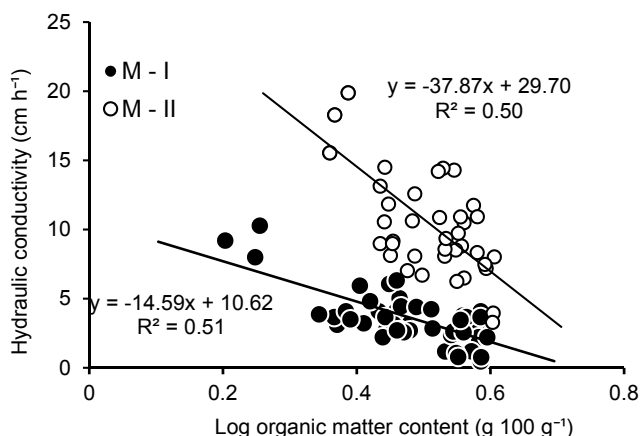


Fig. 7. Relation between logarithmic organic matter content measured as $\text{g } 100 \text{ g}^{-1}$, and the unsaturated hydraulic conductivity of the soils amended with different compost treatments at Measurement I (M-I) and Measurement II (M-II).

contents were not significant before and after rainfall, it can be considered that lowered values of hydraulic properties in the Measurement II were not caused by an increase of organic matter contents and subsequent impacts related to wetting properties of soil. Although water potential difference is a potential factor, it seemed not a possible reason here because I_{ss} also decreased in the Measurement II (Figure 5). The I_{ss} should be remain similar in Measurements I and II, because it represents a situation near saturation, where the initial levels of moisture in soils would not have any effective impact. Furthermore, when the moisture content is high in a soil, water movement through the pores would be easier than that in a comparatively dry soil, improving hydraulic water movement. In contrast, k showed significant decrease in the Measurement II. Accordingly, it can be considered that although the water potential differences might have important effects, it would not be the solitary reason for weakened hydraulic movements in the Measurement II, where the soils were exposed to rainfall for a period of more than 3 weeks.

Dry soils that face rainfall would be subjected to different kinds of physical changes. Aggregates that have been produced in the dry soil would be dissipated producing sludge due to precipitation, and other subsequent processes would take place on the soil surface as well as in the soil matrix, such as particle rearrangements, clogging of pores, and formation crusts. These kinds of changes in soil physical environment might be the reason for the weakened I_{ss} in the Measurement II. Moreover, these effects can be considered as the reasons for the linear regression line between log organic matter content and the k to demonstrate a high slope in the Measurement I compared with that in the Measurement II.

CONCLUSIONS

Data obtained through direct field and laboratory measurements with soils of cultivated plots amended with ten types of composts samples at two rates (10 and 20 Mg ha^{-1}) with control (T0) showed that the processes such as water entry, infiltration rates, k , and S_w are affected by the compost amendments. Considering the overall results of the present study, compost amendments seemed not to improve or accelerate but tend to suppress hydraulic properties of soil, especially at the higher rate of application.

Results revealed that there is a significant difference between measurements made in dry and rainy seasons, which

might have caused mainly by physical changes incurred due to the impacts of rainfall. No improvement in hydraulic properties were observed with AWC treatments compared with MSWC. However, the SOM contents seemed lower in AWC treatments (T9, T10) than most of the MSWC.

Providing high organic matter content to the soil is also important as the original organic matter levels in the soil is very low. Considering the results, T1, T2, T3, and T5 are the treatments that result in high SOM contents. On the other hand, the tested soil was a coarse-textured loamy sand soil where the soils are facing very high average annual rainfall (2400 – 2800 mm). Water drains through very easily making the soil more prone to leaching, removing plant available nutrients from the root zone with the possibility of contaminating groundwater. Therefore, considering the importance of lowering the hydraulic water movements as well, T3 and T5 might be considered as best suited for the tested soil conditions.

Acknowledgements. Authors gratefully acknowledge the financial support provided by the National Research Council (NRC) of Sri Lanka (NRC Grant 14–019).

REFERENCES

- Angin, I., Aksakal, E.L., Oztas, T., Hanay, A., 2013. Effects of municipal solid waste compost (MSWC) application on certain physical properties of soils subjected to freeze-thaw. *Soil Till. Res.*, 130, 58–61.
- Bhattacharyya, R., Chandra, S., Singh, R.D., Kundu, S., Srivastva, A.K., Gupta, H.S., 2007. Long-term farmyard manure application effects on properties of a silty clay loam soil under irrigated wheat-soybean rotation. *Soil Till. Res.*, 94, 2, 386–396.
- Cointreau, S., 2007. The Growing Complexities and Challenges of Solid Waste Management in Developing Countries. World Bank. <http://sandracoireau.com/wp-content/uploads/2011/02/Cointreau-ISWA-Amsterdam-Complexities-and-Challenges-2007.pdf> (accessed 03.11.16.)
- Doerr, S.H., Shakesby, R.A., Walsh, R., 2000. Soil water repellency: its causes, characteristics and hydrogeomorphological significance. *Earth Sci. Rev.*, 51, 33–65.
- Fernandez, M.T.H., Mataix-Solera, J., Lichner, L., Štekauerová, V., Zaujec, A., Garcia Izquierdo, C., 2007. Assessing the microbiological, biochemical, soil-physical and hydrological effects of amelioration of degraded soils in semiarid Spain. *Biologia*, 62, 542–546.
- Głab, T., 2014. Water retention and repellency of a sandy soil amended with municipal compost. *Compost Sci. Util.*, 22, 2, 47–56.
- Głab, T., Żabiński, A., Sadowska, U., Gondek, K., Kopeć, M., Mierzwa-Hersztek, M., Tabor, S., 2018. Effects of co-composted maize, sewage sludge, and biochar mixtures on hydrological and physical qualities of sandy soil. *Geoderma*, 315, 27–35.
- Grau, F., Drechsel, N., Haering, V., Trautz, D., Weerakkody, W.J.S.K., Drechsel, P., Marschner, B., Dissanayake, D.M.P.S., Sinnathamby, V., 2017. Impact of fecal sludge and municipal solid waste co-compost on crop growth of *Raphanus Sativus* L. and *Capsicum Anuum* L. under stress conditions. *Resources*, 6, 3, 26.
- Jakobsen, S., 1995. Aerobic decomposition of organic wastes 2. Value of compost as fertilizer. *Resour. Conserv. Recy.*, 13, 57–71.
- Jodar, J.R., Ramos, N., Carreira, J.A., Pacheco, R., Fernández-Hernández, A., 2017. Quality assessment of compost pre-

- pared with municipal solid waste. *Open Engineering*, 7, 1, 221–227.
- Karak, T., Paul, R.K., Sonar, I., Nath, J.R., Boruah, R.K., Dutta, A.K., 2016. Nickel dynamics influenced by municipal solid waste compost application in tea (*Camellia sinensis* L.): a cup that cheers. *Int. J. Environ. Sci. Technol.*, 13, 2, 663–678.
- Leelamanie, D.A.L., 2014. Initial water repellency affected organic matter depletion rates of manure amended soils in Sri Lanka. *J. Hydrol. Hydromech.*, 62, 4, 309–315.
- Leogrande, R., Lopodota, O., Vitti, C., Ventrella, D., Montemurro, F., 2016. Saline water and municipal solid waste compost application on tomato crop: Effects on plant and soil. *J. Plant Nutr.*, 39, 4, 491–501.
- Lichner, L., Hallett, P., Feeney, D., Ďugová, O., Šír, M., Tesář, M., 2007a. Field measurement of soil water repellency and its impact on water flow under different vegetation. *Biologia*, 62, 5, 537–541.
- Lichner, L., Orfánus, T., Nováková, K., Šír, M., Tesář, M., 2007b. The impact of vegetation on hydraulic conductivity of sandy soil. *Soil Water Res.*, 2, 59–66.
- Liyanage, T.D.P., Leelamanie, D.A.L., 2016. Influence of organic manure amendments on water repellency, water entry value, and water retention of soil samples from a tropical Ultisol. *J. Hydrol. Hydromech.*, 64, 2, 160–166.
- Martínez-Blanco, J., Lazcano, C., Boldrin, A., Muñoz, P., Rieradevall, J., Møller, J., Antón, A., Christensen, T.H., 2013. Assessing the environmental benefits of compost use on-land through an LCA perspective. In: *Sustainable Agriculture Reviews*. Springer Netherlands, pp. 255–318.
- Maule, C.P., Fonstad, T.A., Vanapalli, S.K., Majumdar, G., 2000. Hydraulic conductivity reduction due to ponded hog manure. *Can. Agr. Eng.*, 42, 4, 157–164.
- National Atlas of Sri Lanka, 2007. Second Edition. Survey Department of Sri Lanka, Colombo, Sri Lanka.
- Panabokke, C.R., 1996. Soils and agro-ecological environments of Sri Lanka. Natural Resources Series No.2. Natural Resources, Energy and Science Authority, Colombo, Sri Lanka.
- Peltre, C., Gregorich, E.G., Bruun, S., Jensen, L.S., Magid, J., 2017. Repeated application of organic waste affects soil organic matter composition: Evidence from thermal analysis, FTIR-PAS, amino sugars and lignin biomarkers. *Soil Biol. Biochem.*, 104, 117–127.
- Philip, J., 1969. Theory of infiltration. In: *Adv. Hydrosci.*, Elsevier. Academic Press, New York, pp. 215–296.
- Rowell, M.J., Coetzee, M.E., 2003. The measurement of low organic matter contents in soils. *S. Afr. J. Plant Soil*, 20, 2, 49–53.
- Shaver, T.M., Peterson, G.A., Sherrod, L.A., 2003. Cropping intensification in dryland systems improves soil physical properties: regression relations. *Geoderma*, 116, 149–164.
- Soil Survey Staff, 2014. *Keys to Soil Taxonomy*. 12th ed. USDA-Natural Resources Conservation Service, Washington, DC.
- Wallis, M.G., Scotter, D.R., Horne, D.J., 1991. An evaluation of the intrinsic sorptivity water repellency index on a range of New Zealand soils. *Soil Res.*, 29, 3, 353–362.
- Wang, Z., Wu, L., Wu, Q.J., 2000. Water-entry value as an alternative indicator of soil water-repellency and wettability. *J. Hydrol.*, 231, 76–83.
- World Health Organization, 1999. *What a waste: Solid waste management in Asia*. Urban Development Sector Unit. East Asia and Pacific Region. Washington, DC.
- Yazdanpanah, N., Mahmoodabadi, M., Cerdà, A., 2016. The impact of organic amendments on soil hydrology, structure and microbial respiration in semiarid lands. *Geoderma*, 266, 58–65.
- Zhang, R., 1997. Determination of soil sorptivity and hydraulic conductivity from the disk infiltrometer. *Soil Sci. Soc. Am. J.*, 61, 1024–1030.

Received 13 November 2017

Accepted 11 June 2018

Impact of armour layer on the depth of scour hole around side-by-side bridge piers under ice-covered flow condition

Mohammad Reza Namaee, Jueyi Sui*

Environmental Engineering Program, University of Northern British Columbia, 3333 University Way, Prince George, BC, Canada.

* Corresponding author. E-mail: jueyi.sui@unbc.ca

Abstract: In the present study, experiments were conducted in a large-scale flume to investigate the issue of local scour around side-by-side bridge piers under both ice-covered and open flow conditions. Three non-uniform sediments were used in this experimental study. Analysis of armour layer in the scour holes around bridge piers was performed to inspect the grain size distribution curves and to study the impact of armour layer on scour depth. Assessments of grain size of deposition ridges at the downstream side of bridge piers have been conducted. Based on data collected in 108 experiments, the independent variables associated with maximum scour depth were assessed. Results indicate that the densimetric Froude number was the most influential parameter on the maximum scour depth. With the increase in grain size of the armour layer, ice cover roughness and the densimetric Froude number, the maximum scour depth around bridge piers increases correspondingly. Equations have been developed to determine the maximum scour depth around bridge piers under both open flow and ice covered conditions.

Keywords: Armour layer; Local scour; Bridge pier; Ice cover; Non-uniform sand; Erosion of river-bed.

INTRODUCTION

Bed scour may be a natural occurrence or due to manmade changes to a river. Depending on the intensity of approaching flow for sediment transport, local scour process around bridge piers is classified as either clear-water scour or live bed scour. Local scour around bridge pier is a process of scouring as the result of installation of artificial obstacles such as weirs, abutments and piers in rivers (Richardson et al., 1993). More specifically, flow contraction in rivers caused by installation of hydraulic constructions such as bridge piers and abutments can lead to substantial local alteration of the flow patterns and significant increase of shear stress. As the result of increased shear stress around the hydraulic structures which is itself direct consequence of increased turbulence, flow velocities and the complex flow structures (downwelling, upwelling, horseshoe vortices) causes increased sediment entrainment at the river bed which eventually results in development of local scour holes (Török et al., 2014). The main feature of the flow around a pier is the system of vortices which develop around the pier. These vortex systems have been discussed by many researchers (Kothyari et al., 1992; Melville and Raudkivi, 1977; Melville and Sutherland, 1988; Raudkivi and Ettema, 1983, to mention only a few). One of the phenomena associated with characteristics of flow in the vicinity of bridge piers is the development of armour layer. Bed armouring process typically occurs in streams with non-uniform bed materials. This phenomenon occurs mainly due to selective erosion process in which the bed shear stress of finer sediment particles exceeds the associated critical shear stress for movement. As a consequence, finer sediment particles are transported and leave coarser grains behind. Through this process, the coarser grains get more exposed to the flow while the remaining finer grains get hidden among larger ones (Mao et al., 2011). Armour layer is also partially due to the reduced exposure of the flow with those sediments inside the scour hole zone (Sui et al., 2010). For the same bed sediments, Dey and Raika (2007) found that the scour depth around bridge piers with an armour layer is less than that without armour layer. Froehlich (1995) stated that the thickness of

the natural armour-layer is up to one to three times the particle grain size of armour-layer. Raudkivil and Ettema (1985) found that due to the local flow structure around a pier, local scour may either develop through the armour layer and into the finer, more erodible sediment, or it may trigger a more extensive localized type of scour caused by the erosion of the armour layer itself. Sui et al. (2010) studied clear-water scour around semi-elliptical abutments with armoured beds. The results showed that for any bed material having the same grain size, with the increase in the particle size of armour-layer, scour depth will decrease. Török et al. (2014) investigated armour layer development in a scour hole around a single groin in laboratory. The main goal of their research was to study bed morphology, sediment transport, bed composition and hydrodynamics under conditions when bed armour development is expected. Guo (2012) studied the relevant scour mechanism of clear water scour around piers and proposed a scour depth equation. Zhang et al. (2012) studied bed morphology and grain size characteristics around a spur dyke. It was found that the mean grain size and the geometric standard deviation of the bed sediment are two important parameters in characterizing the changes of the bed morphologies and the bed compositions around the spur dyke. Kothyari et al. (1992) concluded that an increase in the geometric standard deviation of sediment gradation (σ_g) would lead to a decrease in scour depth because of the armouring effect on the bed.

The presence of ice cover imposes a solid boundary to flow. The velocity profile under ice-covered condition is totally different compared to open channel flow. Under ice-covered condition, the maximum velocity occurs between channel bed and the bottom of the ice cover and is dependent on the relative roughness of these two boundaries (Sui et al., 2010). The velocity drops to zero at each boundary due to the no-slip boundary condition, resulting in a parabola-shaped profile (Zabilansky et al., 2006). The presence of ice cover has been found to increase local scour depth around bridge piers by 10%–35% (Hains and Zabilansky, 2004). Also, as pointed out by Wang et al. (2015, 2016), the appearance of bridge piers and abutments in channel has different impacts on ice accumulation under ice

cover. Based on experiments in laboratory, Wu et al. (2014) claimed that with the increase in ice cover roughness, scour depth bridge around bridge abutments increased, correspondingly. The impact of ice on sediment transport in a stream is typically most significant during ice formation and breakup (Ettema and Kempema, 2012; Sui et al., 2000). Ice cover can either increase or decrease bed load and suspended sediment transport depending on the type of ice cover (Ettema and Kempema, 2012; Sui et al., 2000). Ettema et al. (2000) proposed a method for estimating sediment transport rate in ice-covered alluvial channels. Wu et al. (2014) investigated the impact of ice cover on local scour around bridge abutment. Results show that with increase in densimetric Froude number, there is a corresponding increase in the scour depth. Results also showed that with increase in grain size of the armour layer, the maximum scour depth decreases and with increase in ice cover roughness, the maximum scour depth increases correspondingly (Wu et al., 2014).

Up to date, research work regarding the impact of ice cover on local scour in the vicinity of bridge piers is limited. In present study, three non-uniform sediments and two types of ice cover are used to study the development of armour layer in the scour hole around four pairs of bridge piers as well as to investigate the impact of ice cover and armour layer on the maximum scour depth under ice covered conditions.

EXPERIMENT SETUP

Experiments were carried out in a large-scale flume at the Quesnel River Research Centre of the University of Northern British Columbia. The flume is 38.2 m long, 2 m wide and 1.3 m deep, as showed in Figure 1a. The longitudinal slope of the channel bed was 0.2 percent. A holding tank with a volume of 90 m³ was located at the upstream of the flume to keep a constant discharge during each experimental run. To create different velocities, three valves were connected to adjust the amount of water into the flume. Two sand boxes were filled with natural non-uniform sediment. These sand boxes were spaced 10.2 m away from each other and were 30 cm deep and 5.6 m and 5.8 m in length, respectively. Three types of non-uniform sediments with different grain sizes were used in this experimental study. The natural non-uniform sediments had median grain sizes of 0.50 mm, 0.47 mm and 0.58 mm and the geometric standard deviation (σ_g) of 2.61, 2.53 and 1.89, respectively. According to Dey and Barbhuiya (2004), sediments used in this study can be treated as non-uniform since σ_g is larger than 1.84. Four pairs of bridge piers with different diameters of 6 cm, 9 cm, 11 cm and 17 cm were used. Inside each sand box, a pair of bridge piers was placed symmetrically to the centre line of flume. The distance from the centre line of each pier to the flume centre is 25 cm, as illustrated in Figure 1b.

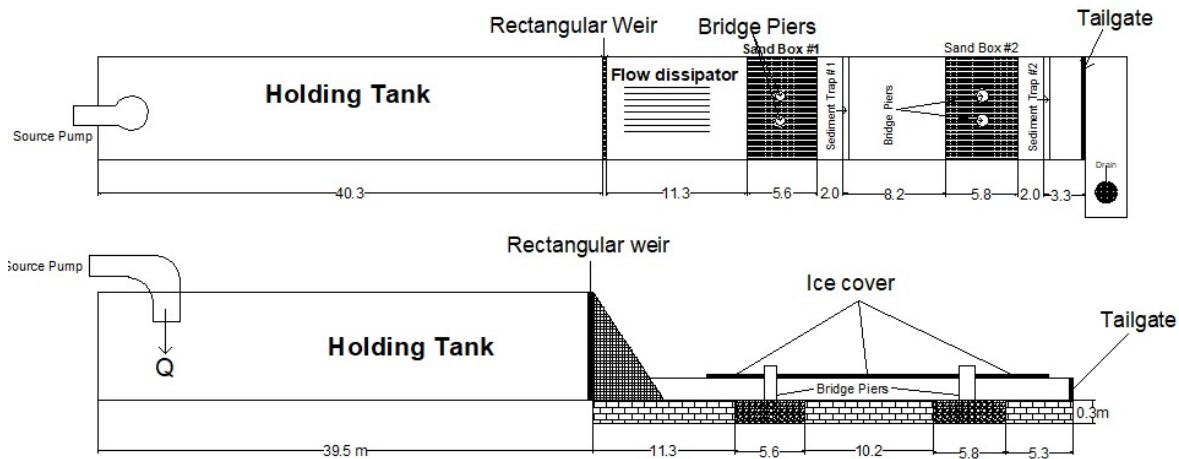


Fig. 1. Experimental setup. (a) Plan view and vertical view of experiment flume.

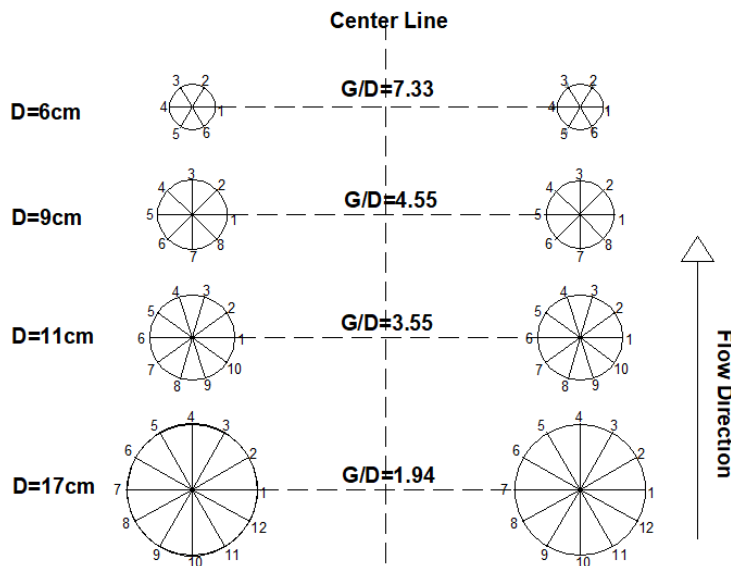


Fig. 1. Experimental setup. (b) The spacing ratio and measuring points around the circular bridge piers.

Water level in the flume was controlled by adjusting the tailgate. In front of the first sand box, a SonTek incorporated 2D Flow Meter was installed to measure flow velocities and water depth during experiment runs. A staff gauge was also installed in the middle of each sand box to manually verify water depth. Velocity fields in scour holes were measured using a 10-MHZ Acoustic Doppler Velocimeter (ADV). The ADV is a high-precision instrument that can be used to measure 3D flow velocity in a wide range of environments including laboratories, rivers, estuaries, and the ocean (Cea et al., 2007). Styrofoam panels which were used to model ice cover, had covered the entire surface of flume. In present study, two types of model ice cover were used, namely smooth cover and rough cover. As showed in Figure 2, the smooth cover was the surface of the original Styrofoam panels while the rough cover was made by attaching small Styrofoam cubes to the bottom of the smooth cover. The dimensions of Styrofoam cubes were 2.5 cm × 2.5 cm and were spaced 3.5 cm apart. A total of 108 flume experiments were completed under both open channel and ice-covered flow conditions. In terms of different boundary conditions (open channel, smooth covered and rough covered flow conditions), for each sediment type and each boundary condition, 12 experiments were done. Experimental runs were taken under clear-water scour conditions. After 24 hours, the flume was gradually drained, and the scour and deposition pattern around the piers was measured. To accurately read the scour depth at different locations and to draw scour hole contours, the outside perimeter of each bridge pier was equally divided and labeled as the reference points. The measurement of scour hole was subject to an error of ±0.03 cm.



Fig. 2. Rough model ice cover on water surface.

After each experiment, sand samples within the scour hole which represent armour layer were collected. The samples were taken from the top layer of 5 mm of the armour layer in each scour hole. The sampling process is based on the sampling methodology for collecting armour samples proposed by Bunte and Abt (2001). The collected sand samples were eventually sieved and the mediums grain size of armour layer (D_{50}) was calculated. The scour contours were also plotted by using Surfer 13, Golden Software. In present study, 108 Experiments (36 experiments for each sediment type) were conducted under open channel, smooth covered and rough covered conditions. For each sediment type, 12 experiments were done for open flow condition, 12 experiments for smooth ice-covered flow condition and 12 experiments for rough ice-covered flow condition, respectively. Flow depth in the flume was controlled by adjusting downstream tailgate. The flow depth ranges from 9 cm to 28 cm. The flow velocity ranges between 7.0 cm/s and 27.09 cm/s.

RESULTS

Scour patterns and bed morphology

Figure 3 shows the scour morphology and developed armour layer around the 17-cm-pier. Results indicate that the geometry of the scour holes under open flow condition is approximately similar to that under ice-covered flow condition. As shown in Figure 3, the armour layer covers the scour holes around bridge pier. At the downstream of bridge pier, a deposition ridge was developed. Figure 4 shows the scour contours and bed morphology around the 11-cm-pier under smooth covered flow condition for three different sediments. Under the same flow condition and ice-covered condition, the maximum scour depth occurs in channel bed with the finest sediment ($D_{50} = 0.47$ mm). Due to the horseshoe vortex system, the maximum depth of scour hole is located at the upstream face of the piers, and the scour hole extends along the sides of the piers towards the downstream face of the pier where the wake vortex exists. This scouring process around bridge piers is substantially due to the merging of the locally enhanced flow at the sides of the pier with the turbulent horseshoe vortices in front of the piers. Besides, sediment deposition ridge which is developed at the downstream of the piers, travels further downstream as vortex shedding occurs. Under the same flow condition and ice-covered condition, as the sediment gets coarser, the turbulence of flow between the piers slightly decreases. Thus, with respect to Figure 4, a slight deposition which is caused by the jet-like flow has developed between piers, especially for channel bed with sediment of $D_{50} = 0.47$ mm. Figure 5a shows the variation in scour depth elevation for 3 different sediments under smooth ice-covered flow condition, while Figure 5b shows the variation in scour depth elevation for sediment of $D_{50} = 0.58$ mm under conditions of open channel, smooth ice-covered and rough ice-covered flows. The following results are obtained from the Figure 5a and Figure 5b:

Under the same boundary condition (either covered flow or open flow), the maximum scour depth is located at the upstream nose of the pier (at point 9 of the 11-cm-pier as showed in Figure 1b). The primary horseshoe vortex which is stronger at the front face of pier is responsible for this. As confirmed by Muzzammil and Gangadhariah (2003), the primary horseshoe vortex which generates in front of a pier is the main reason for scour over the entire scouring process. Results showed that the interaction between the primary horseshoe vortex and the finer sediment is more intense than that of coarser sediment. Also, the lowest scour hole is located at point 4 which is behind the pier as showed in Figure 5a.



Fig. 3. Armour layer developed around the 17-cm-pier.

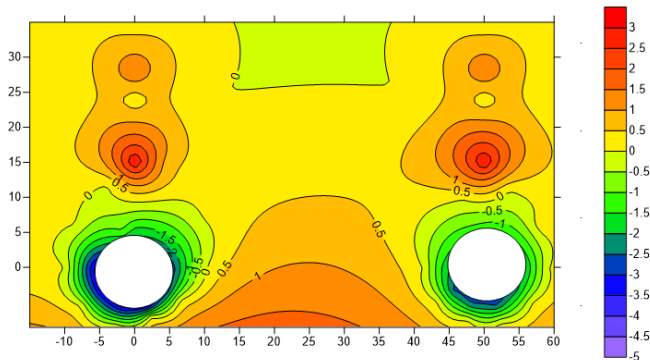


Fig. 4a. Scour morphology and the deposition ridge around the 11-cm-pier under smooth ice-covered condition for $D_{50} = 0.50$ mm.

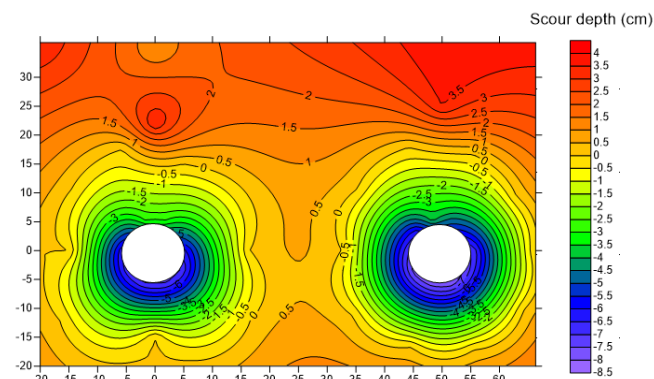


Fig. 4b. Scour morphology and the deposition ridge around the 11-cm-pier under smooth ice-covered condition for $D_{50} = 0.47$ mm.

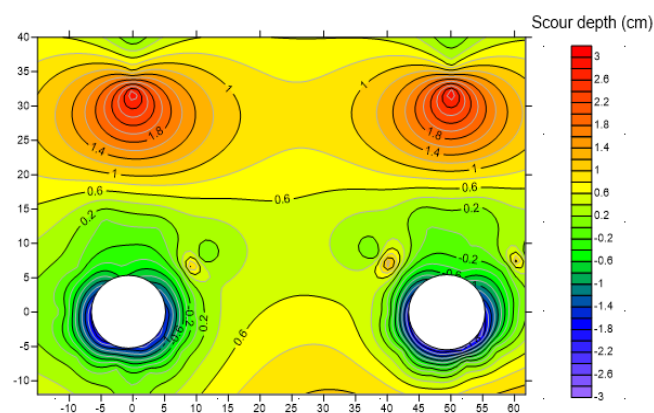


Fig. 4c. Scour morphology and the deposition ridge around the 11-cm-pier under smooth ice-covered condition for $D_{50} = 0.58$ mm.

Figure 5b shows that, for the same sediment (such as $D_{50} = 0.47$ mm), the deepest scour hole has occurred under rough ice-covered flow condition. Besides, regardless of flow cover, the maximum scour depth is located at the upstream face, namely, location point 7 for the 9-cm-pier, similar to that of the 11-cm-pier. According to Sui et al. (2010), the existence of an ice cover on water surface doubles the wetted perimeter compared to that under open flow condition, and alters the hydraulics of an open channel by imposing an extra boundary to the flow. As a consequence, the maximum flow velocity is shifted towards the channel bed. The velocity profile is significant changed (comparing to that under open flow condition). Thus, the strength of primary horseshoe vortices under ice-covered flow condition is amplified, this leads to more intense scour depths. Under covered flow condition, the roughness of ice cover has significant impacts on velocity field and flow characteristics, namely, the rougher the ice cover, the more effects on velocity field and flow characteristics. For channel bed with the

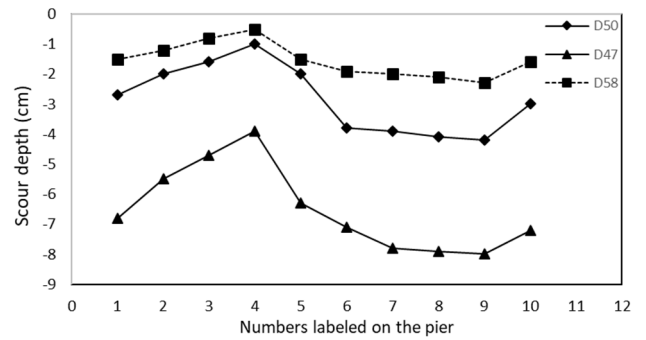


Fig. 5a. Scour profiles around the 11-cm-pier under smooth ice-covered flow condition.

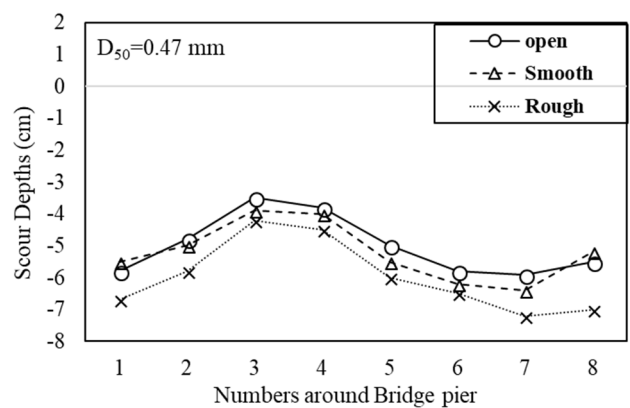


Fig. 5b. Scour profiles around the 9-cm-pier under ice-covered and open channel flow condition for $D_{50} = 0.47$ mm.

same sediment, the rough ice cover will lead to a deeper scour hole comparing to that of smooth ice-cover.

Figure 6a shows the pattern of scour hole and deposition ridge around the 11-cm pier under rough covered flow condition ($D_{50} = 0.58$ mm), while Figure 6b shows scour depths around the 9-cm-pier under different boundary conditions for $D_{50} = 0.47$ mm. Results indicate that, regardless of the roughness of ice cover and grain size of sediment, the maximum scour depths always occur at the upstream front face of bridge piers. It has been observed from experiments that the horseshoe vortex shifts the maximum downflow velocity closer to the pier in the scour hole. Besides, under covered condition, the strength of this downflow jet is intensified. The eroded sand particles are carried around the pier by the combined action of accelerating flow and the spiral motion of the horseshoe vortex. As clearly showed in Figure 6a, the deposition ridge has been formed downstream of the pier. Melville and Coleman (2000) stated that the wake-vortex system acts like a vacuum cleaner sucking up stream bed material and carrying the sediment moved by the horseshoe vortex system and by the downward flow to the downstream of the pier. However, wake vortices are normally not as strong as the horseshoe vortices and therefore, they are not able to carry the same amount of sediment load as that carried by the horseshoe vortex. Hereby, sediment deposition occurs downstream of bridge piers in the form of deposition mound as shown in Figure 6a.

Scour area and scour volume

Accurate determination of scour volume and scour area is important in practical decision-making for the control of local scour and safe design of countermeasures. However, there is very limited research work for examining the scour volume and scour area under ice-covered flow condition. Wu et al. (2014)



Fig. 6a. a view of the scour pattern and deposition ridge around the 11-cm pier under rough ice-covered condition ($D_{50} = 0.58$ mm).

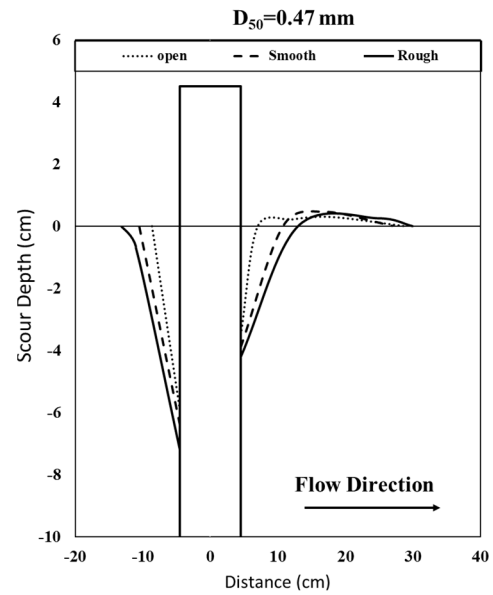


Fig. 6b. Cross sections of scour and deposition ridge around the 9-cm-piers under open channel, smooth and rough covered flow conditions ($D_{50} = 0.47$ mm).

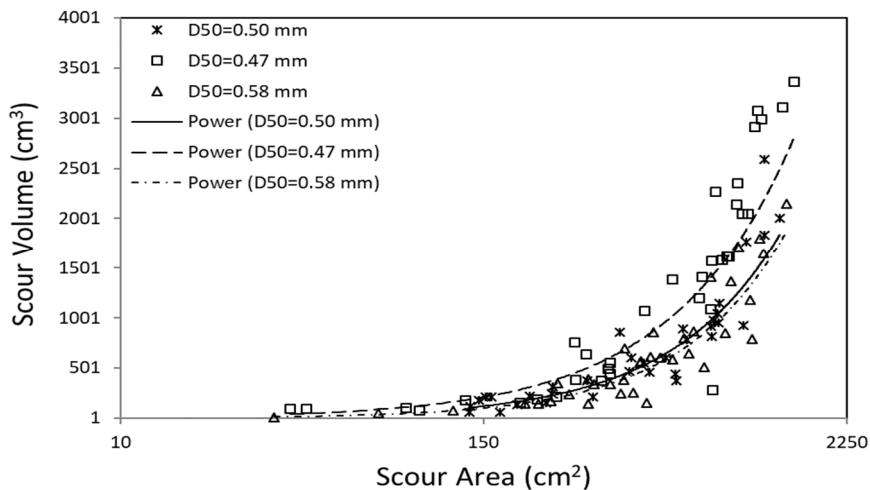


Fig. 7. Relationship between scour volume and scour area.

found that there was a linear correlation between scour depth and volume of scour hole around bridge abutments under ice covered condition. Khwairakpam et al. (2012) developed two formulae to estimate scour volume and scour area around a vertical pier under clear water condition in terms of approach flow depth and pier diameter. Figure 7 gives the relationship between scour volume (V) and scour area (A) in terms of grain size of sediment. These relationships can be described as follows:

Under open flow condition:

$$V = 0.229 A^{1.256} \tag{1}$$

Under ice-covered flow condition:

$$V = 0.465 A^{1.158} \tag{2}$$

In which V is volume of scour hole (cm^3) and A is surface area of scour hole. The following results are obtained from the scour volume and scour area analysis.

(a) In terms of grain size of sediment, under the same flow condition, the finest sediment ($D_{50} = 0.47$ mm) yielded the largest scour volume and scour area and the impact of ice cover on scour volume and scour area is more significant for finer sediment type. On the other hand, under the same flow conditions, the coarsest sediment (namely, $D_{50} = 0.58$ mm) yielded the smallest scour volume and scour area.

(b) In terms of flow cover, results indicated that the flow under ice-covered condition led to larger amount of scour volume and scour area. It was found that, the maximum amount of scour volume and scour area occurred under rough covered flow condition. Also, under the same flow condition, intense scouring process around bridge piers with smaller pier spacing has been observed, especially in channel bed with the finest sediment.

Grain size analysis of armour layer

Sieve analyses (ASTM D422-63) were performed to obtain the grain size distribution of the three non-uniform sediments. The grain size distribution curves for these three non-uniform sediments used in this experimental study are displayed in Figure 8. Sieve analyses revealed that the material collected was almost exclusively coarser than 0.075 mm (#200 sieve). The sediments were classified according to the unified soil classification system (ASTM D2487-11). All three sediments were classed as poorly-graded sands (SP).

As the experiments initiated, the armour layer evolution gradually started to develop inside the scour hole. The first sign of armour layer development was inside the scour hole at the upstream face of the pier where the downflow and horseshoe vortex exists and in which the armour layer was denser. The armour layer then extended to the sides and downstream of the pier, where the armour layer particles were more separated from each other and it eventually disintegrates at the end of the deposition ridge. Results showed that the armour layer which was formed on the deposition ridges was composed of finer sediment particles compared to those of armour layer formed inside the scour holes. The maximum depth of scour hole remained quite constant once the armour layer was formed which is due to the slope stability caused by formation of the armour layer. The samples of armour layer developed within the scour

hole were collected for each experimental run and the D_{50} of the armour layers were extracted from armour layer grain size distribution graphs (described as D_{50A}). Figure 9 displays the distribution curves of grain sizes of armour layer in scour hole around the 11-cm-pier for $D_{50} = 0.50$ mm compared to those of the original sands and deposition ridge under rough covered flow condition. Table 1 also shows the grain size characteristics of samples of armour layers in scour holes around the 11-cm-pier compared to those of correspondingly deposition ridges for three sands under rough covered flow condition. One can see from Table 1, the armour layer generated in sand bed of $D_{50} = 0.58$ mm is coarser than that in sand beds of $D_{50} = 0.47$ mm and $D_{50} = 0.50$ mm. To better distinguish the difference in grain size distributions between the samples of armour layers in scour holes and the samples of the associate deposition ridges, the grain size distributions are separately displayed in Figures 10(a-b). Results indicate that the armour layer generated in sand bed of $D_{50} = 0.58$ mm is the coarsest comparing to those of $D_{50} = 0.47$ mm and $D_{50} = 0.50$ mm. Regarding the deposition ridge in sand bed of $D_{50} = 0.58$ mm, the deposition ridge is covered by coarsest sand particles comparing to those of $D_{50} = 0.47$ mm and $D_{50} = 0.50$ mm. With decrease in D_{50} of the original sand, the grain size of the armour layer decreases correspondingly. These results are in good agreement with findings of Wu et al (2015) who investigated the armour layer in scour holes around square and semi-circular abutments.

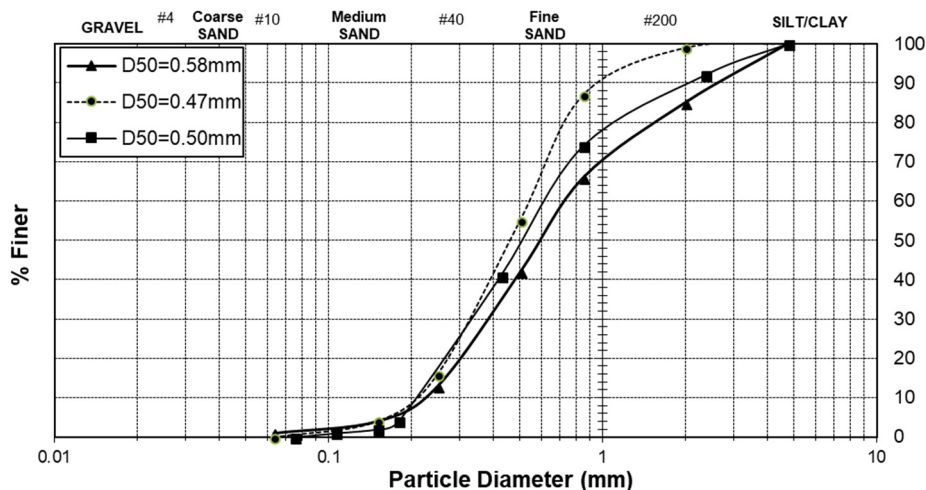


Fig. 8. Grain size distribution curves of three non-uniform sands used in this study.

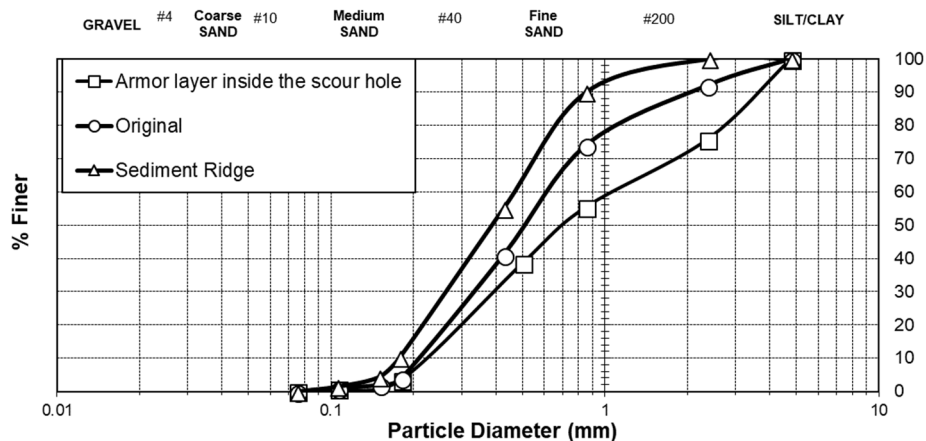


Fig. 9. Grain size distribution curves of the armour layer in scour hole around the 11-cm-pier, original sand and deposition ridge for sand bed of $D_{50} = 0.50$ mm under rough covered condition.

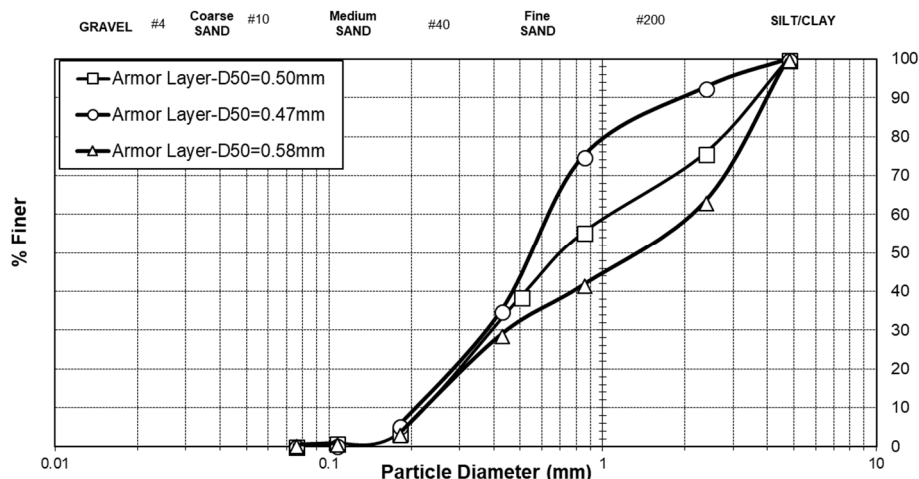


Fig. 10a. Grain size distributions of armour layer samples in scour hole generated from three sands around the 11-cm-pier.

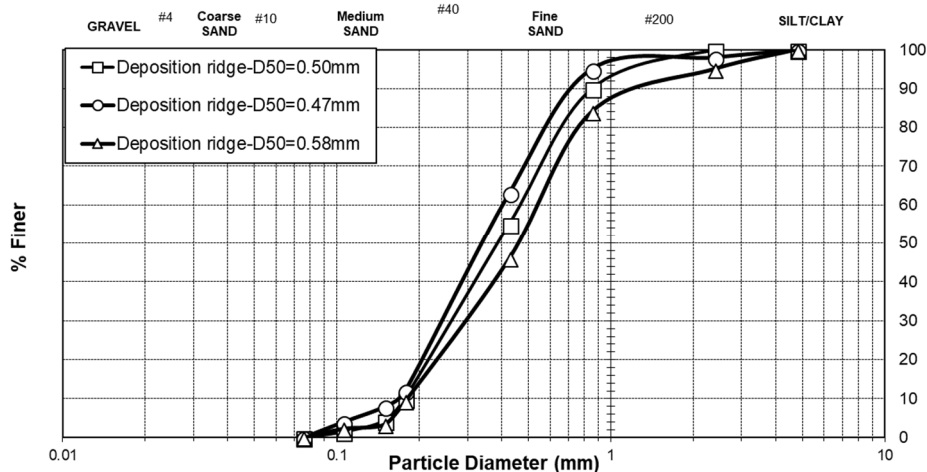


Fig. 10b. Grain size distributions of samples of deposition ridge generated from three sands downstream of the 11-cm-pier.

Table 1. Grain size characteristics of samples of armour layer in scour hole around the 11-cm-pier under rough covered flow condition compared to those of associated deposition ridge.

	D_{10} (mm)	D_{16} (mm)	D_{30} (mm)	D_{50} (mm)	D_{60} (mm)	D_{84} (mm)	D_{90} (mm)	Geometric standard deviation (σ_g)	Uniformity coefficient (C_u)	Coefficient of curvature (C_c)
Composition of armour layer (D_{X_A})										
Sample 1, for $D_{50} = 0.50$ mm	0.22	0.28	0.40	0.70	1.10	3.30	3.80	3.43	5.00	0.66
Sample 2, for $D_{50} = 0.47$ mm	0.21	0.26	0.38	0.55	0.62	1.40	2.10	2.32	2.95	1.11
Sample 3, for $D_{50} = 0.58$ mm	0.23	0.28	0.39	1.40	2.10	3.80	4.00	3.68	9.13	0.31
Composition of deposition ridge (D_{X_R})										
Sample 1, for $D_{50} = 0.50$ mm	0.18	0.21	0.27	0.40	0.48	0.75	0.88	1.89	2.67	0.84
Sample 2, for $D_{50} = 0.47$ mm	0.17	0.19	0.24	0.34	0.40	0.63	0.72	1.82	2.35	0.85
Sample 3, for $D_{50} = 0.58$ mm	0.18	0.21	0.30	0.47	0.53	0.90	1.30	2.07	2.94	0.94

Determination of scour depth with influence of armour layer

Considering a bridge pier in a river whose flow is assumed to be steady and uniform, Breusers et al. (1977) pointed out that

following parameters may influence the scouring phenomenon as follows: 1) variables characterizing the fluid such as acceleration due to gravity (g) and density of fluid (ρ_w); 2) variables characterizing the bed material such as sediment density (ρ_s), median grain size of the bed material (D_{50B}) and median grain

size of sediment particles of the armor layer; 3) variables characterizing the flow such as depth of approaching flow (y_0) and the mean velocity of approaching flow (U); 4) variables characterizing the bridge pier and channel geometry such as pier shape and size and channel width. In addition to above-mentioned parameters, in the present study, the effect of ice cover roughness is an important parameter which must be considered. Therefore, conceptually at least, with influence of armour layer in scour hole around bridge pier, the maximum scour depth of scour hole may be evaluated by means of a general formula for computation:

$$y_{\max} = f(U, g, D_{50A}, D_{50B}, n_b, n_i, D, B, y_0, \rho_w, \rho_s) \quad (3)$$

In which, y_{\max} is the maximum depth of scour hole around bridge pier; D_{50A} is the median grain size of armour layer; n_b is the Manning roughness coefficient of channel bed; n_i is Manning roughness coefficient of ice cover; D is the diameter of bridge pier; B is the channel width; ρ_w and ρ_s are the density of water and sediment, respectively, with $\Delta\rho = \rho_s - \rho_w$. Through dimensional analysis by means of Buckingham π theories, the maximum depth of scour hole can be expressed as follows

$$\frac{y_{\max}}{D_{50A}} = f\left(\frac{U}{\sqrt{(\Delta\rho/\rho_w)gD_{50A}}}, \frac{D_{50A}}{D_{50B}}, \frac{n_i}{n_b}, \frac{D_{50A}}{y_0}, \frac{D_{50A}}{B}, \frac{D_{50A}}{D}\right) \quad (4)$$

The term $Fr_0 = \frac{U}{\sqrt{(\Delta\rho/\rho_w)gD_{50A}}}$ is called densimetric

Froude number and is a criterion of hydraulic conditions for assessment of the incipient motion of bed material (Aguirre-Pe et al., 2003). It is a term that describes the incipient motion of the sediment articles. The larger the densimetric Froude number, the larger shear stress is needed to transport the sediment particles. Eq. (4) can be also expressed as follows:

$$\frac{y_{\max}}{D_{50A}} = A(Fr_0)^a \left(\frac{D_{50A}}{D_{50B}}\right)^b \left(\frac{n_i}{n_b}\right)^c \left(\frac{D_{50A}}{y_0}\right)^d \left(\frac{D_{50A}}{B}\right)^e \left(\frac{D_{50A}}{D}\right)^f \quad (5)$$

Since the value of D_{50A}/B is truly tiny, the term D_{50A}/B can be neglected from Eq. (5). Besides, the term (D_{50A}/y_0) can be also ignored from Eq. (5) due to its weak correlation with (y_{\max}/D_{50A}) . Therefore, the following parameters have been used to assess the relative maximum scour depth (MSD) of scour hole (y_{\max}/D_{50A}) around bridge pier.

$$\frac{y_{\max}}{D_{50A}} = A \left(\frac{D_{50A}}{D_{50B}}\right)^a \left(\frac{D_{50A}}{D}\right)^b \left(\frac{n_i}{n_b}\right)^c (Fr_0)^d \quad (6)$$

In the case of open channel flow condition, the ratio of roughness coefficient of ice cover to roughness coefficient of channel bed would be omitted from Eq. (6). Each of the independent dimensionless variables of Eq. (6) were assessed separately to study their impact on the local scour around bridge piers.

a) Variation of relative MSD (y_{\max}/D_{50A}) with densimetric Froude number (Fr_0)

Figure 11 illustrates the variation of relative MSD with densimetric Froude number (Fr_0). With increase in Fr_0 , the relative MSD increases correspondingly. Besides, under the same Fr_0 , the values of the relative MSD under ice-covered conditions are

larger than those under open flow condition. On the other hand, with the same values of relative MSD, the larger value of densimetric Froude number is needed to initiate sediment transportation for the open channel flow condition which means that a lower values of shear stress is needed to initiate motion for sediment transportation under ice-covered flow conditions.

b) Variation of relative MSD (y_{\max}/D_{50A}) with the grain size of armour layer (D_{50A}/D_{50B})

Figure 12a illustrates the variation of relative MSD (y_{\max}/D_{50A}) against ratio of grain size of armour layer (D_{50A}/D_{50B}) distinguished by different pier sizes. Regardless of size of bridge pier, as the grain size of armour layer (D_{50A}/D_{50B}) increases, the relative MSD of scour hole decreases and vice versa. From Figure 12b, one can see that the variation of relative MSD (y_{\max}/D_{50A}) against ratio of (D_{50A}/D_{50B}) distinguished by different covered conditions. Regardless of flow cover, the relative MSD (y_{\max}/D_{50A}) decreases as the grain size of armour layer (D_{50A}/D_{50B}) increases. Under rough covered condition, the relative MSD (y_{\max}/D_{50A}) showed a sharper descending trend with the grain size of armour layer (D_{50A}/D_{50B}) compared to those of under both smooth covered and open flow conditions. Also, under smooth covered flow condition, the relative MSD (y_{\max}/D_{50A}) showed a sharper descending trend with the grain size of armour layer (D_{50A}/D_{50B}) compared to those of under open flow condition. The reason for this is due to strong turbulent flows and different velocity fields close to channel bed which are caused by ice cover, and it get more intensified under rough covered flow condition. Similar results were also reported by Dey and Raikar (2007).

c) Variation of relative MSD (y_{\max}/D_{50A}) with the pier spacing (D_{50A}/D)

Figure 13 illustrates the variation of relative MSD (y_{\max}/D_{50A}) with ratio of the pier spacing (D_{50A}/D) distinguished by different covered conditions. Regardless of flow cover, the relative MSD (y_{\max}/D_{50A}) decreases with increase in ratio of the pier spacing (D_{50A}/D). Under rough covered condition, the relative MSD (y_{\max}/D_{50A}) showed a sharper descending trend with the pier spacing (D_{50A}/D) compared to those of under both smooth covered and open flow conditions. Besides, under the same values of (D_{50A}/D), the rough ice-covered flow has resulted in largest relative MSD.

d) Variation of relative MSD (y_{\max}/D_{50A}) with roughness of ice cover (n_i/n_b)

As pointed out by Mays (1999), due to a relatively smooth concrete-like surface of the Styrofoam panel, the roughness of the model smooth ice-cover was assumed to be 0.013. In terms of model rough ice-cover, Li (2012) reviewed several methods for calculating the Manning's coefficient for ice cover, the following equation can be used depending on the size of the small cubes:

$$\frac{n_i}{k_s^{1/6}} = \frac{(8g)^{-1/2} (R/K_s)^{1/6}}{0.867 \ln(12R/K_s)} \quad (7)$$

In which, K_s is the average roughness height of the ice cover underside and R is the hydraulic radius. By using Eq. (7), a Manning's coefficient of 0.021 was determined as the roughness coefficient of model rough ice cover. This value also agrees with result of Hains et al. (2004). To calculate channel bed roughness coefficient for non-uniform sand bed, the following equation proposed by Hager (1999) was used:

$$n_b = 0.039 D_{50}^{1/6} \tag{8}$$

Therefore, the roughness coefficient of sand bed n_b is determined as 0.0109 for sand bed of $D_{50} = 0.47$ mm, 0.0110 for sand bed of $D_{50} = 0.050$ mm, and 0.0113 for sand bed of $D_{50} = 0.58$ mm, respectively. Results indicate that with increase in n_i/n_b , the relative MSD (y_{max}/D_{50A}) increases correspondingly. Following Equations (9) and (10) are developed to predict the relative MSD (y_{max}/D_{50A}) under ice-covered condition and open flow condition, respectively.

Open flow condition:

$$\frac{y_{max}}{D_{50A}} = 1.433 (Fr_0)^{1.289} \left(\frac{D_{50A}}{D_{50B}}\right)^{-0.190} \left(\frac{D_{50A}}{D}\right)^{-0.488} \quad R^2 = 0.85 \tag{9}$$

Ice-covered flow condition:

$$\frac{y_{max}}{D_{50A}} = 47.190 (Fr_0)^{0.892} \left(\frac{D_{50A}}{D_{50B}}\right)^{-0.652} \left(\frac{D_{50A}}{D}\right)^{-0.367} \left(\frac{n_i}{n_b}\right)^{0.484} \tag{10}$$

$R^2 = 0.88$

According to Equation (9) and Equation (10), the most significant variable is the densimetric Froude number since this variable has the largest power comparing to all other variables. Figure 14 showed the comparison of calculated relative MSD (y_{max}/D_{50A}) to those observed under open flow condition, and Figure 15 show the comparison of calculated relative MSD (y_{max}/D_{50A}) to those observed under ice-covered flow condition. As showed in Figures 14 and 15, the calculated relative MSD (y_{max}/D_{50A}) agreed well with those observed under both open flow condition and ice-covered condition.

To better specify the correlation of different dimensionless variables of Equation (10) with each other and their impact on the relative MSD (y_{max}/D_{50A}), different combination of those dimensionless variables are generated in Table 2. As one can see from Table 2 the densimetric Froude number is the most dominant parameter since its individual R^2 coefficient is 0.784. The next dominant term is ratio of grain size of armour layer (D_{50A}/D_{50B}) with R^2 coefficient of 0.694. With respect to combination of two terms, the combination of (D_{50A}/D_{50B}) and (Fr_0) is the most accurate one with R^2 equal to 0.787. With respect to combination of three terms, the combination of (n_i/n_b); (D_{50A}/D); (Fr_0) is the most accurate with R^2 equal to 0.857.

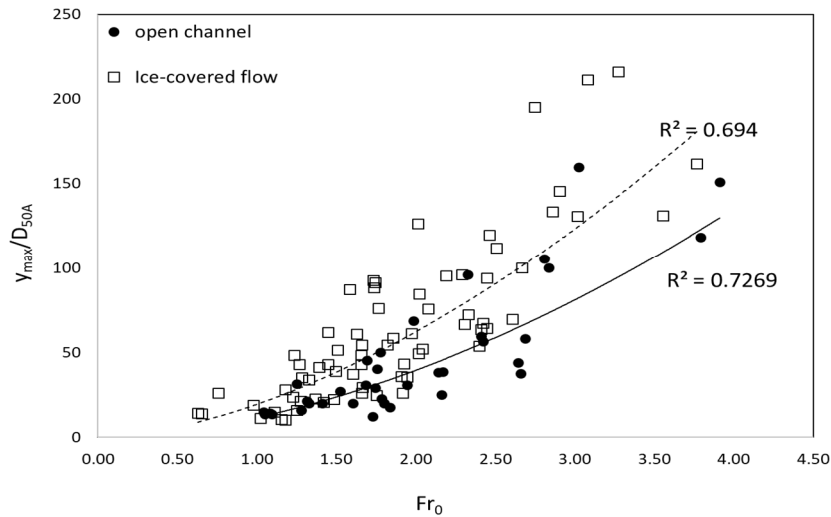


Fig. 11. Relation between the relative MSD (y_{max}/D_{50A}) with densimetric Froude number (Fr_0).

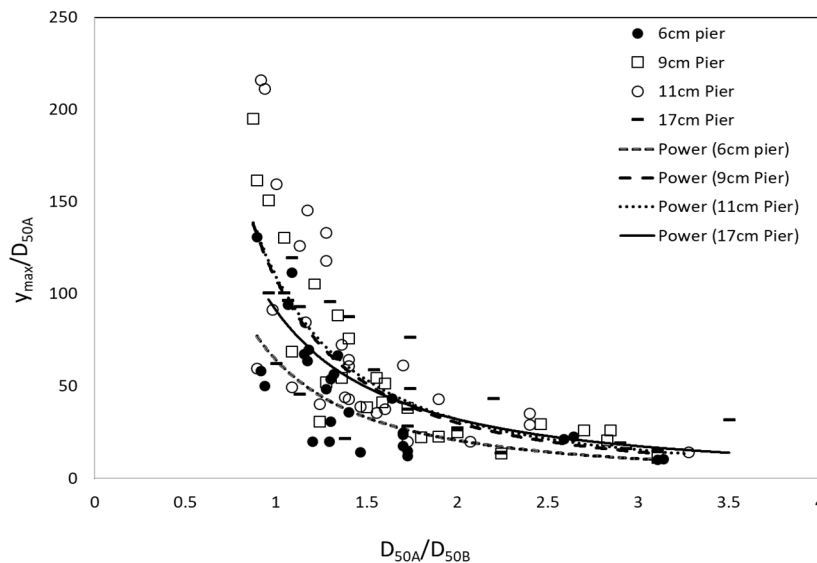


Fig. 12a. Variation of relative MSD (y_{max}/D_{50A}) with (D_{50A}/D_{50B}) distinguished by pier size.

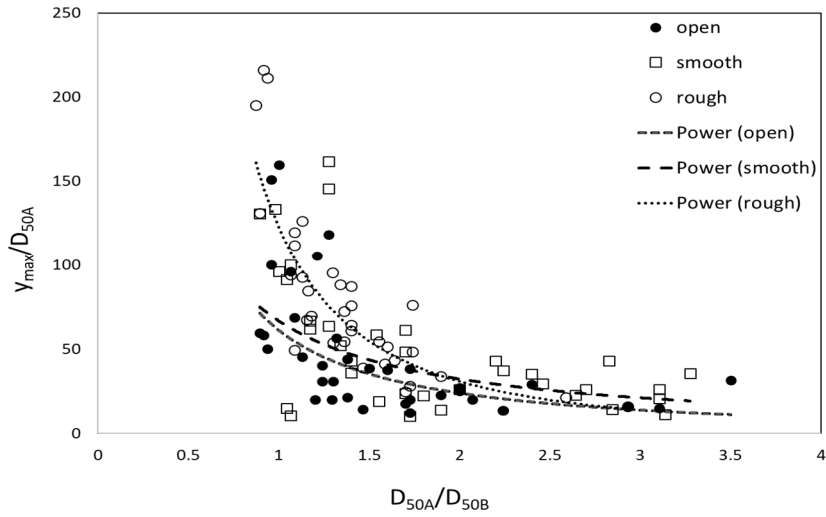


Fig. 12b. Variation of relative MSD (y_{max}/D_{50A}) with (D_{50A}/D_{50B}) distinguished by different covered conditions.

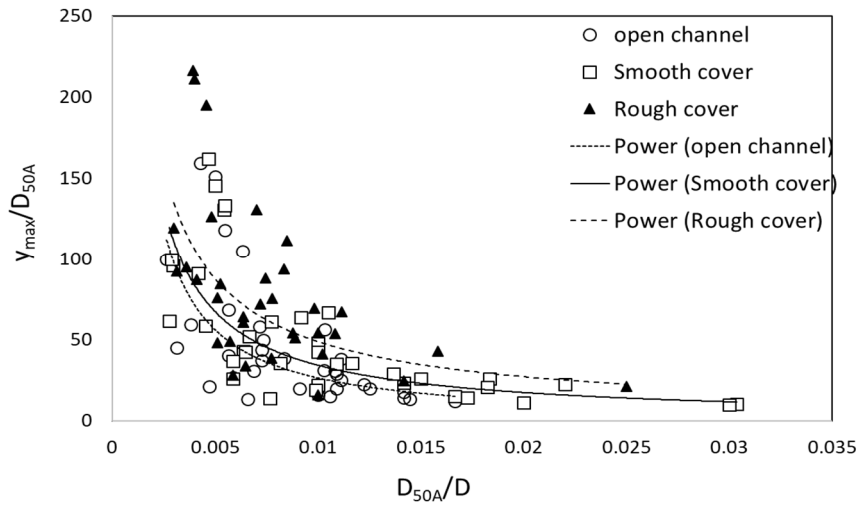


Fig. 13. Variation of relative MSD (y_{max}/D_{50A}) with the ratio of pier spacing (D_{50A}/D) distinguished by different covered conditions.

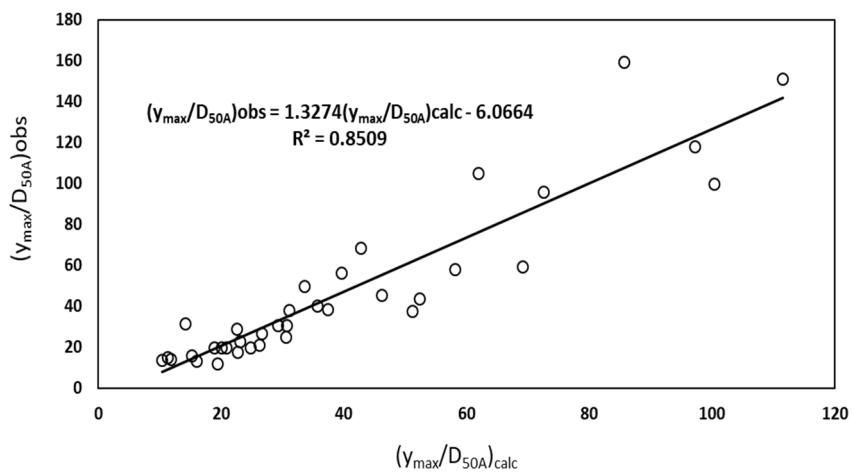


Fig. 14. Comparison of calculated relative MSD (y_{max}/D_{50A}) to those observed under open flow condition.

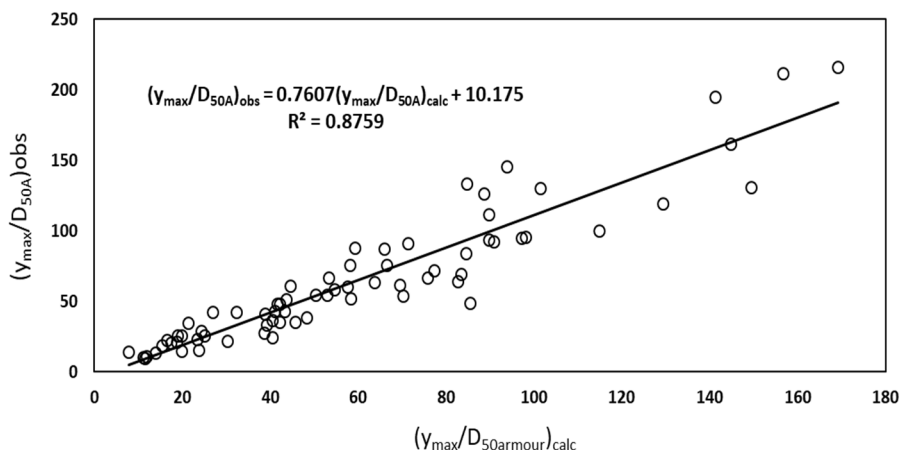


Fig. 15. Comparison of calculated relative MSD (y_{max}/D_{50A}) to those observed under ice-covered flow condition.

Table 2. Different combinations of dimensionless variables.

$y_{max}/D_{50A} = f()$	R^2	Equation
$(D_{50A}/D_{50B}); (n_i/n_b); (D_{50A}/D); (Fr_0)$	0.890	$47.190(D_{50A}/D_{50B})^{-0.652}(n_i/n_b)^{0.484}(D_{50A}/D)^{-0.367}(Fr_0)^{0.892}$
$(n_i/n_b); (D_{50A}/D); (Fr_0)$	0.857	$21.573(n_i/n_b)^{0.613}(D_{50A}/D)^{-0.555}(Fr_0)^{1.13}$
$(D_{50A}/D_{50B}); (D_{50A}/D); (Fr_0)$	0.856	$7.948(D_{50A}/D_{50B})^{-0.772}(D_{50A}/D)^{-0.32}(Fr_0)^{0.889}$
$(D_{50A}/D_{50B}); (n_i/n_b); (Fr_0)$	0.806	$47.215(D_{50A}/D_{50B})^{-1.132}(n_i/n_b)^{0.008}(Fr_0)^{0.859}$
$(D_{50A}/D_{50B}); (Fr_0)$	0.787	$45.658(D_{50A}/D_{50B})^{-1.132}(Fr_0)^{0.859}$
$(D_{50A}/D_{50B}); (n_i/n_b); (D_{50A}/D)$	0.756	$7.948(D_{50A}/D_{50B})^{-1.329}(n_i/n_b)^{0.313}(D_{50A}/D)^{-0.370}$
$(D_{50A}/D_{50B}); (D_{50}/D)$	0.748	$26.245(D_{50A}/D_{50B})^{-1.577}(D_{50}/D)^{-0.252}$
$(D_{50A}/D_{50B}); (n_i/n_b)$	0.742	$841.012(D_{50A}/D_{50B})^{-1.776}(n_i/n_b)^{0.533}$
(Fr_0)	0.784	$19.345(Fr_0)^{1.6851}$
(D_{50A}/D_{50B})	0.694	$110.9(D_{50A}/D_{50B})^{-1.83}$
(D_{50}/D)	0.568	$0.4123(D_{50}/D)^{-0.992}$
(n_i/n_b)	0.137	$5617.1(n_i/n_b)^{1.1492}$

CONCLUSIONS

In present study, to investigate the impact of armour layer and ice cover on scour depth around bridge piers, three non-uniform sediments and four pairs of model piers were used to conduct 108 experiments in a large-scale flume under both open flow condition and ice-covered flow condition. Following conclusions can be drawn from the present study.

1) Although the scour depth under ice-covered flow condition was larger comparing to that under open flow condition, the geometry of the scour holes under open flow condition is similar to that under ice-covered flow condition. Results showed that, regardless of flow cover, the maximum scour depth decreases with increase in the grain size of armour layer. Also, although the maximum depth of scour hole around largest pier was deepest, the grain size distribution of armor layer in scour hole around larger piers did not show a significant difference from those around smaller piers.

2) Under the same flow condition and same covered condition, the maximum scour depth occurs in channel bed with the finest sediment. Due to the horseshoe vortex system, maximum scour depth is located at the upstream face of the piers and extends along the sides of the piers towards the rear side of the pier where wake vortex exists. Due to effect of ice cover, the horseshoe vortex shifts the maximum downflow velocity closer to the pier in the scour hole. Thus, the strength of down-

flow gets more intensified which lead to a larger and wider deposition ridge downstream of the pier.

3) Under the same flow condition, both scour volume and scour area of scour hole in the finest sand bed are largest comparing to those in channel bed with coarser sands. With respect to the impact of ice cover, it was found that both scour volume and scour area of scour hole under rough covered flow condition are largest comparing to those under both smooth covered condition and open flow condition.

4) Based on data collected in laboratory, two formulae have been developed to predict the relative MSD (y_{max}/D_{50A}) under both open flow condition and ice-covered condition. Following dimensionless variables are considered in the proposed formulae for determining the relative MSD (y_{max}/D_{50A}): densimetric Froude number (Fr_0), grain size of armour layer (D_{50A}/D_{50B}), pier spacing (D_{50A}/D), and roughness of ice cover (n_i/n_b). Results showed that the calculated relative MSD (y_{max}/D_{50A}) agreed well with those observed under both open flow condition and ice-covered condition.

5) Results showed with increase in densimetric Froude number (Fr_0), the relative MSD increases correspondingly. Besides, under the same Fr_0 , the values of the relative MSD under ice-covered conditions are larger than those under open flow condition. Results also indicate that, under ice-covered flow condition, a smaller value of densimetric Froude number is needed to initiate movement of sediment comparing to that

under open flow condition which can be justified by the higher flow velocity near channel bed under ice-covered flow conditions and its impact on the threshold of sediment motion.

REFERENCES

- Aguirre-Pe, J., Olivero, M.L., Moncada, A.T., 2003. Particle densimetric Froude number for estimating sediment transport. *Journal Hydraul. Eng.*, 129, 6, 428–437.
- Breusers, H.N.C., Nicollet, G., Shen, H.W., 1977. Local scour around cylindrical piers. *Journal of Hydraulic Research*, 15, 3, 211–252.
- Bunte, K., Abt, S.R., 2001. Sampling surface and subsurface particle-size distributions in wadable gravel-and cobble-bed streams for analyses in sediment transport, hydraulics, and streambed monitoring. Gen. Tech. Rep. RMRS-GTR-74. US Department of Agriculture, Forest Service, Rocky Mountain Research Station, Fort Collins, CO, 428 p. 74.
- Cea, L., Puertas, J., Pena, L., 2007. Velocity measurements on highly turbulent free surface flow using ADV. *Experiments in Fluids*, 42, 3, 333–348.
- Dey, S., Barbhuiya, A.K., 2004. Clear-water scour at abutments in thinly armored beds. *Journal of Hydraulic Engineering*, 130, 7, 622–634.
- Dey, S., Raikar, R., 2007. Clear-water scour at piers in sand beds with an armor layer of gravels. *Journal of Hydraulic Engineering*, 133, 703–711.
- Ettema, R., Braileanu, F., Muste, M., 2000. Method for estimating sediment transport in ice-covered channels. *Journal of Cold Regions Engineering*, 14, 3, 130–144.
- Ettema, R., Kempema, E.W., 2012. River ice effects on gravel bed channels. In: Church, M., Biron, P.M., Roy, A.G. (Eds.): *Gravel-Bed Rivers: Processes, Tools, Environments*. Wiley, pp. 523–540.
- Froehlich, D.C., 1995. Armor limited clear water construction scour at bridge. *Journal of Hydraulic Engineering, ASCE* 121, 490–493.
- Guo, J., 2012. Pier scour in clear water for sediment mixtures. *Journal of Hydraulic Research*, 50, 1, 18–27.
- Hager, W., 1999. *Wastewater Hydraulics: Theory and Practice*. Springer, Berlin, New York.
- Hains, D.B., Zabilansky, L.J., (2004). Laboratory test of scour under ice: Data and preliminary results. U.S. Army Engineer Research and Development Center, Cold Regions Research and Engineering Laboratory, Hanover, New Hampshire, Technical Report TR-04-9 (http://www.crrel.usace.army.mil/techpub/CRREL_Reports/reports/TR04-9.pdf).
- Hains, D., Zabilansky, L.J., Weisman, R.N., 2004. An experimental study of ice effects on scour at bridge piers. In: *Cold Regions Engineering and Construction Conference and Expo*, Edmonton, Alberta, 16–19 May 2004.
- Khwairakpam, P., Ray, S.S., Das, S., Das, R., Mazumdar, A., 2012. Scour hole characteristics around a vertical pier under clear water scour conditions. *ARPJ J. Eng. Appl. Sci.*, 7, 6, 649–654.
- Kothyari, U.C., Garde, R.C.J., Ranga Raju, K.G., 1992. Temporal variation of scour around circular bridge piers. *Journal of Hydraulic Engineering*, 118, 8, 1091–1106.
- Li, S.S., 2012. Estimates of the Manning's coefficient for ice-covered rivers. In: *Proceedings of the Institution of Civil Engineers-Water Management*, Vol. 165, No. 9, pp. 495–505. Thomas Telford Ltd.
- Mao, L., Cooper, J., Frostick, L., 2011. Grain size and topographical differences between static and mobile armour layers. *Earth Surface Processes and Landforms*, 36, 10, 1321–1334.
- Mays, L.W. (Ed.), 1999. *Hydraulic Design Handbook*. McGraw-Hill Professional Publishing, New York.
- Melville, B.W., Raudkivi, A.J., 1977. Flow characteristics in local scour at bridge piers. *Journal of Hydraulic Research*, 15, 4, 373–380.
- Melville, B.W., Sutherland, A.J., 1988. Design method for local scour at bridge piers. *Journal of Hydraulic Engineering*, 114, 10, 1210–1226.
- Melville, B.W., Coleman, S.E., 2000. *Bridge Scour*. Water Resources Publications.
- Muzzammil, M., Gangadhariah, T., 2003. The mean characteristics of horseshoe vortex at a cylindrical pier. *Journal of Hydraulic Research*, 41, 3, 285–297.
- Raudkivi, A.J., Ettema, R., 1983. Clear-water scour at cylindrical piers. *Journal of Hydraulic Engineering*, 109, 3, 338–350.
- Raudkivi, A.J., Ettema, R., 1985. Scour at cylindrical bridge piers in armored beds. *J. Hydraul. Eng.*, 111, 4, 713–731.
- Richardson, E.V., Harrison, L.J., Richardson, J.R., Davis, S.R., 1993. *Evaluating Scour at Bridges*. Report No. HEC 18. 2nd edition. Federal Highway Administration, Washington, DC.
- Sui, J., Wang, D., Karney, B., 2000. Sediment concentration and deformation of riverbed in a frazil jammed river reach. *Canadian Journal of Civil Engineering*, 27, 6, 1120–1129.
- Sui, J., Wang, J., Yun, H.E., Krol, F., 2010. Velocity profiles and incipient motion of frazil particles under ice cover. *International Journal of Sediment Research*, 25, 1, 39–51.
- Török, G.T., Baranya, S., Rütther, N., Spiller, S., 2014. Laboratory analysis of armor layer development in a local scour around a groin. In: *Proceedings of the International Conference on Fluvial Hydraulics River Flow*. EPFL, Lausanne, Switzerland, pp. 3–5.
- Wang, J., Shi, F., Chen, P., Wu, P., Sui, J., 2015. Impacts of bridge abutments on the critical condition for initiation of ice cover – an experimental study. *Journal of Hydrology and Hydromechanics*, 63, 4, 327–333.
- Wang, J., Hua, J., Sui, J., Wu, P., Liu, L., Chen, P., 2016. The impacts of bridge pier on ice jam evolution – an experimental study. *Journal of Hydrology and Hydromechanics*, 64, 1, 75–82.
- Wu, P., Hirshfield, F., Sui, J., Wang, J., Chen, P.P., 2014. Impacts of ice cover on local scour around semi-circular bridge abutment. *Journal of Hydrodynamics*, 26, 1, 10–18.
- Wu, P., Hirshfield, F., Sui, J., 2015. Armour layer analysis of local scour around bridge abutments under ice cover. *River Research and Applications*, 31, 6, 736–746.
- Zabilansky, L.J., Hains, D.B., Remus, J.I., 2006. Increased bed erosion due to ice. In: *Current Practices in Cold Regions Engineering*, pp. 1–12.
- Zhang, H., Nakagawa, H., Mizutani, H., 2012. Bed morphology and grain size characteristics around a spur dyke. *International Journal of Sediment Research*, 27, 2, 141–157.

Received 16 April 2018

Accepted 23 July 2018

Mathematical modeling of shallow-water flows on steep slopes

Yufang Ni^{1*}, Zhixian Cao¹, Qingquan Liu²

¹ State Key Laboratory of Water Resources and Hydropower Engineering Science, Wuhan University, Wuhan 430072, China.

² Department of Mechanics, Beijing Institute of Technology, Beijing 100081, China.

* Corresponding author. Tel.: +86 131-6329-2052. E-mail: yufangni@whu.edu.cn

Abstract: A 2D hydrodynamic (labeled as CAR) model has been proposed in a rectangular Cartesian coordinate system with two axes within the horizontal plane and one axis along the vertical direction (global coordinates), considering the effects of bed slope on both pressure distribution and bed shear stresses. The CAR model satisfactorily reproduces the analytical solutions of dam-break flow over a steep slope, while the traditional Saint-Venant Equations (labeled as SVE) significantly overestimate the flow velocity. For flood events with long duration and large mean slope, the CAR and the SVE models present distinguishable discrepancies. Therefore, the proposed CAR model is recommended for applications to real floods for its facility of extending from 1D to 2D version and ability to model shallow-water flows on steep slopes.

Keywords: 2D shallow-water equations; Steep slopes; Dam-break flows; Rectangular Cartesian coordinate system; Global coordinates.

INTRODUCTION

Shallow-water hydrodynamic models and their extensions involving sediment transport have been widely used in hydraulic engineering and geomorphological studies over the past few decades (Cao et al., 2017; Huang et al., 2014; Li et al., 2017, 2018a, 2018b; Qian et al., 2015). The prototype is the traditional Saint-Venant equations (Barré de Saint-Venant, 1871), which can be obtained by assuming a vertical hydrostatic pressure distribution and integrating three-dimensional Reynolds-averaged Navier-Stokes equations over the flow depth (Toro, 2001; Wu, 2007). Yet the assumption of small slope is invalid for cases with realistic steep terrain (Denlinger and O'Connell, 2008; Juez et al., 2017).

The governing equations of granular flows described by the continuum theory bear a superficial resemblance to the shallow-water equations (Mangeney-Castelnaud et al., 2005). Since the granular flows often take place on steep slopes, it is inevitable to incorporate the steep slope effects in the mathematical models. Savage and Hutter (1989) introduced the presence of steep slope by adopting local coordinates with one axis along the bed and the other axis perpendicular to the bed. Then Savage and Hutter (1991) derived 1D governing equations in a curvilinear coordinate system (local coordinates) aligned with the curved bed, which were later extended by Greve et al. (1994) to study 3D granular flows along a bottom profile that was weakly curved downward and plane laterally. Gray et al. (1999) modeled the realistic complex basal topography by defining an orthogonal curvilinear reference surface and then superposing shallow basal topography on it. Since the topographic data for natural spaces is mainly based on digital elevation models (DEMs), which are referenced to global coordinates, the aforementioned models have to map the original data to local coordinates. In this connection, Denlinger and Iverson (2004) developed a nonhydrostatic model in global coordinates, accounting for the effects of nonzero vertical accelerations. Juez et al. (2013) simulated granular flows using both global and local coordinates, assuming hydrostatic pressure distribution normal to the bed. Castro-Orgaz et al. (2015) further modified the nonhydrostatic model, including the effects of vertical motion

without the ad hoc assumptions adopted by Denlinger and Iverson (2004).

As for shallow-water flows, Bouchut et al. (2003) and Keller (2003) introduced a new 1D shallow-water model in a curvilinear coordinate system aligned with the bottom topography, which relaxed the restriction of small slopes of the Saint-Venant equations and was valid for arbitrary slopes. Ancey et al. (2008), Cao et al. (2015) and Fernandez-Feria (2006) applied the modified version of the Saint-Venant equations in local coordinates to model shallow water flows on uniform slopes. As establishing models in global coordinates can simplify the mathematical expressions of governing equations and the process of data handling, Denlinger and O'Connell (2008) followed the nonhydrostatic model proposed by Denlinger and Iverson (2004), which was then further developed by Cantero-Chinchilla et al. (2017) and Castro-Orgaz and Hager (2017). On the other hand, Juez et al. (2017), Van Emelen (2014) and Van Emelen et al. (2014) built hydrodynamic models in global coordinates following Juez et al. (2013). Van Emelen (2014) and Van Emelen et al. (2014) concluded that for rapid flows such as dam-break flows, no difference appears between traditional and modified models; however, differences are detectable for uniform flows on slope with bed angles higher than 10°. Juez et al. (2017) investigated the influence of gravity effects on bed load transport over steep slopes.

In the present work, a shallow-water hydrodynamic model is established in global coordinates, based on the assumption of hydrostatic pressure distribution normal to the bed. In addition, the bed slope is incorporated in the calculation of bed shear stresses. This paper aims to shed new insights on the bed slope effects by comparing the performance of the traditional Saint-Venant equations and the proposed model in applications to four dam-break flood events.

MATHEMATICAL MODEL

Governing equations

The effects of bed slope on both pressure distribution and bed shear stresses are considered in the governing equations here, which is different from the traditional Saint-Venant equa-

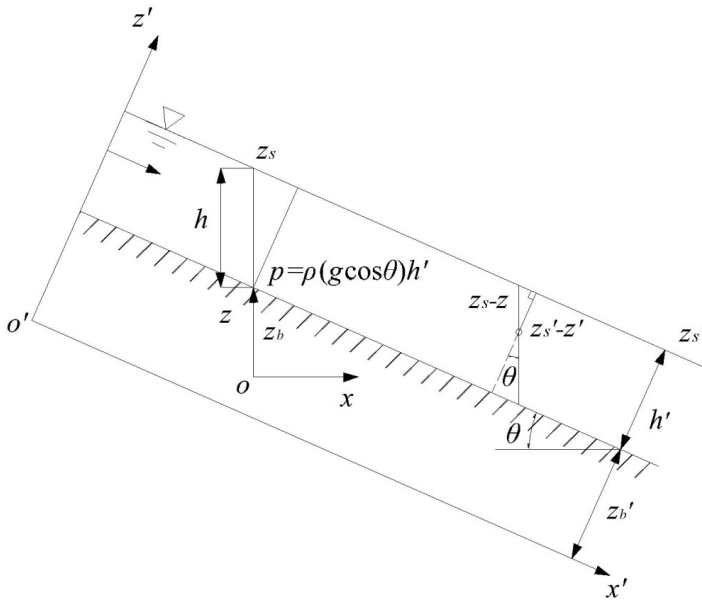


Fig. 1. Sketch for local and global coordinates.

tions valid for small slopes. Figure 1 illustrates the comparison of local and global coordinates. In local coordinates ($x'o'z'$), the pressure distribution normal to the bed is

$$p = \rho g \cos \theta \cdot (z_s' - z') \quad (1)$$

where ρ is the density of water; g is gravitational acceleration; θ is the slope angle of the bed; z_s' is the free surface in local coordinates. According to geometric relation, the vertical pressure distribution in global coordinates (xoz) is

$$p = \rho g \cdot \cos^2 \theta \cdot (z_s - z) \quad (2)$$

Note that in the traditional Saint-Venant equations (with the assumption of small slopes so there is $\cos \theta \approx 1$), the vertical pressure distribution in global coordinates (xoz) is

$$p = \rho g \cdot (z_s - z) \quad (3)$$

Substitutions of Equations (1)–(3) into time-averaged 3D momentum equations of incompressible flow in corresponding Cartesian coordinate systems, together with integrations along flow depth, yield three sets of depth-averaged equations, respectively (Wu, 2007).

The 1D governing equations derived with Equation (1) in local coordinates are given as follows

$$\text{SWE: } \begin{cases} \frac{\partial h'}{\partial t} + \frac{\partial(h'u')}{\partial x'} = 0 \\ \frac{\partial(h'u')}{\partial t} + \frac{\partial}{\partial x'}(h'u'^2 + \frac{1}{2} g \cos \theta \cdot h'^2) = \\ gh' \sin \theta - g \cos \theta \cdot h' \frac{\partial z_b'}{\partial x'} - \frac{1}{\rho} \tau_b' \end{cases} \quad (4)$$

where t is time; x' is the downstream coordinate; h' is the flow depth perpendicular to the bed; u' is the depth-averaged stream-wise flow velocity; z_b' is the bed elevation in local coordinates; τ_b' is the bed shear stress. This model is referred to as SWE (modified shallow water equations) in this paper. Since its 2D version is complex, only 1D version is presented here.

As for Equations (2) and (3), the corresponding governing equations are built in global coordinates and therefore the 2D versions can be readily derived

$$\frac{\partial h}{\partial t} + \frac{\partial(hu)}{\partial x} + \frac{\partial(hv)}{\partial y} = 0 \quad (5a)$$

$$\frac{\partial(hu)}{\partial t} + \frac{\partial(hu^2)}{\partial x} + \frac{\partial(huv)}{\partial y} = -\frac{\partial}{\partial x}(\frac{1}{2} g' h^2) - g' h \frac{\partial z_b}{\partial x} - \frac{1}{\rho} \tau_{bx} \quad (5b)$$

$$\frac{\partial(hv)}{\partial t} + \frac{\partial(huv)}{\partial x} + \frac{\partial(hv^2)}{\partial y} = -\frac{\partial}{\partial y}(\frac{1}{2} g' h^2) - g' h \frac{\partial z_b}{\partial y} - \frac{1}{\rho} \tau_{by} \quad (5c)$$

where x and y are the horizontal Cartesian coordinates; h is the vertical flow depth; u and v are the depth-averaged velocity components in the x - and y -directions; z_b is the vertical bed elevation; τ_{bx} and τ_{by} are the bed shear stresses in the x - and y -directions, respectively. According to Equation (2), there is

$$g' = \begin{cases} g \cdot \cos^2 \theta & \text{if } \sqrt{u^2 + v^2} > 0 \\ 0 & \text{else} \end{cases} \quad (6)$$

The model with Equations (5) and (6) is referred to as the CAR (the first three letters of ‘‘Cartesian’’) model in this paper. On the other hand, the traditional Saint-Venant equations with $g' = g$ are labeled as the SVE (Saint-Venant Equations) model.

Model closure

To close the governing equations above, the Manning formula is employed here to evaluate the bed shear stresses

$$\tau_{bx} = \rho \frac{n^2 \cdot g}{(h \cos \theta)^{1/3}} \cdot \frac{u \sqrt{u^2 + v^2}}{\cos \theta} \quad (7a)$$

$$\tau_{by} = \rho \frac{n^2 \cdot g}{(h \cos \theta)^{1/3}} \cdot \frac{v \sqrt{u^2 + v^2}}{\cos \theta} \quad (7b)$$

where n is the Manning roughness coefficient. As mentioned above, there is $\cos \theta \approx 1$ in the SVE model. For the SWE model, the angle-related terms would not be included in Equation (7) due to the consistency between the axis and the flow direction.

The cosine value of the bed angle of the computational grid (i, j) in the CAR model is given by

$$\cos \theta(i, j) = 1 / \sqrt{1 + (\frac{z_{bi+1,j} - z_{bi-1,j}}{2 \cdot \Delta x})^2 + (\frac{z_{bi,j+1} - z_{bi,j-1}}{2 \cdot \Delta y})^2} \quad (8)$$

where Δx and Δy are the spatial steps; the subscripts i and j denote the spatial node indexes in the x - and y -directions, respectively.

Numerical algorithm

Equation (5) constitutes a hyperbolic system which can be written in a quasi-linear form as

$$\frac{\partial \mathbf{U}}{\partial t} + \frac{\partial \mathbf{F}}{\partial x} + \frac{\partial \mathbf{G}}{\partial y} = \mathbf{S} \quad (9)$$

$$\mathbf{U} = \begin{bmatrix} h \\ hu \\ hv \end{bmatrix} \quad (10a)$$

$$\mathbf{F} = \begin{bmatrix} hu \\ hu^2 + 0.5g'h^2 \\ huv \end{bmatrix} \quad (10b)$$

$$\mathbf{G} = \begin{bmatrix} hv \\ huv \\ hv^2 + 0.5g'h^2 \end{bmatrix} \quad (10c)$$

$$\mathbf{S} = \mathbf{S}_b + \mathbf{S}_f = \begin{bmatrix} 0 \\ -g'h \frac{\partial z_b}{\partial x} \\ -g'h \frac{\partial z_b}{\partial y} \end{bmatrix} + \begin{bmatrix} 0 \\ -\frac{1}{\rho} \tau_{bx} \\ -\frac{1}{\rho} \tau_{by} \end{bmatrix} \quad (10d)$$

where \mathbf{U} is the vector of conserved variables; \mathbf{F} and \mathbf{U} are the convective flux vectors of the flow in the x - and y - directions, respectively; \mathbf{S}_b is the source term related to the pressure force at the bed; \mathbf{S}_f is the source term involving bed shear stresses. Under the framework of finite volume method, an explicit discretization of Equation (9) gives (Hou et al., 2013a, 2013b; Huang et al., 2015)

$$\mathbf{U}_{i,j}^* = \mathbf{U}_{i,j}^n + \Delta t \cdot \mathbf{S}_{f,i,j}^{n+1} \quad (11)$$

$$\mathbf{U}_{i,j}^{n+1} = \mathbf{U}_{i,j}^* - \Delta t \cdot \left[\frac{(\mathbf{F}_{i+1/2,j}^* - \mathbf{F}_{i-1/2,j}^*)}{\Delta x} + \frac{(\mathbf{G}_{i,j+1/2}^* - \mathbf{G}_{i,j-1/2}^*)}{\Delta y} \right] + \Delta t \cdot \mathbf{S}_{bi,j}^* \quad (12)$$

where the superscript n denotes the time step index; Δt is the time step; $\mathbf{F}_{i+1/2,j}^*$, $\mathbf{F}_{i-1/2,j}^*$, $\mathbf{G}_{i,j+1/2}^*$, and $\mathbf{G}_{i,j-1/2}^*$ represent the inter-cell fluxes.

The friction source term in Equation (11) is evaluated by the splitting point-implicit method (Bussing and Murmant, 1988; Huang et al., 2015). The Monotone Upstream-centered Schemes for Conservation Laws (MUSCL) method is used in data reconstruction to achieve second-order accuracy in space and a second-order Runge-Kutta method is employed to solve Equation (12) to obtain second-order accuracy in time (Hou et al., 2013b; Liang and Marche, 2009). A robust approach designed by Hou et al. (2013a) is utilized, preserving non-negative water depth in data reconstruction and transforming the slope source term into fluxes so that the whole scheme satisfies the C-property and can deal with the wet-dry interfaces properly. Given that neighboring grids might possess different

values of g' , a centered method, i.e., the FORCE scheme, is utilized to calculate the inter-cell fluxes (Toro, 2009). The corresponding numerical stability is controlled by a decreasing function of the dimension parameter α (Qian et al., 2017; Toro, 2009)

$$\Delta t = Cr \cdot \max\left(\frac{|u_{i,j}| + \sqrt{gh_{i,j}}}{\Delta x}, \frac{|v_{i,j}| + \sqrt{gh_{i,j}}}{\Delta y}\right)^{-1} \quad (13)$$

$$0 < Cr \leq \sqrt{2\alpha - 1} / \alpha \quad (14)$$

where Cr represents the Courant number. For present 2D modeling, there is $\alpha = 2$. A value of $Cr = 0.5$ is adopted throughout the paper.

RESULTS AND DISCUSSION

Four flood events are employed to compare the aforementioned models. To quantify the differences between solutions, the dimensionless discrepancy is defined with the L^1 -norm

$$L^1 = \frac{\sum |h_{OBJ} - h_{REF}|}{\sum h_{REF}} \quad (15)$$

where the subscript REF denotes results chosen as the reference; and the subscript OBJ denotes results to be compared.

Idealized dam-break flow on a steep slope

Fernandez-Feria (2006) provided analytical solutions for frictionless dam-break flows upon non-horizontal beds. Here the methodology introduced in Fernandez-Feria (2006) has been adopted to derive analytical solutions for case with a bed inclining angle of 30° . Following Fernandez-Feria (2006), the results are given in local coordinates and are expressed in terms of dimensionless variables, with the initial water depth H_0 at the dam wall and $\sqrt{gH_0}$ as the length scale and the velocity scale, respectively. The dimensionless spatial step is set to $\Delta x = 0.01$, satisfying the criteria of mesh independence.

Figure 2 shows the analytical and the numerical solutions for the advancing flow fronts with time. Apparently, the results calculated by the traditional SVE model deviate greatly from the analytical solutions while those computed by the other two models match rather well with the analytical solutions. Figure 3 illustrates the flow depth and the velocity profiles at four instants of time. The SWE and the CAR predictions agree well with the analytical solutions. However, the SVE model overestimates the flow velocity, demonstrating that the SVE model *does not* apply to cases with steep slopes.

Experimental dam-break flow in cascade reservoirs with steep slope

The experiment was carried out at State Key Laboratory of Hydraulic and Mountain River Engineering of Sichuan University (Xue et al., 2011). As shown in Figure 4, ten probes were placed along the bottom to record the flow depth. Two flat plates were vertically set as dams in the flume. Once the force acting on the plate exceeded the ultimate bearing capacity equaling to the hydrostatic pressure in the water depth of 0.53 m., the plate would fall down in less than 0.35 s, simulating an instantly filled dam break. Initial water depths of reservoirs were

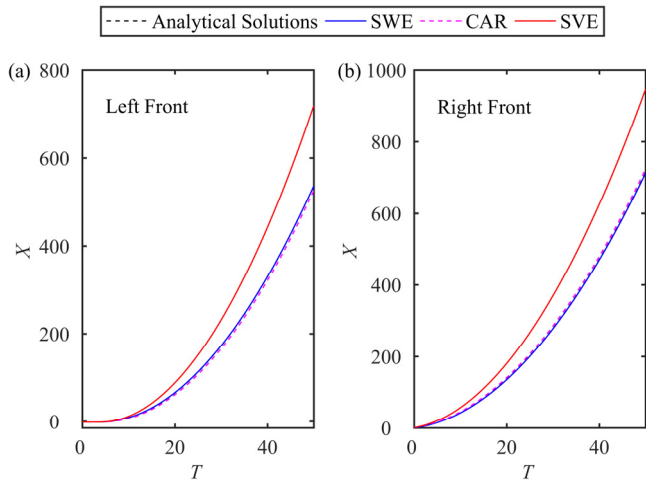


Fig. 2. Analytical and numerical solutions of the locations of the advancing flow fronts with time: (a) left front; (b) right front.

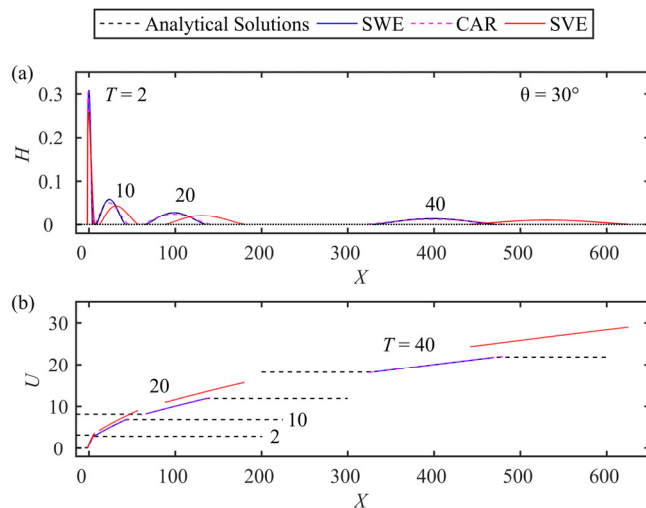


Fig. 3. Analytical and numerical solutions of the flow at four instants of time: (a) depth profiles; and (b) velocity profiles. The black dash lines in (b) are plotted outside the flow region to delineate more clearly the analytical solutions obtained for the velocity of the flow fronts.

0.494 m and 0.496 m for the upstream and the downstream dams, respectively. In line with the mesh independence analysis, a mesh of $\Delta x = 0.005$ m is adopted here.

Table 1. Calibrated values of Manning roughness for two models.

Model	Manning Roughness n	Dam-break time (s)
SVE	0.0170	2.38
	0.0177	2.40
	0.0180	2.41
CAR	0.0150	2.38
	0.0155	2.40
	0.0160	2.41

According to Xue et al. (2011), the downstream dam broke due to the overloading, 2.4 s after the collapse of the upstream dam. This is used to calibrate the Manning roughness for the SVE and the CAR models, with the aforementioned capacity being the criterion of dam break. The calibration results are listed in Table 1, with values of 0.0177 and 0.0155 for the SVE and the CAR models respectively. This is in accordance with the fact that the traditional SVE model neglects the effects of bed slope so that a larger value of Manning roughness is demanded to prevent the flood from propagating too fast, as compared to the CAR model.

Figure 5 shows the computed depth hydrographs by the CAR and the SVE models at ten gauging points as compared against the measured data (Xue et al., 2011). Although different values of Manning roughness have been adopted in the two models, the results are qualitatively and quantitatively similar, both reproducing the measured data satisfactorily. Given the short duration of about 6 s, the difference between the two models is minor and can only be manifested by the calibrated Manning roughness even though the bottom slope is 12° .

Presumed glacier-lake outburst flooding

A sudden outburst of a glacier-lake in Pengqu Basin, Tibet, China has been presumed for numerical studies in several previous works (Cao et al., 2007; Wang et al., 2010; Yue et al., 2008). The topography provided in DEM is shown in Figure 6a, with the initial condition the same as that in Wang et al. (2010). The Manning roughness of the whole domain is set to $n = 0.05$. The hydrographs of flow depth of four points have been recorded, located at P1 (15561 m, 5928 m), P2 (13053 m, 6954 m), P3 (10659 m, 8550 m), and P4 (5472 m, 18240 m).

Figure 6 illustrates the evolution of the free surface of the GLOF simulated by the CAR model, which is qualitatively similar to that of Wang et al. (2010). Figure 7 shows the depth hydrographs of four selected points. Note that P1 and P2 are located within the glacial-lake. The fictitious vibration of flow depth in Figure 7b dictates that the model employed by Wang et

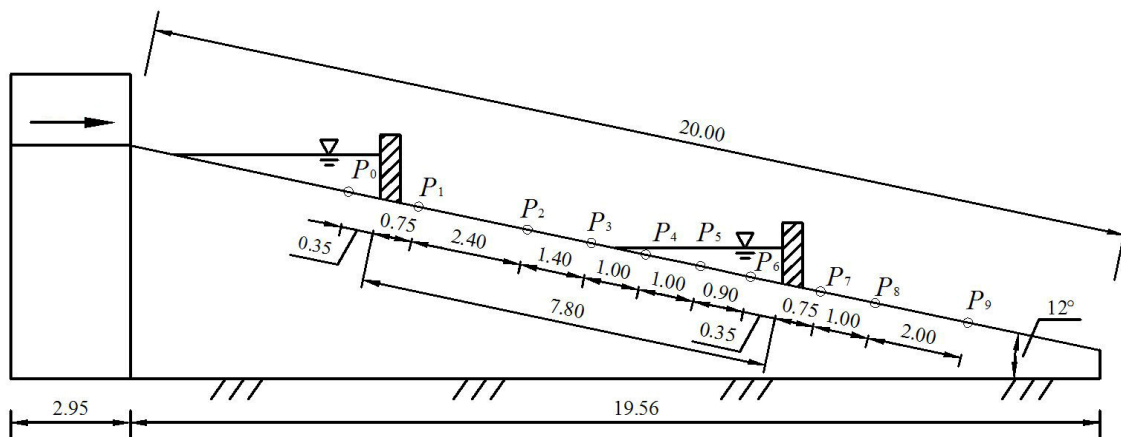


Fig. 4. Sketch of the flume and the layout of gauging points (unit: m).

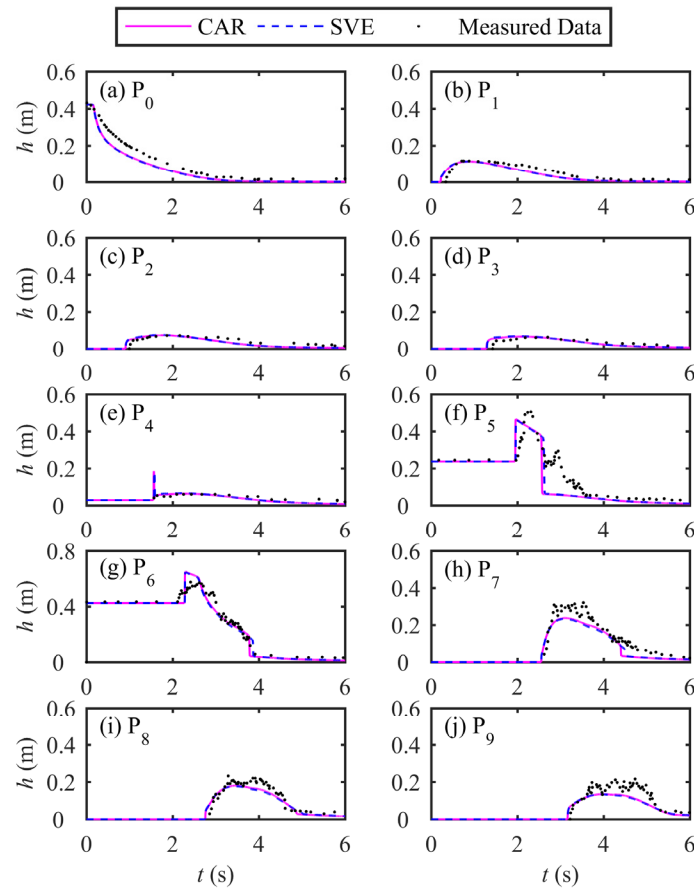


Fig. 5. Computed depth hydrographs compared against measured data.

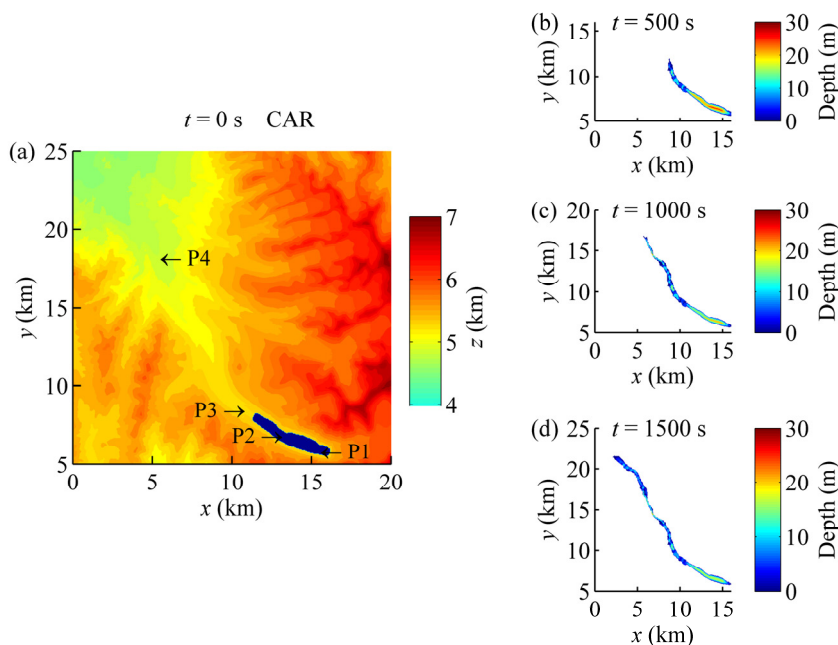


Fig. 6. Top view: (a) the study area and the initial state of the glacier-lake; and (b)–(d) distributions of flow depth.

al. (2010) was not well-balanced. On the contrary, the results given by the CAR and the SVE models feature a period of static state for both P1 and P2, demonstrating the enhanced performance of the numerical models used in the present work. On the other hand, the curves given by the two models are almost indistinguishable in Figure 7. Table 2 presents the quantitative differences between those two results and both the L^1 -norm and the

relative error of arriving time at Point P4 are larger than those at Point P3, in line with the fact that P4 is downstream of P3.

Although the simulation has been carried out for 25 min, the discrimination between the two models remains minor. This is because the average slope of the main channel is 8.3% (Wang et al., 2010), still within the range of small slope. Hence, the SVE model holds its validity in application to cases with small slopes.

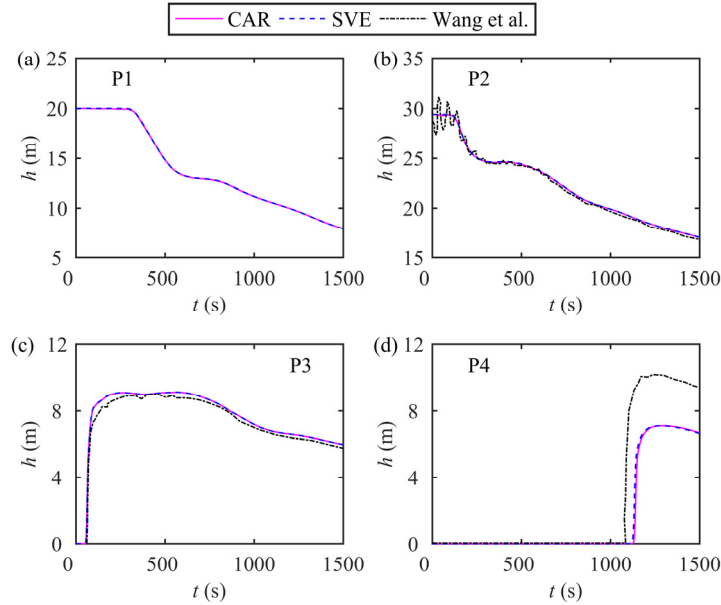


Fig. 7. Hydrographs of flow depth at P1–P4.

Table 2. Comparison of the results calculated by two models at Points P3 and P4.

Point	Model	L^1 (%)	Arriving time (s)	Relative error (%)
P3	SVE	/	44.71	/
	CAR	0.08	44.78	0.15
P4	SVE	/	1100.58	/
	CAR	2.31	1108.09	0.68

Hypothetical dam-break flood induced by the sudden release of a barrier lake

Since the SVE and the CAR models exhibit minor difference in flood events with short duration or small bed slope, a relatively large-scaled catchment is designated here, covering an area of $10 \text{ km} \times 8 \text{ km}$. A barrier lake with a volume of more than 160000 m^3 , is presumed to collapse completely. The maximum water depth before the dam is 20 m. The average channel slope along the thalweg is approximately 21.9%, with the piecewise linear expression given below

$$e = \begin{cases} 0.00 & \text{if } x \leq 0 \text{ km} \\ 0.60 & \text{if } x \leq 0.4 \text{ km} \\ 0.54 & \text{if } x \leq 0.9 \text{ km} \\ 0.36 & \text{if } x \leq 1.9 \text{ km} \\ 0.24 & \text{if } x \leq 4.9 \text{ km} \\ 0.12 & \text{if } x > 4.9 \text{ km} \end{cases} \quad (16)$$

The lateral cross sections are designed to be parabolic and symmetric for simplicity, with eight points P1–P8 selected along the thalweg, which are located at 0.2 km, 1.4 km, 2.6 km, 3.8 km, 5.0 km, 6.2 km, 7.4 km, and 8.6 km downstream of the dam (Figure 8). The Manning roughness is supposed to be $n = 0.025$ throughout the whole region. The spatial steps are $\Delta x = \Delta y = 20 \text{ m}$.

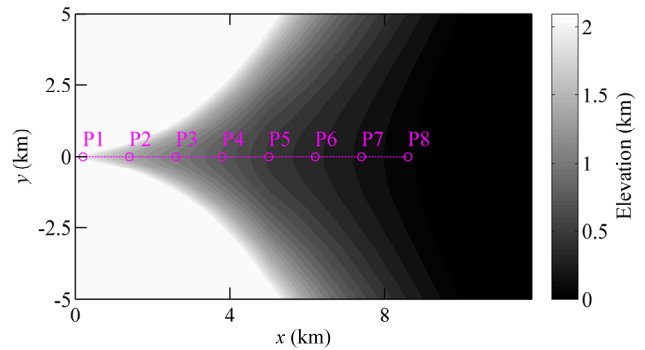


Fig. 8. Top view of the study area.

Figure 9 illustrates the distributions of flow depth at four instants of time. The flood computed by the CAR model propagates slower than that simulated by the SVE model. Correspondingly, the flow depth from the CAR modeling is deeper than that predicted by the SVE model at the same location.

A set of increased Manning roughness has been chosen for the SVE model to test if an increased drag force, which can slow down the propagation of flood, would make up for the neglect of bed slope effects in the SVE model. The arriving times computed by the SVE model with $n = 0.025$ are set as references, and those calculated by the SVE models with tuned Manning roughness and the CAR model minus the references are the lag times. Figure 10 illustrates that an increased roughness coefficient adopted by the SVE model does slow down the propagation of flood, but the corresponding upward concave curves deviate remarkably from that of the CAR model, which features a downward concavity. Essentially, the influence of an increased drag force accumulates downstream while the discrepancy of the CAR and the SVE model is in line with the bed slope. Since an increased drag force cannot compromise the neglect of bed slope effects in the SVE model, the CAR model is recommended for flood events, especially those featuring both long durations and steep bed slopes.

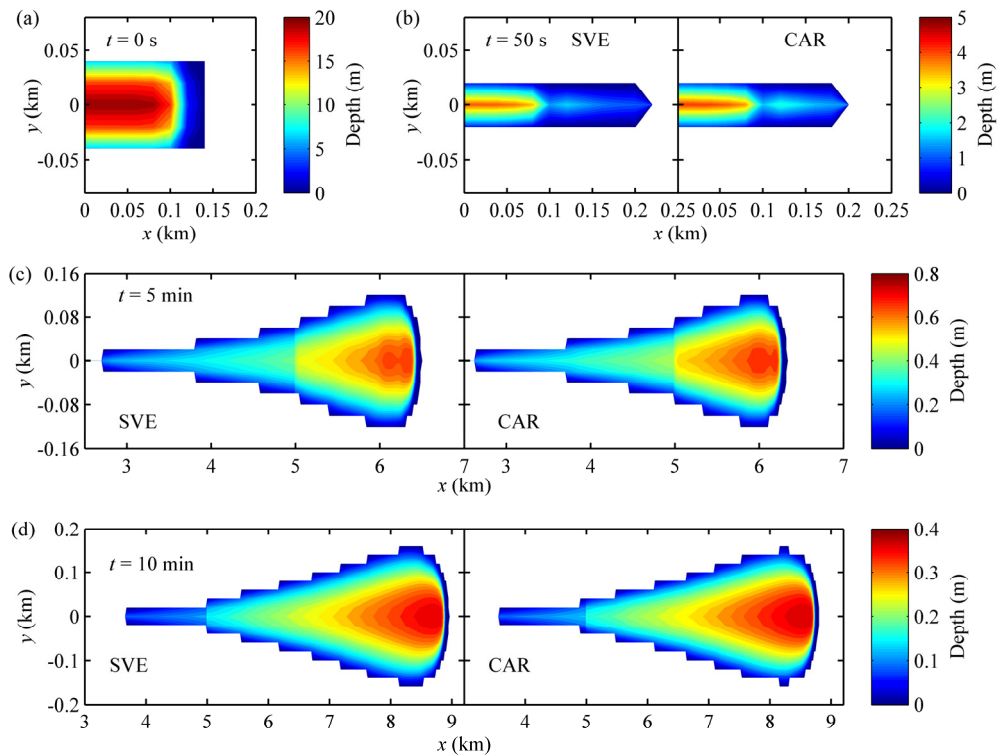


Fig. 9. Distributions of flow depth at four instants of time.

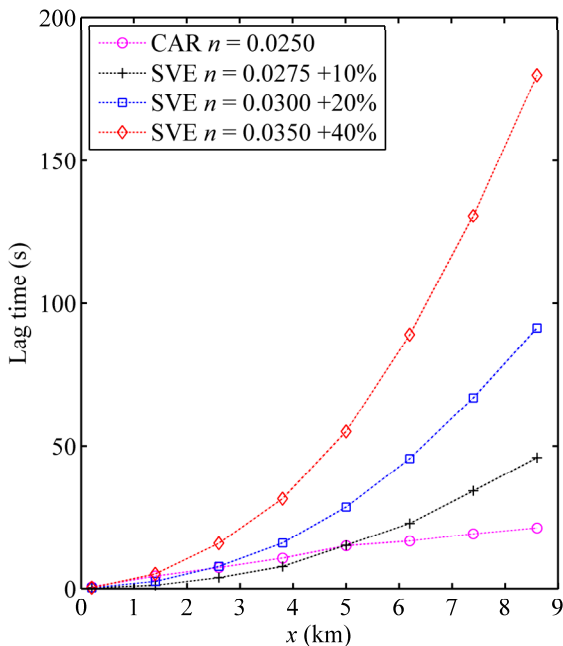


Fig. 10. Lag times of flood arriving at eight points predicted by different model or values of Manning roughness. The results computed by SVE model with the Manning roughness set to 0.025 are chosen as references.

CONCLUSIONS

A 2D hydrodynamic (labeled as CAR) model has been proposed for shallow water flows over steep slopes in a Cartesian coordinate system with two axes within the horizontal plane and one axis along the vertical direction, taking into account the bed slope when calculating pressure distribution and bed shear

stresses. A well-balanced finite volume method, which achieves second-order accuracy in time and space, has been adopted to solve the governing equations.

The CAR model is tested against the analytical solutions of an idealized dam-break flow over a steep slope, along with the traditional SVE model and the modified SWE model. Both the CAR and the SWE models satisfactorily reproduce the analytical solutions, while the SVE model overestimates the flow velocity so it does not apply to cases with steep slopes. Although the CAR and the SVE models give results with minor differences for cases with short duration or small mean slope, the SVE model keeps predicting a faster propagation of flood. In this connection, a flood event has been designed with longer duration and larger average slope, and the two models present distinguishable discrepancies. Extensively, an increased drag force cannot compromise the neglect of bed slope effects in the SVE model. Hence, the proposed CAR model is advocated for applications for its facility of extending from 1D to 2D version and simple data handling as opposed to the SWE model.

Extensions of the present work can focus on the fully coupled shallow water hydro-sediment-morphodynamic models incorporating rainfall and infiltration and their practical applications, such as rainfall-induced flash floods in watersheds.

Acknowledgements. The work reported in this paper is funded by the Natural Science Foundation of China (Grant Nos. 11432015 and 51279144).

REFERENCES

Ancey, C., Iverson, R.M., Rentschler, M., Denlinger, R.P., 2008. An exact solution for ideal dam-break floods on steep slopes. *Water Resour. Res.*, 44, 1, W01430.
 Barré de Saint-Venant, A.J.C., 1871. *Théorie du mouvement non permanent des eaux, avec application aux crues des rivières et à l'introduction des marées dans leur lits.* *Comptes*

- Rendus des séances de l'Académie des Sciences, 73, 1871, 237–240. (In French.)
- Bouchut, F., Mangeney-Castelnau, A., Perthame, B., Vilotte, J., 2003. A new model of Saint Venant and Savage–Hutter type for gravity driven shallow water flows. *C. R. Acad. Sci. Paris*, 336, 6, 531–536.
- Bussing, T.R.A., Murmant, E.M., 1988. Finite-volume method for the calculation of compressible chemically reacting flows. *AIAA J.*, 26, 9, 1070–1078.
- Cantero-Chinchilla, F.N., Castro-Orgaz, O., Khan, A.A., 2017. Depth-integrated non-hydrostatic free-surface flow modelling using weighted-averaged equations. *Int. J. Numer. Mech. Fluids*, 87, 1. DOI: 10.1002/fld.4481.
- Cao, Z.X., Yue, Z., Li, X., Che, T., 2007. Two-dimensional mathematical modeling of flooding over erodible sediment bed. Proceedings of the 32nd IAHR Congress, Venice, Italy. CD-ROM, IAHR, Madrid.
- Cao, Z.X., Hu, P., Hu, K., Pender, G., Liu, Q.Q., 2015. Modeling roll waves with shallow water equations and turbulent closure. *J. Hydraul. Res.*, 53, 2, 161–177.
- Cao, Z.X., Xia, C.C., Pender, G., Liu, Q.Q., 2017. Shallow water hydro-sediment-morphodynamics equations for fluvial processes. *J. Hydraul. Eng.*, 143, 5, 02517001.
- Castro-Orgaz, O., Hager, W.H., 2017. *Non-Hydrostatic Free Surface Flows*. Springer International Publishing AG, Cham, Switzerland.
- Castro-Orgaz, O., Hutter, K., Giraldez, J.V., Hager, W.H., 2015. Nonhydrostatic granular flow over 3-D terrain: New Boussinesq-type gravity waves? *J. Geophys. Res.*, 120, 1–28.
- Denlinger, R.P., Iverson, R.M., 2004. Granular avalanches across irregular three-dimensional terrain: I. Theory and computation. *J. Geophys. Res.*, 109, F01014.
- Denlinger, R.P., O'Connell, D.R.H., 2008. Computing nonhydrostatic shallow-water flow over steep terrain. *J. Hydraul. Eng.*, 134, 11, 1590–1602.
- Fernandez-Feria, R., 2006. Dam-break flow for arbitrary slopes of the bottom. *J. Eng. Math.*, 54, 4, 319–331.
- Gray, J.M.N.T., Wieland, M., Hutter, K., 1999. Gravity-driven free surface flow of granular avalanches over complex basal topography. *Proc. R. Soc. Lond. A*, 455, 1841–1874.
- Greve, R., Koch, T., Hutter, K., 1994. Unconfined flow of granular avalanches along a partly curved surface. I. Theory. *Proc. R. Soc. Lond. A*, 445, 399–413.
- Hou, J., Liang, Q., Simons, F., Hinkelmann, R., 2013a. A 2D well-balanced shallow flow model for unstructured grids with novel slope source term treatment. *Adv. Water Resour.*, 52, 107–131.
- Hou, J., Liang, Q., Simons, F., Hinkelmann, R., 2013b. A stable 2D unstructured shallow flow model for simulations of wetting and drying over rough terrains. *Comput. Fluids*, 82, 132–147.
- Huang, W., Cao, Z.X., Carling, P., Pender, G., 2014. Coupled 2D hydrodynamic and sediment transport modeling of megaflood due to glacier dam-break in Altai Mountain, Southern Siberia. *J. Mt. Sci.*, 11, 6, 1442–1453.
- Huang, W., Cao, Z.X., Qi, W., Pender, G., Zhao, K., 2015. Full 2D hydrodynamic modelling of rainfall-induced flash floods. *J. Mt. Sci.*, 12, 5, 1203–1218.
- Juez, C., Murillo, J., García-Navarro, P., 2013. 2D simulation of granular flow over irregular steep slopes using global and local coordinates. *J. Comput. Phys.*, 255, 166–204.
- Juez, C., Soares-Fraza, S., Murillo, J., García-Navarro, P., 2017. Experimental and numerical simulation of bed load transport over steep slopes. *J. Hydraul. Res.*, 55, 4, 455–469.
- Keller, J.B., 2003. Shallow-water theory for arbitrary slopes of the bottom. *J. Fluid Mech.*, 489, 345–348.
- Li, J., Cao, Z.X., Qian, H.L., Liu, Q.Q., Pender, G., 2017. A depth-averaged two-phase model for fluvial sediment-laden flows over erodible beds. *Adv. Water Resour.*, in press. <https://doi.org/10.1016/j.advwatres.2017.08.014>
- Li, J., Cao, Z.X., Hu, K., Pender, G., Liu, Q.Q., 2018a. A depth-averaged two-phase model for debris flows over fixed beds. *Int. J. Sediment Res.*, 33, 4, 462–477.
- Li, J., Cao, Z.X., Hu, K., Pender, G., Liu, Q.Q., 2018b. A depth-averaged two-phase model for debris flows over erodible beds. *Earth Surf. Process. Landforms*, 43, 817–839.
- Liang, Q., Marche, F., 2009. Numerical resolution of well-balanced shallow water equations with complex source terms. *Adv. Water Resour.*, 32, 873–884.
- Mangeney-Castelnau, A., Bouchut, F., Vilotte, J. P., Lajeunesse, E., Aubertin, A., Pirulli, M., 2005. On the use of Saint Venant equations to simulate the spreading of a granular mass. *J. Geophys. Res.*, 110, B09103.
- Qian, H.L., Cao, Z.X., Pender, G., Liu, H.H., Hu, P., 2015. Well-balanced numerical modelling of non-uniform sediment transport in alluvial rivers. *Int. J. Sediment Res.*, 30, 2, 117–130.
- Qian, H.L., Cao, Z.X., Liu, H.H., Pender, G., 2017. Numerical modeling of alternate bar formation, development and sediment sorting in straight channels. *Earth Surf. Process. Landforms*, 42, 4, 555–574.
- Savage, S.B., Hutter, K., 1989. The motion of a finite mass of granular material down a rough incline. *J. Fluid Mech.*, 199, 177–215.
- Savage, S.B., Hutter, K., 1991. The dynamics of avalanches of granular materials from initiation to runout. Part I: Analysis. *Acta Mechanica*, 86, 1, 201–223.
- Toro, E., 2001. *Shock-Capturing Methods for Free-Surface Shallow Flows*. Chichester, U. K.: Wiley.
- Toro, E.F., 2009. *Riemann Solvers and Numerical Methods for Fluid Dynamics: A Practical Introduction*. 3rd Ed. Springer-Verlag, Berlin.
- Van Emelen, S., 2014. Breaching processes of river dikes: effects on sediment transport and bed morphology, (Doctoral dissertation). Retrieved from DIAL. (<http://hdl.handle.net/2078.1/151925>). Université catholique de Louvain, Leuven, Belgium.
- Van Emelen, S., Zech, Y., Soares-Fraza, S., 2014. Limitations of the shallow water assumptions for problems involving steep slopes: Application to a dike overtopping test case. In: *River Flow 2014*, Lausanne, pp. 1669–1677.
- Wang, X., Cao, Z.X., Pender, G., Neelz, S., 2010. Numerical modeling of flood flows over irregular topography. *Proc. ICE – Water Manage.*, 163, WM5, 255–265.
- Wu, W., 2007. *Computational River Dynamics*. Taylor & Francis, London, UK.
- Xue, Y., Xu, W., Luo, S., Chen, H., Li, N., 2011. Experimental study of dam-break flow in cascade reservoirs with steep bottom slope. *J. Hydrol. B*, 23, 4, 491–497.
- Yue, Z., Cao, Z., Li, X., Tao, C., 2008. Two-dimensional coupled mathematical modeling of fluvial processes with intense sediment transport and rapid bed evolution. *Sci. China Ser. G-Phys. Mech. Astron.*, 51, 9, 1427–1438.

Received 22 January 2018

Accepted 30 May 2018

The role of sampling strategy on apparent temporal stability of soil moisture under subtropical hydroclimatic conditions

Lei Gao^{1,2}, Yaji Wang^{1,3}, Josie Geris², Paul D. Hallett⁴, Xinhua Peng^{1*}

¹ State Key Laboratory of Soil and Sustainable Agriculture, Institute of Soil Science, Chinese Academy of Sciences, Nanjing 210008, PR China. E-mail: lgao@issas.ac.cn

² School of Geosciences, University of Aberdeen, Aberdeen, UK. E-mail: j.geris@abdn.ac.uk

³ University of Chinese Academy of Sciences, Beijing, 10049, China. E-mail: wangyaji@issas.ac.cn

⁴ School of Biological Sciences, University of Aberdeen, Aberdeen, UK. E-mail: paul.hallett@abdn.ac.uk

* Corresponding author. Tel.: +86 25 86881198. Fax: +86 25 86881000. E-mail: xhpeng@issas.ac.cn

Abstract: Subtropical regions have clay-rich, weathered soils, and long dry periods followed by intense rainfall that produces large fluctuations in soil water content (SWC) and hydrological behavior. This complicates predictions of spatio-temporal dynamics, as datasets are typically collected at too coarse resolution and observations often represent a duration that is too short to capture temporal stability. The aim of the present study was to gain further insights into the role of temporal sampling scale on the observed temporal stability features of SWC order to aid the design of optimal SWC sampling strategies. This focused on both sampling frequency and total monitoring duration, as previous analyses have not considered both of these sampling aspects simultaneously. We collected relatively high resolution data of SWC (fortnightly over 3.5 years) for various soil depths and under contrasting crops (peanuts and citrus) at the red soil region of southeast China. The dataset was split into a three-year training period and a six-month evaluation period. Altogether 13 sampling frequencies (intervals ranging from 15 to 240 days) and eight monitoring duration periods (between three and 36 months) were derived from the training period to identify temporal stability features and the most time stable location (MTSL). The prediction accuracies of these MTSLs were tested using the independent evaluation data. Results showed that vegetation type did affect the spatio-temporal patterns of SWC, whereby the citrus site exhibited a stronger temporal variation and weaker temporal stability than the peanut site. However, the effects of both sampling frequency and observation duration were more pronounced, irrespective of the role of vegetation type or soil depth. With increasing sampling interval or decreasing monitoring duration, temporal stability of SWC was generally overestimated; by less than 10% when sampling interval increased from every 15 to 240 days and by up to 40% with duration decreasing from 36 to 3 months. Our results suggest that sampling strategies and trade-offs between sampling interval and duration should focus on capturing the main variability in hydro-climatological conditions. For subtropical conditions, we found that sampling once every 45 days over 24 months to be the minimum sampling strategy to ensure errors in SWC temporal stability of less than 10%.

Keywords: Sampling strategy; Subtropical climate; Temporal stability; Vegetation type; Soil moisture prediction.

Abbreviations: ARE: Absolute value of relative error; CV_T: Coefficient of variation over time; MRD: Mean relative difference; MTSL: Most time stable location; RD: Relative difference; RE: Relative error; SDRD: Standard deviation of relative difference; SWC: Soil water content.

INTRODUCTION

Soil water content (SWC) exerts important controls on evapotranspiration and runoff generation processes (e.g. Boulet et al., 2015). It is a key state variable to many eco-hydrological models (Brandyk et al., 2016). In turn, SWC is a function of many factors, including soil texture, land use (including vegetation), soil depth, topography and climate (Canton et al., 2016), which leads to strong and nonlinear spatio-temporal variations in SWC dynamics (Buttafuoco et al., 2005).

Capturing such SWC patterns is therefore complex and challenging (Gao et al., 2016a), hence many studies seek to replace extensive SWC measurements with less labor-intensive approaches (e.g. Burns et al., 2016; Korres et al., 2015; Martini et al., 2015; Stockinger et al., 2014). Some efforts involve exploring novel sensing methodologies (e.g. via remote sensing or cosmic ray sensors (e.g. Zreda et al., 2012)) which integrate small scale heterogeneity and offer new insights into larger scale moisture dynamics. On the other hand, there is a need to increase efficiency of traditional point scale measurements, which still provide more accurate measurements locally than

novel sensing methodologies. One common methodology to reduce those monitoring efforts is referred to as temporal stability, first put forward by Vachaud et al. (1985). It reflects the persistence of a spatial pattern of soil moisture in an area over time, which has been applied in many environments, ranging from humid (Gao et al., 2015b) to arid areas (Shen et al., 2016), and from forest (Korres et al., 2015) to agriculture ecosystems (Rivera et al., 2014).

The concept of temporal stability of SWC is widely used for various research and application purposes, for example to validate remotely sensed data (Cosh et al., 2006), optimize monitoring schemes (Brocca et al., 2010), fill in missing values (Dumedah and Coulibaly, 2011), assimilate data (Pan et al., 2012), estimate spatial mean SWCs (Biswas, 2014), predict spatial distribution (Hu and Si, 2016), upscale from surface to profile scale (Gao et al., 2016b), downscale from field to plot scale (Nasta et al., 2018), and improve the space-time resolution of data (Zhu et al., 2017). The performance of these applications typically depends on the strength of temporal stability. It has been recognized that the sampling frequency (or interval) and the duration of the monitoring period are important compo-

nents that affect the “apparent” features of temporal stability (Martínez et al., 2014; Vanderlinden et al., 2012).

Owing to variations in study aims and objectives, studies on temporal stability of SWC have used data which were collected at different sampling intervals, e.g. ranging from every 10 min (Guber et al., 2008), to daily (Heathman et al., 2009) to more than monthly (Wang et al., 2015b) and over different length of monitoring periods, e.g. ranging from approximately one month (Cosh et al., 2004) to one year (Li et al., 2016) to 10 years (Liu and Shao, 2014). This is a limiting factor to the generalization of the temporal stability application (Wang et al., 2015a), e.g. as it inhibits wider interpretations from individual studies. So far, those studies that considered the impact of sampling frequency did not find significant differences in temporal stability characteristics derived from data with sampling interval differences in the order of a few hours (Cosh et al., 2006), a few days (Guber et al., 2008) or one month (Martínez et al., 2014). However, the temporal stability index of each investigated frequency used in these studies was generally presented as the mean of all sub-datasets (e.g. Rivera et al., 2014), which mainly reflects the errors related to scale effects and ignores the uncertainties from a single sampling. Though the study of Cosh et al. (2006) compared the differences of temporal stability characteristics of different sampling intervals using single sampling strategy, the ranges of frequencies investigated were limited, i.e. within 24 hours. In practice, however, single sampling at a specific interval, monthly or longer, is typically applied as a most cost-effective strategy, and these results may be more affected by temporal sampling frequency than considering the mean of all sub-datasets (Hu et al., 2012).

Although the spatial pattern of SWC is generally time-stable, the “apparent” temporal stability strength could be affected by the span of the sampling period, as suggested by Vanderlinden et al. (2012). A few studies explored this issue but found inconsistent or even contradictory results. For example, Cosh et al. (2006) reported that the temporal stability of SWC was similar among four seasons and a whole year in the Washita watershed, southwestern Oklahoma. However, for an area in central Saskatchewan, Canada, Biswas and Si (2011) found that temporal stability with the same season was much stronger than between different seasons. Furthermore, for a site on the Loess Plateau, China, Liu and Shao (2014) found that the relationships between temporal stability and the duration of sampling period depended on the type of the vegetation based on a 10-year study period. These inconsistent results could be associated with different strengths of seasonal hydro-climatological variability mainly caused by the differences in climate, soil properties as well as vegetation type, as suggested by Martínez et al. (2014) and Wang et al. (2015a). It appears that such differences would be particularly evident in hydroclimatic regions where seasonal variability is extreme, such as tropical climates where long dry periods are followed by intense periods of rainfall.

Vegetation type and soil depth have been proven to be important factors that influence the temporal stability of SWC. Generally, vegetation activity appears to weaken the temporal stability of SWC (e.g. Cassel et al., 2000; Wang et al., 2015a), while the temporal stability typically increases with soil depth (e.g. Choi and Jacobs, 2007). Nevertheless, whether the influences of sampling strategy on temporal stability of SWC vary with vegetation types and soil depth in such areas with strong seasonal hydro-climatological variability is still unclear.

This study aims to gain further insights into the role of temporal sampling scales on the observed temporal stability of soil moisture. More specifically, the temporal sampling scales refers to the balance of how often in time and for how long a monitor-

ing period in total. To explore these impacts under relatively extreme hydroclimatic conditions of the tropics, we investigate these at agricultural sites of the Chinese red soil region where strong climatic variability drives a highly dynamic soil moisture regime. Red soil is also an important resource of China and covers an area of 2.18 million km². Seasonal drought from July to September is a big challenge faced in this region with regard to the productivity of crops (Zhao et al., 2012). In addition, the temporal stability concept has been proven to be an effective tool to improve agricultural water management in this region by providing precise SWC information (Gao et al., 2015b and 2016a). Optimizing sampling strategies is important so that temporal stability can be effectively characterized in this region.

The specific objectives were to 1) identify spatio-temporal patterns of SWC for two contrasting cropping practices at four soil layers in an agricultural landscape of the Chinese Red soil region; 2) for these different sites, evaluate the role of sampling frequency (i.e. the interval between sampling occasions) and the duration of the monitoring period on temporal stability features and mean SWC prediction and 3) based on the outcomes of (1) and (2), explore potential applications to inform temporal sampling strategies for similar temporal stability studies.

MATERIALS AND METHODS

Study area

SWC data were collected in the Sunjia agricultural catchment (116°53'58" – 116°54'28"E, 28°13'45" – 28°14'12"N), a recognized Critical Zone Observatory located in Yingtan, Jiangxi province, China (Fig. 1). The area has a typically warm and humid subtropical monsoon climate. Mean annual precipitation is ~1800 mm and annual potential evapotranspiration is ~1200 mm. There is a strong climatic seasonality with a distinct dry (July to September) and wet (April to June) season. The dry season receives less than 20% of annual rainfall, while potential evapotranspiration rates amount to more than 45% of the annual total. In contrast, more than 50% of the annual precipitation occurs during the wet season (Zhao et al., 2012).

The dominant crop types for upland at Sunjia are peanut (*Arachis hypogaea*) and citrus (*Citrus reticulata*), which have distinctly different patterns in root water absorption (Tahir et al., 2016). Cultivation histories of the two vegetation types are approximately 25 years, both of which replaced tea plantations (*Camellia sinensis*) in the early 1990s. The growing seasons for peanut is from April to August and for citrus from April to October. Unlike rice fields in the region, both peanut and citrus do not receive any irrigation water.

Soils at the study site were derived from Quaternary red clays and are classified as Ultisols based on the USDA Soil Taxonomy classification system (Soil Survey Staff, 2010). Although the overall soil classification is similar, there are differences in the soil physical properties associated with the two vegetation types. Key differences include a higher clay content and soil organic carbon content for soils at the citrus site than those at the peanut site (Table 1). In addition, the saturated hydraulic conductivity of soils under peanut is up to an order of magnitude higher than under citrus at surface 20 cm soil layer (Table 1). This can be associated with the different soil management practices (i.e. tillage) for peanut and citrus.

Data collection

Nine monitoring locations with an approximate spacing of 15 m in a transect along the slope were chosen for each vegeta-

Table 1. Soil properties of different soil layers within 0–100 cm for peanut and citrus sites.

Vegetation type	depth cm	Sand %	Silt %	Clay %	BD* g/cm ³	SOC* g/kg	K _s * cm/day
Peanut	0–20	38.4±9.3	27.5±4.3	34.1±5.4	1.34±0.12	10.7±3.0	162.7±104.1
	20–40	35.1±10.0	28.6±4.1	36.3±7.4	1.41±0.09	5.3±1.4	16.2±27.6
	40–60	36.3±7.8	27.1±3.2	36.7±5.9	1.40±0.11	4.0±0.7	16.4±15.6
	60–80	34.7±7.8	27.3±3.1	38.0±6.2	1.38±0.12	3.7±0.9	13.8±18.1
	80–100	33.6±7.0	27.2±3.6	39.2±5.5	1.42±0.09	3.2±0.7	9.6±9.1
Citrus	0–20	41.3±4.3	24.9±2.1	33.8±3.1	1.38±0.08	13.6±2.6	18.8±12.5
	20–40	35.9±6.0	25.1±2.2	39.0±4.7	1.42±0.06	5.7±1.4	4.0±2.9
	40–60	33.5±2.9	24.4±1.6	42.1±4.0	1.45±0.11	3.6±0.5	5.7±8.0
	60–80	33.8±5.0	26.0±4.8	40.2±5.7	1.41±0.06	3.2±0.6	8.8±7.2
	80–100	34.7±4.1	24.5±5.5	40.8±8.2	1.45±0.08	2.7±0.4	10.4±12.8

*BD = bulk density; SOC = soil organic carbon; K_s = soil saturated hydraulic conductivity. All the values were the mean values of nine locations by arithmetic method.

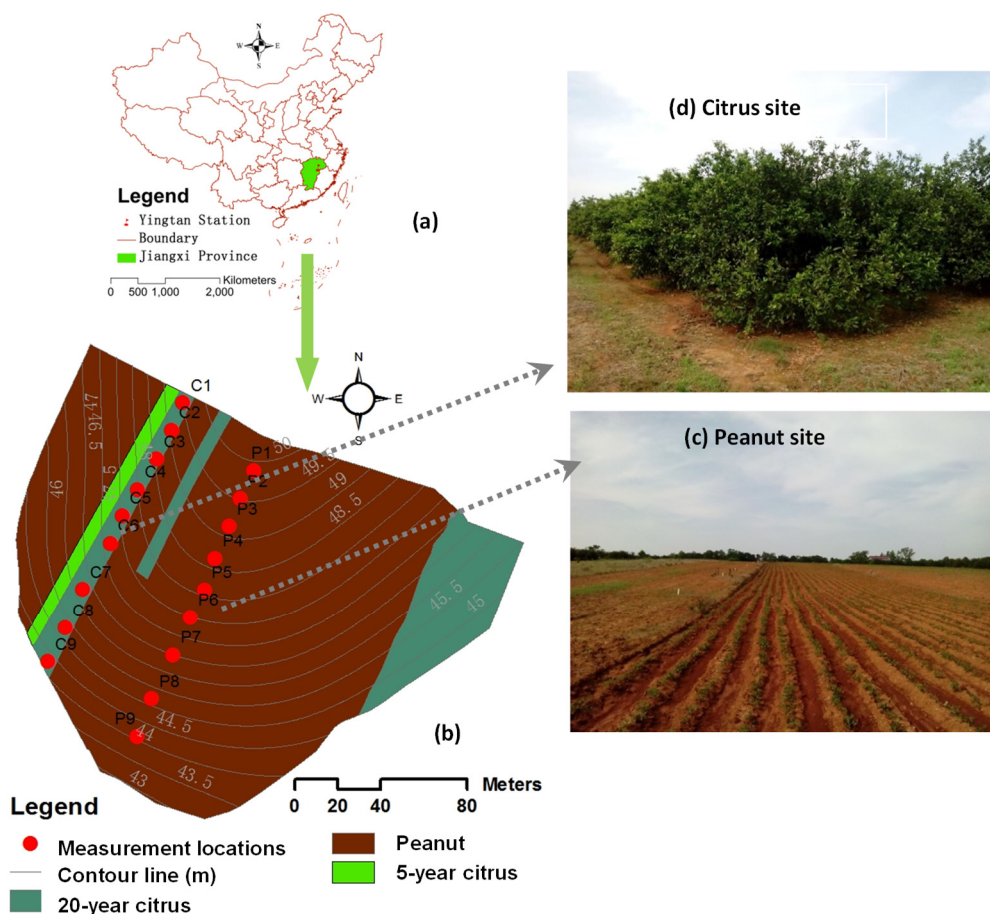


Fig. 1. Location of the studied slope (a) and spatial distribution of monitoring locations across the slope (b) for peanut (c) and citrus (d) sites.

tion type to measure SWC (see Fig. 1). To eliminate possible influences from topography and climate, the two transects were nearly parallel along the same slope with peanut and citrus, respectively. The topography of the two transects was similar, with a slope length of approximately 150 m and the elevation ranging from 44 to 50 m (Fig. 1). Soil layer thickness for both transects varied between approximately 5.0 m and 6.5 m depending on slope position. A 2-m polyvinyl chloride access tube with a diameter of 5 cm was installed at each location in early 2013. Each tube was capped at the bottom with a watertight seal, and a removable cap was placed on top to prevent water entering the tube.

The volumetric SWC was measured using a size-matched portable TDR TRIME-PICO-IPH probe, with the length of 18 cm, measuring accuracy of 2% and repeat accuracy 0.3%

(IMKO, Ettlingen, Germany). Since properties of the studied soil were within those ranges tested and calibrated by the manufacturer, we initially used the factory-set calibration curve to translate the dielectric constant of the soil into SWC. In addition, to avoid drifts in the data of this portable probe, its consistency was checked via a calibration in dry and water-covered glass beads (the depth of water film lower than 2mm) every two months (see also Zhu et al., 2017). This involved the standard procedure recommended in the user manual. From July 2013 to December 2016, with an approximate time interval of 15 days, SWC was collected at 20 cm intervals to a depth of 160 cm on 79 occasions. For the purpose of this study, at each sampling date, the collected SWCs were transferred to mean values for layers of 0–40, 40–80, 80–120, and 120–160 cm soil depth.

Data analysis

First, the 3.5-year dataset was used to identify general temporal variations and temporal stability of SWC in the study area. Next, to test the impacts of the sampling strategy on the behavior of temporal stability, the full dataset was split into a training period (from July, 2013 to June, 2016) and evaluation period (from July to December, 2016). A range of sampling frequencies (varying intervals between sampling occasions) and periods (varying total duration of the monitoring period) were obtained from the training period by re-sampling analysis. For each sampling strategy, temporal stability analysis was performed to obtain the temporal stability index and identify the MTSL. The evaluation period was used to evaluate the prediction accuracy based on the identified MTSLs.

Re-sampling analysis

The dataset of the 36 months training period was re-sampled for 13 sampling intervals (once every 15, 30, 45, 60, 75, 90, 105, 120, 135, 150, 180, 210 and 240 days) and eight sampling duration periods (36, 30, 24, 18, 12, 9, 6, and 3 months). All of the possible sub-datasets for each sampling strategy were obtained to cover the whole training period. The aim of getting all the possible sub-datasets was to separate the changes of temporal stability caused by the temporal uncertainty of SWC and by temporal sampling scale itself.

The number of sub-datasets for each sampling interval was determined by its value divided by the shortest sampling interval (i.e. 15 days). For example, for the sampling strategy with 120-day sampling interval, the number of the sub-dataset was eight (i.e. 120 by 15). The approach to obtain the eight sub-datasets is that beginning from eight different dates (from the first, second and until the eighth date) with the same sampling interval of 120 days (see Fig. 2a).

Similarly, the number of the sub-datasets for each sampling period duration was calculated based on the longest period (i.e. 36 months) and the period of the sub-dataset. For example, the number of the sub-datasets for a 6-month sampling period is calculated from 36 months by six months. The six sub-datasets were obtained beginning from the first, seventh, 13th until 31st month with 6-month duration (see Fig. 2b).

Temporal stability analysis

Relative difference analysis was used to evaluate the temporal stability of SWC with the mean relative difference

(MRD) and standard deviation of relative difference (SDRD) indices. Relative difference (RD) is the difference between an individual measurement of SWC at location i time j , $SWC_j(i)$, and the mean SWC, $\overline{SWC_j}$ of the same time. It provides an estimation of the unbiased difference between them:

$$RD_j(i) = \frac{SWC_j(i) - \overline{SWC_j}}{\overline{SWC_j}} \quad (1)$$

where

$$\overline{SWC_j} = \frac{1}{N} \sum_{i=1}^N SWC_j(i) \quad (2)$$

N is the number of measurement locations ($N = 9$ in the present study).

Temporal mean RD and its standard deviation at location i , $MRD(i)$ and $SDRD(i)$ are defined as:

$$MRD(i) = \frac{1}{m} \sum_{j=1}^m RD_j(i) \quad (3)$$

and

$$SDRD(i) = \sqrt{\frac{1}{m-1} \sum_{j=1}^m (RD_j(i) - MRD(i))^2} \quad (4)$$

for which m is the number of measurement occasions, totaling 67 for the training period and 79 for the whole study period. The MRD and SDRD represent the bias and the precision of the location when used for predicting the mean SWC, respectively. In this study, the location with the lowest SDRD values was chosen as the MTSL, which can be used to predict the mean SWC with an offset by the corresponding MRD value (Starks et al., 2006):

$$\overline{SWC_j} = \frac{SWC_j(i)}{1 + MRD(i)} \quad (5)$$

Here, we could not obtain the true value of the temporal stability index from the field data. One alternative to overcome this is to employ the dataset with the longest sampling period and the shortest sampling interval for temporal stability analysis. As such, the temporal stability index (i.e. SDRD) of the full dataset (i.e. 15-day sampling interval over 36 months) was here considered as the “true value”, while the SDRD of any of the

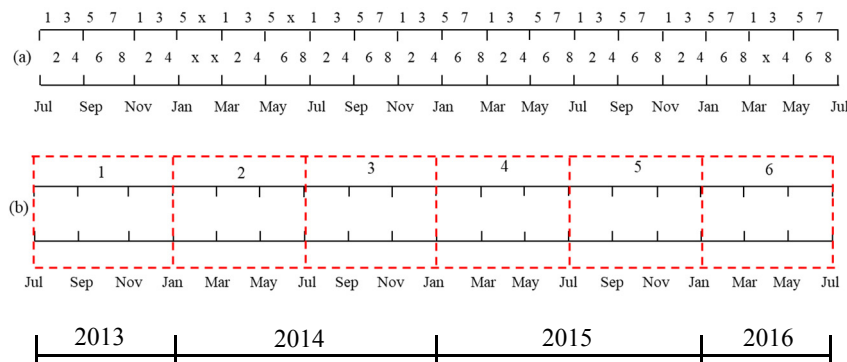


Fig. 2 Example diagrams of sampling strategies explored in the present study, showing the structure of 120 days as an example for sampling intervals (a) and 6 months for sampling periods (b). For (a): the sampling occasions with the same number belong to the same sub-dataset; numbers 1–8 represent the eight sub-datasets and x are occasions for which no data were available. For (b): numbers 1–6 represent the six sub-datasets with the same sampling interval of 15 days (not shown in the schematic).

sub-sets was the “apparent” value (cf., Rivera et al., 2014; Western and Blöschl, 1999). The scale effect on temporal stability was reflected by the deviation of mean SDRD values of all sub-datasets to the “true value” for each sampling strategy.

The error introduced by a single sampling related to neglecting of inner variations, considered as the “uncertainty” here, was reflected by the maximum deviation in all the sub-datasets. Using the dataset of the evaluation period, the prediction accuracy was assessed by the deviation between the observed and predicted mean SWCs. The deviations between “apparent” SDRD and its “true value” and between the predicted mean SWC and observed SWC were expressed by the index of relative error (RE) and the related maximum RE (Max-RE), absolute value of relative error (ARE) and its mean and maximum, Mean-ARE and Max-ARE.

RESULTS

Spatio-temporal patterns in soil water content (SWC)

Dynamics of spatial mean SWC (nine locations along the slope for each vegetation type) during the full study period (from July 2013 to December 2016) suggested that both vegetation type and soil depth affected the temporal variation of SWC (Fig. 3). Overall, temporal variations of SWC for citrus were stronger than for peanut. This is evident across the full depth range, where the coefficients of variation over time (CV_T) were consistently higher for citrus than for peanut (Table 2). It was also found that the differences of the variation between the two vegetation types were larger for deeper soil depths than shallow ones (Table 2).

The temporal stability of SWC, denoted by SDRD, was stronger for peanut than citrus at all four soil layers (Table 2). The location of the MTSLS, identified by the lowest SDRD values, varied with depth for both peanut and citrus. For example, the MTSLS for peanut were at P6 for the 0–40 cm depth, while at P3 for the other three depth ranges. For citrus, these locations were P7 and P1, respectively (Table 2).

Influences of temporal sampling strategies on temporal stability of SWC

In general, sampling frequency affected the averaged SDRD values only slightly (Fig. 4). Compared to the “true value”, the relative errors (REs) of 91 out of 104 cases (13 sampling intervals at four soil layers for two vegetation types in total) were lower than 5% (RE values not shown in Figure 4). This was the case for all sampling interval increases from every 15 days up to 150 days. However, when the sampling interval was longer than once every 150 days, the SDRD was increasingly underestimated. Accordingly, the largest ARE (12.7%) was derived for the longest sampling interval (i.e. 240-days).

The maximum REs (Max-REs) of sampling strategies increased largely with longer sampling intervals. This was inde-

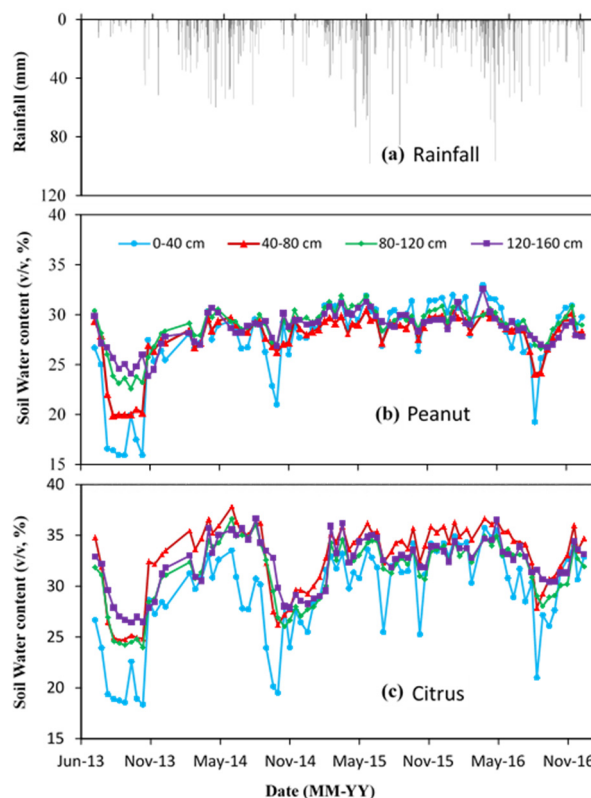


Fig. 3. Temporal dynamics of rainfall (a) and spatial mean soil water content (SWC) from July, 2013 to December, 2016 for peanut (b) and citrus sites (c) at 0–40, 40–80, 80–120, and 120–160 cm soil layers.

pendent of depth where all the errors over 50% occurred for the longest sampling interval (i.e. once every 240 days) for all the four soil depth ranges (Fig. 4). When the sampling interval was shorter than 60 days (i.e. every 15, 30, and 45 days), corresponding Max-REs were less than 10% (Fig. 4). However, for some cases, such as 40–80 and 80–120 cm for the peanut site, the Max-REs were even less than 10% when sampling intervals were 90 days or less (Fig. 4). Significant differences were found for the peanut site among four soil depths except for the 40–80 vs. 80–120 cm soil layer ($p < 0.05$, t-test). For the citrus site, however, only the error of the 0–40 cm soil layer was significantly less than those of the 80–120 and 120–160 cm soil layers.

Changes of averaged SDRD values with the sampling period increasing from 3 months to 36 months could be divided into two stages: slight fluctuations for a sampling duration >12 month, but a fast increase when duration changed from 3 to 12 months. For durations >12 months, the AREs for SDRD were generally less than 10% for both peanut and citrus (Fig. 5). However, AREs rose sharply to more than 30% for sampling durations <12 months (Fig. 5). The generally negative errors

Table 2. Statistics of soil water content (SWC) from July, 2013 to December, 2016 of temporal mean values, temporal coefficient of variation (CV_T), mean standard deviation of relative difference (SDRD), most temporal stability location (MTSL) based on the method with the lowest SDRD values at 0–40, 40–80, 80–120, and 120–160 cm soil layers for peanut and citrus sites.

Soil depth (cm)	Peanut				Citrus			
	0–40	40–80	80–120	120–160	0–40	40–80	80–120	120–160
Mean SWC	27.6a	27.8a	28.9a	28.6a	29.2a	32.9b	31.3a	32.1b
CV_T	15.0	9.5	7.1	6.1	15.9	10.6	10.3	8.2
Mean SDRD	3.9	3.3	5.0	6.7	5.8	5.6	6.1	6.8
MTSL	P6	P1	P1	P1	P7	P3	P3	P3
SDRD of MTSL	2.6	1.6	2.6	4.0	3.0	3.3	3.2	3.4

Mean SWCs flowed by different letters indicating significantly different between peanut and citrus sites ($p < 0.05$, paired samples t-test).

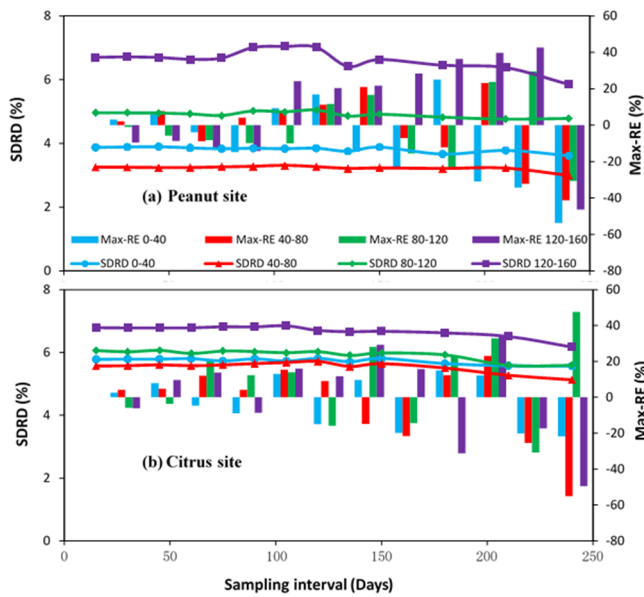


Fig. 4. Changes of temporal stability of soil water content (SWC) with 13 sampling intervals for peanut (a) and citrus (b) sites at 0–40, 40–80, 80–120, and 120–160 cm soil layers during the training period (from July, 2013 to June, 2016), represented by the standard deviation of relative difference (SDRD) and its maximum relative error (Max-RE) of sub-datasets.

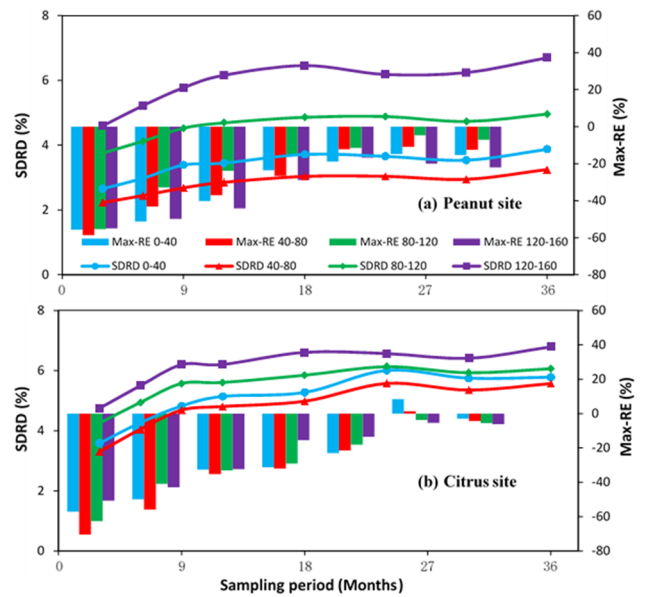


Fig. 5. Changes of temporal stability of soil water content (SWC) with eight sampling periods for peanut (a) and citrus (b) sites at 0–40, 40–80, 80–120, and 120–160 cm soil layers during the training period (from July, 2013 to June, 2016), represented by the standard deviation of relative difference (SDRD) and its maximum relative error (Max-RE) of sub-datasets.

Table 3. Criterion of sampling interval and period to meet standard deviation of relative difference (SDRD) and soil water content (SWC) prediction with mean absolute value of relative error (Mean-ARE) over all sub-datasets lower than 10% for peanut and citrus sites at 0–40, 40–80, 80–120, and 120–160 cm soil layers.

Vegetation type	Soil depth cm	Sampling interval		Sampling period	
		SDRD	Mean SWC	SDRD	Mean SWC
Peanut	0–40	240 (4)	240 (4)	12 (23)	3 (5)
	40–80	240 (4)	240 (4)	18 (34)	3 (5)
	80–120	240 (4)	240 (4)	9 (17)	3 (5)
	120–160	210 (5)	240 (4)	12 (23)	3 (5)
Citrus	0–40	240 (4)	240 (4)	12 (23)	3 (5)
	40–80	240 (4)	240 (4)	18 (34)	3 (5)
	80–120	240 (4)	240 (4)	9 (17)	3 (5)
	120–160	240 (4)	240 (4)	9 (17)	3 (5)

Number in the brackets stands for the occasions of sampling required.

Table 4. Criterion of sampling interval and period to meet standard deviation of relative difference (SDRD) and soil water content (SWC) prediction with maximum absolute value of relative error (Max-ARE) over all sub-datasets lower than 10% for peanut and citrus sites at 0–40, 40–80, 80–120, and 120–160 cm soil layers.

Vegetation type	Soil depth cm	Sampling interval		Sampling period	
		SDRD	Mean SWC	SDRD	Mean SWC
Peanut	0–40	60 (17)	45 (22)	—	24 (46)
	40–80	90 (12)	105 (10)	—	12 (23)
	80–120	90 (12)	180 (6)	24 (46)	6 (11)
	120–160	45 (22)	105 (10)	—	12 (23)
Citrus	0–40	75 (14)	75 (14)	24 (46)	18 (34)
	40–80	45 (22)	60 (17)	24 (46)	24 (46)
	80–120	45 (22)	90 (12)	24 (46)	18 (34)
	120–160	45 (22)	90 (12)	24 (46)	9 (17)

“—” means that no investigated sampling frequency or sampling period meeting the requirement.

suggest that the temporal stability of SWC was overestimated for short sampling periods. For the shortest sampling period duration (i.e. 3 months), the mean errors of sub-datasets were highest.

The differences in Max-AREs among soil layers for peanut site were significant except for 0–40 vs. 40–80 cm and 0–40 vs. 120–160 cm soil layers ($p < 0.05$, t-test) while no significant differences were observed among any of the soil layers for the

citrus site. Significant differences between the two vegetation types were observed at deeper soil layers (i.e. 80–120 and 120–160 cm). Nevertheless, changing sampling frequency and duration did not change the ranks of relative magnitude for mean SDRD for both peanut and citrus sites, which were identical to that under the full dataset.

The errors of temporal stability with changing sampling intervals from scale effects (Mean-RE) and from the uncertainties (Max-REs) varied greatly. Taking the longest sampling interval (i.e. every 240 days) for the 36-month period as an example, the two sources of errors were -6.7% vs. -53.7% , -7.9% vs. -41.3% , -3.5% vs. -30.6% , and -12.7% vs. -46.3% for peanut and -3.7% vs. -21.8% , -7.9% vs. -55.1% , -7.8% vs. -47.6% , and -9.1% vs. -49.4% for the citrus site. The ratios between the scale effect and uncertainties from the temporal variation of inner scale ranged from 0.1 to 0.4. However, the differences of the errors from the two sources become more comparable when the sampling period decreased from 36 months to 3 months, with the ratio changing from 0.8–1.5.

Requirements for sampling intervals and period duration to meet the criterion of ARE less than 10% for the mean and maximum SDRD of all sub-datasets are shown in Tables 3 and 4, respectively. Long sampling periods appeared to be required to meet the criterion. For example, around 5 sampling occasions were sufficient to ensure the AREs of mean SDRD were less than 10% for a total sampling duration of 36 months. However, corresponding sampling occasions need to be increased to 17–34 sampling occasions for shorter monitoring periods (Table 3). Both sampling interval and period duration required should improve largely to meet the maximum errors of all the sub-datasets lower than 10% (Table 4). For example, the sampling interval should not be longer than 60 days for peanut at 0–40 cm to obtain Max-ARE of all the sub-datasets around 10% (Table 4). For some extreme cases, i.e. citrus site at 0–40, 40–80, and 120–160 cm, Max-AREs were consistently higher than 10% for all the investigated sampling periods.

Influences of temporal sampling strategy on mean SWC prediction

Prediction accuracy was generally high for most sampling strategies. Figures 6 and 7 show that Mean-ARE is always less than 5% except for citrus with a short sampling period, e.g. 3 or 6 months (Fig. 7). These high prediction accuracies suggested that the temporal stability technique would generally be an appropriate tool for mean SWC prediction, even for a long sampling interval (e.g. once every 240 days) or for short sampling periods (e.g. 3 months).

Mean-AREs were more constant with changing sampling frequencies than sampling periods. Taking the citrus site as an example, when the sampling interval increased from 15 days (67 occasions) to 210 days (5 occasions), the Mean-AREs remained more or less the same for the four soil layers (Fig. 6), but with decreasing sampling period from 36 months (67 occasions) to 3 months (5 occasions), they increased consistently (Fig. 7). Max-AREs, however, increased much more with increasing sampling intervals and decreasing periods compared to mean errors. For example, the Max-AREs increased from 4.2% to 16.1% for peanut and from 5.7% to 21.7% for citrus at 0–40 cm when sampling intervals increased from 15 days to 240 days (Fig. 6).

Generally, the prediction accuracy of mean SWC was better for the peanut than the citrus site. The Mean-AREs of the different sampling frequencies for peanut were lower than for citrus at all four soil layers ($p < 0.05$, t-test), with the mean

values of 2.5% vs. 3.6%, 1.7% vs. 3.1%, 1.7% vs. 4.2% and 2.2% vs. 2.6%, respectively (Fig. 6). Relative to the differences between the two vegetation types, the differences among soil layers were smaller. No significant differences were observed in the Mean-AREs between 0–40 and 120–160 cm and between 40–80 and 80–120 cm soil layers ($p > 0.05$, t-test).

DISCUSSION

Influence of vegetation on spatio-temporal patterns in SWC

Soil water content of peanut and citrus sites exhibited different spatio-temporal patterns: stronger temporal variations, weaker temporal stability and lower mean SWC prediction accuracies were found under citrus than for peanut. Such differences may be related to (a combination of) the differences in soils and vegetation characteristics between them.

Firstly, soils at the citrus site have generally more clay compared to those at the peanut site (Table 1). These differences in clay can be mainly related to a different degree of soil erosion (Jarasiunas and Kinderiene, 2016) which is higher for peanut than for citrus. In general, agriculture has shown to exacerbate soil erosion in this region. Zhao et al. (2012) reported that soil loss under crop production was three times higher than under forest land use. By preferentially removing clay, soil erosion can increase sand and decrease clay contents for agricultural soils (Lai, 1998). Higher clay content is generally associated with relatively weaker temporal variation of SWC (Wang et al., 2017). This was inconsistent with observations in the present study, which showed that citrus had a larger clay content and stronger temporal variation in SWC.

In addition, relative differences in soil hydraulic properties between the two vegetation types do not directly support the stronger temporal variation of SWC for the citrus site. Due to the traditional tillage at the peanut site (generally in late March), the K_s of soils under this land use was 6–9 times higher than that at the citrus site at 0–20 cm soil at the time of sampling (early May, 2014). However, there is also a strong temporal variability in the soil hydraulic properties, which might not fully reflect the differences between sites as presented in Table 1. For example, for the same hillslope and based on tension infiltrometer data, Zhang et al. (2016) found that the temporal variation in soil effective porosity and site contribution to water flux for a tilled crop (watermelon) was much stronger than for citrus.

As such, the diverse temporal dynamics in soil moisture under citrus may be related to the characteristics of vegetation. In addition to the preferential flow in root channels, root water uptake could also explain the differences observed between the moisture dynamics. Citrus trees generally use more water with uptake from over a larger range of depth (>100 cm) than a peanut crop (within 20 cm). Therefore, citrus trees could be associated with stronger temporal SWC dynamics by decreasing the SWC in the dry season and allowing for more water storage in soils during the rainy and winter seasons (Fader et al., 2015). This may be exemplified by the sharp drop in the SWC in September 2014, which was more pronounced for citrus than for the peanut site (Fig. 3).

Responses of “apparent” temporal stability to temporal sampling strategies

Results showed that the temporal stability of SWC has a tendency to be overestimated with increasing sampling intervals (only when >150 days) and decreasing the total duration of the sampling period. The extent of the overestimation was

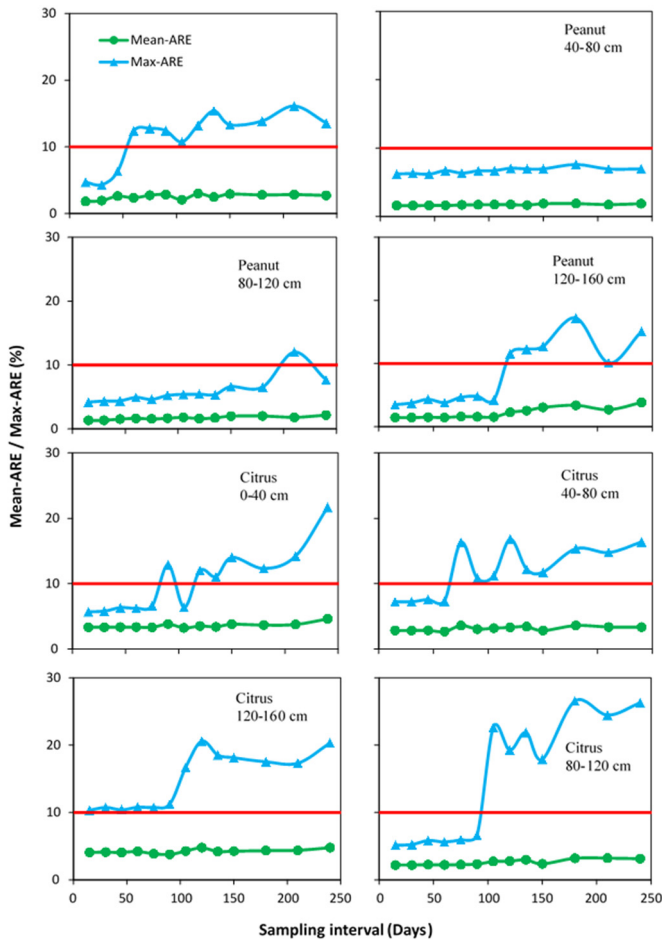


Fig. 6. Changes of prediction accuracy of soil water content (SWC) with 13 sampling intervals for peanut (a) and citrus (b) sites at 0–40, 40–80, 80–120, and 120–160 cm soil layers during the validation period (from July, 2016 to December, 2016), represented by the mean value and maximum of absolute value of relative error, Mean-ARE and Max-ARE, respectively.

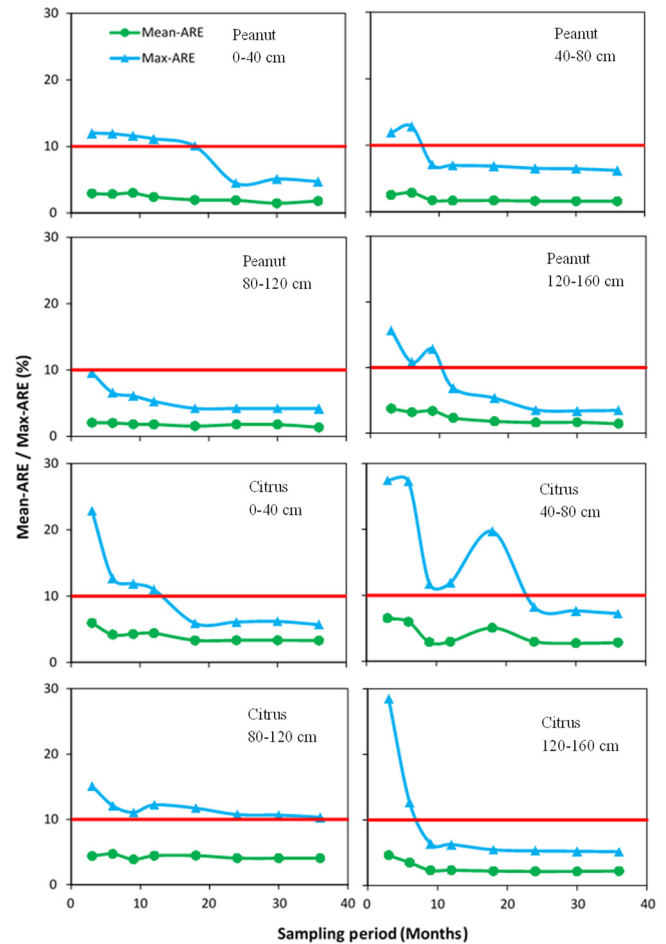


Fig. 7. Changes of prediction accuracy of soil water content (SWC) with eight total sampling durations for peanut (a) and citrus (b) sites at 0–40, 40–80, 80–120, and 120–160 cm soil layers during the validation period (from July, 2016 to December, 2016), represented by the mean value and maximum of absolute value of relative error, Mean-ARE and Max-ARE, respectively.

much lower with increasing sampling intervals than for decreasing the duration of the monitoring period.

In the present study area, seasonal dynamics of SWC were strong (see Fig. 3), which appears to affect the temporal stability of SWC due to the seasonal controlling factors such as meteorological effects (Cho et al., 2016) and vegetation characteristics (Wang et al., 2015a). The overestimation could be due to the neglect of the variation within or between seasons when sampling frequency is low (e.g. less than one season) or when the total sampling period is short (e.g. shorter than one whole season cycle). Such under-sampled variation would have a general tendency to lead to an overestimation of temporal stability, as suggested previously by Biswas (2014) and Gao et al. (2015a). In addition, large study extent generally leads to high similarity of the spatial patterns, which decreases the requirements of the temporal sampling strategy (Zhang et al., 2015). As such, the temporal sampling strategy may play a less important role in affecting the “apparent” temporal stability features in areas with weak seasonal patterns or at a relatively large spatial scale. SDRD values were much more constant with changing sampling intervals (Fig. 4) than sampling duration periods (Fig. 5). These diverse influences are probably related to the “aliasing” effect, which refers to the effect of spatial or temporal inner information partly “folded back” from low frequency to high frequency in sampling theory (Jenkins and

Watts, 1968). In other words, a stronger “aliasing” effect was always detected with changing spatial or temporal sampling spacing or interval, than for changes in the sampling duration or monitoring period. This “aliasing” effect has previously been reported for studies in groundwater (Gelhar, 1993), soil moisture (Western and Blöschl, 1999), and soil saturated hydraulic conductivity (Gao et al., 2012). In this study, temporal stability information of SWC which “folded back” from low sampling frequency to high frequency might be responsible for the stronger influences of sampling period than sampling frequency on temporal stability of SWC. This is supported by earlier findings by Western and Blöschl (1999), who found that sample spacing had no effect on the apparent variance of SWC, which was ascribed to the “aliasing” effect. Relatively small impacts of sampling frequency on temporal stability of SWC extended previous reports by Rivera et al. (2014) who found that the temporal stability did not change with sampling intervals in a limited range from 7 to 28 days in the Central Valley of Chile. However, Gao et al. (2012) predicted that this “folded back” phenomenon would diminish or even disappear with increasing sampling intervals. This might explain that larger differences were eventually observed when sampling intervals were very high (e.g. 210 days or 240 days).

Wider implications for sampling strategy design

The temporal stability index (i.e. SDRD) was more sensitive to the duration of the sampling period than the sampling interval. Therefore, it is reasonable to suggest that for a given number of sampling occasions, it would be best to target occasions that capture the longer term natural variability in moisture conditions. In other words, it would be recommended to focus on long term monitoring rather than high frequency (short intervals) monitoring. In comparison to decreasing sampling intervals, a good distribution of limited sampling occasions within a long sampling period was more efficient to decrease the uncertainty in the temporal stability. For example, this can be demonstrated clearly by comparing results from two cases (C1 and C2) with similar sampling occasions but diverse sampling strategies: e.g. C1 with a 45-day sampling interval over a 36-month period (22 occasions) and C2 with a 15-day sampling interval over a 12-month period (23 occasions). Significant differences in the errors ($p < 0.01$, t-test) between the two strategies indicated that it was reasonable to spend more effort extending the sampling period than improving frequency, when balancing between cost and accuracy.

The required sampling strategy differed when only considering the scale effect and considering errors both from sampling scale and uncertainties. By evaluating the mean over all the sub-datasets, the errors of such values were caused only by temporal scale effects. For similar study sites, any sampling strategy with a sampling interval shorter than 240 days and a sampling period no shorter than 12 months with measurement occasions more than 5 may be recommended. However, it should be noted that here we employed a single sampling and did not collect all possible sub-datasets within the actual sampling strategy, which has inevitably introduced uncertainties by ignoring variations between sites. It would therefore be necessary to extend the temporal sampling scales to decrease the uncertainties.

Considering the error both from sampling scale and uncertainties, sampling once every 45 days over 24 months could result in errors less than 10% in most cases (Table 4). Since we intentionally explored sampling strategies for a case study with high variability in hydroclimatologic and related SWC, we assume that these recommendations would be appropriate for a large range of sites, and certainly for those sites exposed to less variability. To be safe in practice, a 45-day sampling interval is suggested to minimize potential impacts from more variable years or crops that may alter SWC dynamics even more than citrus. Clearly, there is a need for more data from (sub)tropical climates to explore a broader range of vegetation, soil management and soil characteristics.

Similar sampling frequencies were also recommended by Martínez-Fernández and Ceballos (2005) who suggested to sample monthly for a temporal stability study in the central sector of the Duero basin, Spain. The importance of keeping a suitable sampling frequency to get insights of seasonal processes was previously emphasized by Guber et al. (2008) and Rivera et al. (2014). A complete seasonal cycle was important to capture seasonal dynamics of temporal stability caused by season-variable hydro-climatological conditions and vegetation phenology (Wang et al., 2015a). Nevertheless, the sampling period proposed in this study is also longer than reported previously, such as a one-year sampling period suggested by Martínez-Fernández and Ceballos (2005). A longer sampling period may be needed to account for the strong inter-annual variation of meteorological factors among the three-year study period, e.g. with rainfall of 1351, 1939 and 2193 mm, in consecutive

years respectively (Fig. 3). Different rainfall total between years would affect the relationships between temporal stability and related factors. For example, Wang et al. (2015a) reported a significant decrease in the effects of vegetation on temporal stability when rainfall increased from 566 mm to 604 mm in a semi-arid grassland.

There were no consistent differences observed in the identified most efficient sampling strategies for the different vegetation types and soil depths, as noted above. With regards to the Max-AREs of SDRD, the recommended sampling frequency for peanut was greater at 0–40 cm, smaller at 40–80 and 80–120 cm, and comparable at 120–160 cm than citrus site (Table 5). This suggests that the critical requirements could not be explained only by detected differences in spatio-temporal patterns between vegetation types and among soil depths. Other factors, such as extreme weather conditions, preferential flow pathways and “hotspots” of subsurface flow might play an important role in determining such requirements. Dynamics of preferential flow or subsurface flow can result in varying relationships between SWC at different spatial locations (Zhu et al., 2017).

Finally, dynamics in rainfall result in another important factor that can affect the temporal stability behavior of SWC (Lee and Kim, 2017). While the exact influences of rainfall event dynamics on key hydrological processes also depend on local conditions (e.g. soils, slope position and microtopography), it is known that during and directly after rainfall events, these can be different from before. There is additional work needed to evaluate if and how such effects translate into changes of temporal stability behavior. Such information is critical to arrange sampling dates (e.g. with respect to occurrence of the rainfall events) that allow for capturing accurate temporal stability information of SWC. To our knowledge, previous studies have not taken this into account and mainly focused on year- or season-scale. Instead, those and the study employed a middle way to eliminate immediate rainfall event effects, i.e. all the sampling occurred at least two days after a rainfall event. As such, by excluding rainfall event conditions, we recognize that this may still result in a departure of observed data from “real world” situations to some extent, yet we focused here on the key longer term patterns. The effect of short term rainfall dynamics on temporal stability behavior should receive more attention in the future. This would require higher temporal resolution data collection than employed here.

CONCLUSIONS

Impacts of temporal sampling strategy on temporal stability behaviors of SWC were analyzed for peanut and citrus sites at four soil layers from a 3.5-year dataset (from July, 2013, to December, 2016) in the subtropical Chinese red soil region. The following conclusions were drawn:

(1) Vegetation type played an important role in affecting spatio-temporal SWC patterns. In the present study, SWC at the peanut site exhibited less temporal variation, stronger temporal stability and greater prediction accuracy of mean SWC compared to the citrus site ($p < 0.05$, paired samples t-test). These differences were mainly caused by the diverse characteristics of the vegetation itself, e.g. root water uptake.

(2) With increasing sampling interval or decreasing monitoring duration, temporal stability of SWC was generally overestimated and affected more by the duration of the total sampling period than the interval between sampling occasions. With increasing intervals between sampling occasions, errors of temporal stability were mainly caused by the increasing uncer-

tainties and with decreasing sampling periods, however, the errors caused by scale effect and uncertainties were comparable.

(3) Sampling design strategies in future studies on temporal stability of SWC should consider distributing limited sampling occasions over a long sampling period, rather than focusing on high frequency sampling. More specifically, balancing cost and accuracy, a sampling strategy with 45-day sampling interval over 24 months is recommended in study areas similar to our site. If only mean SWC prediction is desired, the sampling interval and period duration could be further decreased. No significant differences between recommended sampling strategies were observed for peanut and citrus sites among four different soil layers. Therefore, employing uniform sampling strategies for different vegetation types and soil layer depths was reasonable here.

Although precise recommended sampling strategies are referential to areas with the same or similar climates, vegetation types and soils, the need for long-term rather than high frequency monitoring has wider applications. Nevertheless, for areas where differences in spatial patterns for SWC inter- or intra-seasons is weak, it is reasonable to infer that required sampling intervals and sampling periods could be less. Since previous studies have speculated that the effects of sampling strategies might be more variable under climates with strong seasonality, we consider that the results here represent an extreme scenario that allows for widespread adoption.

Acknowledgements. Financial support for this research was provided through the joint China-UK Red Soil Critical Zone project funded by the National Natural Science Foundation of China (NSFC: 41771263; 41571130053) and the United Kingdom Natural Environment Research Council (NE/N007611/1). Additional funding was provided by the “135 innovation project” from the Chinese Academy of Sciences (CAS:ISSASIP1648). Special thanks go to the staff of the Ecological Experimental Station of Red Soil of the Institute of Soil Science of CAS.

REFERENCES

- Biswas, A., 2014. Season- and depth-dependent time stability for characterizing representative monitoring locations of soil water storage in a hummocky landscape. *Catena*, 116, 38–50.
- Biswas, A., Si, B.C., 2011. Identifying scale specific controls of soil water storage in a hummocky landscape using wavelet coherency. *Geoderma*, 165, 50–59.
- Boulet, A., Prats, S.A., Malvar, M.C., González-Pelayo, O., Coelho, C.O.A., Ferreira, A.J.D., Keizer, J.J., 2015. Surface and subsurface flow in eucalyptus plantations in north-central Portugal. *J. Hydrol. Hydromech.*, 63, 193–200.
- Brandyk, A., Kiczko, A., Majewski, G., Kleniewska, M., Krukowski, M., 2016. Uncertainty of Deardorff's soil moisture model based on continuous TDR measurements for sandy loam soil. *J. Hydrol. Hydromech.*, 64, 23–29.
- Brocca, L., Melone, F., Moramarco, T., Morbidelli, R., 2010. Spatial-temporal variability of soil moisture and its estimation across scales. *Water Resour. Res.*, 46, W02516.
- Burns, T.T., Berg, A.A., Cockburn, J., Tetlock, E., 2016. Regional scale spatial and temporal variability of soil moisture in a prairie region. *Hydrol. Process.*, 30, 3639–3649.
- Buttafuoco, G., Castrignanò, A., Castrignano, E., Dimase, A.C., 2005. Studying the spatial structure evolution of soil water content using multivariate geostatistics. *J. Hydrol.*, 311, 202–218.
- Canton, V., Rodríguez-Caballero, E., Contreras, S., Villagarcía, L., Li, X.Y., Solé-Benet, A., Domingo, F., 2016. Vertical and lateral soil moisture patterns on a Mediterranean karst hillslope. *J. Hydrol. Hydromech.*, 64, 209–217.
- Cassel, D.K., Wendroth, O., Nielsen, D.R., 2000. Assessing spatial variability in an agricultural experiment station field: opportunities arising from spatial dependence. *Agron. J.*, 92, 706–714.
- Cho, E., Zhang, A., Choi, M., 2016. The seasonal difference in soil moisture patterns considering the meteorological variables throughout the Korean peninsula. *Terr. Atmos. Ocean. Sci.*, 27, 907–920.
- Choi, M., Jacobs, J.M., 2007. Soil moisture variability of root zone profiles within SMEX02 remote sensing footprints. *Adv. Water Resour.*, 30, 883–896.
- Cosh, M.H., Jackson, T.J., Bindlish, R., Prueger, J.H., 2004. Watershed scale temporal and spatial stability of soil moisture and its role in validating satellite estimates. *Remote Sens. Environ.*, 92, 427–435.
- Cosh, M.H., Jackson, T.J., Starks, P., Heathman, G., 2006. Temporal stability of surface soil moisture in the Little Washita River watershed and its applications in satellite soil moisture product validation. *J. Hydro.*, 323, 168–177.
- Dumedah, G., Coulibaly, P., 2011. Evaluation of statistical methods for infilling missing values in high-resolution soil moisture data. *J. Hydrol.*, 400, 95–102.
- Fader, M., von Bloh, M., Shi, S., Bondeau, A., Cramer, W., 2015. Modelling Mediterranean agro-ecosystems by including agricultural trees in the LPJmL model. *Geosci. Model. Dev.*, 8, 3545–3561.
- Gao, L., Shao, M.A., Wang, Y.Q., 2012. Spatial scaling of saturated hydraulic conductivity of soils in a small watershed on the Loess Plateau, China. *J. Soils Sediments*, 12, 863–875.
- Gao, L., Shao, M.A., Peng, X.H., She, D.L., 2015a. Spatio-temporal variability and temporal stability of water contents distributed within soil profiles at a hillslope scale. *Catena*, 132, 29–36.
- Gao, L., Lv, Y.J., Wang, D.D., Tahir, M., Peng, X.H., 2015b. Can shallow-layer measurements at a single location be used to predict deep soil water storage at the slope scale? *J. Hydrol.*, 531, 534–542.
- Gao, L., Lv, Y.J., Wang, D.D., Tahir, M., Biswas, A., Peng, X.H., 2016a. Soil water storage prediction at high space-time resolution along an agricultural hillslope. *Agric. Water Manag.*, 165, 122–130.
- Gao, X.D., Zhao, X.N., Brocca, L., Lv, T., Huo, G.P., Wu, P.T., 2016b. Upscaling of soil moisture content from surface to profile: multistation testing of observation operators. *Hydrol. Earth Syst. Sci. Discuss.* DOI: 10.5194/hess-2016-617.
- Gelhar, L.W., 1993. *Stochastic Subsurface Hydrology*. Prentice Hall, Englewood Cliffs, 390 p.
- Guber, A.K., Gish, T.J., Pachepsky, Y.A., van Genuchten, M.T., Daughtry, C.S.T., Nicholson, T.J., Cady, R.E., 2008. Temporal stability in soil water content patterns across agricultural fields. *Catena*, 73, 125–133.
- Heathman, G.C., Larose, M., Cosh, M.H., Bindlish, R., 2009. Surface and profile soil moisture spatio-temporal analysis during an excessive rainfall period in the Southern Great Plains, USA. *Catena*, 78, 159–169.
- Hu, W., Tallon, L.K., Si, B.C., 2012. Evaluation of time stability indices for soil water storage upscaling. *J. Hydrol.*, 475, 229–241.
- Hu, W., Si, B.C., 2016. Estimating spatially distributed soil water content at small watershed scales based on decomposi-

- tion of temporal anomaly and time stability analysis. *Hydrol. Earth Syst. Sci.*, 12, 6467–6503.
- Jarasiunas, G., Kinderiene, L., 2016. Impact of agro-environmental systems on soil erosion processes and soil properties on hilly landscape in Western Lithuania. *J. Environ. Eng. Landsc.*, 24, 60–69.
- Jenkins, G.M., Watts, D.G., 1968. *Spectral Analysis and its Applications*. Holden-Day, San Francisco, 525 p.
- Junqueira Junior, J.A., Mello, C.R., Owens, P.R., Mello, J.M., Curi, N., Alves, G.J., 2017. Time-stability of soil water content (SWC) in an Atlantic Forest - Latosol site. *Geoderma*, 288, 64–78.
- Korres, W., Reichenau, T.G., Fiener, P., Koyama, C.N., Bogen, H.R., Cornelissen, T., Baatz, R., Herbst, M., Diekkrüger, B., Vereecken, H., Schneider, H., 2015. Spatio-temporal soil moisture patterns – A meta-analysis using plot to catchment scale data. *J. Hydrol.*, 520, 326–341.
- Lai, R., 1998. Soil erosion impact on agronomic productivity and environment quality. *Crit. Rev. Plant Sci.*, 17, 319–464.
- Lee, E., Kim, S., 2017. Pattern similarity based soil moisture analysis for three seasons on a steep hillslope. *J. Hydrol.*, 551, 484–494.
- Li, X.Z., Shao, M.A., Jia, X.X., Wei, X.R., 2016. Profile distribution of soil–water content and its temporal stability along a 1340-m long transect on the Loess Plateau, China. *Catena*, 137, 77–86.
- Liu, B.X., Shao, M.A., 2014. Estimation soil water storage using temporal stability in four land uses over 10 years on the Loess Plateau, China. *J. Hydrol.*, 517, 974–984.
- Martínez-Fernández, J., Ceballos, A., 2005. Mean soil moisture estimation using temporal stability analysis. *J. Hydrol.*, 312, 28–38.
- Martínez, G., Pachepsky, Y.A., Vereecken, H., 2014. Temporal stability of soil water content as affected by climate and soil hydraulic properties: a simulation study. *Hydrol. Process.*, 28, 1899–1915.
- Martini, E., Wollschläger, U., Kögler, S., Behrens, T., Dietrich, P., Reinstorf, F., Schmidt, K., Weiler, M., Werban, U., Zacharias, S., 2015. Spatial and temporal dynamics of hillslope-scale soil moisture patterns: Characteristic states and transition mechanisms. *Vadose Zone J.*, 14, 4, vzj2014.10.0150. DOI: 10.2136/vzj2014.10.0150.
- Nasta, P., Penna, D., Brocca, L., Zuecco, G., Romano, N., 2018. Downscaling near-surface soil moisture from field to plot scale: A comparative analysis under different environmental conditions. *J. Hydrol.*, 557, 97–108.
- Pan, F., Pachepsky, Y., Jacques, D., Guber, A., Hill, R.L., 2012. Data assimilation with soil water content sensors and pedotransfer functions in soil water flow modeling. *Soil Sci. Soc. Am. J.*, 76, 829–844.
- Rivera, D., Lillo, M., Granda, S., 2014. Representative locations from time series of soil water content using time stability and wavelet analysis. *Environ. Monit. Assess.*, 186, 9075–9087.
- Shen, Q., Gao, G.Y., Hu, W., Fu, B.J., 2016. Spatial-temporal variability of soil water content in a cropland shelterbelt-desert site in an arid inland river basin of Northwest China. *J. Hydrol.*, 540, 873–885.
- Soil Survey Staff, 2010. *Keys to Soil Taxonomy*. 11th ed. United States Department of Agriculture, Natural Resources Conservation Service, Washington, 338 p.
- Starks, P.J., Heathman, G.C., Jackson, T.J., Cosh, M.H., 2006. Temporal stability of soil moisture profile. *J. Hydrol.*, 324, 400–411.
- Stockinger, M.P., Bogen, H.R., Lücke, A., Diekkrüger, B., Weiler, M., Vereecken, H., 2014. Seasonal soil moisture patterns: Controlling transit time distributions in a forested headwater catchment. *Water Resour. Res.*, 50, 5270–5289.
- Tahir, M., Lv, Y.J., Gao, L., Hallett, P.D., Peng, X.H., 2016. Soil water dynamics and availability for citrus and peanut along a hillslope at the Sunjia Red Soil Critical Zone Observatory (CZO). *Soil Till. Res.*, 163, 110–118.
- Vachaud, G., Passerat De Silans, A., Balabanis, P., Vauclin, M., 1985. Temporal stability of spatially measured soil water probability density function. *Soil Sci. Soc. Am. J.*, 49, 822–828.
- Vanderlinden, K., Vereecken, H., Hardelauf, H., Herbst, M., Martínez, G., Cosh, M.H., Pachepsky, Y., 2012. Temporal stability of soil water contents: A review of data and analysis. *Vadose Zone J.*, 11, 4, vzj2011.0178. DOI: 10.2136/vzj2011.0178.
- Wang, T.J., Wedin, D.A., Franz, T.E., Hiller, J., 2015a. Effect of vegetation on the temporal stability of soil moisture in grass-stabilized semi-arid sand dunes. *J. Hydrol.*, 521, 447–459.
- Wang, Y.Q., Hu, W., Zhu, Y.J., Shao, M.A., Xiao, S., Zhang, C.C., 2015b. Vertical distribution and temporal stability of soil water in 21-m profiles under different land uses on the Loess Plateau in China. *J. Hydrol.*, 527, 543–554.
- Wang, T.J., Liu, Q., Franz, T.E., Li, R.P., Lang, Y.C., Fiebrich, C.A., 2017. Spatial patterns of soil moisture from two regional monitoring networks in the United States. *J. Hydrol.*, 552, 578–585.
- Western, A.W., Blöschl, G., 1999. On the spatial scaling of soil moisture. *J. Hydrol.*, 217, 203–224.
- Zhang, P.P., Shao, M.A., Zhang, X.C., 2015. Scale-dependence of temporal stability of surface-soil moisture in a desert area in northwestern China. *J. Hydrol.*, 527, 1034–1044.
- Zhang, Z.B., Lin, L., Wang, Y., Peng, X.H., 2016. Temporal change in soil macropores measured using tension infiltrometer under different land uses and slope positions in subtropical China. *J. Soils Sediments*, 16, 854–863.
- Zhao, Y., Zhang, B., Hill, R., 2012. Water use assessment in alley cropping systems within subtropical China. *Agroforest Syst.*, 84, 243–259.
- Zhu, Q., Zhou, Z.W., Duncan, E.W., Lv, L.G., Liao, K.H., Feng, H.H., 2017. Integrating real-time and manual monitored data to predict hillslope soil moisture dynamics with high spatio-temporal resolution using linear and non-linear models. *J. Hydrol.*, 545, 1–11.
- Zreda, M., Shuttleworth, W., Zeng, X., Zweck, C., Desilets, D., Franz, T., Rosolem, R. 2012. COSMOS: the cosmic-ray soil moisture observing system. *Hydrology and Earth System Sciences*, 16, 4079–4099.

Received 23 January 2018
Accepted 5 September 2018

Estimation of water use of *Pinus tabulaeformis* Carr. in Loess Plateau of Northwest China

Shengqi Jian, Zening Wu, Caihong Hu*

College of Water Conservancy & Environmental, Zhengzhou University, Science road 100, Zhengzhou, China.

* Corresponding author. E-mail: jiansq@zzu.edu.cn

Abstract: Tree transpiration plays a determining role in the water balance of forest stands and in seepage water yields from forested catchments, especially in arid and semiarid regions where climatic conditions are dry with severe water shortage, forestry development is limited by water availability. To clarify the response of water use to climatic conditions, sap flow was monitored by heat pulse velocity method from May to September, 2014, in a 40-year-old *Pinus tabulaeformis* Carr. plantation forest stands in the semiarid Loess Plateau region of Northwest China. We extrapolated the measurements of water use by individual plants to determine the area-averaged transpiration of the woodlands. The method used for the extrapolation assumes that the transpiration of a tree was proportional to its sapwood area. Stand transpiration was mainly controlled by photosynthetically active radiation and vapor pressure deficit, whereas soil moisture had more influence on monthly change in stand transpiration. The mean sap flow rates for individual *P. tabulaeformis* trees ranged from 9 to 54 L d⁻¹. During the study period, the mean daily stand transpiration was 1.9 mm day⁻¹ (maximum 2.9 and minimum 0.8 mm day⁻¹) and total stand transpiration from May to September was 294.1 mm, representing 76% of the incoming precipitation over this period. Similar results were found when comparing transpiration estimated with sap flow measurements to the Penman–Monteith method (relative error: 16%), indicating that the scaling procedure can be used to provide reliable estimates of stand transpiration. These results suggested that *P. tabulaeformis* is highly effective at utilizing scarce water resources in semiarid environments.

Keywords: Sap flow; Transpiration; Scaling up; *Pinus tabulaeformis*; Loess Plateau.

INTRODUCTION

Land degradation is one of the most serious ecological problems in the world and is concerned by most countries (Liu et al., 2010; Moran et al., 2009). Desertification is a type of land degradation, which occurred in arid, semi-arid and part of semi-humid areas (Huang et al., 2011). It is induced by the un-coordination between population and land development, which results in soil erosion by water and wind (Duniway et al., 2010; Zuo, 2014). The vegetation restoration using woody species has been encouraged worldwide for gaining the multiple benefits (Malagnoux, 2007) such as soil erosion control (Huang et al., 2011), sediment reduction (Moran et al., 2009), hydrological regime regulation (Yaseef et al., 2009) and carbon sequestration (Zhao et al., 2011). However, woody species can consume more water by evapotranspiration than other vegetation types, such as natural grassland (Cao et al., 2009). Soils can also strongly dry out in both deeper and shallow soils after applying vegetation restoration (e.g., Cao et al., 2011; Wang et al., 2010; Yaseef et al., 2009). More extreme soil desiccation due to the initially promoted afforestation has led to negative impacts such as decreasing restoration effort (Liu et al., 2010; Rodríguez-Caballero et al., 2012; Wang et al., 2011), vegetation deterioration and difficulties in renewal and reforestation (Chen et al., 2008), unstable agriculture crop production (Wang et al., 2008), and decreasing ecosystem services (Chazdon, 2008; Liu et al., 2008).

To control the serious soil erosion and restore the degraded ecosystems of the Loess Plateau, large scale vegetation restoration programs have been implemented by the government since the 1950s (Fu et al., 2012; Issa et al., 2011). Fast-growing trees with wood of practical utility were selected historically in the vegetation restoration practice of the region. *Pinus tabulaeformis* Carr. have been regarded as a prominent reforestation species because of its advantages of drought tolerance, fast

growth, and wood utilization (Chen et al., 2008). However, there is a concern about the sustainability of these plantations with regard to their potentially high water consumption and a shortage of water resources in the region. Du et al. (2011) vapor pressure deficit, solar radiation and soil moisture had varying influences on sap flux density in *Robinia pseudoacacia*, *Quercus liaotungensis* and *Armeniaca sibirica*, the sap flow of these species was not very sensitive to changes in soil water conditions. The results suggested that typical indigenous species can manage the water consumption conservatively under both drought and wet conditions. Zhang et al. (2015) used Granier-type thermal dissipation probes in a black locust (*Robinia pseudoacacia*) plantation and up scaled stand transpiration from individual measurements of stem sap flow. they found that although the stand transpiration is controlled by multiple factors, those contributing to a significant difference vary with time scales. Some factors (e.g. soil moisture) may only be detected upon long-term observations. Similarly, Jiao et al. (2016) suggested that the black locust plantation has adapted to local soil water condition by reducing transpiration, and the major water loss from the plantation was not transpiration. There are no studies reporting stand-scale water use for *P. tabulaeformis*. There is thus an urgent need to quantitatively investigate the water use of these plantations for comprehensive understanding of their ecological properties and for water resource management on the region (Derak and Cortina, 2014; Zhang et al., 2009).

Plant water use can be quantified by several methods, for example the lysimeter method, the large-tree photometer method, the ventilated chamber method, the chemical tracer method, the isotopes tracer method, and thermally based sap-flow methods (Jiao et al., 2011). Among these methods, the sap flow methods make it feasible to estimate plant water use in situ with relatively high temporal resolution and very little disturbance to

the site. Moreover, the sap flow technique is the only method for investigating forest water use in some conditions, for example in forests on steep slopes or in very small forest stands. Four sap flow methods are currently available for quantification of plant water use in the field, including heat-pulse (Cortina et al., 2011), heat balance (Wang et al., 2013), thermal dissipation probe (TDP) (Granier, 1987) methods and heat field deformation (Han et al., 2012). All four sap flow methods are based on using the thermal dissipation properties of the water flow through the plant stem to estimate sap flux density. The TDP method, which was originally developed by Granier (1987), is now widely used in many studies of tree water use owing to the advantages of easy installation, simple sensor outputs recording, simple sap flow calculations, high accuracy and reliability, and relatively low cost. In homogeneous forests, estimates of water use by the TDP method agree well with estimates obtained by use of other sap flow methods or micrometeorological methods (Xiao et al., 2011). The TDP method is a reliable approach to measure forest tree water use, but which often influenced by environment factors; so it was necessary to investigate how sap flow varies with environmental factors, which would improve our general understanding of the water balance analysis for revegetation activities in the Loess Plateau, and provide a practical water management measure in such areas.

In current study, the TDP method was used to estimate water use of middle-aged *P. tabulaeformis* plantation in the semiarid region of Loess Plateau, China. We hypothesized that the TDP method would measure forest tree water use accurately. The main objective of the study was to estimate the stand-scale transpiration of plantations in the region. Additionally, for characterizing the stand-scale transpiration at this site, the among-tree variation and diurnal and seasonal patterns of the transpiration were analyzed for the growing season. The study would enrich the database to assess forest stand water balance and further provide valuable information for forest management in the region.

MATERIALS AND METHODS

Study area description

The study was conducted in the Anjiapo catchment, Dingxi County (35°35'N, 104°39'E) of Gansu province in western Chinese Loess Plateau (Fig.1). The annual precipitation (from 1956 to 2010) is 421 mm with great seasonal variations. Over

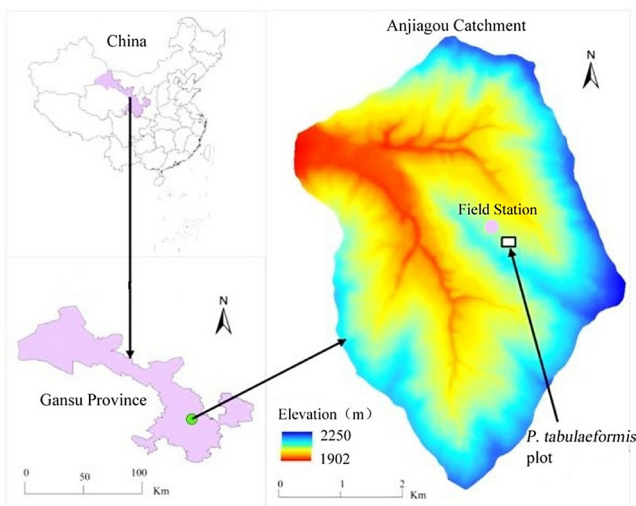


Fig. 1. Location of Anjiapo Catchment and the *P. tabulaeformis* plantation plot.

60% of the precipitation falls between July and September and over 50% occurs in form of storms. According to more than 50 years (1954–2004) of monitored data, the precipitation showed a decreased trend while the temperature continued to increase during the past decades, which means that the local climate has become drier and warmer. The mean annual pan evaporation is about 1515 mm, the annual mean temperature is 8.5°C, solar radiation is 932.6 MJ m⁻² per year, and the frost free period is 160 days (Bai and Wang, 2011; Zhang et al., 2010). The average depth to water table is over 50 m and the typical loess soil has a uniform texture and moderate permeability (0.1–1.2 cm min⁻¹) (Ma et al., 2012). Soil bulk density ranged from 1.03 g cm⁻³ to 1.51 g cm⁻³, water content at field capacity ranged from 15% to 23% (mass percentage) and at wilting moisture content is 5% (mass percentage) (Han et al., 2012; Zhang et al., 2010). Silt, clay, and sand content is 75.59%, 9.17% and 15.24%, respectively.

Sap flow measurements

The experiments were conducted in *P. tabulaeformis* plantation from May to September 2014. Three representative *P. tabulaeformis* experimental plots of 10 m × 10 m size were selected randomly on the south-facing slope of the Dianganliang Ridge in the Anjiapo catchment, for measurements of vegetation growth and sap flow. The *LAI* of the trees in the three plots was 2.65±0.31 (mean±SD), tree height was 10.15±3.64 m (mean±SD), and diameter at breast height (DBH) was 20.3±3.7 cm (mean±SD). The root distribution of *P. tabulaeformis* was shallow (Jian et al., 2015), more than 90% of the roots was concentrated in the 0–100 cm soil depth.

We used heat pulse meters (SF-L, Greenspan Technology Pty Ltd, Germany) to measure sap flow of *P. tabulaeformis*. A total of 18 *P. tabulaeformis* individuals, out of the three plots were selected (6 from each plot) representing a range of properties (Table 1; Fig. 2). The heat pulse velocity probes were installed in the tree stems at 130 cm above the soil surface, and implanted 20 mm deep into the xylem of each tree.

The wound diameter was 2 mm. Before insertion, each probe was coated with silicone gel to ensure good thermal contact between probe elements and sapwood. After insertion, the exposed cambium was covered with silicon gel to reduce evaporation, and then covered again with aluminum foil to minimize effects of ambient air temperature fluctuations and solar radiation (Swanson and Whitfield, 1981). The CR1000 data logger (Campbell Scientific, Logan, UT, USA) was used to record sap flux density every 10 minutes. Sap flow velocity (V_s , mm h⁻¹) was calculated following the method of Edwards and Booker (1984):

$$V_s = V_h' (0.505 F_m + F_i) \quad (1)$$

where, V_h' (mm h⁻¹) is the heat pulse velocity, F_m is the volume fraction of the woody material, and F_i is the volume fraction of water. The calculation of F_m and F_i for each tree required the following inputs: fresh weight (W_f , kg), oven-dried weight (W_d , kg), and weight of water in the same volume as the sapwood sample (W_i , kg). On this basis, F_m is:

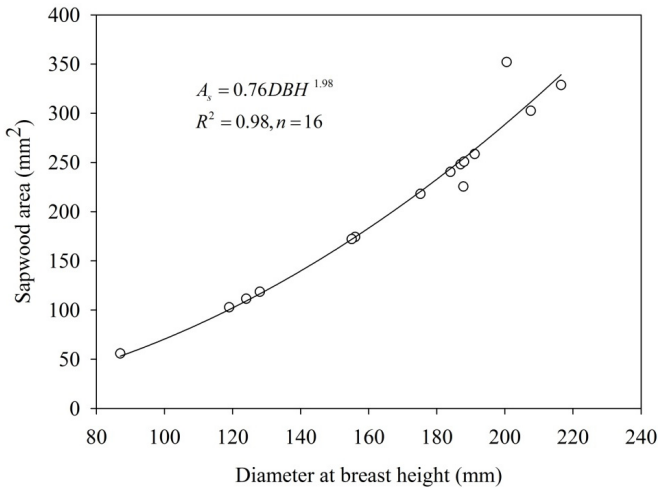
$$F_m = \frac{W_d}{1620W_i} \quad (2)$$

$$\text{and } F_i \text{ is: } F_i = \frac{W_f - W_d}{W_i} \quad (3)$$

Table 1. Tree height (TH), sapwood area (SA), and diameter at breast height (DBH) of each individual tree with sap flow measurements at three plots.

No.	Plot1			Plot2			Plot3		
	TH(m)	DBH(cm)	SA(cm ²)	TH(m)	DBH(cm)	SA(cm ²)	TH(m)	DBH(cm)	SA(cm ²)
1	9.68	19.1	2.58	10.25	19.2	3.21	13.65	19.5	3.11
2	13.21	21.1	3.11	11.26	20.3	3.34	12.68	20.4	3.52
3	11.53	17.5	2.18	8.54	17.6	2.63	12.14	21.6	3.13
4	11.52	20.6	3.02	8.64	17.5	2.55	10.62	18.6	2.94
5	8.83	20.3	2.84	9.52	18.7	3.05	9.57	17.9	2.73
6	7.51	18.7	2.51	7.68	19.6	3.09	9.77	17.1	2.66
A_c	--	--	54.13	--	--	59.57	--	--	57.29

Note: There were 20 trees in plot 1 and plot 2, respectively, 19 trees in plot 3. The total sapwood area in each plot (A_c) was calculated based on Fig. 2.


Fig. 2. The relationships between sapwood and diameter at breast height.

Sapwood sample was selected with five replications. Firstly, their W_f was measured. Secondly, sapwood sample was completely immersed into the distilled water. The distilled water was placed in the metering cylinder. The volume change between before immersed and after immersed were compared, and weight of water in the same volume as the sapwood sample, W_i was calculated. Finally, sapwood sample was put in the oven and oven-dried it at 80°C. Then, after W_d was determined, F_m and F_i were calculated. The averages of F_m and F_i were used to calculate the V_s value. The average values of F_m and F_i were 0.36 and 0.27, respectively.

Sap flux (SF , mm³ h⁻¹) is a function of the velocity of sap flow and the area of conducting wood in which the flow occurs:

$$SF = V_s A_c \quad (4)$$

where, A_c (mm²) is the area of conducting wood.

Daily cumulative sap flow (SF_c , kg d⁻¹) in sample trees is essentially equal to the daily sums of transpiration for time periods of one day or longer (Čermák et al., 1995). The dynamic response of the measured sap flow to atmospheric forcing occurred virtually immediately. SF was so tightly coupled to the climatic variables that no time shift was needed to fit a simple static microclimatic model to estimate SF (Blackman and Brodribb, 2011).

Tree transpiration (E_t , kg m⁻² d⁻¹) was expressed as sap flux on the sapwood area at breast height. In order to calculate sap flux (kg m⁻² h⁻¹) for a given tree, V_s (Eq. (1)) was divided by the sap wood area of the tree.

Tree-level sap flow was scaled up to the stand level to calculate stand transpiration (E_s , kg d⁻¹) based on the trees' estimated sapwood areas. We assumed that the water velocity on a given date was the same per unit of sap flow area (i.e., that

velocity did not vary within the sapwood in different trees). Therefore, E_s was estimated as:

$$E_s = \sum_{i=1}^n E_{si} = \sum_{i=1}^n E_{sti} \frac{A_{T,sw}}{A_{S,sw}} \quad (5)$$

where, E_{si} (kg d⁻¹) represents the stand transpiration on day i , E_{sti} (kg d⁻¹) represents the sample tree transpiration on day i , $A_{T,sw}$ (mm²) is the total stand's sapwood area, and $A_{S,sw}$ (mm²) is a given sample tree's sapwood area.

Canopy transpiration (E_c , mm d⁻¹) equals E_c weighted by the canopy's projected area. Crown projection areas were estimated from below the crown by sighting vertically at various positions around each tree. We measured the distances between the stem and the outermost projected point of the branches in all directions, and then drew the proportional lengths on standard cross-section paper to estimate the crowns' projection areas.

Meteorological measurements

An automated weather station (AG1000, Onset Computer Corporation, Pocasset, MA, USA) was situated located about 100 m away on an open field from the experimental field. The meteorological variables were wind speed and direction, air temperature, relative humidity, net and photosynthetically active radiation, soil temperature, soil moisture, soil heat flux, rainfall, and atmospheric pressure. The sensors were installed at two levels in 2 and 3 m above the ground. Rainfall was measured with a tipping-bucket rain gauge, 1.5 m above ground (model TE525, metric; Texas Electronics, Dallas, TX). Volumetric soil moisture was measured by means of TDR probes (Decagon Devices, Pullman, WA, USA), installed at four soil depths (10, 20, 30 and 40 cm). Also, soil water content was measured every 30 days by means of oven-drying to validate the soil moisture data provided by the probes during the study period. Soil bulk density was measured at each soil layer where the soil moisture probes were installed by cutting ring method.

The meteorological data were measured at a frequency of 10 Hz, recorded every 5 min using a CR1000 data logger (Campbell Scientific Inc., Logan, UT), then stored as 30-min mean values, whereas rainfall and wind data were stored as the 10-min mean values. We averaged the measured data in one day as the daily vapor pressure deficit and daily photosynthetically active radiation.

We used data from the weather station to estimate evapotranspiration with the Penman-Monteith equation (Allen et al., 1998):

$$ET_0 = \frac{0.408\Delta(R_n - G) + \gamma(900/T + 273)u_2(e_2 - e_a)}{\Delta + \lambda(1 + 0.34u_2)} \quad (6)$$

where R_n is net radiation at the plant surface (MJ m⁻² d⁻¹), G is

soil heat flux ($\text{MJ m}^{-2} \text{d}^{-1}$), Δ is vapor pressure curve slope ($\text{kPa } ^\circ\text{C}^{-1}$), γ is psychrometric constant ($\text{kPa } ^\circ\text{C}^{-1}$), T is mean air temperature ($^\circ\text{C}$), u_2 is wind speed at 2 m height (m s^{-1}), and $e_s - e_a$ is saturation vapor pressure deficit (kPa).

The plant evapotranspiration (ET_c) is given by:

$$ET_c = k_c \cdot ET_0 \quad (7)$$

where k_c is the crop coefficient. *P. tabulaeformis* is mature in our experiment, so in this paper, $k_c = 0.69$ for *P. tabulaeformis* (Wang et al., 2009).

$$T_c = ET_c - E_p \quad (8)$$

where T_c is the potential transpiration (mm day^{-1}) and E_p is the potential evaporation (mm day^{-1}), which is calculated (Jones, 1985) as follows:

$$E_p = ET_c \times (1 - 0.43LAI) \quad LAI \leq 1$$

$$E_p = \frac{ET_c}{1.1e^{-0.4LAI}} \quad LAI > 1 \quad (9)$$

where, LAI is the leaf area index. The actual plant transpiration (T_a) and actual soil evaporation (E_a) are presented as:

$$T_a = k_s \cdot T_c, \quad E_a = k_s \cdot E_p \quad (10)$$

where, k_s is the soil water stress coefficient, which is calculated as follows:

$$k_s = \frac{\ln(A_w + 1)}{\ln(101)}, \quad A_w = \frac{H - H_{wp}}{H_f - H_{wp}} \quad (11)$$

where, H is the soil water content, H_f is the field capacity, and H_{wp} is the wilting moisture.

Data analyses

Stepwise multiple regression analyses were carried out to analyze the relationships between daily changes in stand transpiration and environmental factors (soil water content, photosynthetically active radiation, vapor pressure deficit and potential evapotranspiration). All statistical analyses were conducted with the SPSS software package version 18.0 (IBM, USA). The regression equations were done using SigmaPlot version 11.0 (Systat Software, Chicago, Illinois, USA).

RESULTS

Diurnal variation of sap flow density

During the whole growing season, sap flow density in *P. tabulaeformis* had distinct diurnal variation. Three diurnal variation examples of sap flow density in *P. tabulaeformis* in a sunny day (1st June), a cloudy day (14th June) and a rainy day (18th June) were shown in Fig. 3. Sap flow density was small and relatively steady at night and before dawn under the three weather conditions. Sunny day: sap flow rate increased gradually after 6:30, reached a peak at 13:00, with a value of $0.184 \text{ cm}^3 \text{ cm}^{-2} \text{ min}^{-1}$, then gradually decreased after 14:30, sharply decreased after 18:00, and sap flow was low after 20:30. The results indicated that the sap flow rate in *P. tabulaeformis* had no significant ‘noon–depression’ phenomenon. At noon, it is possible that the stomata of *P. tabulaeformis* are not completely closed, so that transpiration continues. Sap flow density on cloudy and rainy days started to increase in the morning about 1 h later than on the sunny day (Fig. 3). In the sunny day, Q and D had the same trend with the daily course of sap flow density, clearly shown by the coincidentally high and low values (Fig. 3A), and there was 1–2 h time lag between sap flow and D , but no significant time lag with Q . Coefficients of determination (R^2) for the relation of Q and D with sap flow for the three days with different weather conditions (Table 2) show that high R^2 was found in sunny day, and low R^2 in rainy day.

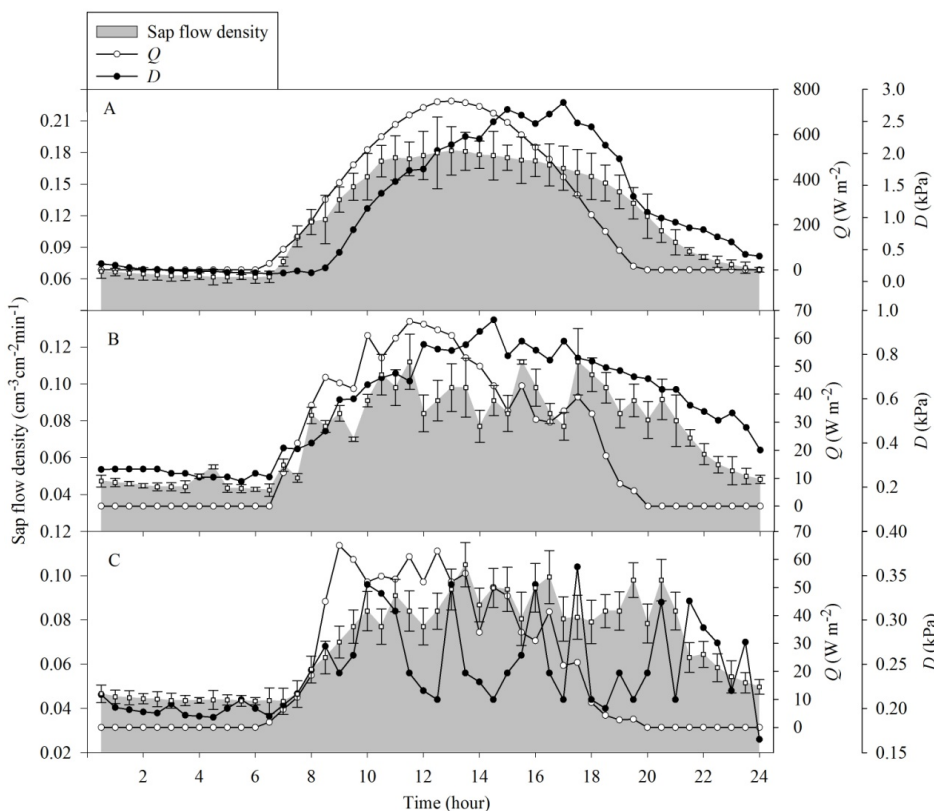


Fig. 3. Half-hourly patterns of photosynthetically active radiation (Q), vapour pressure deficit (D) and half-hourly patterns of sap flow density under different weather conditions for *P. tabulaeformis*. A, sunny day (1st June); B, cloudy day (14th June); C, rainy day (18th June). The values of sap flow density represent the mean \pm SD.

Table 2. Partially adjusted coefficients of determination R^2 and significance levels P for the relation between transpiration and significant environmental factors between sap flow density and significant environmental factors for days with three contrasting weather conditions. Half-hourly patterns of photosynthetically active radiation (Q), vapour pressure deficit (D).

Environment factors	Partial coefficient and significance	Weather conditions		
		Sunny day	Cloudy day	Rainy day
Q	R^2	0.847	0.381	0.115
	P	<0.0001	<0.05	0.16
D	R^2	0.816	0.324	0.109
	P	<0.0001	<0.05	0.09

Daily variations of stand transpiration

The observation period was hot, relatively rainy and humid (Figs. 4B and C). The mean daily transpiration of *P. tabulaeformis* was found to be 1.9 mm day^{-1} , ranging from 0.78 to 2.9 mm day^{-1} . The mean daily transpiration rates (mean \pm SD) in May, June, July, August and September were 1.8 ± 0.2 , 1.6 ± 0.3 , 2.2 ± 0.2 , 2.1 ± 0.2 , and $1.3\pm 0.3 \text{ mm day}^{-1}$, respectively. Cumulative transpiration determined with the sap flow method of 291.4 mm amounted to 89% of total rainfall of this period (Figs. 4A and C).

The higher transpiration (E_c) coincided with higher values of daily photosynthetically active radiation (Q_o) and mean daily vapour pressure deficit (D_z) normalized by daylight hours (Figs.

4A and B). Such as on 11st May and 17th June, transpiration rates were 2.21 and 2.45 mm day^{-1} . Water demand was low as a result of cloudy day. Daily patterns of transpiration of *P. tabulaeformis* showed relatively low values under sunny weather condition from 24th May to 8th June, experienced with 15 days dry period, although Q_o remained higher values (Figs. 4A, B and C).

Transpiration calculated with Penman–Monteith equation and measured with heat pulse method

Daily variations in stand transpiration measured with the heat pulse method (E_{HP}) were similar to the transpiration calculated with Penman–Monteith equation (E_{PM}). E_{PM} overestimated transpiration by about 16% for *P. tabulaeformis* in comparison with E_{HP} (Fig. 5).

Correlation between stand transpiration of *P. tabulaeformis* and the environmental factors

Volumetric soil water content of the soil layer from 0 to 10 cm was the highest and changed obviously with rainfall with standard deviation of 5.3%. Soil water contents and variation coefficient in deeper soil layers were relatively low (Fig. 6). Soil water content at 10 cm depth responded to rain events if the cumulative rainfall over a 3 to 5 days period exceeded 10 to 12 mm. Single rain events of less than 10 mm had little effect on soil water content at 20 cm, 30 cm and 40 cm depths (Fig. 6).

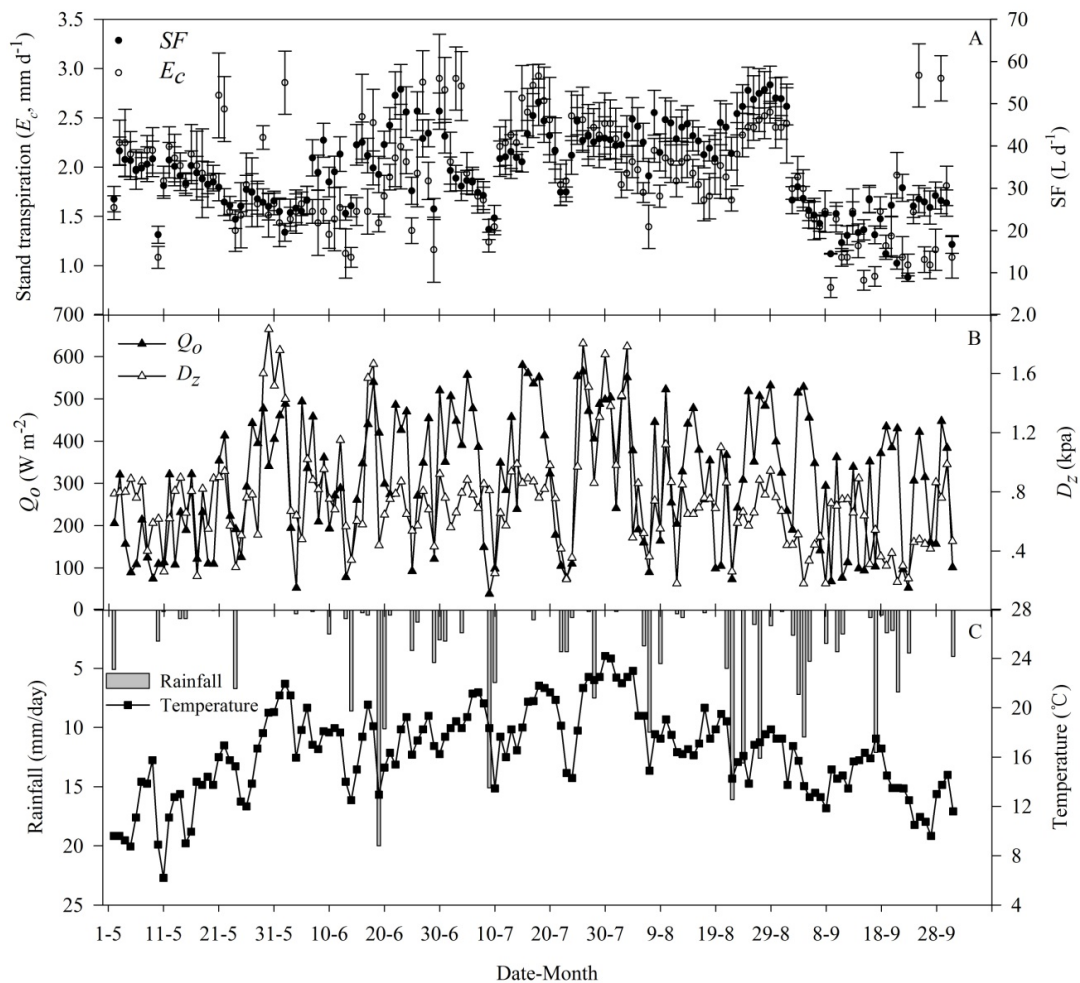


Fig. 4. Daily values for (A) sap flow rate and stand transpiration during the observation period (1st May to 30th September), data represent the mean values of the three plots for *P. tabulaeformis*. (B) Daily vapor pressure deficit (D_z) and daily photosynthetically active radiation (Q_o). (C) Temperature and precipitation. The values of E_c and SF represent the mean \pm SD.

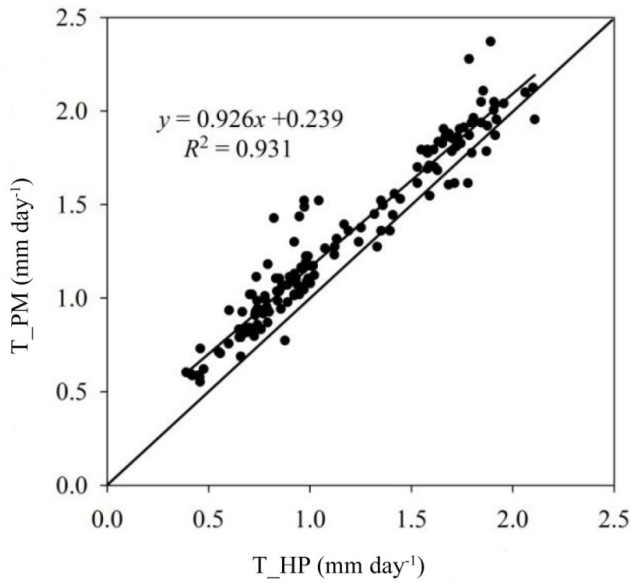


Fig. 5. Comparison between stand transpiration values determined by T_HP (the heat pulse method) and those calculated by T_PM (Penman–Monteith equation) throughout the observed period. Each data point represents a daily mean value.

Coefficients of determination (R^2) of daily vapor pressure deficit (D_z), daily photosynthetically active radiation (Q_o), air temperature (T_a), soil water content (SWC) and potential evapotranspiration (ET_0) versus stand transpiration in each month were presented in Table 3. During the experimental period, daily changes in transpiration correlated with Q_o ($R^2 = 0.305$ – 0.802) and D_z ($R^2 = 0.311$ – 0.824), however, in May the lowest values of R^2 were found. Meanwhile, SWC had the highest values of R^2 in May.

The multiple linear regression of the stand transpiration in each month of *P. tabulaeformis* with the SWC , D_z , Q_o , T_a , and ET_0 was presented in Table 4. The stand transpiration in *P. tabulaeformis* was correlated to D_z , Q_o and T_a in August. The SWC was the only factor affecting the stand transpiration in May. But the stand transpiration was related to D_z and Q_o in other months.

To elucidate response patterns of transpiration to environmental factors, daily mean transpiration was correlated with Q_o and D_z conditions obtained at the study site 2m above ground. Total transpiration increased sharply with D_z at low levels ($D_z < 0.9$ kPa), but tended to level off at higher D_z values (Fig. 7a). The data increases in Q_o up to values of 0–500 $W m^{-2}$ produced a reasonably linear increase in transpiration, after which transpiration tended to level off for higher values of Q_o (Fig. 7b).

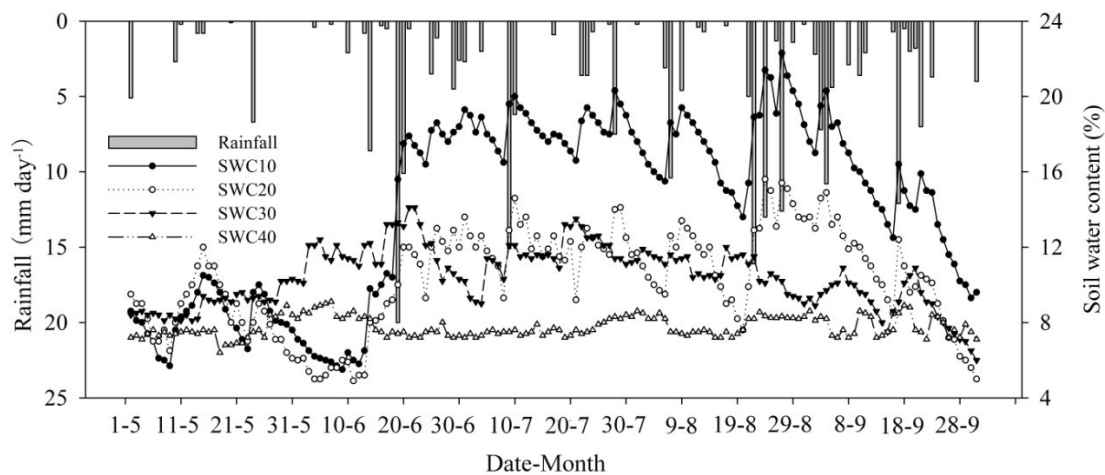


Fig. 6. The dynamic variation of rainfall events and volumetric soil water contents in 10 cm (SWC10), 20 cm (SWC20), 30 cm (SWC30), and 40 cm (SWC40) below the soil surface.

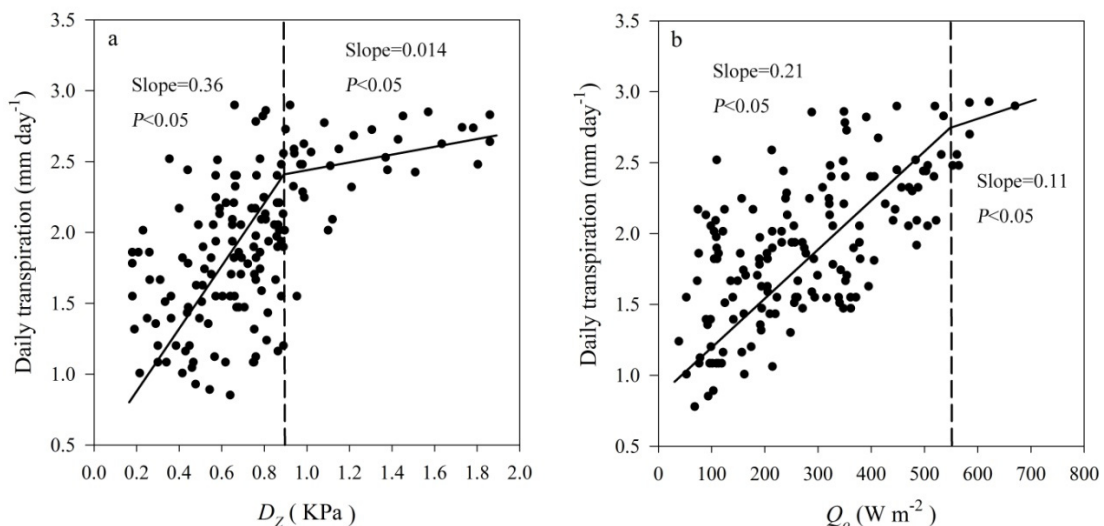


Fig. 7. The relationships between daily mean transpiration rate and daily vapor pressure deficit (D_z) and daily photosynthetically active radiation (Q_o).

Table 3. Partially adjusted coefficients of determination R^2 and significance levels P for the relation between transpiration and significant environmental factors such as daily vapor pressure deficit (D_z), daily photosynthetically active radiation (Q_0), air temperature (T_a), soil water content (SWC), and potential evapotranspiration (ET_0), for May, June, July, August, and September 2014; the number of values is $n = 153$.

Environment factors	Partial coefficient and significance	Month				
		May	June	July	August	September
Q_0	R^2	0.305	0.765	0.783	0.802	0.711
	P	<0.05	<0.0001	<0.0001	<0.0001	<0.0001
D_z	R^2	0.311	0.824	0.694	0.733	0.795
	P	<0.05	<0.0001	<0.0001	<0.0001	<0.0001
T_a	R^2	0.502	0.514	0.465	0.672	0.582
	P	<0.01	<0.01	<0.01	<0.01	<0.01
SWC	R^2	0.802	0.505	0.306	0.415	0.426
	P	<0.0001	<0.01	<0.01	<0.01	<0.01
ET_0	R^2	0.311	0.206	0.453	0.336	0.240
	P	<0.05	<0.05	<0.05	<0.05	<0.05

Table 4. The multiple linear correlation equations between daily stand transpiration (E_c), and environmental factors for individual months during the observation period (1st May–30th September 2014) for *P. tabulaeformis*; n is number of values (days); the independent variables are daily vapor pressure deficit (D_z), daily photosynthetically active radiation (Q_0), daily mean air temperature (T_a), soil water content (SWC) and potential evapotranspiration (ET_0).

Month	Regression equations	R^2	F	n
May	$E_c = 0.986 + 0.197SWC$	0.756*	49.866	31
June	$E_c = 2.034 + 0.502 D_z + 1.345 \times 10^{-3} Q_0$	0.806*	60.234	30
July	$E_c = 2.037 + 0.366 D_z + 1.215 \times 10^{-3} Q_0$	0.824*	55.122	31
August	$E_c = 3.345 + 0.157 D_z + 1.005 \times 10^{-3} Q_0 - 8.64 \times 10^{-2} T_a$	0.836*	50.475	31
September	$E_c = 1.976 + 0.119 D_z + 2.034 \times 10^{-3} Q_0$	0.791*	63.120	30

*indicates significant difference ($P < 0.05$).

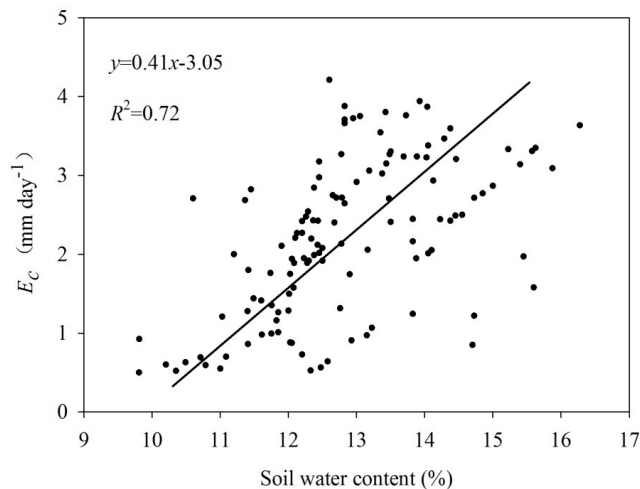


Fig. 8. Changes in E_c in response to changes in soil moisture at 0–40 cm below the soil surface. Curves represent the results of linear regression

The results revealed that the variation in sap velocity could be expressed as a linear function of soil moisture (Fig. 8), and the regression equation had a high coefficient of determination (R^2).

DISCUSSION

Comparison between *P. tabulaeformis* transpiration and total evaporation

Our results showed an underestimation of transpiration determined by the sap flow method, as compared with the Penman–Monteith equation. That was in contradiction to those of authors who conclude that the extrapolation of stem-level flows to the transpiration of a canopy often produces a systematic overestimation of transpiration (Duniway et al.,

2010; Ma et al., 2001; Wang et al., 2009). The steady-state assumption of a constant proportionality between sap flow rates and leaf area for all stems is generally advanced to explain this overestimation. The small discrepancy between sap flow method and Penman–Monteith equation might be due to two different factors in our case. First, the calculated *P. tabulaeformis* transpiration rate was assumed to be nearly equal to the sum of the transpiration from all sunlit leaves, and the majority of leaves were assumed to be sunlit. However, a more accurate value of total leaf area of a *P. tabulaeformis* might be slightly greater than that obtained from the field, though there were no experimental data to confirm this in the present study. The second possible source of error may be that the contribution of evaporation from the soil surface in the Penman–Monteith equation is not taken into account by the sap flow method. Subtracting soil evaporation from total evaporation, Fig. 5 could give acceptable results with daily differences of less than 16% between the sap flow method extrapolated to whole *P. tabulaeformis* and Penman–Monteith equation, suggesting that sap flow measurements can be used to provide reliable estimates of stand transpiration in the study area.

Transpiration variation

In previous studies, sap flow was measured by heat pulse method in similar environmental condition; sap flow of individual longleaf pine was 2–142 L d⁻¹ (Bosch et al., 2014) and the stand-level transpiration of Norway spruce was 1.4–2.8 mm d⁻¹ (Alsheimer et al., 1998). These values agreed closely with those obtained for *P. tabulaeformis* in the current study (9–56 L d⁻¹). In the whole growing season, the sap wood area of *P. tabulaeformis* varied regularly from day to night, especially on sunny days (Fig. 3). Giorio and Giorio (2003) also reported that the variation of sap flow for olive tree in the sunny days was greater than in the cloudy days. Xiong et al. (2003) pointed out

that the sap flow of *Larix principis-rupprechtii*, which was one of the most principal species for afforestation in northwest China, changes regularly from day to night in later growth season in both typical sunny and cloudy days, but the sap flow rate in the sunny days was greater than that of the cloudy days. In the night, the sap flow rate was slow and rapidly increased with the solar radiation and air temperature in the morning. Yan et al. (1999) reported that *Juglans mandshurica* had several peaks during a single day of sap flow rate, and sap flow continued during night, but sap flow rate was much lower and maintained constant. Sun et al. (2002) also indicated that night sap flow rate of *Betula platyphylla* was only 11–40 % of that of the day and the variation of sap flow rate in sunny days was greater than that of cloudy days. In the current study, sap flow rates in different weather conditions had different influence factors. The diurnal and seasonal variations of sap flow rate in *P. tabulaeformis* under different weather conditions were in agreement with the previous studies.

Although *P. tabulaeformis* is regarded as a tree species of potentially high water consumption in the region, in our research, however, total stand transpiration of the *P. tabulaeformis* plantation (about 40 years) was 291.4 mm during the growing season of 2014 and related to environmental factors. The relatively small estimates of stand transpiration can be attributed to the low sap wood area of the stand. However, considering the relatively low *P. tabulaeformis* and the age of the plantation, questions are arising about whether the stand transpiration of the young growth of *P. tabulaeformis* in the same region is higher, and how much stands of corresponding ages in a valley site transpire. These issues should be considered carefully when assessing and analyzing long-term water budgets of *P. tabulaeformis* plantations in relation to their growth and sustainability in the region.

The response of sap flow to environmental factors

Zhang et al. (2009) indicated that D_z and solar radiation affected the stand transpiration of apple trees (*Malus domestica* Borkh.) greatly and the sap flow rate increased with the D_z and solar radiation in the sunny days (Xiong et al., 2003). The average daily stand transpiration of two eucalyptus (*Eucalyptus urophylla* S. T. Blake) plantations was significantly related to available soil water content and daily D_z (Yin et al., 2003). In the experiment presented in this article, the trunk sap flow rate in *P. tabulaeformis* was found as the function of the D_z and Q_0 , but the two environmental factors affecting the sap flow rate varied in each month. An another study in northeast China showed that air temperature, relative humidity, and Q_0 were also the major three factors affecting sap flow rate of *Betula platyphylla* on clear days, but the importance of the three factors was varied in different growth stages (Sun et al., 2002).

The soil surface was often considered as a source of water vapor as important as plant leaves (Rodríguez-Caballero et al., 2012). The transpiration response of *P. tabulaeformis* to greater water use was shown to exhibit low R^2 values with increasing Q_0 and D_z (Table 3), indicating that Q_0 and D_z were not the single influenced factors, considering the low rainfall of 16.4 mm in May (Fig. 4C).

Transpiration was frequently restricted by soil water availability in the upper soil profile, but *P. tabulaeformis* could still meet their water demand. The transpiration rates maintained high values, despite high temperature and intense radiation on representative clear days for *P. tabulaeformis* (Figs. 4A and B). This was due to the deeper, more developed rooting systems. Our previous study had reported that the root distribution pat-

terns of *P. tabulaeformis* in the same area (Jian et al., 2014). The roots of *P. tabulaeformis* can reach as deep as 2.8 m. The majority of uptake roots were concentrated in the upper 1.0 m of soil (Liu et al., 2012). Root water uptake from deeper soil layer, transported to the upper soil layer at night. This phenomenon was very important in arid and semi-arid area, which can make the plants maintain the transpiration (Gao et al., 2011).

CONCLUSIONS

Because of insufficient water availability in the semiarid region of Loess Plateau, accurate estimation of water consumption by a forest stand is crucial for understanding water-use characteristics. Use of the sap flow method enabled us to quantify forest stand transpiration in this loess hill and gullied area, because stand transpiration can be estimated by monitoring the sap flow in stems without consideration of ground unevenness and topographical heterogeneity. Further studies, including investigations of transpiration of *P. tabulaeformis* with different age classes and of understory vegetation, evaporation of soil and tree canopies, and other water flow elements in stand, for example runoff, are required to resolve these uncertainties.

Acknowledgement. This project was supported by National Key Research Priorities Program of China (2016YFC0402402); National Natural Science Foundation of China (31700370); The Special Research Fund of Yellow River Institute of Hydraulic Research (HKY-JBYW-2018-10); Drought Meteorological Science Research fund (IAM201705); National Natural Science Foundation of China (51409116); Startup Research Fund of Zhengzhou University (1512323001); Institution of higher learning key scientific research project, Henan Province (16A570010); China postdoctoral science foundation (2016M602255); Henan province postdoctoral science foundation.

REFERENCES

- Allen, R.G., Pereira, L.S., Reas, D., Smith, M., 1998. Crop evapotranspiration guidelines for computing crop water requirements. FAO Irrigation and Drainage Paper 56. Food and Agriculture Organization of the United Nations, Rome, Italy.
- Alsheimer, M., Köstner, B., Falge, E., Tenhunen, J.D., 1998. Temporal and spatial variation in transpiration of Norway spruce stands within a forested catchment of the Fichtelgebirge, Germany. *Ann. For. Sci.*, 55, 103–124.
- Bai, Y., Wang, Y., 2011. Spatial variability of soil chemical properties in a Jujube slope on the Loess Plateau of China. *Soil Sci.*, 176, 10, 550–558.
- Blackman, C.J., Brodribb, T.J., 2011. Two measures of leaf capacitance: insights into the water transport pathway and hydraulic conductance in leaves. *Funct. Plant Biol.*, 38, 2, 118–126.
- Bosch, D.D., Marshall, L.K., Teskey, R., 2014. Forest transpiration from sap flux density measurements in a Southeastern Coastal Plain riparian buffer system. *Agric. For. Meteorol.*, 187, 72–82.
- Cao, L., Zhang, K., and Zhang, W. 2009. Detachment of road surface soil by flowing water. *Catena*, 76, 2, 155–162.
- Cao, C.Y., Jiang, S.Y., Zhang, Y., Zhang, F.X., Han, X.S., 2011. Spatial variability of soil nutrients and microbiological properties after the establishment of leguminous shrub *Caragana microphylla* Lam. plantation on sand dune in the Horqin Sandy Land of Northeast China. *Ecol. Eng.*, 37, 10, 1467–1475.
- Čermák, J., Cienciala, E., Kučera, J., 1995. Individual variation of sap-flow rate in large pine and spruce trees and stand transpiration: a pilot study at the central. *J. Hydrol.*, 168, 109–120.
- Chazdon, R.L., 2008. Beyond deforestation: restoring forests and ecosystem services on degraded lands. *Science*, 320, 5882, 1458–1460.

- Chen, H.S., Shao, M.A., Li, Y.Y., 2008. Soil desiccation in the Loess Plateau of China. *Geoderma*, 143, 1–2, 91–100.
- Cortina, J., Amat, B., Castillo, V., Fuentes, D., Maestre, F.T., Padilla, F., Rojo, L., 2011. The restoration of vegetation cover in the Iberian southeast. *J. Arid Environ.*, 75, 12, 1377–1384.
- Du, S., Wang, Y.L., Kume, T., Zhang, J.G., Otsuki, K., Yamanaka, N., Liu, G.B., 2011. Sapflow characteristics and climatic responses in three forest species in thesemiarid Loess Plateau region of China. *Agric. For. Meteorol.*, 151, 1–10.
- Duniway, M.C., Snyder, K.A., Herrick, J.E., 2010. Spatial and temporal patterns of water availability in a grass–shrub ecotone and implications for grassland recovery in arid environments. *Ecohydrology*, 3, 1, 55–67.
- Derak, M., Cortina, J., 2014. Multi-criteria participative evaluation of *Pinus halepensis* plantations in a semiarid area of southeast Spain. *Ecol. Indic.*, 43, 8, 56–58.
- Edwards, W.R.N., Booker, R.E., 1984. Radial variation in the axial conductivity of *Populus* and its significance in heat pulse velocity measurement. *J. Exp. Bot.*, 35, 551–561.
- Fu, W., Huang, M., Gallichand, J., Shao, M.A., 2012. Optimization of plant coverage in relation to water balance in the Loess Plateau of China. *Geoderma*, 173, 134–144.
- Gao, X., Wu, P., Zhao, X., Shi, Y., Wang, J., 2011. Estimating spatial mean soil water contents of sloping jujube orchards using temporal stability. *Agric. Water Manage.*, 102, 1, 66–73.
- Giorio, P., Giorio, G., 2003. Sap flow of several olive trees estimated with the heat-pulse technique by continuous monitoring of a single gauge. *J. Exp. Bot.*, 49, 9–20.
- Granier, A., 1987. Evaluation of transpiration in a Douglas-fir stand by means of sap flow measurements. *Tree Physiol.*, 3, 309–319.
- Huang, M.B., Barbour, S.L., Si, B.C., Elshorbagy, A., Zettl, J., 2011. Infiltration and drainage processes in multi-layered coarse soils. *Can. J. Soil Sci.*, 91, 2, 169–183.
- Han, L. X., Wang, Y. K., Li, X. B., Zhang, P., 2012. Improved irrigation scheduling for pear-jujube trees based on trunk diameter sensing data. *Afr. J. Biotech.*, 11, 7, 1597–1606.
- Issa, O.M., Valentin, C., Rajot, J.L., Cerdan, O., Desprats, J.F., Bouchet, T., 2011. Runoff generation fostered by physical and biological crusts in semi-arid sandy soils. *Geoderma*, 167–168, 1, 22–29.
- Jiao, F., Wen, Z.M., An, S.S., 2011. Changes in soil properties across a chronosequence of vegetation restoration on the Loess Plateau of China. *Catena*, 86, 2, 110–116.
- Jiao, L., Lu, N., Sun, G., Ward, E.J., Fu, B.J., 2016. Biophysical controls on canopy transpiration in a black locust (*Robinia pseudoacacia*) plantation on the semi-arid Loess Plateau, China. *Ecohydrology*, 9, 1068–1081.
- Jian, S.Q., Zhao, C.Y., Fang, S.M., Yu, K., 2015. The distribution of fine root length density for six artificial afforestation tree species in Loess Plateau of Northwest China. *Forest Sys.*, 43, 1, 1–9.
- Jones, C., 1985. CERES-Maize: a stimulation model of maize growth and development. NTIS, Springfield, Virginia, USA.
- Liu, J.G., Li, S.X., Ouyang, Z.Y., Tam, C., Chen, X.D., 2008. Ecological and socioeconomic effects of China's policies for ecosystem services. *Proc. Natl. Acad. Sci. USA* 105, 28, 9477–9482.
- Liu, W.Z., Zhang, X.C., Dang, T.H., Ouyang, Z., Li, Z., Wang, J., Wang, R., Gao, C.Q., 2010. Soil water dynamics and deep soil recharge in a record wet year in the southern Loess Plateau of China. *Agric. Water Manage.*, 97, 8, 1133–1138.
- Liu, C., Du, T., Li, F., Kang, S., Li, S., Tong, L., 2012. Trunk sap flow characteristics during two growth stages of apple tree and its relationships with affecting factors in an arid region of northwest China. *Agric. Water Manage.*, 104, 2, 193–202.
- Ma, L.Y., Sun, P.S., Ma, L.Y., 2001. Sapwood area calculation and water use scaling up from individual trees to stands of Chinese pine and black locust. *Journal of Beijing Forestry University*, 23, 4, 1–5 (In Chinese with English abstract).
- Ma, L.H., Wu, P.T., Wang, Y.K., 2012. Spatial distribution of roots in a dense jujube plantation in the semiarid hilly region of the Chinese Loess Plateau. *Plant Soil*, 354, 1–2, 57–68.
- Malagnoux, M., 2007. *Arid Land Forests of the World: Global Environmental Perspectives*. FAO, Rome.
- Moran, M.S., Scott, R.L., Keefer, T.O., Emmerich, W.E., Hernandez, M., Nearing, G.S., Paige, G.B., Cosh, M.H., O'Neill, P.E., 2009. Partitioning evapotranspiration in semiarid grassland and shrubland ecosystems using time series of soil surface temperature. *Agric. For. Meteorol.*, 149, 1, 59–72.
- Rodríguez-Caballero, E., Cantón, Y., Chamizo, S., Afana, A., Solé-Benet, A., 2012. Effects of biological soil crusts on surface roughness and implications for runoff and erosion. *Geomorphology*, 145–146, 4, 81–89.
- Sun, H.Z., Zhou, X.F., Zhao, H.X., 2002. A research on stem sap flow dynamic of *Betula platyphylla*. *Acta Ecologica Sinica*, 22, 9, 1387–1391.
- Swanson, R.H., Whitfield, D.W.A., 1981. A numerical analysis of heat pulse velocity theory and practice. *J. Exp. Bot.*, 32, 1, 221–239.
- Wang, X.L., Sun, G.J., Jia, Y., Li, F.M., Xu, J.Z., 2008. Crop yield and soil water restoration on 9-year-old alfalfa pasture in the semiarid Loess Plateau of China. *Agric. Water Manage.*, 95, 3, 190–198.
- Wang, Y.Q., Fan, J., Shao, M.A., 2009. Evapotranspiration of three types of plants in water–wind erosion crisscross regions in the Loess Plateau. *Acta Ecol. Sin.*, 29, 10, 5386–5394. (In Chinese with English abstract).
- Wang, Y.Q., Shao, M.A., Shao, H.B., 2010. A preliminary investigation of the dynamic characteristics of dried soil layers on the Loess Plateau of China. *J. Hydrol.*, 381, 1–2, 9–17.
- Wang, Y.Q., Shao, M.A., Zhu, Y.J., Liu, Z.P., 2011. Impacts of land use and plant characteristics on dried soil layers in different climatic regions on the Loess Plateau of China. *Agric. For. Meteorol.*, 151, 4, 437–448.
- Wang, B., Zhang, G.H., Shi, Y.Y., Zhang, X.C., 2013. Effect of natural restoration time of abandoned farmland on soil detachment by overland flow in the Loess Plateau of China. *Earth Surf. Proc. Land.*, 38, 14, 1725–1734.
- Xiao, B., Wang, Q., Zhao, Y., Shao, M., 2011. Artificial culture of biological soil crusts and its effects on overland flow and infiltration under simulated rainfall. *Appl. Soil Ecol.*, 48, 1, 11–17.
- Xiong, W., Wang, Y.H., Xu, D.Y., 2003. Regulation of water use for transpiration of *Larix Principi-Rupprechtii* plantation and its response on environmental factors in southern Ningxia Hilly area. *Scientia Silvae Sinicae*, 39, 2, 1–7.
- Yan, C.R., Downey, A., Han, X.G., Chen, L.Z., 1999. A study on sap flow *Juglans mandshurica* of growth season in deciduous broadleaf forest Beijing mountain area. *Acta Ecologica Sinica*, 37, 6, 793–797.
- Yaseef, N.R., Yakir, D.E., Rotenberg, S.G., Cohen, S., 2009. Ecophysiology of a semi-arid forest: partitioning among water balance components and its implications for predicted precipitation changes. *Ecophysiology*, 3, 2, 143–154.
- Yin, G.C., Zhou, G.Y., Wang, X., Chu, G.W., Huang, Z.H., 2003. A study on sap flow rate density of two eucalyptus (*Eucalyptus ueophylla*) plantation in southeastern China by heat-pulse method. *Acta Ecologica Sinica*, 23, 10, 1984–1990.
- Zhang, G.H., Tang, M.K., Zhang, X.C., 2009. Temporal variation in soil detachment under different land uses in the Loess Plateau of China. *Earth Surf. Proc. Land.*, 34, 9, 1302–1309.
- Zhang, P., Wang, Y.K., Zhan, J.W., Wang, X., Peng, W., 2010. Scheduling irrigation for jujube (*Ziziphus jujuba* Mill.). *Afr. J. Biotech.*, 35, 5694–5703.
- Zhang, J.G., Guan, J.H., Shi, W.Y., Yamanaka, N., Du, S., 2015. Inter annual variation in stand transpiration estimated by sap flow measurement in a semi-arid black locust plantation, Loess Plateau, China. *Ecophysiology*, 8, 137–147.
- Zhao, Y., Peth, S., Hallett, P., Wang, X.Y., Giese, M., Gao, Y.Z., Horn, R., 2011. Factors controlling the spatial patterns of soil moisture in a grazed semi-arid steppe investigated by multivariate geostatistics. *Ecophysiology*, 4, 1, 36–48.
- Zuo, Q.T., Hu, D.S., Dou, M., Zhang, X., Ma, J.X., 2014. Framework and Core System of the Most Stringent Water Resource Management System Based on the Concept of Human-Water Harmony. *Resour. Sci.*, 36, 5, 906–912. (In Chinese with English abstract)

Received 6 July 2017

Accepted 12 June 2018

The influence of observed and modelled net longwave radiation on the rate of estimated potential evapotranspiration

Jitka Kofroňová^{1,2*}, Miroslav Tesař¹, Václav Šípek¹

¹ The Institute of Hydrodynamics of the Czech Academy of Sciences, Pod Pařankou 30/5, Prague, 166 12, Czech Republic.

² Department of Physical Geography and Geocology, Faculty of Science, Charles University in Prague, Albertov 6, Prague, 128 43, Czech Republic.

* Corresponding author. E-mail: kofronova@ih.cas.cz

Abstract: Longwave radiation, as part of the radiation balance, is one of the factors needed to estimate potential evapotranspiration (PET). Since the longwave radiation balance is rarely measured, many computational methods have been designed. In this study, we report on the difference between the observed longwave radiation balance and modelling results obtained using the two main procedures outlined in FAO24 (relying on the measured sunshine duration) and FAO56 (based on the measured solar radiation) manuals. The performance of these equations was evaluated in the April–October period over eight years at the Liz experimental catchment and grass surface in the Bohemian Forest (Czech Republic). The coefficients of both methods, which describe the influence of cloudiness factor and atmospheric emissivity of the air, were calibrated. The Penman-Monteith method was used to calculate the PET. The use of default coefficient values gave errors of 40–100 mm (FAO56) and 0–20 mm (FAO24) for the seasonal PET estimates (the PET was usually overestimated). Parameter calibration decreased the FAO56 error to less than 20 mm per season (FAO24 remained unaffected by the calibration). The FAO56 approach with calibrated coefficients proved to be more suitable for estimation of the longwave radiation balance.

Keywords: Radiation balance; Longwave radiation; Potential evapotranspiration; Penman-Monteith; Calibration.

INTRODUCTION

Evapotranspiration is one of the main fluxes in the global water cycle and is the dominant controlling factor of climate and hydrology at the local and global scales. In terms of quantity, it is the second most dominant process (after precipitation) of dry land hydrology, accounting for approximately 65% of the precipitation returning to the atmosphere (Shi et al., 2008). It affects agricultural water use, ecosystem functioning and aridity/humidity conditions. It is also a fundamental factor controlling energy and mass exchange between terrestrial ecosystems and the atmosphere (Fischer et al., 2005).

The overall process of evapotranspiration is determined by two main factors: firstly by the amount of available energy, and secondly by the amount of available water. Potential evapotranspiration (PET) represents its maximum rate under conditions of sufficient water supplies. Hence, PET is primarily affected by weather parameters and surface characteristics (Allen et al. 1998, Yin et al., 2008). Several equations for the estimation of PET have been designed, each of which corresponds to site-specific conditions. In general, three distinct approaches can be identified: aerodynamic (Dalton, 1802), energy balance (Pristley and Taylor, 1972) and a combined approach (Penman, 1948). The energy necessary for the process of evapotranspiration is primarily represented by incoming shortwave solar radiation. The significant effect of longwave radiation (emitted mainly by the Earth and the atmosphere) on the total radiation balance has also been documented (e.g. by Duarte et al., 2006; Kjaersgaard et al., 2009; Temesgen et al., 2007). The longwave radiation serves as a cooling mechanism for the Earth's surface and hence reduces the available energy for the evaporation. Nevertheless, studies quantifying the influence of the net longwave radiation balance on the PET values are sparse (e.g. Yin et al., 2008). Net radiation (Rn) is an elementary variable used in several methods of PET estimation based on the energy

balance, and represents the difference between the total incoming and outgoing radiation fluxes, i.e. net shortwave radiation (Rns) and net longwave radiation (Rnl) (Allen et al., 1998; Irmak et al., 2010). Rns is typically measured using pyranometers, and is readily available at numerous meteorological stations. However, measurements of Rnl are limited due to technical and economic factors (Carmona et al., 2017; Irmak et al., 2010; Temesgen et al., 2007). Radiation formulas from FAO56 (Allen et al., 1998, Rn_{FAO56}) and FAO24 (Doorenbos and Pruitt, 1977, Rn_{FAO24}) are therefore often used to estimate this quantity. The Rn_{FAO56} equation is based on the ratio of the observed to the maximum possible incoming shortwave radiation, while the Rn_{FAO24} equation is based on the ratio of the actual duration of sunshine to the maximum possible duration of daylight hours. Since the data of actual duration of sunshine for Rn_{FAO24} is often unavailable, the FAO56 method serves as a basis for the estimation of Rnl (Kjaersgaard et al., 2009). However, these formulas cannot be used universally, meaning that a comparison with site-specific conditions is necessary (Matsui and Osawa, 2015). They contain several coefficients recommended by Allen et al. (1998) that originate in local calibration based on site-specific conditions. Multiple authors reported that different empirical coefficients work better for model-based representations in different locations (Arellano et al., 2016; Carmona et al., 2017; Irmak et al., 2003a; Kjaersgaard et al., 2007b; Yin et al., 2008). The reason is that besides the surface temperature the longwave radiation (both outgoing and incoming) is influenced by local conditions, e.g. by soil type, structure of vegetation, influence of nearby high trees or buildings, concentration of CO₂ and water vapour, and the presence of clouds and dust particles in the atmosphere (Allen et al., 1998). However, only some of these factors are taken into account in the above mentioned equations (cloudiness factor and atmospheric emissivity). The variability in the remaining ones is the main reason why the site-specific coefficient values are neces-

sary. The modelled values of Rn_{FAO56} using the default coefficients have been observed to be generally less negative than the measured values. This concerns e.g. humid (Yin et al., 2008), sub-humid and semiarid places (Irmak et al., 2010). The variability of Rn_{FAO56} parameters may result in incorrectly estimated PET in hydrological studies. The reason for that is the insufficient reduction of a positive short wave energy balance. Hence, higher PET values can then be observed as more energy is available (compared to a measured energy balance). The influence of inaccurately estimated Rn on the rate of PET is still poorly examined (Irmak et al., 2003b; Yin et al., 2008).

The aims of this study are therefore: (i) to compare the values of Rn estimated by the FAO56 (Allen et al., 1998) and FAO24 (Doorenbos and Pruitt, 1977) approaches with observed values based on a dataset covering eight years; (ii) to calibrate the coefficients used in Rn_{FAO56} and Rn_{FAO24} longwave radiation equations for an experimental site in the Bohemian Forest; and (iii) to investigate the influence of the chosen Rn estimation approach on the rate of PET calculated by a Penman-Monteith equations (Monteith, 1965).

DATA AND METHODS

Site description and instrumentation

The data for this study were obtained in an area of the *Liz experimental catchment* (49°04'N, 13°41'E). It is located in a forested, mountainous region that serves as a headwater area for numerous flood events in the Czech Republic. The altitude of the catchment extends from a minimum of 828 m.a.s.l. to a maximum of 1074 m.a.s.l. Using the Köppen climate classification, the site lies in the Dfb zone, which is characterised by a humid continental climate with an approximately uniform precipitation distribution and warm summers. More information about the experimental site can be found e.g. in Votrubová et al. (2017).

All meteorological variables necessary for the modelling were measured at 15-minute (2010–2015) and 10-minute intervals (2016–2017) at the automatic meteorological station located at 830 m.a.s.l (Fig. 1). The necessary datasets contain air temperature (Vaisala HMP45, Finland), relative air humidity (Vaisala HMP45, Finland), wind speed (Vaisala WAA151, Finland), atmospheric pressure (Vaisala PTB110, Finland), and actual duration of sunshine (Meteoservis SD5, CZE). Radiation balance was measured using a CNR1 instrument consisting of two pyranometers CM3 (measuring incoming and outgoing shortwave radiation) and two pyrgeometers CG3 (used for incoming and outgoing longwave radiation) (Kipp & Zonen, Netherlands). Radiation data are available only for the vegetation season (April–October), since in the winter the sensors may be covered by snow. In the meteorological station the short grass canopy is grown, but it is surrounded by high trees and forest is in the neighbourhood (50 meters from the fence).

Experimental methods

Radiation balance (Rn)

The values of net longwave radiation were calculated using the FAO56 or FAO24 approaches and they were compared with the measured ones obtained from the pyrgeometers.

Net radiation, which is often used in PET equations, is defined as:

$$Rn = Rns - Rnl = (SW_{\downarrow} - SW_{\uparrow}) + (LW_{\downarrow} - LW_{\uparrow}) \quad (1)$$

where the net radiation Rn [$MJ m^{-2} d^{-1}$] is the numerical differ-



Fig. 1. Meteorological station surroundings.

ence between the net shortwave radiation Rns [$MJ m^{-2} d^{-1}$] and the net longwave radiation Rnl [$MJ m^{-2} d^{-1}$]. The net short- and longwave radiation (Rns and Rnl , respectively) represent the difference between their incoming (SW_{\downarrow} , LW_{\downarrow}) and outgoing components (SW_{\uparrow} , LW_{\uparrow}). The general equation for the estimation of Rnl by FAO56 manual (Allen et al., 1998) originates from the Stefan-Boltzmann law, and can be described as:

$$Rnl = \sigma \left[\frac{T_{MAX(K)}^4 + T_{MIN(K)}^4}{2} \right] \cdot (a_1 - a_2 \sqrt{e_a}) \cdot \left(b_1 \cdot \frac{R_s}{R_{so}} - b_2 \right) \quad (2)$$

Net longwave radiation with coefficients determined in the FAO56 (Allen et al., 1998) approach is given by:

$$Rnl = \sigma \left[\frac{T_{MAX(K)}^4 + T_{MIN(K)}^4}{2} \right] \cdot (0.34 - 0.14 \sqrt{e_a}) \cdot \left(1.35 \cdot \frac{R_s}{R_{so}} - 0.35 \right) \quad (3)$$

where σ is the Stefan-Boltzmann constant [$4,895 \cdot 10^{-9} MJ m^{-2} d^{-1} K^{-4}$], T_{MAX} and T_{MIN} are the maximum and the minimum air temperature [K], e_a is the actual vapour pressure [kPa], R_s is the total incoming shortwave solar radiation [$MJ m^{-2} d^{-1}$] and R_{so} is the calculated clear-sky solar radiation [$MJ m^{-2} d^{-1}$]. The values $a_1 = 0.34$, $a_2 = -0.14$, $b_1 = 1.35$ and $b_2 = 0.35$ are coefficients recommended by the FAO56 manual that can be modified according to the specific region.

Clear-sky solar radiation can be expressed as:

$$R_{so} = (c_1 + c_2 \cdot z) R_a \quad (4)$$

where c_1 and c_2 are coefficients, z station elevation above sea level [m], and R_a is the extraterrestrial radiation [$MJ m^{-2} d^{-1}$]. Using the methodology in FAO56, the coefficients are defined as $c_1 = 0.75$ and $c_2 = 0.00002$.

The general methodology in FAO24 (Doorenbos and Pruitt, 1977) for calculating Rnl is given by the equation:

$$Rnl = (\sigma T_K^4) \cdot (a_1 - a_2 \sqrt{e_a}) \cdot \left(b_1 + b_2 \frac{n}{N} \right) \quad (5)$$

In the Rn_{FAO24} approach, this equation is used in the following form:

$$Rnl = (\sigma T_K^4) \cdot (0.34 - 0.044\sqrt{e_a}) \cdot \left(0.1 + 0.9 \frac{n}{N}\right) \quad (6)$$

where T_K is the daily mean air temperature [K], e_a is the actual vapour pressure [kPa], n is the actual duration of sunshine [hrs] and N is the number of daylight hours [hrs]. Default values for the coefficients introduced in the FAO24 paper are therefore $a_1 = 0.34$, $a_2 = 0.044$, $b_1 = 0.1$ and $b_2 = 0.9$.

Sensitivity analyses and model calibration

The site specific calibration of the Rnl model coefficients is one of the primary aims of the article. Prior to the calibration the sensitivity analyses (SA) was conducted in order to investigate the influence of particular coefficients on the model performance. The simplest type of SA that varies the input factors (e.g. model coefficients) of the simulation model from their nominal values one at a time (OAT) was used (Pianosi et al., 2016). The procedure was based on changing one parameter at a time and the remaining ones were kept fixed. The sensitivity of the output to the changes in the input factors was observed by calculating the rate of change of the objective function (RMSE in our case). Based on the SA the calibration of model coefficients was done using the genetic algorithm. All the chosen parameters were calibrated simultaneously.

Potential evapotranspiration (PET)

The influence of Rnl on the rate of PET was determined by three different approaches. First, the observed radiation balance was used. Second, the Rnl_{FAO56}/Rnl_{FAO24} equations were used using a default parameters setup. Finally, the calibrated Rnl models coefficients (based on local conditions) were utilized. Potential evapotranspiration was estimated by Penman-Monteith (Monteith, 1965, Eq. 7). Besides the air temperature, wind speed and vapour pressure, the net radiation (Rnl respectively) represents one of the fundamental inputs of this method.

$$\lambda_{PET} = \frac{\Delta(Rn - G) + \rho \cdot c(e_s - e_a) / r_a}{\Delta + \gamma \left(1 + \frac{r_s}{r_a}\right)} \quad (7)$$

where Δ describes the slope of the saturation vapour pressure versus air temperature curve [kPa °C⁻¹], Rn is the net radiation [MJ m⁻² d⁻¹], G is the soil heat flux, γ is the psychrometric constant [kPa °C⁻¹], $e_s - e_a$ is the expression of vapour pressure deficit [kPa] (e_s is the saturation vapour pressure and e_a is the actual vapour pressure), λ is the latent heat of vaporisation [MJ kg⁻¹], ρ is the water density [1000 kg L⁻¹], r_s/r_a is the ratio of surface and aerodynamic resistance [s m⁻¹]. Soil heat flux is neglected in this study as it deals with daily average sums of radiation.

Statistical analysis

The results of the Rnl_{FAO56} and Rnl_{FAO24} formulas (and related different values of PET) were compared with the measured Rnl under different conditions. Total daily, monthly and seasonal average values of Rnl and PET were evaluated. Two error statistics were selected: root mean-square error (RMSE, Eq. 8) and BIAS (Eq. 9). The RMSE involves the square of the difference between the observed and estimated values. Hence, it tends to emphasise larger values of the error in time-series,

while lower values are virtually neglected. The BIAS is the average absolute difference between the observed and estimated values, indicating the magnitude and direction (positive/negative) of each error. The smaller the values of RMSE/BIAS, the more precise are the results. These values are defined as:

$$RMSE = \sqrt{\frac{1}{n} \sum_{i=1}^n (y_i - x_i)^2} \quad (8)$$

$$BIAS = \frac{1}{n} \sum_{i=1}^n (y_i - x_i) \quad (9)$$

where y_i represents the modelled values on the day i , x_i the observed values on the day i , and n is the number of the sample.

For the trend analyses, the Mann-Kendall (MK) test (Kendall, 1938; Mann, 1945) was originally developed. However, the MK test is sensitive to the presence of autocorrelation in the analysed datasets. In the case of a positive lag-one autocorrelation coefficient (which exists in several hydro-meteorological variables), the MK test may falsely detect a trend as the same ordering of data is supported. We therefore used a modification of the MK test, referred to as the trend-free pre-whitening (TFPW-MK) approach, which was originally designed for positively auto-correlated series (Yue et al., 2002). All tests were performed at a significance level of 5% using the daily values of particular variables.

RESULTS

Climate characteristics

The climatic characteristics of the eight years under evaluation (2010–2017) are illustrated in Figure 2. For each year, only the warmer months (April–October) were used, as measurements of longwave radiation are not available in winter. The long-term average daily air temperature was 6.66°C and the average annual sum of precipitation was 851 mm (1975–2017). The air temperatures in the eight evaluated years were mostly higher than the long-term average (the warmest year was 2014 with 8.3°C); only in 2010 and 2013 the air temperatures were slightly lower than average. The average annual precipitation in a given period was 815 mm, which was also lower than the long-term average. The wettest year in the period under evaluation was 2016, and the driest year was 2015 (which was the driest year observed since 1975).

Radiation balance

Seasonal and daily values of the radiation balance and its components are presented in Figure 3. Shortwave (SW) radiation generally reaches positive values during the daytime, and approaches zero at night (Fig. 3a)). The mean daily value of incoming SW radiation was 13.6 MJ m⁻² d⁻¹ and outgoing SW radiation was 2.6 MJ m⁻² d⁻¹ (during the period April–October). The long-term average observed ratio of reflected SW radiation to incoming radiation (albedo) over the underlying grass surface was 18.6%. Incoming SW radiation had a strongly seasonal character, with maximum values reaching 28 MJ m⁻² d⁻¹ during the summer season (June–July). No statistically significant trend was detected (using TFPW-MK test) in either incoming or outgoing SW radiation over the 2010–2017 period (at a significance level of 5%). However, the daily albedo (as the main factor influencing the reflection of radiation) exhibited a significantly decreasing trend during the period of interest,

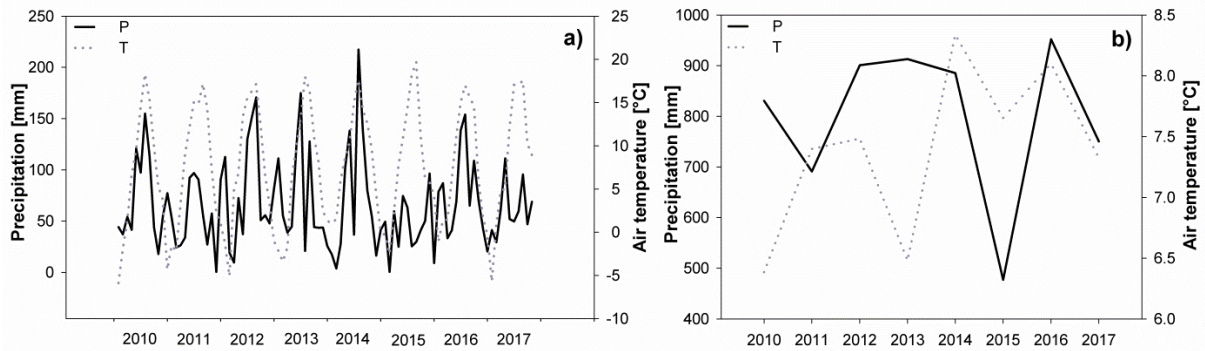


Fig. 2. a) monthly and b) annual climate characteristics of the studied period (January 2010–October 2017).

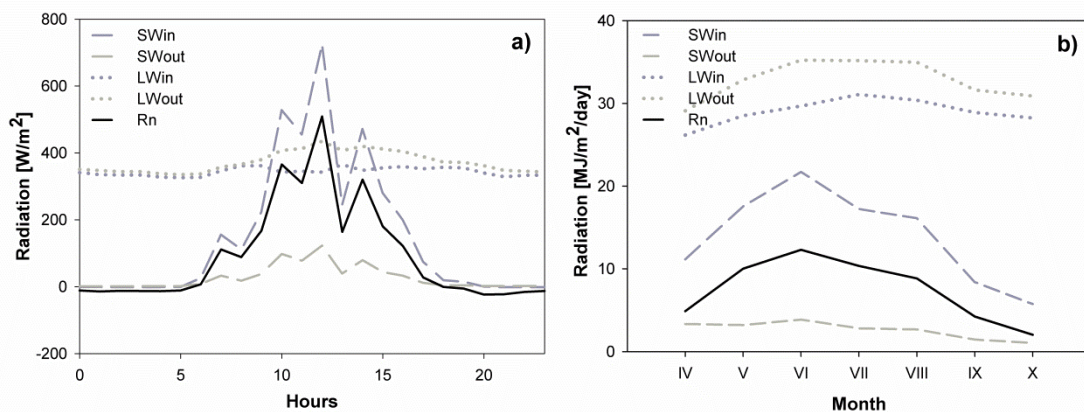


Fig. 3. a) daily (25th April 2014) and b) average seasonal trends in net radiation and its components.

which may be attributable to the long-term evolution of the underlying grass cover.

The observed longwave (LW) radiation exhibited more stable daily and seasonal (annual respectively) patterns (Fig. 3). The mean daily incoming LW radiation was $29.4 \text{ MJ m}^{-2} \text{ d}^{-1}$ and mean daily outgoing LW radiation was $33.0 \text{ MJ m}^{-2} \text{ d}^{-1}$. Altogether, the mean daily net LW radiation (Rnl) was $-3.5 \text{ MJ m}^{-2} \text{ d}^{-1}$. Daily values of Rnl ranged between -9.3 and $0 \text{ MJ m}^{-2} \text{ d}^{-1}$. The mean monthly Rnl reached maximum value of $-4.1 \text{ MJ m}^{-2} \text{ d}^{-1}$ in July and a minimum value of $-2.3 \text{ MJ m}^{-2} \text{ d}^{-1}$ in October. The sub-daily pattern of LW radiation was also rather stable (in comparison with SW radiation), with a slight increase in outgoing LW radiation during daylight hours, correlating with an increase in the incoming SW radiation. The variation in incoming LW radiation can be linked to the variation in absolute vapour pressure in the air. Similarly to SW radiation, the TFPW-MK test did not reveal any statistically significant trend in LW radiation series over the studied period.

As the sum of the incoming and outgoing SW and LW radiation, Rn typically demonstrates strong seasonal variation, with maximum in summer and minimum in winter (Fig. 3b)). In general, Rn is positive during the day and negative at night. Maximum monthly averages approached $10 \text{ MJ m}^{-2} \text{ d}^{-1}$ during the summer season (June–July), and in the autumn the values usually decreased to zero. The average daily value in the period April–October was $7.5 \text{ MJ m}^{-2} \text{ d}^{-1}$, with a maximum of $16 \text{ MJ m}^{-2} \text{ d}^{-1}$. With respect to the separate contributions of SW and LW radiation, the outgoing LW radiation reduces the amount of energy from the incoming SW radiation by 31% on average. No statistically significant trends were observed in daily Rn values in the period 2010–2017.

Estimated net longwave radiation (Rnl)

Rnl was estimated using the FAO56 ($\text{Rnl}_{\text{FAO56}}$) and FAO24 ($\text{Rnl}_{\text{FAO24}}$) approaches. Average values of error statistics (compared to observed values) are presented in Figure 4. These results show that $\text{Rnl}_{\text{FAO24}}$ performed better than $\text{Rnl}_{\text{FAO56}}$ in comparison with the measured values. The $\text{Rnl}_{\text{FAO56}}$ method had a strong tendency to underestimate the rate of Rnl; that is, the estimated Rnl was less negative than the observed value. Average BIAS values ranged from 1 to $1.5 \text{ MJ m}^{-2} \text{ d}^{-1}$ for the $\text{Rnl}_{\text{FAO56}}$ method, while its maximum value was only $0.5 \text{ MJ m}^{-2} \text{ d}^{-1}$ in the case of $\text{Rnl}_{\text{FAO24}}$ (Fig. 4c)). Average annual RMSE values were always higher than $1.4 \text{ MJ m}^{-2} \text{ d}^{-1}$ when using the $\text{Rnl}_{\text{FAO56}}$ approach, but ranged between 1.0 and 1.25 in the case of FAO24 (Fig. 4a)). The $\text{Rnl}_{\text{FAO56}}$ method produced the highest differences from measured Rnl in 2010, 2016 and 2017. Analyses of monthly averages did not show any seasonal trend in the dissimilarities between measured and modelled Rnl data.

Further, all coefficients included in the $\text{Rnl}_{\text{FAO56}}$ and $\text{Rnl}_{\text{FAO24}}$ methods were calibrated. This parameter calibration was preceded by sensitivity analyses (results not shown). The values of chosen objective function (RMSE) were shown to be relatively insensitive to changes in some input coefficients values and thus the calibration of all parameters was not necessary. The least sensitive parameters were c_1 and c_2 , so their values were kept at the default recommended values ($c_1 = 0.75$ and $c_2 = 0.00002$).

The reason for the calibration procedure was to investigate whether it was possible to introduce site-specific values of parameters in order to give a more efficient estimation of Rnl. Initially, all years were first calibrated separately, and different coefficients for each year were determined. Altogether, three

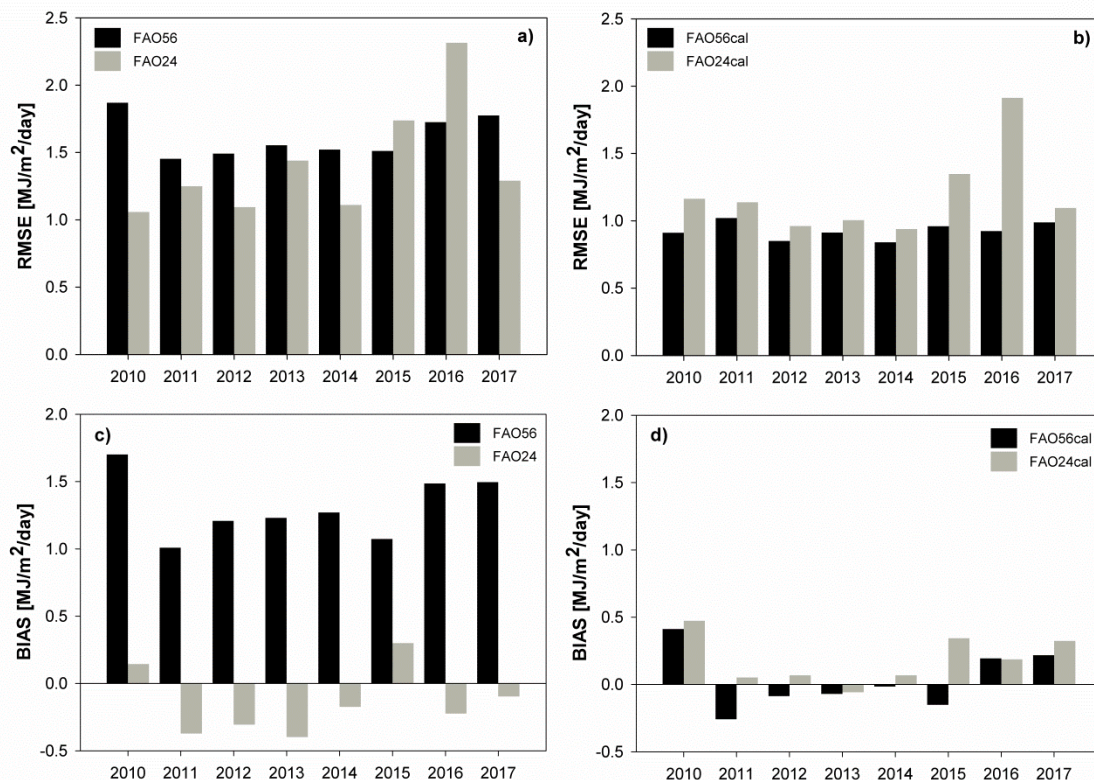


Fig. 4. Error statistics of average daily Rnl modelled using a) FAO56 and c) FAO24 against measured values with default parameter values and b) FAO56 and d) FAO24 after overall calibration.

coefficients were simultaneously calibrated (a_1 and a_2 , which express atmospheric emissivity, and b_1 from the cloudiness factor). The parameter b_2 was taken as a complement of b_1 to 1, as proposed by Allen et al. (1994). For the whole period of eight years, three different sets of coefficients were evaluated (Table 1). The first of these were based on the default parameter values (obtained from the literature); the second were calibrated for each year separately (in order to obtain the best possible model efficiency); and the last originated from the overall calibration (i.e. for the entire period 2010–2017). The resulting parameter values are given in Table 2 for Rn_{FAO56} and in Table 3 for Rn_{FAO24} . As mentioned in the previous section, Rnl calculated using the Rn_{FAO56} approach differed notably from the measured values. However, this inconsistency was effectively improved by the coefficient calibration (Table 1). RMSE decreased approximately by 50% on average and BIAS merely diminished. In case of Rn_{FAO24} there were no distinct changes (the RMSE decreased by 15% on average and BIAS

remained very low), which can be attributed to the very satisfactory match between the observed and calculated Rnl using default Rn_{FAO24} parameter values (Fig. 4). The use of overall calibrated coefficient values (instead of the season-specific calibration) did bring only a very little deterioration of error statistics in both Rn_{FAO56} and Rn_{FAO24} estimation methods (Table 1). Therefore the use of the single coefficient values for the entire period was justified. However, Figure 5 demonstrates a significant deficiency of the Rn_{FAO24} approach, which is represented by a less linear relation between the modelled and observed Rnl values. The values are more widely scattered around the 1:1 line than for Rn_{FAO56} , despite representing a better average (reflected by more satisfactory RMSE and BIAS statistics). Although the Rn_{FAO56} generally corresponds better to the distribution of observations, the absolute values were more biased using the default parameter values. Hence, after the calibration of coefficients, Rn_{FAO56} represents a more plausible approach.

Table 1. Comparison of values of error statistics [$MJ\ m^{-2}\ d^{-1}$] before and after calibration of coefficients for Rn_{FAO56} and Rn_{FAO24} .

	Default parameter values				Calibrated for each year				Overall calibration			
	RMSE		BIAS		RMSE		BIAS		RMSE		BIAS	
	FAO56	FAO24	FAO56	FAO24	FAO56	FAO24	FAO56	FAO24	FAO56	FAO24	FAO56	FAO24
2010	1.87	1.06	1.70	0.14	0.88	0.97	0.02	0.05	0.91	1.16	0.41	0.47
2011	1.45	1.25	1.01	-0.37	0.99	1.12	-0.20	0.06	1.02	1.14	-0.26	0.05
2012	1.49	1.09	1.21	-0.31	0.86	0.95	-0.34	0.08	0.85	0.96	-0.09	0.07
2013	1.55	1.44	1.23	-0.40	0.93	0.99	0.98	-0.09	0.91	1.00	-0.07	-0.06
2014	1.52	1.11	1.27	-0.17	0.85	0.93	0.57	0.07	0.84	0.94	-0.01	0.07
2015	1.51	1.74	1.07	0.30	0.95	1.31	0.27	-0.05	0.96	1.35	-0.15	0.34
2016	1.73	2.31	1.49	-0.22	0.87	1.87	0.13	0.08	0.92	1.91	0.19	0.19
2017	1.77	1.29	1.49	-0.10	0.96	1.09	0.28	0.40	0.99	1.09	0.22	0.32
2010–2017	1.61	1.39	1.20	-0.11	0.91	1.20	0.21	0.04	0.93	1.19	0.03	-0.03

Table 2. Different sets of coefficients for Rn_{FAO56} .

FAO56	original	2010	2011	2012	2013	2014	2015	2016	2017	2010–2017
a1	0.34	0.34	0.32	0.35	0.33	0.325	0.315	0.35	0.35	0.3
a2	-0.14	-0.1	-0.1	-0.12	-0.101	-0.1	-0.1	-0.1	-0.1	-0.1
b1	1.35	1.12	1.12	1.13	1.15	1.09	1.05	1.1	1.1	1.08
b2	-0.35	-0.12	-0.12	-0.13	-0.15	-0.09	-0.05	-0.1	-0.1	-0.08
c1	0.75	0.75	0.75	0.75	0.75	0.75	0.75	0.75	0.75	0.75
c2	0.00002	2E-05	2E-05	2E-05	2E-05	2E-05	2E-05	2E-05	2E-05	0.00002

Table 3. Different sets of coefficients for Rn_{FAO24} .

FAO24	original	2010	2011	2012	2013	2014	2015	2016	2017	2010–2017
a1	0.34	0.31	0.33	0.33	0.33	0.33	0.33	0.3	0.33	0.33
a2	0.044	0.05	0.11	0.11	0.11	0.11	0.1	0.11	0.1	0.113
b1	0.1	0.2	0.25	0.25	0.26	0.255	0.3	0.4	0.2	0.265
b2	0.9	0.8	0.75	0.75	0.74	0.745	0.7	0.6	0.8	0.735

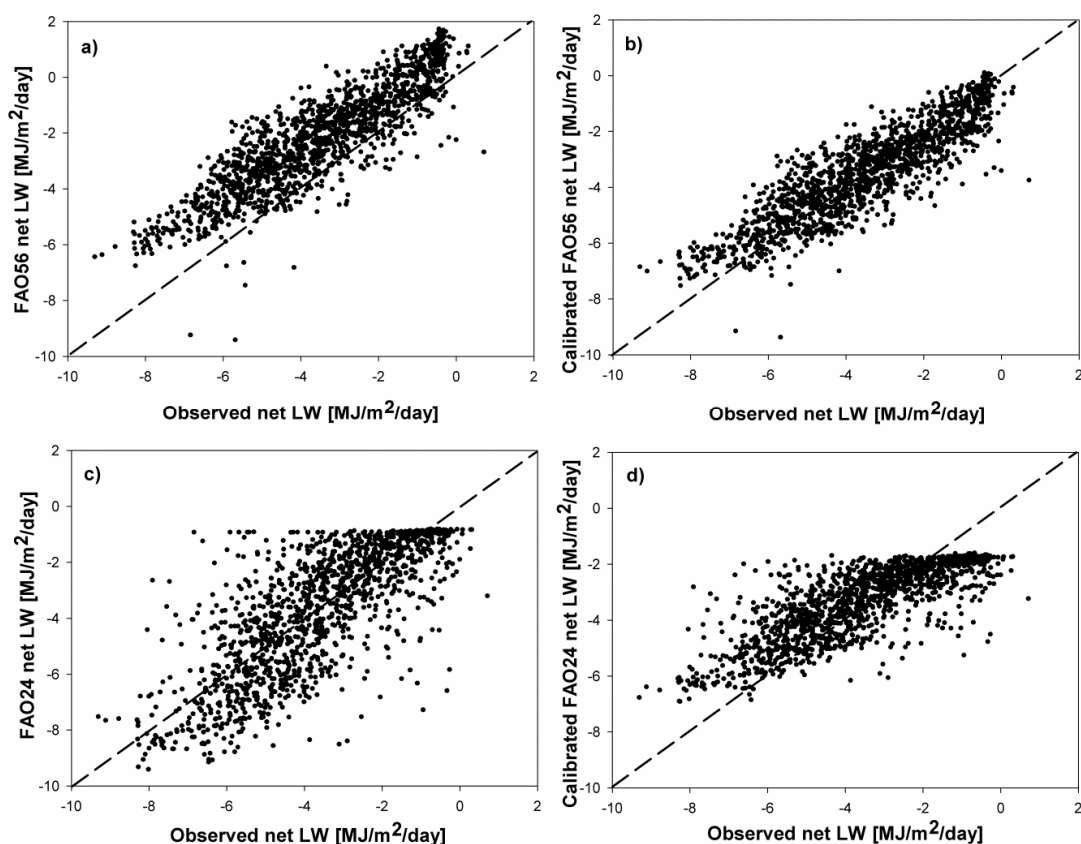


Fig. 5. Relationship between the observed and estimated daily net LW (Rn_{FAO56} and Rn_{FAO24} , a) and c) before calibration and b) and d) after overall calibration of coefficients.

Influence of the chosen Rnl method on PET estimation

Potential evapotranspiration was estimated using the combined method of Penman-Monteith (Monteith, 1965). The influence of the measured and estimated Rnl values in the PET equation on the resulting value of evapotranspiration was investigated. The datasets used for estimated Rnl were represented by the values obtained by Rn_{FAO56} and Rn_{FAO24} approaches using: (a) default parameter values and (b) a single parameter set arising from the overall calibration. The reference PET (obtained using the measured Rnl) ranged from 270 mm to 433 mm over one season (April–October). The average daily values were between 1.9 to 2.2 mm/day in all inspected seasons (Fig. 6). Maximum daily values occurred during summer (June–

July). When using Rnl modelled using Rn_{FAO56} and Rn_{FAO24} methods, the seasonal PET based on the Rn_{FAO56} was higher by 40 to 100 mm per a season, while the values of the differences were only up to 20 mm for the Rn_{FAO24} method. The daily average differences were from 0.3 to 0.4 mm/day for Rn_{FAO56} method and up to 0.2 mm/day for Rn_{FAO24} (Fig. 7b)). The overall calibration of the Rn_{FAO56} coefficients (last column of Table 2) caused a significant decrease in the differences between the values for PET obtained from the measured and estimated Rnl datasets for all years (except 2010 and 2012). Generally, it resulted in very similar values as those obtained by the Rn_{FAO24} method before calibration. The Rn_{FAO24} results showed that overall calibration was not necessary. It even resulted in poorer PET estimation in majority of years when the differences in

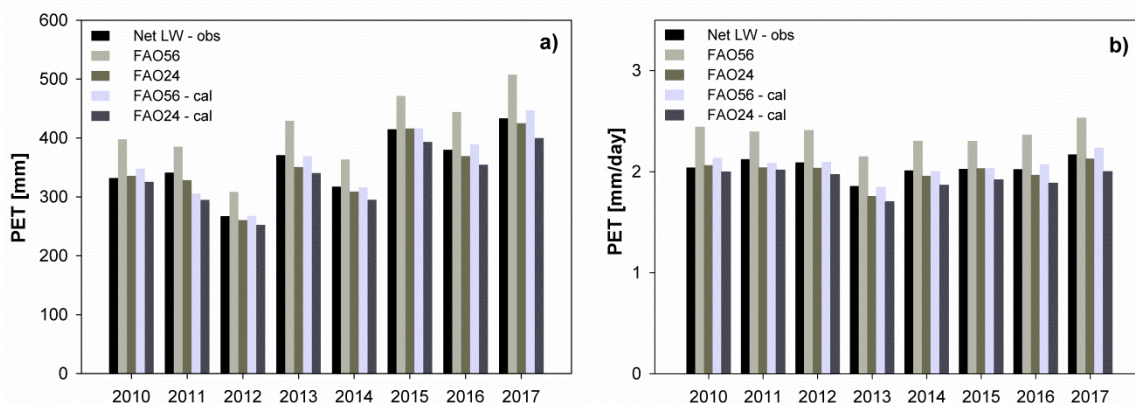


Fig. 6. Estimated a) seasonal and b) daily PET in all years of studied period using Penman-Monteith model.

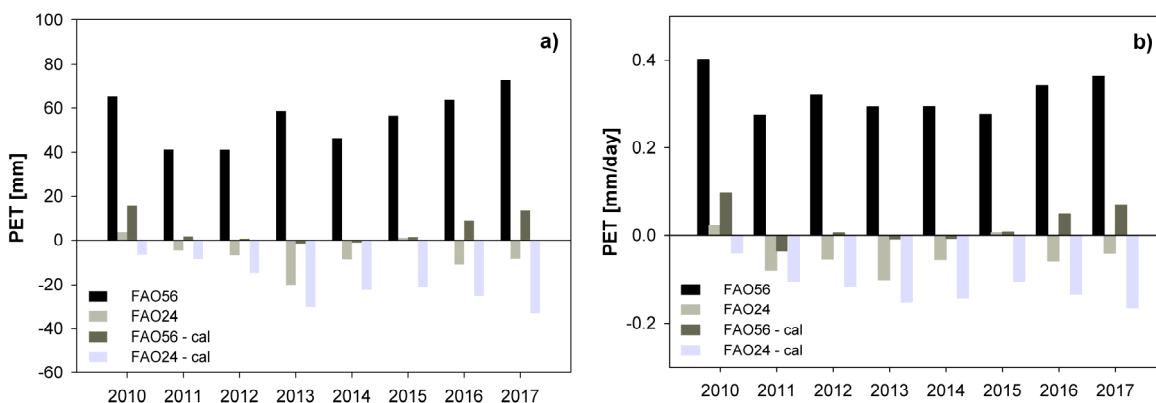


Fig. 7. Absolute differences in PET between the reference PET and those obtained by Rn_{FAO56} / Rn_{FAO24} (default sets of coefficients) and $Rn_{FAO56-cal} / Rn_{FAO24-cal}$ (overall calibration), using Penman-Monteith estimation method: a) in seasonal values; b) in daily average values.

PET regularly exceeded 20 mm per a season or 0.2 mm/day (Fig. 7). The distribution of the differences in PET values (calculated vs. measured Rnl) over the season was uniform, and no statistically significant trend was identified.

DISCUSSION

The influence of net longwave radiation estimation approach on the determination of PET was examined. Longwave radiation was continuously measured between 2009 and 2017. These measurements were not taken during the winter months, as snow cover on the radiation sensors would have influenced the measurements. Hence, a different number of days in each year were analysed (since the measurements did not start and end on specific dates each year, but were dictated by presence of snow cover). No inter-seasonal comparison could therefore be carried out due to the different measurement periods used in each year. Despite this factor, the uniqueness of this study lies in the length of the measurement period. Some previous studies focusing on the estimation of Rnl were restricted to shorter time periods, e.g. one (Yin et al., 2008) or three years (Carmona et al., 2017).

In the present study, the default configuration of the Rn_{FAO56} method has a strong tendency to overestimate Rnl and hence PET in each year examined. Confirming the results of this study, Carmona et al. (2017) also reported overestimation of Rn_{FAO56} approach in the temperate and sub-humid climate

regime of Tandil (Argentina). Conversely, the Rnl was somewhat underestimated in other locations (Matsui and Osawa, 2015; Yin et al., 2008). This can be explained by the non-reference conditions that are likely to be present at every location except the ones where the coefficients were derived. The reason can lie in different influence of the surface characteristics (vegetation type and age), trees and buildings in the surroundings or different presence of small particles and CO₂ in the atmosphere. All these factors can influence the longwave radiation balance.

As a result, many researchers have agreed that the calibration of coefficients (expressing the cloudiness factor and atmospheric emissivity) should be carried out based on local conditions (Allen et al., 1998; Carmona et al., 2014; Jensen et al., 1990; Kjaersgaard et al., 2007b, 2009; Matsui and Osawa, 2015; Müller et al., 2014; Yin et al., 2008). The calibration of Rn_{FAO56} coefficients can give rise to a significant improvement compared to measured radiation values (e.g. Matsui and Osawa, 2015). Carmona et al. (2014) found that the coefficients proposed by Allen et al. (1998) provided the highest values of errors in the results. However, after local calibration or when using the coefficients proposed by Jensen et al. (1990) (specifically for humid areas), the RMSE was reduced from around 28% to $\pm 15\%$. The outcomes of this study are in agreement with this improved performance of the Rn_{FAO56} method after calibration.

The Rn_{FAO24} performed better than Rn_{FAO56} over the entire study period, and the calibration of coefficients enhanced the results only to a limited extent. However, this concerned only the average error statistics and the distribution of daily values. Rn_{FAO24} was notably biased when compared to the measured ones (Fig. 5). As the distribution of Rn_{FAO24} was limited by the value of $-0.9 \text{ MJ m}^{-2} \text{ d}^{-1}$, which is conditioned by a zero duration of sunshine on any given day. On these days, low values of SW radiation (embedded in the Rn_{FAO56} cloudiness correction) can be still observed, and the Rn_{FAO56} therefore enables a more accurate estimation of low Rnl values. The limit is undermined by the limited amount of water vapour that can be held in the air at certain air temperature (saturation vapour pressure). There is no comparable evidence from the use of this method in other locations and climate conditions.

Standard Penman-Monteith equation was chosen for the estimation of PET. Since Rn is one of the variables used in this approach, the use of Rn_{FAO56} and Rn_{FAO24} modelling proved to have the effect on PET calculation (Detlefsen and Plauborg, 2001, in Kjaersgaard et al., 2007b). Estimated PET was usually overestimated in the period under study when using the Rn_{FAO56} approach. A similar effect was observed by Yin et al. (2008), who found overestimations of up to 27%. On the other hand, Rn_{FAO24} tended to underestimate the PET results in all years (except for 2010). Calibration of coefficients improved the PET results in the entire period. Three additional PET estimation methods (Pristley and Taylor method, 1972, Kimberly-Penman method, Wright, 1982 and Thom and Oliver method, 1977) were examined in a side-experiment in order to observe the sensitivity of results. The types and magnitudes of the errors were very similar in all of the utilised PET estimation methods. This was given by the fact that all the chosen methods are simplified versions of the original Penman-Monteith equation. In general, the calibration of coefficients based on local conditions gave more accurate PET estimates (compared to the use their default values). This is of significant importance for the modelling practice as it can reduce the uncertainty in the estimation of the PET rate, which is one of the two key factors determining the amount of actual evapotranspiration (AET). The inaccurately estimated AET inevitably leads to inaccurate water balance equation components estimation, although the model performance (based on error statistics) could be satisfactory (Šípek and Tesař, 2017).

While the Rn_{FAO56} approach is widely used in modelling practice (e.g. Kjaersgaard et al., 2009), Rn_{FAO24} is rarely used (due to a lack of information on the actual sunshine duration). The accuracy of both modelling approaches without parameter calibration (coefficients describing atmospheric and cloud conditions) is questionable, as it can vary for different locations and climate conditions. In this study, the default Rn_{FAO24} generally performed better, but only when observing average error statistics. The distribution of daily values was more variable than in the case of Rn_{FAO56} (especially after its calibration). Hence, the modelling of PET using the estimated Rnl requires a parameter calibration that reflects the site-specific conditions (Allen et al., 1998; Jensen et al., 1990).

SUMMARY AND CONCLUSIONS

Potential evapotranspiration by Penman-Monteith (Monteith, 1965) method was evaluated at the Liz catchment using the measured net longwave radiation (Rnl) and results of calculation from the FAO56 (Rn_{FAO56}) and FAO24 (Rn_{FAO24}) Rnl equations. The study showed that Rn_{FAO56} has a strong tendency to underestimate the values of LW radiation balance while

using default set of coefficients. The calibration of coefficients generated significant improvements over the entire studied period (2010–2017) when using Rn_{FAO56} . While RMSE of Rn_{FAO56} decreased approximately by 50% on average (and BIAS merely diminished), Rn_{FAO24} exhibits small or no improvements with values decreasing by 15% on average in case of RMSE. BIAS remained unaffected by the calibration procedure. Following this calibration, the Rn_{FAO56} approach was found to be more reliable, since the distribution of LW radiation values corresponded better to the observed values (in addition to the values of RMSE and BIAS). The distribution of values of LW using Rn_{FAO24} approach, which relies on the duration of sunshine, was affected by the fact that some SW radiation is observed even when no sunshine is recorded. As a result, the estimation of PET using default parameter values in Rn_{FAO56} method produced seasonal difference of 40–100 mm from the values estimated based on the measured radiation balance; these differences reached only 20 mm on average per season in the case of Rn_{FAO24} using default coefficients. The errors in PET significantly decreased after calibration (up to 20 mm per season), and hence the local calibration of coefficients is strongly recommended when using the Rn_{FAO56} procedure. This proposed approach will lead to more accurate hydrological simulation in terms of water balance equation components estimation.

Acknowledgements. This research was supported by the Czech Science Foundation (GA CR 16-05665S), the institutional support of the Czech Academy of Sciences, Czech Republic (RVO: 67985874), and by the programme framework of the Strategy AV21. Radiation data were available through the courtesy of the Faculty of Civil Engineering, Czech Technical University in Prague.

REFERENCES

- Allen, R.G., Smith, M., Perrier, A., Pereira, L.S., 1994. An update for the definition of reference evapotranspiration. *ICID Bulletin*, 43, 2, 35–92.
- Allen, R.G., Pereira, L.S., Raes, D., Smith, M., 1998. Crop evapotranspiration – Guidelines for computing crop water requirements. FAO Irrigation and Drainage Paper 56, Rome, 300 p.
- Arellano, M.G., Irmak, S., 2016. Reference (potential) evapotranspiration. I: Comparison of temperature, radiation, and combination-based energy balance equations in humid, sub-humid, arid, semiarid and mediterranean-type climates. *Journal of Irrigation and Drainage Engineering*, 142, 4, 21 p.
- Carmona, F., Rivas, R., Caselles, C., 2014. Estimation of daytime downward longwave radiation under clear and cloudy skies conditions over sub-humid region. *Theoretical and Applied Climatology*, 115, 281–295.
- Carmona, F., Rivas, R., Kruse, E., 2017. Estimating daily net radiation in the FAO Penman-Monteith method. *Theoretical and Applied Climatology*, 129, 89–95.
- Dalton, J., 1802. Experimental essays on the constitution of mixed gases: On the force of steam or vapor from water or other liquids in different temperatures, both in a Torricelli vacuum and in air; on evaporation; and on expansion of gases by heat. Manchester Literary Philosophical Society Mem. Proceedings, 5, 536–602.
- Doorenbos, J., Pruitt, W.O., 1977. Guidelines for predicting crop water requirements. FAO Irrigation and Drainage Paper 24, Rome, 179 p.
- Duarte, H.F., Dias, N.L., Maggioletto, S.R., 2006. Assessing daytime downward longwave radiation estimates for clear

- and cloudy skies in Southern Brazil. *Agricultural and Forest Meteorology*, 139, 171–181.
- Fisher, J.B., DeBiase, T.A., Qi, Y., Xu, M., Goldstein, A.H., 2005. Evapotranspiration methods compared on a Sierra Nevada forest ecosystem. *Environmental Modelling & Software*, 20, 6, 783–796.
- Irmak, S., ASCE, M., Irmak, A., Jones, J.W., Howell, T.A., ASCE, M., Jacobs, J.M., Allen, R.G., ASCE, M., Hoogenboom, G., 2003a. Predicting daily net radiation using minimum climatological data. *Journal of Irrigation and Drainage Engineering*, 129, 4, 256–269.
- Irmak, S., Irmak, A., Allen, R.G., Jones, J.W., 2003b. Solar and net radiation-based equations to estimate reference evapotranspiration in humid climates. *Journal of Irrigation and Drainage Engineering*, 129, 5, 336–347.
- Irmak, S., Mutiibwa, D., Payero, J.O., 2010. Net radiation dynamics: Performance of 20 daily net radiation models as related to model structure and intricacy in two climates. *Transactions of the ASABE*, 53, 4, 1059–1076.
- Jensen, M.E., Burman, R.D., Allen, R.G., 1990. *Evapotranspiration and water requirements*, ASCE Manual 70, New York, 332 p.
- Kendall, M.G., 1938. A new measure of rank correlation. *Biometrika*, 30, 1/2, 81–93.
- Kjaersgaard, J.H., Cuenca, R.H., Plauborg, F.L., Hansen, S., 2007a. Long-term comparisons of net radiation calculation schemes. *Boundary-Layer Meteorology*, 123, 417–431.
- Kjaersgaard, J.H., Plauborg, F.L., Hansen, S., 2007b. Comparison of models for calculating daytime long-wave irradiance using long term data set. *Agricultural and Forest Meteorology*, 143, 49–63.
- Kjaersgaard, J.H., Cuenca, R.H., Martínez-Cob, A., Gavilán, P., plauborg, F., Mollerup, M., Hansen, S., 2009. Comparison of the performance of net radiation calculation models. *Theoretical and Applied Climatology*, 98, 57–66.
- Mann, H.B., 1945. Nonparametric tests against trend. *Econometrica*, 13, 3, 245–259.
- Matsui, H., Osawa, K., 2015. Calibration effects of the net longwave radiation equation in Penman-type methods at Tateno, Japan. *Hydrological Research Letters*, 9, 4, 113–117.
- Monteith, J.L., 1965. Evaporation and the environment. The state and movement of water in living organisms. In: XIX. Symposium of the Society for Experimental Biology, Cambridge University Press, 205–234.
- Müller, J., Dohnal, M., Tesař, M., 2014. Testování parametrizací složek dlouhodobého záření v podmínkách malého šumavského povodí. In: *Hydrologie malého povodí 2014*. Institute of hydrodynamics CAS, Prague, pp. 329–334.
- Penman, H.L., 1948. Natural evaporation from open water, bare soil and grass. *Proceedings of the Royal Society of London. Series A, Mathematical and Physical Sciences*, 193, 120–145.
- Pianosi, F., Beven, K., Freer, J., Hall, J.W., Rougier, J., Stephenson, D.B., Wagener, T., 2016. Sensitivity analyses of environmental models: A systematic review with practical workflow. *Environmental Modelling & Software*, 79, 214–232.
- Pristley, C.H.B., Taylor, R.J., 1972. On the assessment of surface heat fluxes and evaporation using large-scale parameters. *Monthly Weather Review*, 100, 81–92.
- Shi, T., Guan, D., Wang, A., Wu, J., Jin, C., Han, S., 2008. Comparison of three models to estimate evapotranspiration for a temperate mixed forest. *Hydrological Processes*, 22, 3431–3443.
- Šípek, V., Tesař, M., 2017. Year-round estimation of soil moisture content using temporally variable soil hydraulic parameters. *Hydrological Processes*, 31, 1438–1452.
- Temesgen, B., Eching, S., ASCE, M., Frame, K., 2007. Comparing Net Radiation Estimation Methods: CIMIS versus Penman-Monteith. *Journal of Irrigation and Drainage Engineering*, 133, 265–271.
- Thom, A.S., Oliver, H.R., 1977. On Penman's equation for estimating regional evaporation. *Quarterly Journal of the Royal Meteorological Society*, 103, 345–357.
- Votrubová, J., Dohnal, M., Vogel, T., Šanda, M., Tesař, M., 2017. Episodic runoff generation at Central European headwater catchments studied using water isotope concentration signals. *Journal of Hydrology and Hydromechanics*, 65, 2, 114–122.
- Wright, J.L., 1982. New evapotranspiration crop coefficients. *Journal of Irrigation and Drainage Engineering*, 108, 1, 57–74.
- Yin, Y., Wu, S., Zheng, D., Yang, Q., 2008. Radiation calibration of FAO56 Penman-Monteith model to estimate reference crop evapotranspiration in China. *Agricultural Water Management*, 95, 77–84.
- Yue, S., Pilon, P., Phinney, B., Cavadias, G., 2002. The influence of autocorrelation on the ability to detect trend in hydrological series. *Hydrological Processes*, 16, 1807–1829.

Received 11 September 2018

Accepted 18 January 2019

Evaluation and validation of the ASCE standardized reference evapotranspiration equations for a subhumid site in northeastern Austria

Reinhard Nolz^{1*}, Marek Rodný²

¹ Institute of Hydraulics and Rural Water Management; Department of Water, Atmosphere and Environment; University of Natural Resources and Life Sciences, Vienna (BOKU), Muthgasse 18, 1190 Wien, Austria.

² Institute of Hydrology, Slovak Academy of Sciences, Dúbravská cesta 9, 841 04 Bratislava, Slovak Republic.

* Corresponding author. Tel.: +43 1 47654 81500. E-mail: reinhard.nolz@boku.ac.at

Abstract: Employing evapotranspiration models is a widely used method to estimate reference evapotranspiration (ET_{REF}) based on weather data. Evaluating such models considering site-specific boundary conditions is recommended to interpret ET_{REF} -calculations in a realistic and substantiated manner. Therefore, we evaluated the ASCE standardized ET_{REF} -equations at a subhumid site in northeastern Austria. We calculated ET_{REF} -values for hourly and daily time steps, whereof the former were processed to sum-of-hourly values. The obtained data were compared to each other and to ET -values measured by a weighing lysimeter under reference conditions. The resulting datasets covered daily data of the years 2004 to 2011.

Sum-of-hourly values correlated well ($r^2 = 0.978$) with daily values, but an RMSE of 0.27 mm specified the differences between the calculation procedures. Comparing the calculations to lysimeter measurements revealed overestimation of small ET_{REF} -values and underestimation of large values. The sum-of-hourly values outperformed the daily values, as r^2 of the former was slightly larger and RMSE was slightly smaller. Hence, sum-of-hourly computations delivered the best estimation of ET_{REF} for a single day. Seasonal effects were obvious, with computations and measurements being closest to each other in the summer months.

Keywords: Weighing lysimeter; Calculations; Hourly; Sum-of-hourly; Daily time steps.

INTRODUCTION

Evapotranspiration (ET) comprises processes of water vapor transport in the soil-plant-atmosphere system. These processes are driven by energy fluxes and vapor pressure deficit, and they are influenced by characteristics of soil and vegetation. Reference evapotranspiration (ET_{REF}) is defined as vaporization from a standardized surface – usually grass with specific attributes and not short of water – under the given meteorological conditions (Allen et al., 1998). ET-models incorporate relevant physical principles and specific parameters representing vegetation characteristics, and therefore enable calculating ET_{REF} based on atmospheric boundary conditions. A main advantage of ET-models is the availability and standardization of weather data as input (Allen et al., 2011). Other techniques such as weighing lysimeters allow measuring ET more accurately, but they require cost-intensive equipment. Therefore, weighing lysimeters are traditionally utilized to produce reference values for developing and validating ET-models (e.g., Aboukhaled et al., 1982; Doorenbos and Pruitt, 1977).

Several researchers tested the well-known equation after Penman and Monteith (PM) in different environments and declared it generally applicable (Allen et al., 1994; Jensen et al., 1990); hence, the Food and Agriculture Organization of the United Nations (FAO) recommended the PM-equation as standard procedure for computing ET_{REF} (FAO56; Allen et al., 1998). In this context, ET_{REF} serves as basis for calculating plant water requirements by means of standardized crop coefficients. Consequently, the PM-equation became widely accepted, and in 2005 the Environmental and Water Resources Institute of the American Society of Civil Engineers (ASCE) published a standardized equation with standardized calculation procedures (ASCE-EWRI, 2005). The declared intention was to “bring commonality to the calculation of ET_{REF} and to provide

a standardized basis for determining or transferring crop coefficients for agricultural and landscape use” (ASCE-EWRI, 2005). For daily or longer time steps, the FAO56- and the ASCE-calculation procedures are identical (except for updated coefficients for calculating clear sky solar radiation in the ASCE version). The main update concerned the calculations of ET_{REF} on hourly time steps, which became more important due to the manifold application options and the increased availability of weather data in shorter than daily intervals (ASCE-EWRI, 2005). The central modification involved the modeling of the surface, which is assumed being short crop with an approximate height of 0.12 m (similar to clipped, cool-season grass). Its properties are expressed by the parameter of surface resistance (r_s), which is recommended to be for daily periods $r_s = 70 \text{ s m}^{-1}$, and for hourly calculation $r_s = 50 \text{ s m}^{-1}$ during daytime and $r_s = 200 \text{ s m}^{-1}$ during nighttime (ASCE-EWRI, 2005).

Several studies thoroughly compared ASCE and FAO56 hourly and daily ET_{REF} equations among each other and with empirical equations (e.g., Gavilán et al., 2008; Irmak et al., 2005; Perera et al., 2015). The results indicated limitations of daily computation time steps as they disregard (irregular) diurnal changes in vegetation parameters (e.g., surface resistance, albedo) and weather data (e.g., wind speed, air temperature, vapor pressure deficit). Consequently, replacing daily calculations by sum-of-hourly (soh) calculations proved being advantageous when estimating ET_{REF} (Berengena and Gavilán, 2005; Gavilán, 2008; Irmak et al., 2005; Perera et al., 2015). ET_{REF} equations for daily and sum-of-hourly time steps were evaluated for different regions and climate zones throughout the world. Perera et al. (2015) related the deviations between daily ET_{REF} -values as calculated using the hourly and daily ASCE equations to Köppen climate zones of Australia. In doing so, the authors report good agreement in general, but also an overestimation of daily ET_{REF} based on the hourly equation. The overestimation

was larger in temperate climates compared to arid and tropical conditions. In this regard, Perera et al. (2015) also reported a notable seasonality as the relation between hourly and daily estimates changed with time of year.

Other studies compared ET_{REF} estimates with lysimeter measurements (e.g., Allen et al., 1994; Berengena and Gavilan, 2005; Garcia et al., 2004; Gavilan et al., 2007; Howell et al., 2000; Nolz et al., 2016; Perez et al., 2006; Yoder et al., 2005). An overall conclusion is that calculated ET_{REF} is generally larger than measured ET at small rates and vice versa. Furthermore, deviations seem to be more pronounced under semiarid and windy conditions with a high evaporative demand. Such systematic inconsistencies are usually attributed to advection of sensible heat, estimated input data (e.g., net radiation, soil heat flux) or surface resistance parameters. However, identifying the cause is extremely challenging as several interacting factors could play a role.

The overall objective of this study was to evaluate and validate the ASCE standardized reference evapotranspiration equations for a subhumid site in northeastern Austria. In this regard, the following specific objectives were addressed:

- (i) Identifying differences associated with using hourly and daily time steps of the ASCE calculation procedure;
- (ii) Evaluating computed ET_{REF} in relation to ET-values measured by a precision weighing lysimeter;
- (iii) Evaluating deviations between calculated and measured ET_{REF} considering antecedent rainfall and irrigation;
- (iv) Evaluating deviations between calculated and measured ET_{REF} with respect to seasonal effects.

The study was based on a comprehensive dataset covering several vegetation periods. Due to a specific data processing technique (Nolz et al., 2013a, b) the data contained also ET of rainy days (Nolz et al., 2014). This can be regarded as especially beneficial as many of the above-mentioned studies refer to filtered datasets only.

MATERIALS AND METHODS

The utilized dataset included meteorological data for computing reference evapotranspiration and lysimeter data from 2004 to 2011. All data were measured at an experimental site in Groß-Enzersdorf, in northeastern Austria (48°12'N, 16°34'E; 157 m). The measurement area of approximately 50×50 m was kept with short grass (except for a second lysimeter that was planted with crops alternating year by year). Agricultural fields and some small buildings surrounded the grassland. The adjacent area represents one of the major crop production areas, but also one of the driest regions of Austria. In the period 1981–2010, mean annual precipitation and temperature were 550 mm and 10.7°C, respectively; the climate can be characterized as subhumid (according to Köppen: Cfb – temperate climate without dry season and warm summer).

Meteorological data

Meteorological data were provided by the Central Institute for Meteorology and Geodynamics, Austria (ZAMG). The dataset included hourly data of solar radiation R_s ($MJ \cdot m^{-2} \cdot h^{-1}$), air temperature T (°C), relative humidity RH (%), atmospheric pressure p (kPa), and wind velocity in 10 m height U_{10} ($m \cdot s^{-1}$). Atmospheric pressure records were available only from 2006 to 2011. Daily solar radiation was calculated as hourly sums. According to ZAMG-standards, daily values for relative humidity, air pressure, and wind velocity were derived as average of the respective measurement at 7 a.m., 2 p.m., and 7 p.m. Daily

temperature represents the mean of daily maximum T_{max} and minimum T_{min} . Precipitation per day is the sum of hourly records from 7 a.m. to 7 a.m. of the following day.

Reference evapotranspiration

Reference evapotranspiration was calculated for hourly and daily time steps according to the standardized ASCE Penman-Monteith equation (Eq. 1) (ASCE-EWRI, 2005).

$$ET_{ASCE-PM} = \frac{0.408\Delta(R_n - G) + \gamma \frac{C_n}{T + 273} U_2 (e_s - e_a)}{\Delta + \gamma(1 + C_d U_2)} \quad (1)$$

In this article, calculated daily evapotranspiration for a short reference crop (similar to grass with an approximate height of 0.12 m) is referred to as $ET_{ASCE-PM, d}$ ($mm \cdot d^{-1}$). In this case, the numerator and denominator constant was $C_n = 900$ and $C_d = 0.34$, respectively. For the hourly computations the constants were $C_n = 37$ and $C_d = 0.24$ during daytime (when net radiation $R_n > 0$), and $C_d = 0.96$ during nighttime ($R_n < 0$). Sum-of-hourly (soh) evapotranspiration was computed by summing the hourly values; it is denoted as $ET_{ASCE-PM, soh}$ ($mm \cdot d^{-1}$). All inter-calculations were done according to ASCE-EWRI (2005). The slope of saturation vapor pressure-temperature curve Δ ($kPa \cdot ^\circ C^{-1}$) was calculated as a function of mean air temperature T (°C) in the respective period. Net radiation at vegetation surface R_n ($MJ \cdot m^{-2} \cdot d^{-1}$ or $MJ \cdot m^{-2} \cdot h^{-1}$) is defined as $R_n = R_{ns} - R_{nl}$, where R_{ns} is net solar radiation and R_{nl} is net long-wave radiation. R_{ns} was computed as measured solar radiation R_s minus reflected fraction $\alpha \cdot R_s$ (albedo $\alpha = 0.23$). R_{nl} was calculated as a function of the Stefan-Boltzmann constant ($4.901 \cdot 10^{-9} MJ \cdot K^{-4} \cdot m^{-1} \cdot d^{-1}$ for daily and $2.042 \cdot 10^{10} MJ \cdot K^{-4} \cdot m^{-1} \cdot h^{-1}$ for hourly time steps), actual vapor pressure e_a (kPa), mean absolute temperature T_K (K) in the respective time period, and a dimensionless cloudiness function f_{cd} . The latter is a function of relative solar radiation $R_s \cdot R_{so}^{-1}$, where R_{so} represents calculated clear-sky radiation ($MJ \cdot m^{-2} \cdot d^{-1}$ or $MJ \cdot m^{-2} \cdot h^{-1}$). R_{so} was computed as $R_{so} = K_{ab} \cdot R_a$, with $K_{ab} = a + b$ with the site-specific factors $a = 0.21$ and $b = 0.54$ (Trnka et al., 2005), and extraterrestrial radiation R_a depending on day of year, time of day, and latitude.

Soil heat flux density at the soil surface G ($MJ \cdot m^{-2} \cdot d^{-1}$ or $MJ \cdot m^{-2} \cdot h^{-1}$) was set zero for daily time steps, and for hourly time steps $0.1 \cdot R_n$ and $0.5 \cdot R_n$ at daytime and nighttime, respectively (ASCE-EWRI, 2005). The psychrometric constant γ ($kPa \cdot ^\circ C^{-1}$) is a function of atmospheric pressure p . The missing p -data of the years 2004 and 2005 were compensated by including data from a weather station at a comparable site, only 5 km apart and at the same elevation. T represents the mean air temperature at 1.5 to 2.5 m height (°C). Mean wind velocity at 2 m height U_2 ($m \cdot s^{-2}$) was calculated from measured U_{10} by means of the standard wind profile relationship according to ASCE-EWRI (2005). Saturation vapor pressure e_s (kPa) was calculated as a function of daily maximum and minimum temperature (T_{max} , T_{min}) and measured hourly T , respectively. Actual vapor pressure e_a (kPa) was computed from mean RH and T in the respective daily or hourly time interval. Alternatively, hourly e_a (2004–2011) was averaged to daily values representing the most preferred method according to ASCE-EWRI (2005).

Lysimeter evapotranspiration

Evapotranspiration of grass canopy was measured under reference conditions by means of a weighing lysimeter. The cylin-

drical lysimeter container had an inner diameter of 1.9 m (surface area = 2.85 m²) and a hemispherical bottom with a free draining outlet at 2.5 m depth. Soil was sandy loam soil (0–140 cm) over gravel (140–250 cm). In the course of the study period (2004–2011), top soil was cultivated and grass was renewed early in 2004 and 2007. Grass on and beside the lysimeter was regularly clipped and irrigated, and temporarily fertilized and cleared from weed.

Lysimeter evapotranspiration (ET_{LYS}) was determined by considering changes of soil water within the lysimeter (ΔW) and fluxes across its lower and upper boundary.

The nominal lysimeter weight was quantified by means of a weighing facility, which comprised a mechanical system to transform the weight and an electronic load cell with a measuring accuracy of ± 0.2 kg (Nolz et al., 2013a). The analog output signal was amplified, converted to digital units, averaged and stored on a local server. Logging intervals were 15 minutes from 2004 to 2009 and 10 minutes from 2009 to 2011. The logged values were converted into physical quantities (with a dimension of mass) by means of calibration factors. Dividing by the lysimeter surface area and the density of water resulted in nominal values of soil water content (W_{LYS}) with a dimension of length. It has to be noted that the total mass of the lysimeter (and the solid soil) is unknown, so the values must not be interpreted as absolute water content.

Drainage water was quantified by means of a tipping bucket at the bottom outlet of the lysimeter. Tipping and weighing data were logged at the same time. Counts of tipping were converted into outflow data using a calibration factor and divided by the lysimeter surface area to obtain drainage water (W_{DRAIN}) with a dimension of length (Nolz et al., 2013b).

Soil and drainage water were combined to a nominal time series ($W_{LYS} + W_{DRAIN}$). The time series was processed by means of smoothing functions to facilitate further data interpretation (Nolz et al., 2013b, 2014). Changes between two values of the smoothed time series were attributed to fluxes across the upper boundary of the lysimeter such as evapotranspiration (ET), precipitation (P), and irrigation (I) (Eq. 2).

$$\Delta(W_{LYS} + W_{DRAIN}) = \Delta P + \Delta I - \Delta ET_{LYS} \quad (2)$$

W_{LYS} = soil water content; W_{DRAIN} = drainage water; P = precipitation; I = irrigation; ET_{LYS} = evapotranspiration; all components have the dimension ($L \cdot T^{-1}$).

Consequently, positive values of $\Delta(W_{LYS} + W_{DRAIN})$ – referring to a time interval of 10 or 15 minutes – were attributed to precipitation and irrigation, of which the irrigation events could be identified based on manual notes. Accordingly, negative values of $\Delta(W_{LYS} + W_{DRAIN})$ were considered as lysimeter ET at reference conditions (ET_{LYS}). On this basis, ET_{LYS} was calculated for daily time steps ($ET_{LYS} / \text{mm} \cdot \text{d}^{-1}$), with each day lasting from 7 a.m. to 7 a.m. of the following day.

Comparison and statistical evaluation

The scatter diagrams in the results section illustrate the relation between one dataset as independent variable x and another dataset as dependent variable y (Table 1). The comparisons

were evaluated by means of linear regression of the form $y = a \cdot x + b$ (a = slope, b = intercept, and r^2 = coefficient of determination) and simple error analysis using root mean square error RMSE ($\text{mm} \cdot \text{d}^{-1}$) (Eq. 3).

$$RMSE = \sqrt{\frac{1}{n} \sum_{i=1}^n (y - x)^2} \quad (3)$$

RESULTS AND DISCUSSION

Identifying differences associated with using hourly and daily time steps of the ASCE calculation procedure

For comparing daily ($ET_{ASCE-PM, d}$) with sum-of-hourly reference evapotranspiration ($ET_{ASCE-PM, soh}$), $n = 2922$ data pairs were computed based on the weather data of 2004 to 2011 (Fig. 1). The correlation between the datasets was very good ($r^2 = 0.978$), but the $RMSE = 0.266 \text{ mm} \cdot \text{d}^{-1}$ indicated noticeable differences between single values of the datasets. Comparable characteristics can be found in literature: Gavilan et al. (2008) reported coefficients of correlation $r^2 = 0.986$ and 0.973 , and $RMSE = 0.24$ and $0.36 \text{ mm} \cdot \text{d}^{-1}$ ($n = 1090$) for two semiarid sites in Spain. Irmak et al. (2005) tested both calculation methods for nine reference sites in the United States, resulting in r^2 values between 0.947 and 0.987, and $RMSE$ between 0.25 and $0.56 \text{ mm} \cdot \text{d}^{-1}$ ($n = 366$ – 1826). Perera et al. (2015) presented average values of $r^2 = 0.981$ and $RMSE = 0.281 \text{ mm} \cdot \text{d}^{-1}$ for 40 Australian sites; however, the mean slope ($a = 0.948$) and intercept ($b = 0.195$) indicated considerable deviation from the 1:1 line. Differences between daily and hourly computations are assumed to occur due to averaging of weather data (for the daily values) and due to different surface resistance parameters for daily and hourly calculation steps. In general, both methods have their advantages. Daily calculations, above all, are easier to handle. On the other hand, hourly calculations allow estimating ET_{REF} (and consequently plant water uptake) during the course of day and night, including also dew formation (e.g. Nolz et al., 2014). For longer periods, both methods are expected to deliver similar results. However, the annual sums of the hourly calculation steps were larger than the sums of daily values (Table 2). A similar overestimation of hourly calculations was reported by Perera et al. (2015). When looking more closely to the linear trend and the 1:1 line in Fig. 1, it appears that $ET_{ASCE-PM, soh}$ was slightly larger at moderate ET -rates of around $4 \text{ mm} \cdot \text{h}^{-1}$. Although these deviations are small, they seem to add up to larger differences in the annual sums (Table 2).

Evaluating computed ET_{REF} in relation to ET -values measured by a precision weighing lysimeter

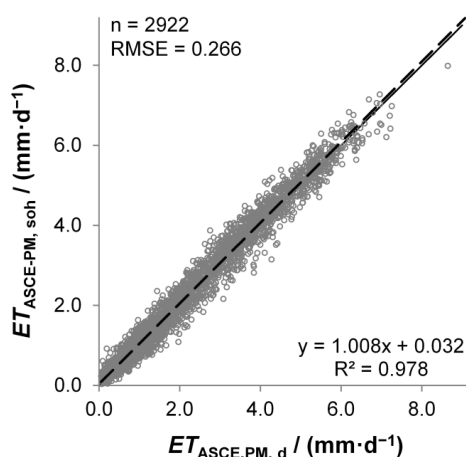
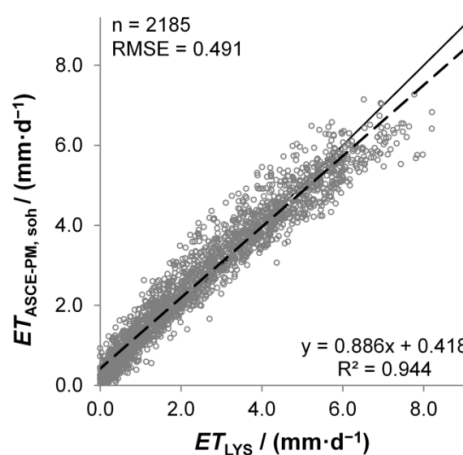
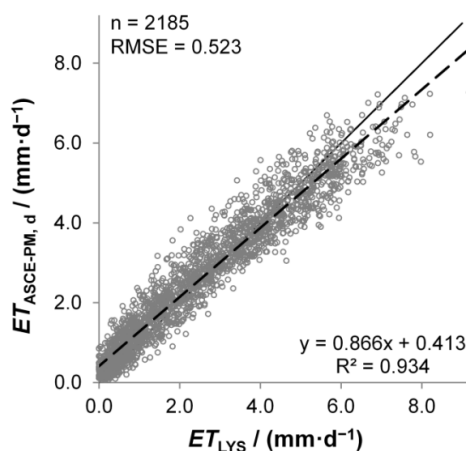
Evapotranspiration data from the reference lysimeter (ET_{LYS}) include the vegetative periods of grass between 2004 and 2011. Some data were missing because of system failures or excluded because of adverse conditions such as snow and frost during winter. Thus, $n = 2185$ daily values (of max. $n = 2920$) remained for evaluation, which is a considerable number compared to other studies. Daily computations ($ET_{ASCE-PM, d}$) correlated well with daily measurements (ET_{LYS}): r^2 was 0.934 and

Table 1. Comparison of datasets from calculations (calc.) and lysimeter measurements (meas.).

	Independent variable x	Dependent variable y
Daily calc. vs. sum-of-hourly calc.	$ET_{ASCE-PM, d} / \text{mm} \cdot \text{d}^{-1}$	$ET_{ASCE-PM, soh} / \text{mm} \cdot \text{d}^{-1}$
Daily calc. vs. daily meas.	$ET_{LYS} / \text{mm} \cdot \text{d}^{-1}$	$ET_{ASCE-PM, d} / \text{mm} \cdot \text{d}^{-1}$
Daily calc. vs. sum-of-hourly meas.	$ET_{LYS} / \text{mm} \cdot \text{d}^{-1}$	$ET_{ASCE-PM, soh} / \text{mm} \cdot \text{d}^{-1}$
Hourly calc. vs. hourly meas.	$ET_{LYS, h} / \text{mm} \cdot \text{h}^{-1}$	$ET_{ASCE-PM, h} / \text{mm} \cdot \text{h}^{-1}$

Table 2. Overview on reference evapotranspiration, air temperature, and precipitation during the studied years.

	Annual sum $ET_{ASCE-PM, d}$ mm	Annual sum $ET_{ASCE-PM, soh}$ mm	Annual mean temperature °C	Annual mean precipitation mm
2004	790	812	10.6	540
2005	792	810	10.3	520
2006	822	845	10.9	520
2007	908	920	11.9	770
2008	836	857	11.7	610
2009	835	854	11.4	560
2010	760	774	10.1	690
2011	846	863	11.3	400

**Fig. 1.** Calculated sum-of-hourly ($ET_{ASCE-PM, soh}$) versus daily ($ET_{ASCE-PM, d}$) reference evapotranspiration.**Fig. 3.** Reference ET computed as sum-of-hourly values ($ET_{ASCE-PM, soh}$) versus lysimeter measurements under reference conditions (ET_{LYS}).**Fig. 2.** Reference ET computed for daily time steps ($ET_{ASCE-PM, d}$) versus lysimeter measurements under reference conditions (ET_{LYS}).

RMSE was $0.523 \text{ mm}\cdot\text{d}^{-1}$ (Fig. 2). The latter indicates the average accuracy that can be expected for any estimated value. Unfortunately, we could not find a comparable lysimeter study stating explicitly the same statistical parameters r^2 and RMSE in literature. A comparable study presenting the standard error of the estimate (SEE, instead of RMSE) was published by Yoder et al. (2005). They related FAO56-ET to lysimeter ET ($n = 296$, data from 5 years), resulting in correlation parameters $a = 0.755$ and $b = 0.709$, a coefficient of correlation $r^2 = 0.909$, and an SEE = $0.31 \text{ mm}\cdot\text{d}^{-1}$. The linear trend line in Fig. 2 illustrates an overestimation of $ET_{ASCE-PM, d}$ at small values and an underestimation at larger values. This is in accordance with results of many other studies (e.g., Allen et al., 1994; Berengena and Gavilan, 2005; Garcia et al., 2004; Gavilan et al. 2007; Howell et al., 2000; Perez et al. 2006; Yoder et al., 2005).

The correlation between sum-of-hourly data ($ET_{ASCE-PM, soh}$) and ET_{LYS} was slightly better than that of the daily time steps: r^2 was 0.944 and RMSE was $0.491 \text{ mm}\cdot\text{d}^{-1}$ (Fig. 3). As the latter represents the average deviation of a single value, sum-of-hourly calculations can be regarded marginally more accurate than the daily calculations with an RMSE = $0.523 \text{ mm}\cdot\text{d}^{-1}$ (Fig. 2). By applying the same method, Gavilan et al. (2007) achieved a correlation with slope $a = 0.82$ and intercept $b = 1.12$; r^2 was 0.92 and RMSE was $0.45 \text{ mm}\cdot\text{d}^{-1}$ (only small dataset of $n = 81$). Thus, a value of $0.5 \text{ mm}\cdot\text{d}^{-1}$ is supposed to represent the expected accuracy when estimating ET_{REF} . Under the given environmental conditions, it is therefore recommended to access hourly weather data and calculate sum-of-hourly values to obtain as accurate as possible estimations of daily of ET_{REF} .

Evaluating deviations between calculated and measured ET_{REF} considering antecedent rainfall and irrigation

Despite the better performance, the course of the trend line in Fig. 3 reflects the same tendency as presented for daily calculations. Above all, it indicates a considerable underestimation of $ET_{ASCE-PM}$ at larger values. Some of these values could be attributed to days at which the lysimeter was irrigated. In such cases, the wetting of the surface might have led to increased evaporation rates at the lysimeter, which are beyond the definition of reference evapotranspiration. Furthermore, antecedent rainfall could have had an influence. To examine if these limitations of lysimeter measurements affected the model validation in general, the available dataset was filtered: Fig. 4 illustrates data pairs of days without rain and irrigation ($n = 1153$). In this case, potential disturbing impacts from unintended evaporation were avoided. Compared to Fig. 3, correlation was similar and RMSE was slightly larger (but still smaller than in Fig. 2).

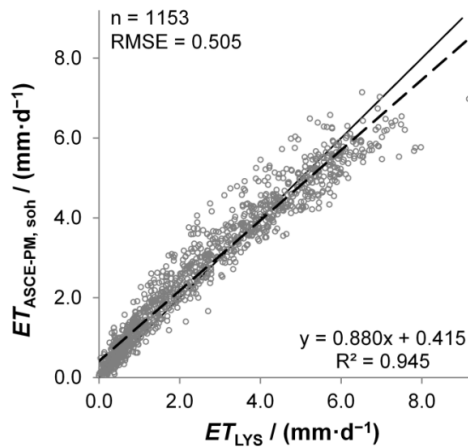


Fig. 4. Calculated ($ET_{ASCE-PM, \text{soh}}$) versus measured (ET_{LYS}) ET at days without rain and irrigation to avoid disturbing influences from unintended evaporation.

Hence, it can be concluded that antecedent rainfall and irrigation events did not bias the presented ET measurements.

As a further filtering approach, only days up to three days after rainfall and irrigation were considered. This was done to guarantee satisfactory soil moisture distribution at the study site and to reduce advection of sensible heat from the surroundings.

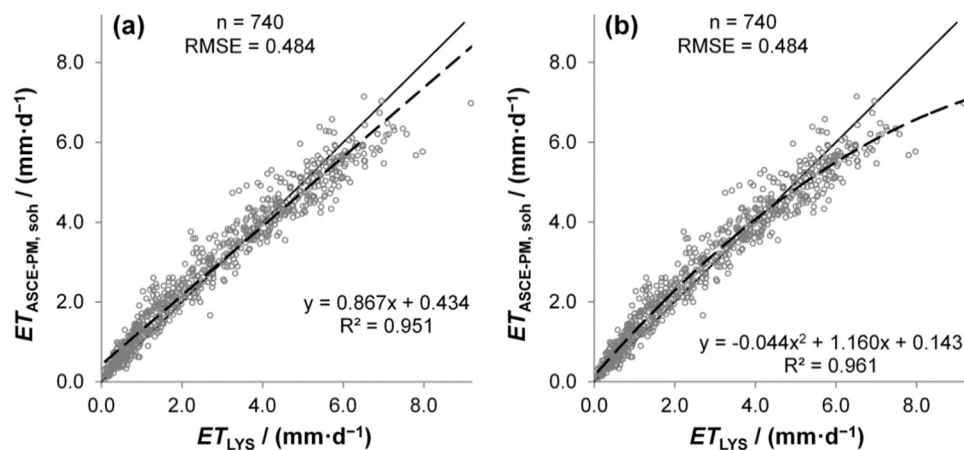


Fig. 5. Calculated ($ET_{ASCE-PM, \text{soh}}$) versus measured (ET_{LYS}) ET at days without rain and irrigation, including only up to three days after rainfall to guarantee homogenous soil moisture distribution at the study site; (a) with linear trend, (b) with polynomial trend.

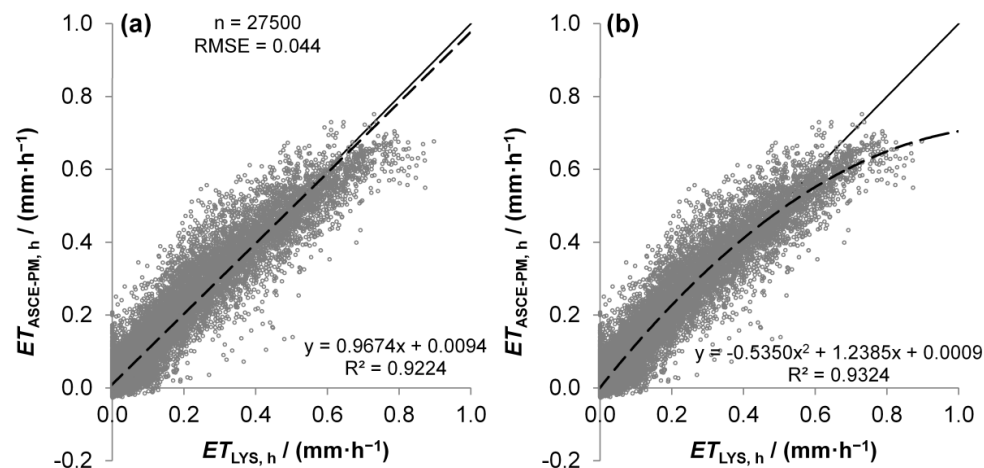


Fig. 6. Hourly calculated ($ET_{ASCE-PM, \text{h}}$) versus hourly measured ($ET_{LYS, \text{h}}$) ET of a 4-year-period (2008 to 2011); (a) with linear trend, (b) with polynomial trend.

In this context, it has to be mentioned that advection of sensible heat at this study site is supposed to have minor impact according to Nolz et al. (2016). The final (reduced) dataset contained $n = 740$ data pairs, which is still comparable to sample sizes of other ET studies (e.g. Gavilan et al., 2008; Irmak et al., 2005). The resulting correlation (Fig. 5a) and the parameters r^2 and RMSE were similar to Fig. 3. From this can be concluded that the dataset and the results are consistent and not influenced by systematic measurement errors.

Nevertheless, it seems that the linear trend in Fig. 5a does not represent the best possible correlation. In fact, r^2 could be increased by fitting a polynomial trend (Fig. 5b). The latter indicates good accordance at small ET -rates, while the calculated values seem to exceed the measurements at moderate rates, and underestimate measurements at large rates. The same characteristic can be deduced from Fig. 2 and Fig. 3.

Hourly calculated and measured data pairs were linearly correlated with an r^2 of 0.922 (Fig. 6), which is comparable to the correlation of daily data (Fig. 2). This indicates that there are no systematic errors between hourly and daily calculation steps.

However, deviations between single values – as reflected by the scatter-plot in Fig. 6 – reveal a larger uncertainty when estimating hourly ET . The respective RMSE was $0.044 \text{ mm}\cdot\text{h}^{-1}$. It is obvious that at ET -rates larger than $0.6 \text{ mm}\cdot\text{h}^{-1}$ lysimeter measurements were considerably larger than the calculated values; on the other hand, measurements between 0.2 and

$0.4 \text{ mm}\cdot\text{h}^{-1}$ were overestimated by calculations. Similar to the daily values, this caused a slight shift of the linear trend illustrated Fig. 6a, and a considerable curvature of the polynomial trend in Fig. 6b. Further interpretations are beyond the scope of this article, but examining this phenomenon in future studies is highly recommended.

Evaluating deviations between daily calculated and measured ET_{REF} with respect to seasonal effects

To be able to evaluate whether the nonlinear relationship arose due to seasonal effects, the scatter plots were separated into the four seasons. In Fig. 7, spring is represented by the months March, April, and May (MAM, Fig. 7a), summer covers June, July, and August (JJA, Fig. 7b), autumn covers September, October, and November (SON, Fig. 7c), and winter covers December, January, and February (DJF, Fig. 7d). It appears that in autumn (Fig. 7c) the trend line is close to the 1:1-line, indicating a very good accordance between measurements and calculations. For the other seasons (Fig. 7a, c, and d), small ET_{REF} -values are overestimated and vice versa – as it is generally the case. Consequently, no distinct seasonal effects can be deduced from the data shown in Fig. 7 compared to the entire data set as shown in Fig. 3.

Furthermore, ratios were calculated of ($ET_{ASCE-PM, \text{soh}} / ET_{ASCE-PM, \text{d}}$) (Fig. 8a), ($ET_{ASCE-PM, \text{soh}} / ET_{LYS}$) (Fig. 8b), and ($ET_{ASCE-PM, \text{d}} / ET_{LYS}$) (Fig. 8c). This was done to be able to evaluate the average difference between the data sets. Fig. 8 contains the ratios of the entire data set (All) as well as single seasons (spring-months – MAM, summer-months – JJA, au-

tumn-months – SON, and winter-months – DJF). The ratios are illustrated as box plots with the median as a dash. A value close to one represents a good accordance of the data sets, while deviations reveal underestimation or overestimation of values. The boxes in Fig. 8 represent the 25 to 75% quantiles, the whiskers indicate the 5 and 95% percentile, and outliers are depicted as crosses. It has to be noted that such ratios strongly depend on the absolute values of ET , which is the reason why large values (outliers) must be accepted in this way of representing. Mean ratios of computed sum-of-hourly values to daily values were 1.00 for the summer months, indicating a very good match on average (Fig. 8a, and Table 3). However, sum-of-hourly values were 5% larger than daily values when considering the entire year. These results are similar to the ratios reported by Perera et al. (2015) for stations with comparable climatic conditions. Calculated values were generally larger than measured ones, as demonstrated by ratios larger than one in Fig. 8b, c, and Table 3. Seasonal differences were obvious, although the ratios for the winter months (DJF) must not be over-interpreted as the grass might have been in dormancy. Overall, the results clearly indicate the best performance of the ET -equations in summer (mean close to one, narrow quantiles). Furthermore, calculations generally overestimated measured values as indicated by values larger 1.00 in Table 3. In March, April, May (MAM) and September, October, November (SON), daily calculations outperformed sum-of-hourly calculations. On the other hand, standard deviations of the sum-of-hourly calculations were smaller, which is in accordance with the smaller RMSE value shown in Fig. 3. The overall conclusion is that sum-of-hourly calculations are expected to deliver

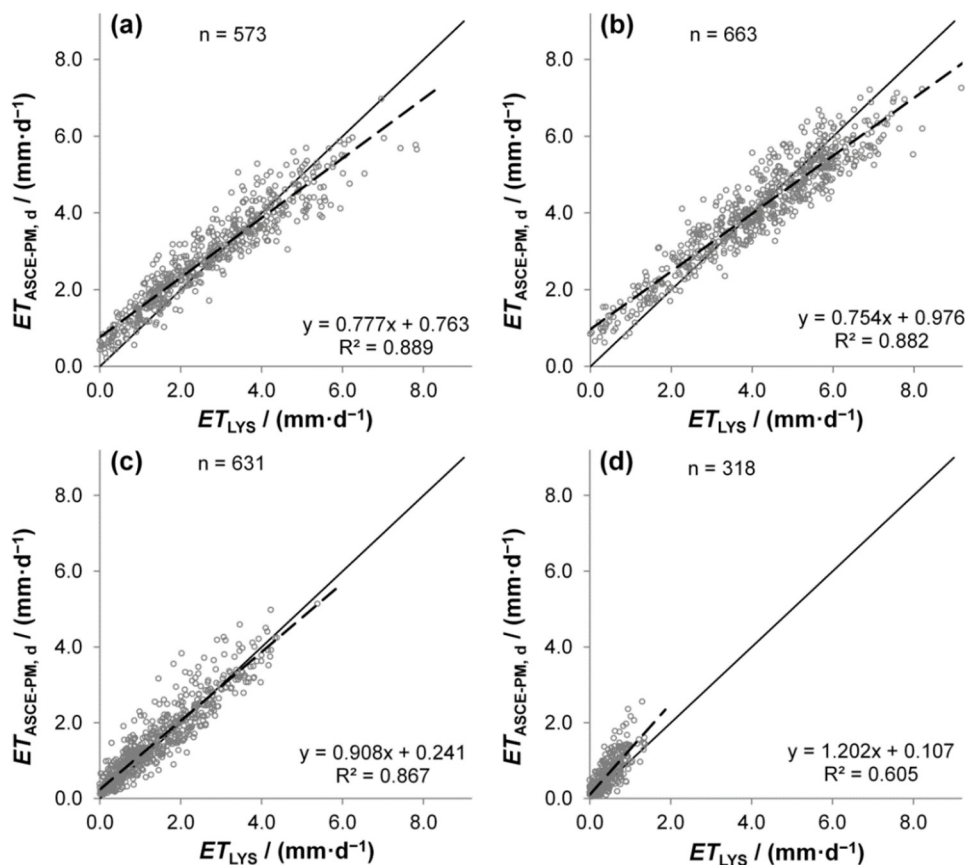


Fig. 7. Evaluation of computed versus measured data with respect to seasonal differences: correlations of spring- (a) and summer-data (b) are similar to the correlation of the entire data set (Fig. 3); autumn-data (c) are more close to the 1:1-line; winter-data (d) do not allow a consistent conclusion based on the correlation.

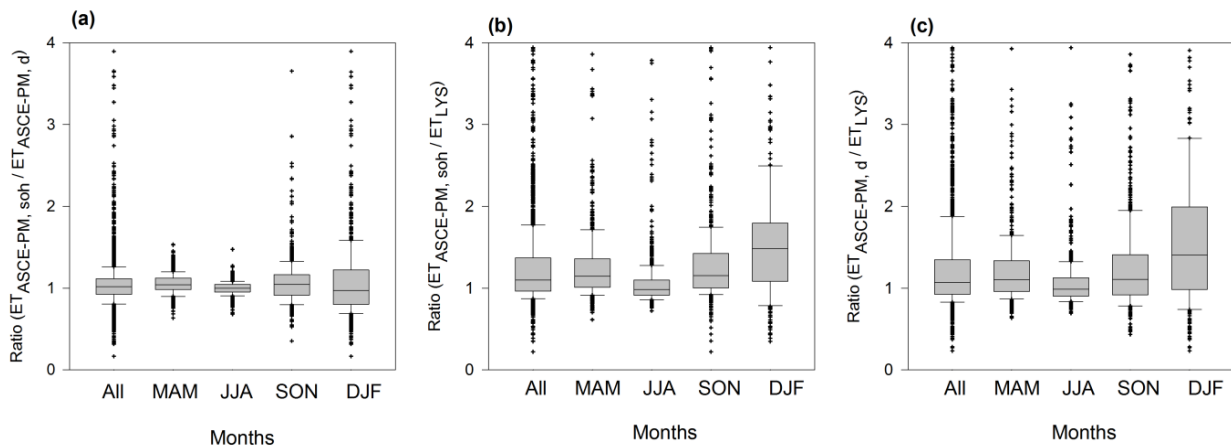


Fig. 8. Ratios of (a) calculated (b), (c) calculated and measured ET values illustrating general (All) and seasonal (MAM, JJA, SON, DJF) differences as deviations from a value of one.

Table 3. Mean values and standard deviations (SD) of the ratios illustrated in Fig. 8.

	Ratio ($ET_{ASCE-PM, soh} / ET_{ASCE-PM, d}$)					Ratio ($ET_{ASCE-PM, soh} / ET_{LYS}$)					Ratio ($ET_{ASCE-PM, d} / ET_{LYS}$)				
Months	All	MAM	JJA	SON	DJF	All	MAM	JJA	SON	DJF	All	MAM	JJA	SON	DJF
Mean	1.05	1.05	1.00	1.07	1.10	1.28	1.27	1.08	1.33	1.66	1.28	1.24	1.09	1.31	1.69
SD	0.32	0.12	0.08	0.27	0.56	0.66	0.56	0.40	0.65	1.03	0.75	0.59	0.46	0.74	1.20

values that are more accurate for a single day. Seasonal effects are observable, but further studies are recommended to determine the underlying causes.

CONCLUSIONS

The ASCE standardized ET_{REF} -equations were evaluated at a subhumid site in northeastern Austria. ET_{REF} -values were calculated for hourly and daily time steps, whereof the former were processed to sum-of-hourly values. (i) Identifying differences associated with using hourly and daily time steps: Sum-of-hourly values correlated well ($r^2 = 0.978$) with values computed on daily time steps, but an RMSE of 0.27 mm specified differences (uncertainties) between the calculation procedures. (ii) Evaluating computed ET_{REF} in relation to ET -values measured by a precision weighing lysimeter: Comparing the calculations to lysimeter measurements confirmed overestimation of small ET_{REF} -values and underestimation of large values as known from other studies. Based on the scatter plots, the sum-of-hourly computations outperformed the daily computations, as r^2 of the former was slightly larger and RMSE was slightly smaller. (iii) Evaluating deviations between calculated and measured ET_{REF} considering antecedent rainfall and irrigation: It was shown that the results were not distorted by antecedent rainfall, irrigation, or insufficient soil water conditions. (iv) Evaluating deviations between calculated and measured ET_{REF} with respect to seasonal effects: Seasonal effects were obvious – with computations and measurements being closest to each other in the summer months. In general, sum-of-hourly computations delivered the best estimation of ET_{REF} for a single day. Daily calculation steps, of course, have the advantage of being simpler. Hence, both calculation methods have their advantages under the given environmental conditions. On the other hand, neither of them results in a fully satisfying estimation of ET_{REF} , so further studies are recommended in this regard.

Acknowledgements. We thank our co-workers from IHLW and the staff from BOKU experimental station in Groß-Enzersdorf for maintaining the lysimeter facilities. We also thank the Central Institute for Meteorology and Geodynamics, Austria (ZAMG) for providing weather data. This article was prepared in the frame of a project that was supported by the Slovak Research and Development Agency (project ID: SK-AT-2015-0018) and by the Austrian Agency for International Cooperation in Education and Research (OeAD-GmbH, project ID: SK 08/2016).

REFERENCES

- Aboukhaled, A., Alfaro, A., Smith, M., 1982. Lysimeters. In: Irrigation and Drainage Paper 39, FAO, Rome (Italy), 73 p.
- Allen, R.G., Smith, M., Perrier, A., Pereira, L.S., 1994. An update for the calculation of reference evapotranspiration. ICID (International Commission on Irrigation and Drainage) Bulletin, 43, 2, 35–92.
- Allen, R.G., Pereira, L.S., Raes, D., Smith, M., 1998. Crop evapotranspiration: guidelines for computing crop water requirements. In: Irrigation and drainage paper 56. Food and Agriculture Organization of the United Nations, Rome.
- Allen, R.G., Pereira, L.S., Howell, T.A., Jensen, M.E., 2011. Evapotranspiration information reporting: I. Factors governing measurement accuracy. Agricultural Water Management, 98, 899–920.
- ASCE-EWRI, 2005. The ASCE standardized reference evapotranspiration equation. In: Allen, R.G., Walter, I.A., Elliott, R., Howell, T., Itenfisu, D., Jensen, M. (Eds.): ASCE-EWRI Task committee report. American Society of Civil Engineers, Reston, VA, 171 p.
- Berengena, J., Gavilán, P., 2005. Reference evapotranspiration estimation in a highly advective semiarid environment. J. Irrig. Drain. Eng., 131, 2, 147–163.
- Doorenbos, J., Pruitt, W.O., 1977. Guidelines for predicting

- crop water requirements. In: Irrigation and drainage paper 24. Food and Agriculture Organization of the United Nations, Rome, 175 p.
- Garcia, M., Raes, D., Allen, R., Herbas, C., 2004. Dynamics of reference evapotranspiration in the Bolivian highlands (Altiplano). *Agric. For. Meteorol.*, 125, 1–2, 67–82.
- Gavilan, P., Berengena, J., Allen, R.G., 2007. Measuring versus estimating net radiation and soil heat flux: Impact on Penman–Monteith reference ET estimates in semiarid regions. *Agric. Water Manage.*, 89, 275–286.
- Gavilán, P., Estévez J., Berengena J., 2008. Comparison of standardized reference evapotranspiration equations in southern Spain. *J. Irrig. Drain. Eng.*, 134, 1–12.
- Howell, T.A., Evett, S.R., Schneider, A.D., Dusek, D.A., Copeland, K.S., 2000. Irrigated fescue grass ET compared with calculated reference grass ET. In: *Proceedings of 4th National Irrigation Symposium, ASAE, Phoenix, AZ*, pp. 228–242.
- Irmak, S., Howell, T.A., Allen, R.G., Payero, J.O., Martin, D.L., 2005. Standardized ASCE Penman–Monteith: impact of sum-of-hourly vs. 24-hour timestep computations at reference weather station sites. *T. ASEA*, 48, 1063–1077.
- Jensen, M.E., Burman, R.D., Allen, R.G., 1990. *Evapotranspiration and irrigation water requirements. ASCE Manuals and Reports on Engineering Practice, No. 70.* American Society of Civil Engineers, New York.
- Nolz, R., Kammerer, G., Cepuder, P., 2013a. Interpretation of lysimeter weighing data affected by wind. *J. Plant Nutr. Soil Sci.*, 176, 200–208.
- Nolz, R., Kammerer, G., Cepuder, P., 2013b. Improving interpretation of lysimeter weighing data. *Die Bodenkultur: J. Land Manage. Food Environ.*, 64, 27–35.
- Nolz, R., Cepuder, P., Kammerer, G., 2014. Determining soil water-balance components using an irrigated grass lysimeter in NE Austria. *J. Plant Nutr. Soil Sci.*, 177, 237–244.
- Nolz, R., Cepuder, P., Eitzinger, J., 2016. Comparison of lysimeter based and calculated ASCE reference evapotranspiration in a subhumid climate. *Theor. Appl. Climatol.*, 124, 315–324.
- Perez, L., Castellvi, F., Martínez-Cob, A., Villalobos, F.J., 2006. A simple parameterization of bulk canopy resistance from climatic variables for estimating hourly evapotranspiration. *Hydrol. Process.*, 20, 515–532.
- Perera, K.C., Western, A.W., Nawarathna, B., George, B., 2015. Comparison of hourly and daily reference crop evapotranspiration equations across seasons and climate zones in Australia. *Agric. Water Manage.*, 148, 84–96.
- Trnka, M., Žalud, Z., Eitzinger, J., Dubrovský, M., 2005. Global solar radiation in Central European lowlands estimated by various empirical formulae. *Agric. For. Meteorol.*, 131, 54–76.
- Yoder, R.E., Odhiambo, L.O., Wright, W.C., 2005. Evaluation of methods for estimating daily reference crop evapotranspiration at a site in the humid Southeast United States. *Appl. Eng. Agric.*, 21, 2, 197–202.

Received 8 January 2018
Accepted 30 October 2018